The University Of Sheffield.

The movement behaviour of solitary and collectively twitching *Pseudomonas aeruginosa* cells on surfaces

Nathan Andrew Costin

A thesis submitted in partial fulfilment of the requirements for the degree of Doctor of Philosophy

The University of Sheffield
Faculty of Science
Department of Physics and Astronomy

January 2023

Acknowledgements

Life, at all length scales, is comprised of individuals overcoming novel, unknown challenges to grow and thrive. Each singular journey is far from isolated and individual experiences are propelled, enriched and enjoyed with those close by. Much like the bacteria that I've witnessed twitch, crawl and expand, over the past four years I have been lucky to be surrounded by countless wonderful people that have made me smile and laugh, challenged me to grow whilst providing support and guidance on the way. Each and every one of you have contributed to the following 150 or so pages, and for that you have my eternal gratitude.

To begin my thanks, there is no one who has had more of an influence on my development as a scientist as my outstanding supervisor, Mack Durham. Never before have I met someone who works harder, pulling ideas and concepts from such a broad range of disciplines to further science. Throughout my entire PhD I have been lucky to experience your dedication, kindness, and when things go wrong, patience, in all aspects of the work we have performed together. Thank you for always encouraging me to think critically, work smartly and use my time wisely, three lessons I will be taking into my life going forward. It has been an enormous pleasure to explore how tiny organisms move.

And along with Mack's stewardship, this thesis could never have been written without my fellow researchers! A huge thank you to Jamie Wheeler for your expertise on all things biological and how to deal with the challenges of academia, I will remember our Falafel King courtyard chats fondly. To Oliver Meacock for the consistent and thorough support in my coding and analysis endeavours, and Mina Mohaghegh for welcoming me to Sheffield and for helping me take my first steps into wet lab work. Last but not least, thank you to Anne Williams for teaching me how to teach and for all the cookies and cinnamon rolls.

No research group acts as an isolated unit, and I would like to extend my heartfelt thanks to Christa Walther, Darren Robinson and Nick van Hateren. Imaging single sheets of bacteria in two channels proved a challenging prospect and without your support this research would not have taken place. A huge thank you to Rachel Bearon for collaborating with us on our twiddling project. Finally, thank you to all members of the Foster Group for welcoming me into Firth Court with open arms. Terry the Turkey Hat will miss his yearly trips to Hathersage!

To Mum, Dad and Ben thank you so, so much for the unbelievable amount of support you have all given me before my PhD, during, and for whatever comes after, I truly would not have made it here without your encouragement. Visiting always provided me with a well deserved rest, whilst

football games, BBQ's and brown dinners were something I always looked forward to. Even when far away, I have always knew that #Merky (Tracey Island) is just a call away, even if it takes a while to work out how to face time.

I've been blessed to have Grandparents who take a keen interest in my life. I'd like to thank you all for always encouraging me to do my best, work hard and enjoy myself. Thanks to Gramma for encouraging me to cook, Popples for getting me to laugh, Grandad for being my source of scientific curiosity, and Grandma for keeping an eye on me, having heated debates, and making sure I stay on track.

My time in Sheffield has been shaped by so many wonderful people, and without them my life would be unrecognisable from today. To Sweden, Dev and Dan, for making the houses we lived in homes. There are many long days in academia, and you were all there to make me smile after a long uphill walk back from work. Whether it be cinema Sundays, watching a football game or just enjoying the view at Bole Hill, a day spent in your company was never a day wasted. Thanks to Britt, Chris and Ale for being the most compassionate, caring and wonderful friends. You all brightened my toughest days and I would have not got to the finish line without you. I'm grateful to James for his lacrosse prowess and masterful musical taste, enjoying every trip across the peaks, training session or night out. For all their help in guiding me to good decisions and helping me through the not so good ones, thanks Sarah and Emily, and all of the coffee along the way. I will be eternally grateful for the support of Charlotte and Laura in all aspects of my life. It's truly a blessing to have friends that are always there to support me and although our web has been stretched across the country I'm delighted it is as strong as ever.

An acknowledgement section from me would be incomplete without mentioning lacrosse, so thank you to Sheffield University Lacrosse Club, Sheffield Universities Men's Lacrosse Club and Sheffield Steelers Lacrosse Club. I've met some fantastic people through each team I've played for, leaving me brimming with confidence and joy after each training session, match or social.

Finally, I'd like to thank past me. Goodness this was difficult, well done for reaching the end.

Attributions

This thesis outlines work that will be submitted as a first author manuscript to a scientific journal in the coming months (**Chapters 2**, **3** and **4**). In addition, this thesis also contains work that will be included in a second manuscript as a co-author (**Chapter 5**). Aside from the contributions noted below, I am solely responsible for all work in this thesis. I am grateful for all of the contributions made to this work, which are as follows:

- Dr William Durham, Dr Oliver Meacock and Dr James Wheeler assisted with design of experiments, development of simulations, and the interpretation of data.
- Dr James Wheeler designed and built the FimX-YFP strain of *Pseudomonas aeruginosa* used in **Chapters** 3 and 4.
- Data from the results in **Figure 23** come from a SPR simulation developed by Dr Oliver Meacock.
- The initial discovery of twiddles in twitching *Pseudomonas aeruginosa* cells was made by Dr James Wheeler.
- The microfluidic experiments outlined in **Chapter** 5 were conceived by Dr William Durham and Dr James Wheeler, and performed and analysed by Dr James Wheeler.
- Professor Rachel Bearon developed a preliminary version of the individual based model presented in **Chapter** 5.
- Dr William Durham and Dr James Wheeler both provided comments on a first draft of this thesis.

Abstract

The opportunistic pathogen *Pseudomonas aeruginosa* uses grappling hook-like appendages called pili to move across surfaces. During early stages of biofilm development, local cell density increases such that bacteria transition from solitary individuals to densely packed monolayers. This thesis resolves how individual bacterial movement behaviour impacts their ability to navigate when they are travelling individually and collectively in densely packed groups.

Collective movement in rod-shaped bacteria is routinely modelled as a two-dimensional nematic system in which neighbouring cells align their orientations, but do not necessarily pull themselves in the same direction. Using massively parallel cell tracking, fluorescent fusions, and an automated analysis pipeline, we show that cells actively reverse their movement direction when travelling in a direction opposite to that of their neighbours. This previously unobserved movement behaviour contributes to a highly polarised state where neighbouring cells actively pull themselves in the same direction. By working together, rather than against one another, this behaviour is predicted to enhance the rate of colony expansion.

We then investigate the role of 'twiddles' in solitary cells performing pili-based chemotaxis. While chemotaxis was previously thought to be solely driven by reversals in movement direction, we experimentally observe that cells can smoothly turn the direction of their movement via a process that we call a 'twiddle'. To resolve the potential role of twiddles in chemotaxis, we developed an individual-based model that was parameterised using experimental data. Our results show that twiddles and reversals can each drive chemotactic response, but show strong differences in the parameter regimes where they are most effective. Our results indicate that *P. aeruginosa* cells use both types of orientation behaviours to maximise their ability to position themselves within nutrient source across different environmental conditions.

Our findings highlight the unique ways that bacteria have evolved to regulate their motility on surfaces.

Contents

List of Tables

List of Figures

Declaration

I, the author, confirm that the Thesis is my own work. I am aware of the University's Guidance on the Use of Unfair Means (www.sheffield.ac.uk/ssid/unfair-means). This work has not been previously been presented for an award at this, or any other, university.

1 Introduction

Movement is a ubiquitous element of life at all length scales, and provides organisms with the means to enhance their evolutionary fitness. An organism's direction of travel changes for a variety of reasons: to reach a food source, to avoid predators or conflicts with competitors. While the movement patterns of many organisms can are highly complex, experiments on bacterial cells have allowed researchers to obtain a deep understanding on how movement behaviour has evolved, because it is relatively easy to obtain data from thousands of individual organisms, that each are genetically identical to one another, in a single laboratory experiment, as they respond to well-defined stimuli. Bacteria use a wide variety of different mechanisms to propel themselves, which is typically biased by altering the rate at which they change their direction of travel [1].

Bacterial movement has been historically focused on how single bacteria use flagella to swim through fluid [2]. Although these studies have revolutionised our understanding of bacterial behaviour (and the physical and molecular mechanism involved), bacteria actually spend large portions of their lives attached to a surface. Whilst surface attached, some bacteria move through twitching motility, a jerky form of motion facilitated by the extension and retraction of a fibre like appendage known as the Type IV pilus [3, 4]. Type IV pili are essential in infection, as they enable bacteria to colonise tissues where they otherwise would not be able to [5, 6]. They also enable the exchange of DNA between cells [7]. Bacteria, in particular *Pseudomonas aeruginosa*, use twitching motility to form clusters with nearby single cells, forming micro-colonies, the sites of future biofilm formation [8, 9].

Bacteria spend the majority of their lives in surface attached biofilms, collectives of millions of surface-attached cells that produce a glue-like matrix containing extracellular polymeric substances (EPS). The matrix provides the constituents with protection from environmental factors such as detachment by flow and a resistance to antibiotic treatment [3, 10, 11]. During biofilm formation, cell density increases beyond a critical value, and collective behaviours begin to emerge, as individual movement becomes highly influenced by physical interactions with neighbouring cells [12, 13]. Collective movement is commonly studied in *P. aeruginosa* monolayers near the edge of expanding colonies, where the cells form single layered, two dimensional sheets [14]. In this two-dimensional environment, the movement of the collective behaves similarly to a liquid crystal and is modelled as an active nematic system [15]. Despite the advancements made in understanding the dynamics of the collective, little consideration has been given to if individual cells can influence collective movement by regulating their behaviour.

Whilst forming a biofilm or living a in a mature one, each bacterium is capable of regulating

its movement by responding to chemical and physical stimuli, driving cells towards more favourable conditions [16, 17]. Developments in the field of microfluidics have allowed for the generation of quantifiable and reliably produced chemical gradients, allowing high resolution studies of bacterial chemotaxis to be performed [18]. Additionally, single *P. aeruginosa* cells have recently been tracked in densely packed monolayers for the first time, revealing new physics that occurs during biofilm development [19]. Utilising these technologies this thesis first investigates how individual bacterial movement behaviour facilitated by twitching motility has the ability to influence the collective properties of a bacterial monolayer and groups of cells at the periphery of the colony. Secondly, we quantify the role a novel form of twitching behaviour has on single cell chemotaxis across surfaces, and how it impacts how cells distribute themselves around a source of nutrients.

1.1 Bacteria have evolved fascinating ways to move

As bacteria occupy nearly every environmental niche it is unsurprising that they have developed a plethora of mechanisms to facilitate movement, and are capable of responding to chemical and physical cues in their surroundings [20, 21]. We begin the upcoming section by providing an overview of different forms of motility that both planktonic and surface associated cells use. As this thesis focuses on the latter, we provide a description of the structure and operation of the type IV pilus machine, and how it is used to facilitate chemotaxis using the Pil-Chp system [22]. After considering how *P. aeruginosa* responds to chemical signals, we then discuss mechanosensing, the process of bacteria detecting and responding to physical stimuli. Finally, we consider the methods used to study twitching motility and how fluorescent labelling is used to resolve how proteins in the Pil-Chp are regulated during pili-based motility.

We will now outline four methods that bacteria have developed to move. Of the four, swimming is by far the most extensively studied, and is typically done so using *Escherichia coli* as a model organism. Swimming is performed whilst *E. coli* is in a planktonic state and is facilitated by multiple flagella that are distributed over the cell body [23]. A flagellum is formed of three main components: a motor that rotates clockwise (CW) or counter clockwise (CCW), a hook that acts as a joint which transfers torque from the motor to the filament, a flexible whip like filament that can be up to 15 μm in length [24]. Swimming motility in *E. coli* is characterised by a series of 'runs' and 'tumbles', driven by CCW and CW rotation of the rotary motor respectively [25]. When driven CCW, a bundle of flagella form and the cell body is propelled forward, giving rise to a run. When the motor rotates CW, the flagella unbundle and the cells comes to a stop and reorients, which is called a 'tumble'. Following a tumble end, *E. coli* swims in a new direction [26]. Typically, *E. coli* travels approximately 25 μm

s^{-1} during runs, which are punctuated by tumbles approximately every second [25, 27]. Rather than having multiple flagella, *P. aeruginosa* has a singular polar flagellum that operates in a 'run-reverse-pause' manner, which arises from an additional phase where the rotary motor intermittently pauses [28]. These different forms of swimming motility are often modelled as a random walk to understand how the different mechanisms or reorientation affect chemotaxis and dispersal [29].

Once surface associated, *P. aeruginosa* ceases to use its flagellum and begins to upregulate virulence factors, including the operation of Type IV pili (TFP), $1-4$ μm long, 7 nm wide fibre like appendages that extend from the pole of the cell [30, 31]. Twitching motility is facilitated by the extension of TFP from the cell pole, attachment of the tip to the surface, and the subsequent retraction of the pilus, exerting forces of up to 100 pN, capable of pulling the cell body at speeds of approximately 0.1 μm s^{-1} [32, 33, 34]. Typically, one pilus is retracted at a time causing the cell body to move but the stochastic detachment of pili give rise to a 'jerky' or 'twitchy' appearance [35, 36]. *P. aeruginosa* drives twitching motility from either of its poles, meaning it is capable of reversing its direction of travel along its long axis [37]. Twitching motility often takes the form of crawling, where the cell body is parallel to the surface, however, cells can also 'walk' upright whilst attached to the surface by a single pole in microfluidics[32]. When crawling, *P. aeruginosa* moves at slower velocities than when compared to when walking, however the persistence length of crawling movement is much greater, giving rise to more directed motion. On the other hand, when walking upright, the persistence length of twitching motility decreases, and *P. aeruginosa* tends to have a much more compact trajectory [38]. A third form of twitching motility is observed over much shorter timescales called 'sling shotting', occurs when the detachment of a single pilus causes a rapid propulsion of the cell body due to the tension in the other pili [36]. It has been observed that the rate of slingshotting increases on softer surfaces, demonstrating how pili-based motility can be affected by the external environment [39].

Swarming is a form of motility that occurs in a thin film of liquid that overlays an agar surface. Swarming typically is associated with increased multiple flagella production, and is commonly studied in *E. coli*, *P. aeruginosa* and *Bacillus subtilis*. Bacteria typically produce surfactants to facilitate swarming [23]. Swarming is distinct from twitching because the former movement is driven by flagella and the latter is driven by pili. In addition, cells form 'rafts' to collectively swarm and any individual seen to leave the raft ceases movement. Swarming requires softer agar, 0.5% w/v, and does not occur on the harder 0.8% w/v agar that is used to study twitching motility [34, 40]. Additionally, experiments on *B. subtilis* that vary the aspect ratio of the cell body and local cell density, have shown that swarming is more likely to occur as aspect ratio increases up to a value of 9.5 (cell length

divided by width), and when cell density is above a minimum value but not so large that the system enters a jammed state, where they are unable to move [40].

Recent studies on bacterial motility have begun to focus on another form of surfaced-attached movement, gliding motility. The first models of gliding motility in *Flavobacterium johnsoniae* proposed a track that wrapped around the entire cell, with adhesins attaching to the surface driving movement [41]. This model was investigated further and resulted in the discovery of the type IX secretion system, comprised of a molecular rack and pinion system, where a helical track wraps around the cell body, and rotary motors cause the adhesins to move around this track, propelling *F. johnsoniae* at speeds of 1.5 μm s^{-1} using proton motive force [42]. Given the helical nature of the track, the body rotates around its long axis as the bacterium is propelled forward [43]. Experimental evidence exists displaying reversals of direction of travel in *F. johnsoniae* gliding motility, however these studies are in their infancy, and there remains much to be uncovered about this form of movement [42].

Studies on cell motility have also been performed using *Myxococcus xanthus* due to its ability to perform two types of movement: social (S) and adventurous (A) motility [44]. S-motility is facilitated through rounds of polar pili extension and retraction that pulls the cell body. S-motility occurs when *M. xanthus* cells are in close proximity to one another, which results in a spatial distribution of clusters of motile cells, and individual immobile cells. This form of behaviour consists of periodic reversals of twitching motility direction which cause the formation of large scale structures such as fruiting bodies [45]. Although the exact mechanism that facilities A-motility is still debated, it is not driven by pili but does allow for individual cells to move, which leads to many single cells being distributed over a surface [46].

1.1.1 The type IV pilus machine

This thesis focuses on twitching motility in *P. aeruginosa* and as such, we will describe the molecular machine that facilitates this form of movement: the type IV pilus [30]. In this section, we describe the TFP machine structure in detail and subsequently outline the roles of each protein that comprises the system, and explain the process of extension, surface attachment, and retraction.

TFP are made of two components, the basal body and the pilus fibre. The basal body is embedded into the cell wall during division, and spans from the inner membrane, across the periplasm and to the outer membrane [47]. This structure is broken down into three components: the pore complex comprised of PilQ and TsaP where the pilus extends out of the cell body, the alignment complex made of PilM, PilN, PilO, and PilP which guides pilus extension, and the motor complex, comprised

of PilC, which the ATPases PilB, PilT and PilU bind to [48].

The process of pilus extension first involves the recruitment of pilin subunits, PilA, to the basal body. During extension, the ATPase PilB is bound to PilC at the bottom of the basal body and polymerizes PilA to form the pilus fibre [49]. Once polymerized, PilA forms into an α helix [50]. Each pilus is capped with PilV, PilW, PilX and PilY1 at the very end. PilY1 has been shown to be a possible adhesin for TFP, allowing for the attachment to surfaces through a von Willebrand domain (for a detailed explanation of the role of a von Willebrand domain in surface attachment see [51]). However, work in this area to identify other means of attachment is ongoing, as $\Delta pilY1$ mutants still adhere to a surface [51, 52]. After extension, PilB decouples from PilC, and the ATPases PilT or PilU exclusively bind, depolymerising PilA and returning it to the periplasm, retracting the pilus [53]. The mutually exclusive binding of PilB and PilT/U facilitates the successive rounds of extension and retraction of the pilus, respectively, which ultimately drives twitching motility. Through non-perturbative fluorescent labelling, it has been recently shown that PilB and PilT bind stochastically, such that that pili constantly switch between extension or retraction, rather than one following the other in a deterministic way [54].

1.1.2 Regulation of the Pil-Chp system

Given PilB and PilT/U are responsible for pilus extension and retraction respectively giving rise to twitching motility, we must consider how this form of movement is regulated. Twitching motility is regulated by the Pil-Chp system, a cluster of proteins that is responsible for regulating chemotaxis on a variety of surfaces and is required for infection [55, 56]. The Pil-Chp system is homologous to the Che chemosensory system in *E. coli*, and some of the functions of the proteins that comprise the Pil-Chp system have been inferred from these similarities [57]. Here we discuss the operation of both the Che and Pil-Chp system, and how the latter drives the direction of twitching motility, and how it is stimulated by mechanical signals.

The Che chemosensory system, which allows swimming *E. coli* cells to climb gradients chemical gradients, is the canonical model for bacterial chemotaxis (**Figure 1**). The Che system controls the CCW or CW rotation of the flagella which are distributed all over the cell body. CCW rotation allows a cell to swim in a relatively straight line (a "run"), whereas CW rotation cause a cell to sharply changes its swimming direction (a "tumble"). The Che system delays tumbles if experiencing an increase nutrient concentration. CW rotation is more likely to occur when phosphorylated CheY binds to the flagellar motor. The phosphorylation of CheY occurs through interactions with the

histidine kinase (CheA) and the methyl accepting chemotaxis proteins (MCPs) that directly bind to the chemical ligands sensed by the cell. Methylation and demethylation of the MCP (by CheR and CheB, respectively) facilitate adaptation, allowing the cell to respond to a wide range of ligand concentrations [58].

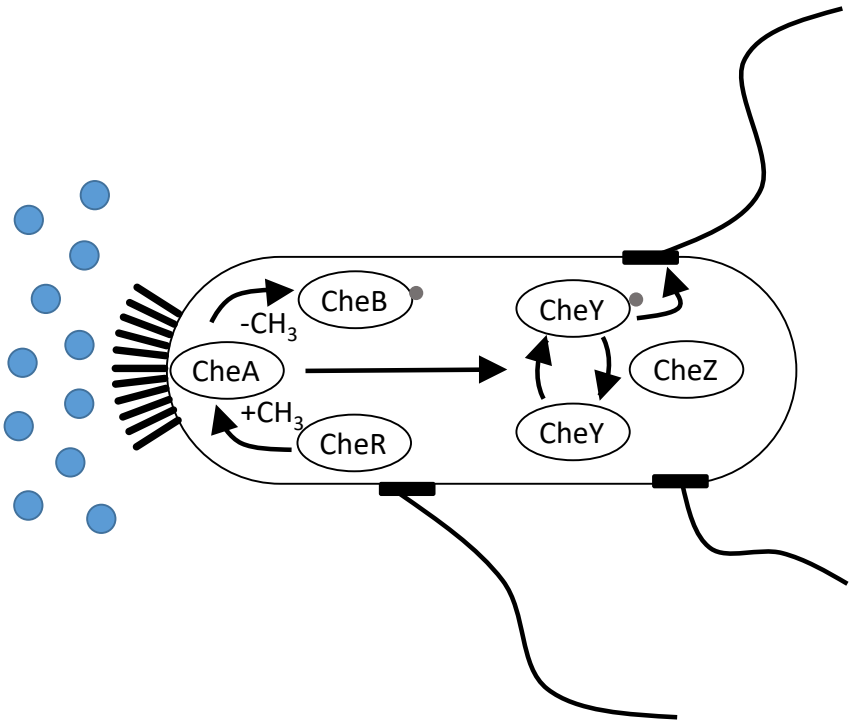

Figure 1: The Che chemosensory system determines the probability of tumble events, allowing swimming *E. coli* cells to generate chemotaxis. Blue circles indicate the chemical ligands that are sensed, black rods indicate methylated chemotaxis proteins (MCPs) and black rectangles indicate the flagellar motors. Gray circles indicate phosphate groups that are transferred between proteins. Adapted from [58].

The proteins that comprise the Pil-Chp system are shown in **Figure 2**. The MCP PilJ is thought to sense external stimuli and is abundant at both cell poles [59]. Given their homology to CheR and CheB, it is anticipated that PilK causes methylation of PilJ and ChpB causes demethylation [60, 61]. PilJ undergoes a conformational change when methylated causing auto-phosphorylation of the histidine kinase ChpA. The phosphate groups are then transferred to two CheY like response regulators PilG and PilH, which in turn interact with PilB, PilZ and FimX to facilitate pilus extension and PilT and PilU to retract the fibre respectively [16, 22, 62].

Given the Pil-Chp system regulates the extension and retraction of pili, it has been studied to show how a bacterium controls its direction of twitching motility. In surface associated *M. xanthus* moving through pili mediated S-motility, it has been observed that the location of the pilus machines is static and equally distributed between each pole, implying that the machines do not move over the cell's lifetime. The pili extension and retraction ATPases PilB and PilT localise in opposing poles,

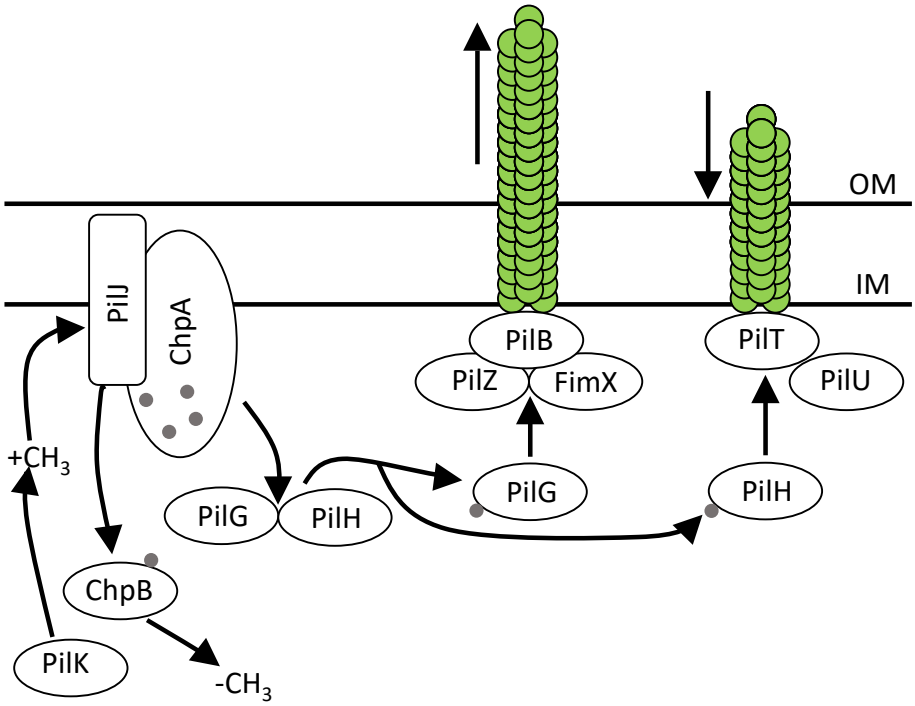

Figure 2: The Pil-Chp system regulates the extension and retraction of pili. Gray circles indicate phosphate groups and black arrows show the interactions between proteins. Adapted from [22].

with PilT occupying the site of pili retraction. PilB and PilT undergo periodic relocalisations in concentration between cell poles controlled by an Frz 'clock'. These relocalisations coincide with a reversal of the direction of twitching motility along the long axis of the cell, as pili retraction swaps to the opposite pole [63]. Dynamic localisation of proteins in the Pil-Chp cluster have also been reported in *P. aeruginosa*, displaying that PilB and PilT localise to both cell poles, whereas PilU, which also has a role in pilus retraction, only localises to the piliated pole [64]. Other proteins also display polar localisation, such as FimX, which is speculated to have a sensing role, and localises to the leading pole along with PilB. In the absence of FimX, PilB does not localise to poles and instead exhibits a diffuse distribution throughout the cytoplasm, suggesting there is an association between the two proteins [64, 65]. In fact, FimX has been shown to be crucial in twitching motility, as the deletion of *fimX* or the removal of key domains on FimX results in reduced twitching motility, or non-polar placement of pilus machines [66].

Although the Pil-Chp system allows *P. aeruginosa* to respond to the presence of a chemoattractant [67], a growing body of evidence suggests that bacteria are also able to regulate their movement in response to mechanical stimuli [22]. Bacteria have evolved a diverse range of systems to mechanically sense their environments. For example, bacteria can sense when they have attached to a surface because it can cause their flagella to stall. In addition, there are outer membrane proteins that can actively sense shear through deformations of the lipid bilayer, or adhesins on the cell body that bind

to a surface and require force to be removed, a mechanical signal that is read by the cell. [68, 69]. Grouped together these are all forms of mechanosensing, the methods bacteria use to mechanically sense their environment. Mechanosensing through PilY1 on the cell envelope has been shown to be particularly important in the upregulation of virulence factors in *P. aeruginosa* to start infection, as these are energetically expensive processes to initiate. The expression of virulence factors via mechanosensing is not specific to any one surface, therefore, it enables the colonisation of a broad range of hosts [70].

Mechanosensing is important for determining the direction of twitching motility. As PilJ has been shown to chemically interact with the pilin subunit PilA, a model has been proposed where mechanical signals are read by the Pil-Chp system. Here, a conformational change in PilA caused by the pilus stretching under tension is read by PilJ [71]. It is not exactly clear how this mechanical input is translated into a signal that leads to the regulation of twitching motility, however recent experiments have shown that pilus facilitated cell movement is directed by mechanotaxis, specifically regulated by PilG and PilH. Mechanotaxis has been implicated in the regulation of the reversals in movement that are observed when one cell collides with another. PilG acts to promote a unipolar pili distribution and drives forward motion of a cell, however, during a collision, the signal from a retracting pilus (or multiple pili) is disturbed, allowing the other response regulator PilH to suppress PilB polarisation which leads to a reversal of direction of travel [17].

1.1.3 Methods of studying bacterial motility

A large range of techniques have been developed to quantify bacterial motility and how it responds to different environmental stimuli. Since the advent of the earliest tracking of single cells by Howard Berg in 1971 [2], many different sophisticated microscopy techniques have been developed to study bacterial motility, allowing for one to simultaneously track of thousands of densely packed bacteria in a single field of view [19], or multiple cells in three dimensions through holographic microscopy [72]. Advances in high magnification microscopy have also allowed us to understand the function of specific components of the Pil-Chp system by quantifying how proteins are temporally and spatially distributed in within the cell [65]. Here, we outline some of the techniques used to investigate bacterial motility.

To investigate single cell movement that occurs during the development of three-dimensional colonies, it is common for colonies to be grown at the interface between agar and air. The agar concentration can be tuned to allow one to selectively isolate swimming, swarming, gliding and

twitching motility. To study twitching motility, the agar must of a sufficient stiffness to prevent flagella motion [23, 71]. Alternatively, interstitial assays, sometimes referred to as 'sandwich assays', investigate twitching motility at the interface between agar and glass, which also facilitate the use of high numerical aperture oil-immersion objectives [34]. A key component of the interstitial assay is that reorientations of the cell body out of the two-dimensional plane and the formation of multiple cell layers are prevented, as a restoring torque on cells at the glass-agar interface acts to keep cell bodies horizontal [73]. These sandwich assays thus allow bacterial monolayers to form, which have been widely used to study active matter (see **Section 1.3.2**) [34]. In addition, keeping cell bodies parallel with the substrate enables the one to image fluorescent protein fusions to visualise how different proteins are distributed within the cell body, because it enables the entire cell to be in focus using epifluorescence microscopy [74].

The use of fluorescent fusions and epifluorescence microscopy has been crucial in understanding the role of the different proteins involved in twitching motility. Lautrop first reported twitching motility in 1961, however, they did not coin the term until 1965 [75, 76]. Despite the fact that twitching motility was discovered almost 60 years ago, it was not until the turn of the millennium that TFP extension and retraction was observed in vitro for the first time. This achievement was made possible through labelling pili with amino-specific Cy3 fluorescent dye, showing that pili undergo Brownian diffusion whilst extending, attach to a surface and become taught during retraction [35]. As previously mentioned, an FrzS clock facilities the periodic reversal of twitching motility in *M. xanthus*. This finding that was confirmed through simultaneous genetic labelling of FrzS with green fluorescent protein (GFP) and pili with Cy3 fluorescent dye, showing that FrsZ-GFP localises to the pole of pili assembly [77]. GFP labelling of PilT in *P. aeruginosa* has also shown that inactivation of the MreB cytoskeleton causes mislocalistion of PilT-GFP and non-polar placement of pilus machines themselves [78]. Understanding the relationship between FimX localisation and the direction of twitching motility is of particular importance to the research performed in this thesis, and it is known that FimX localises with PilB to facilitate pilus extension [64, 65].

Recent research has shown that under nutrient limited conditions *P. aeruginosa* will undergo directed twitching motility, whilst they tend to become non-motile and cluster when nutrients are abundant [74]. Using FimX tagged with red fluorescent protein (RFP), this study showed these different regimes generated distinct distributions along the cell, with a unipolar accumulation of FimX-RFP found in the leading pole of cells undergoing twitching motility, and unlocalised or bipolar distributions of FimX-RFP were predominant when cells were stationary [74]. Thus it is clear that the distribution of fluorescent fusions can be used to infer the movement behaviour of cells.

Microfluidic devices are widely used to quantify bacterial movement behaviour and how it is regulated in response to external stimuli. Most microfluidic devices are fabricated using polydimethylsiloxane (PDMS) which is then bonded to glass coverslip. PDMS is largely chemically inert and non-toxic to bacteria, as well as highly transparent which facilitates microscopic imaging. Microfluidic devices can be used to produce well-defined chemical gradients via molecular diffusion that can be used to measure how bacterial respond to chemical stimuli. For example, microfluidic devices have been used to mimic the microscale ocean environment where nutrient patches constantly appear and dissipate. By designing a microfluidic device capable of simulating the dynamics of these patches, it was found that accumulations of swimming bacteria can rapidly form, allowing the top 20% of fastest cells to benefit from a ten fold increase in nutrient exposure in comparison to non-motile cells [79, 80]. In addition to measuring the response of bacteria to nutrients, microfluidics are also used to test bacterial responses to antibiotics. A recent study has shown the surprising result that *P. aeruginosa* twitches towards concentrations of antibiotics far above their minimum inhibitory concentration. The cells that do so are non-viable and often lyse, releasing pyocins in the process. It was proposed that bacteria initiate this response to antibiotics as they anticipate an attack from a rivalling strain upon sensing the antibiotics [81]. Although microfluidic devices have been used to study the response of twitching *P. aeruginosa* to antibiotics, they have also been used to investigate how bacteria move towards greater concentrations of nutrients [67].

1.1.4 Investigating bacterial chemotaxis

Chemotaxis is the ability of organisms to bias their movement along gradients in concentration. They perform this by sensing and responding to chemical gradients. While twitching mediated chemotaxis has only recently been reported, flagella-based chemotaxis has been studied for decades [67]. Here we summarise the experiments and models used to understand swimming based chemotaxis, and describe how *P. aeruginosa* performs twitching based chemotaxis in a microfluidic device.

Classically, *E. coli* is used as a model organism for studying chemotaxis in swimming motility [82]. Chemotaxis is facilitated through the run and tumble motion of *E. coli*, which is modelled as a biased random walk [83, 84]. *E. coli* extends its run length when experiencing an increase in nutrient concentration, allowing it to move towards favourable conditions at faster speeds. However, when *E. coli* experiences a decrease in chemical gradient it simply reverts back to its basal tumble rate that is observed in the absence of a chemical gradient, responding only when experiencing an increase in chemical gradient which is referred to as an 'optimistic' method of chemotaxis, where *E. coli* responds when life gets better [27]. As *E. coli* is capable of travelling many body lengths in a relatively short

period of time, it must sense a gradient by making comparisons between nutrient concentrations at different time points along its trajectory. These comparisons guide its decision to run or tumble, a strategy referred to as temporal sensing [85]. Swimming based chemotaxis is commonly studied using microfluidic devices due to their ability to generate highly reproducible and readily quantified chemical gradients. Microfluidic devices vary widely in their level of sophistication, for example they have been used to generate non-linear chemical gradients or mimic the complex chemical gradients that form in porous environments [86, 87]. However, swimming is not the only motility type that microfluidics are useful for studying chemotaxis in.

Recently it was shown how single *P. aeruginosa* can actively bias their movement along chemical gradients using twitching motility. A dual inlet microfluidic device was used that generates a one dimensional chemical gradient by flowing a growth medium (DMSO) down one side of the channel and a growth medium mixed with a chemoeffector (succinate) down the other. *P. aeruginosa* cells that were attached to the bottom of the devices were observed to bias their movement towards increased concentrations of both DMSO and succinate. As previously discussed, *P. aeruginosa* is capable of reversing its direction of twitching motility along its long axis, however, in this scenario the bacteria were responding to sensing a decrease in chemical gradient by increasing their rate of reversal [17]. When travelling towards larger DMSO concentrations, *P. aeruginosa* reverses at a basal rate as if there is no chemical gradient present. It was concluded that *P. aeruginosa* adopts a pessimistic chemotaxis strategy, where it responds when life gets worse. Moreover, these experiments demonstrated that *P. aeruginosa* is capable of responding to a change in chemical gradient direction before travelling the length of its body. It was proposed that *P. aeruginosa* employs a spatial strategy for sensing chemical gradients, possibly making comparisons in nutrient concentration between its poles, as opposed to the temporal method used by *E. coli* [67]. In either twitching or swimming chemotaxis, accurately quantifying chemotactic behaviour is essential for the development of the mathematical models that are used to understand how chemotaxis might have evolved to exploit heterogeneous environments [88, 89].

A number of different modelling approaches have been used to both understand the mechanisms that underlie bacterial chemotaxis and how it might affect their evolutionary fitness. Typically, experiments are used to rigorously parameterise models of chemotaxis, for example, measuring how the rates of chemoeffector binding/unbinding impacts the CCW/CW rotation of flagella have been used to simulate *E. coli* chemotaxis [90]. Models of chemotaxis can classified in two main categories: continuum models and individual based models [91, 92]. Continuum models simulate how the density of cells changes in time and space, typically using differential equations. On the other hand, individual

based models (IBMs) simulate the behaviour of single agents, and with a suitable number of agents, population level dynamics are recovered. IBMs are also popular as they allow one to easily model the heterogeneity in a population and behaviour that is dependent on specific stimuli that a cell has experienced at previous time steps [93].

1.2 The bacterial life cycle

Decades of work has been spent understanding how planktonic bacteria move through swimming motility [27]. Although this research is clearly important, bacteria actually spend the majority of their life attached to surfaces in densely packed communities referred to as biofilms [94]. Whilst living in a biofilm, bacteria such as *P. aeruginosa* benefit from protection of dispersal by flow, and an increased tolerance to antimicrobials [95, 96]. Given the huge benefits that bacteria gain from living in biofilms, in this section we outline the process of biofilm formation, describing the signalling pathways and single cell behaviours that control the formation of such a densely packed community of cells.

When a planktonic bacteria attaches to a surface it initiates twitching motility and the production of EPS (**Figure 3**). As individuals grow and divide in patches they begin to form small microcolonies, which then can then form classical mature biofilms. In some species, the biofilm matrix is degraded in mature biofilms in which the constituents emerge back in the planktonic phase, which then can go onto to found new surface attached biofilms [97, 98]. In this study, we define biofilms as large groups of surface associated cells bound together by EPS, and thus we consider bacterial colonies as biofilms, similar to the terminology used in previous studies [34].

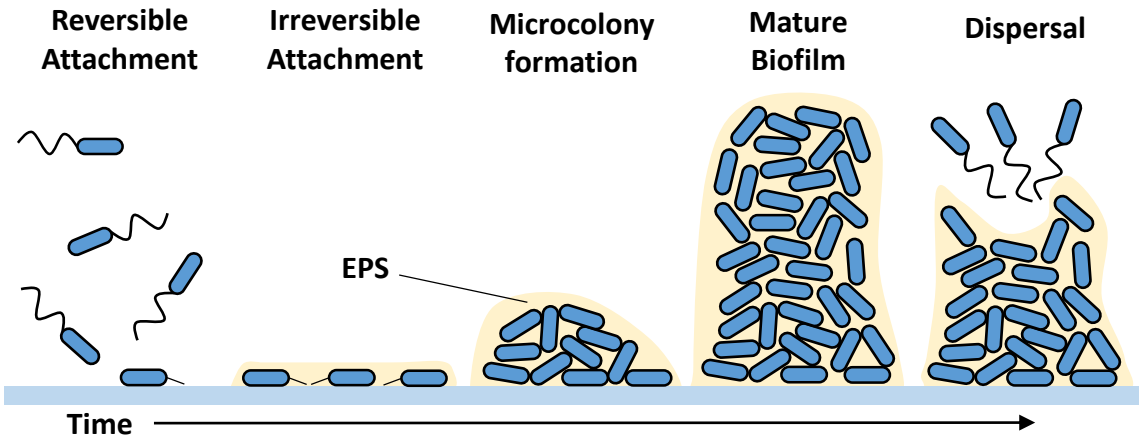

Figure 3: The bacterial life cycle. Adapted from [97, 98].

1.2.1 Surface sensing and attachment

The transition of freely swimming planktonic cells to a surface based sessile life style is often studied using *P. aeruginosa* as a model organism, as it has both a flagellum and the ability to produce pili. The presence of both these appendages is key as although the exact signal that stimulates the transition to surface based life is currently unclear, they are both important in the process [99]. It is widely reported that without a functional flagellum, surface association in *P. aeruginosa* is less likely [14]. Additionally, an increasing number of studies are highlighting that mechanosensing through TFP acts as a trigger for the transition from a planktonic to biofilm state, by regulating gene expression [99].

Although the exact sequence of events that trigger the transition to a biofilm state is unclear, many of the proteins that underpin them have been studied. *P. aeruginosa* often comes into contact with a surface many times, attaching by a single pole, referred to as 'reversible' attachment, before committing to long-term 'irreversible' attachment, where the body is flat on the surface [100]. During reversible attachment, a visit to the surface lasts on average for 30 seconds, however, over the course of many hours, corresponding to multiple divisions of *P. aeruginosa*, the visiting time increases until the cells become irreversibly attached and do not leave the surface. This transition to irreversible attachment is marked by the increase in intracellular concentration of two secondary messengers, the first being cyclic adenosine monophosphate (cAMP) [100]. cAMP has been shown to upregulate TFP biogenesis and the activation of the Pil-Chp system. It also provides a multigenerational memory for *P. aeruginosa* as elevated cAMP levels are passed onto a cell's progeny, and those with increased cAMP concentrations are more likely to become irreversibly attached [101]. The other molecule involved in this transition is the second messenger cyclic diguanylate monophosphate (c-di-GMP) which is produced upon surface contact through the Wsp system, and causes the flagellum to cease rotation. During division there is often an asymmetry between the amount of c-di-GMP in each daughter cell, where the daughter with the lowest concentration is more likely to leave the surface post division. The other daughter containing a greater concentration of c-di-GMP remains surface-attached and begins twitching [102]. We will find out in the upcoming section, that the concentration of intracellular c-di-GMP has a large bearing on the role each cell has in microcolony foundation [103].

1.2.2 Surface exploration and microcolony formation

Once irreversibly attached, bacteria begin to explore a surface, often in search of nutrient rich conditions to form biofilms. When reversibly attached, the body of *P. aeruginosa* is perpendicular to the surface, and the cell moves through the retraction of pili at a single pole. As the cell becomes surface

associated and becomes irreversibly attached, its body is more likely to be parallel to the surface and twitching motility can be directed from either pole [104]. The velocity of upright cells is greater but with a reduced persistence length than flat cells which are slower but exhibit movement that tends to be directed in one direction [38]. During the transition to surface association, two populations of cells arise dictated by the amount of Wsp system activity, and therefore the intracellular concentration of c-di-GMP. Those with small concentrations of c-di-GMP are highly motile and act to explore the surface whereas those with large amounts of c-di-GMP tend to be non-motile but produce large amounts of the biofilm matrix and act as the sites of future microcolony formation [103].

To form a microcolony and initiate biofilm growth, *P. aeruginosa* cells must cluster together and go through many rounds of division. The biofilm martix, and the EPS it is comprised of, mainly polysaccharides, extracellular DNA (eDNA) and lipids, are essential to the foundation of microcolonies and the maintenance of biofilms [105, 106, 107]. One polysaccharide in particular, Psl, acts as a molecular glue binding *P. aeruginosa* to the surface, and is important to the clustering process. As a cell twitches, it leaves behind a trail of Psl, which is then followed by other individuals, resulting in a positive feedback loop causing *P. aeruginosa* to cluster into groups surrounding those that produce the greatest amount of Psl [8]. Evidence shows that Psl screens the physiochemical properties of a surface enabling *P. aeruginosa* to colonise a wide variety of environments [9]. In addition to Psl, eDNA released by bacteria through lysis also causes clusters of cells to form, resulting in biofilm growth at the liquid glass boundary. For submerged biofilms to form, the release of eDNA by cells must be sustained over time, otherwise the local concentration of eDNA will reduce via diffusion and biofilm growth will be inhibited [108]. Although there still many unknowns in the process that leads to biofilm formation, future studies at the single cell level hold promise to elucidate this process.

1.2.3 Biofilm formation provides protection against environmental stresses

A biofilm is defined as a community of bacteria that are attached to a surface and reside in an extracellular matrix [109]. Typically comprised of thousands of individuals, biofilms occupy nearly every environmental niche on the planet, and therefore have impacts on healthcare, agriculture and industry where they can be detrimental or beneficial to people [110, 111]. Biofilms found in nature are often comprised of multiple species of bacteria, however, performing experiments using a single strain removes any interactions between different organisms, thus helping one elucidate the fundamental physical processes that govern biofilm formation, structure, and maintenance [112, 113]. One must, however, keep in mind that single genotype experiments greatly simplify the complex dynamics observed in more typical mixed genotype communities.

Living in a biofilm provides bacteria with protection from a variety of external physical and chemical factors. This protection arises from the extracellular matrix that surround the constituent cells, and the close proximity of individual bacteria to one another. Physically, the extracellular matrix prevents the dispersal of bacteria by fluid flow, and importantly limits molecular diffusion relative to that which occurs in aqueous solution [113, 114]. Limited molecular diffusion means that the penetration of antimicrobial molecules into a biofilm is reduced and therefore treatment through antibiotics is not as effective. Additionally, when in biofilms bacteria often produce beta-lactamases to degrade antibiotics, and have the capability to activate multidrug efflux pumps to remove antimicrobials from their bodies, allowing them to survive much greater concentrations than planktonic cells [109]. Not only is the effectiveness of antibiotic treatment limited by biofilms, due to the increased proximity of bacteria to one another and the fact that biofilms promote plasmid stability, the chance that cells horizontally exchange genes that confer antibiotic resistance is much larger in biofilms [115, 116], which has significant clinical relevance.

The structure of a biofilm is heavily influenced by the capacity of its constituents to twitch and the properties of the substrate it grows on, which can have a knock on effect on their antibiotic tolerance [117, 118]. They are typically three dimensional structures consisting of cells in a sheet at the base, that are more likely to be oriented out of plane with decreasing distance to the centre, forming a dome or in other circumstances a mushroom shape with a stalk and cap [113, 117, 119]. Mutations in the Pil-Chp system can alter the morphology of a biofilms, for example $\Delta pilA$ mutants cannot form the cap of the classical mushroom shaped biofilm [117]. Biofilms grown on substrates with greater hydrogel polymer chain lengths have increased aspect ratios, with large heights and smaller widths compared to those grown on hydrogels with short polymer chains which leads to biofilms that are flatter and wider. These shapes are controlled by the mesh size of the hydrogel the cells are growing on through twitching motility, as those with larger meshes lead to decreased twitching speeds triggering clustering and form more dome shaped biofilms. Those with smaller meshes and therefore smaller pore sizes enabled pili to attach more often, enabling increased twitching speeds, and less clustering of cells resulting in flatter biofilms. These factors have implications for antibiotic treatment as cells at the centre of large aspect ratio, dome shaped biofilms were found to more likely to survive treatment with colistin, compared to those at the middle of flatter and wider biofilms, simply because the antibiotic molecules cannot penetrate into the interior of the former biofilm [118].

Along with the influence of the substrate on biofilm structure, cells are sorted in a biofilm according to their shape. As shown by both experiments and simulations, cells sort themselves into different regions of a biofilm. Spherical cells tend to get transported to the top of the biofilm, which

can benefit them provided the nutrient source originates from above the collective. Rod shaped cells tend to accumulate at the edges and base of the biofilm, and therefore benefit if the nutrient source originates below the collective [112, 120].

Not only do physical processes influence the structure of biofilms, they themselves exert forces on their surroundings. As the biofilm grows, the radial stresses generated internally are transmitted to substrates by via adhesion, which can cause softer surfaces to buckle. For example, buckling has been observed on sheets of epithelial eukaryotic cells, giving bacterial pathogens a means to enter host tissues [121]. Although biofilm growth can provide fitness benefits in many cases, biofilms growing in soil can be detrimentally impacted by rapid biofilm development. In particular, if a biofilm grows quickly, the pore in which it resides can become blocked so that fluid flow, and the nutrients it carries, are directed to slower growing biofilms [122].

Even bacteria cannot escape the common idiom 'all good things must come to an end' as biofilms do not last forever. The biofilm life cycle ends with the biofilm matrix degrading and the emergence of planktonic cells [123]. In a medical setting, the emergence of planktonic cells is a mechanism for the spread of diseases [124]. Dispersal has a variety of triggers, for example oxygen depletion, limited nutrient availability or stress arising from the accumulation of waste products. These stresses are typically localised at the centre of the biofilm where transport is limited, and leads to decreased production of c-di-GMP [98]. As discussed in **Section 1.2.1**, increases in c-di-GMP concentration trigger the transition from a planktonic to sessile life style and the production of the biofilm matrix. The biofilm matrix itself is produced to a lesser extent when c-di-GMP is produced in lower concentrations and is degraded by enzymes produced by the bacteria [125]. Of course, biofilms can face a premature end through removal by physical force or through the treatment of antimicrobials such as those found in Manuka honey, which prevents biofilm formation or eradicates them [98, 126].

With their common occurrence in nature, it is clear that biofilms have the potential to give bacteria huge fitness advantages through protection from environmental factors and antimicrobial treatment [97, 114]. Once in an established biofilm, bacteria even exert physical pressure on the substrate they are on to facilitate infection [121]. Much has been uncovered about the establishment and maintenance of biofilms in recent years, including how physical properties of their constituents such as shape influences biofilm architecture [112]. We now seek to understand the role of individual or collective movement in biofilm development.

1.3 Collective movement

Over the course of biofilm formation, cell density increases such that the movement of cells transitions from the that of solitary cells to groups of bacteria that are collectively migrating across the surface [34]. Similar phenomena have been observed in flocks of birds [127], insect colonies [128], and in even crowds of humans [129], which all display collective movement at length scales much larger than that of their constituents when above a critical density [130]. In these systems, the constituents are able to draw in energy and use it to generate movement, and exhibit physical interactions with their neighbours [15]. The field of active matter, a relatively new branch of physics, has developed to describe the complex dynamics observed in these systems.

1.3.1 Properties of active matter

Active matter can be described as a system that exists outside of thermodynamic equilibrium, that is comprised of densely packed constituents that draw in energy from their surroundings to perform work [131]. The constituents of active matter interact with their neighbours such that their correlation in their orientation extends over distances that exceed the length scale of a single member. The constituents of a system can be referred to as either 'nematic' or 'polar' depending on how they exert forces on each other (**Figure 4**). For example, a dividing rod shaped bacterium such as *P. aeruginosa* exerts an extensional force along its long axis which can be described as nematic, whereas when it exhibits directed twitching motility, the force that it exerts is applied in one direction, and therefore can be described as polar [132]. To model collective dynamics observed in active matter systems, these local interactions are often coarse grained and described with continuum models.

Liquid crystals are a form of matter that have both liquid properties, such as fluid flow, and crystalline properties, like a periodic arrangement of its constituents. One class of liquid crystal, a nematic, is characterised by the long range orientational order of its rod like constituents along their major axis. The orientation of a liquid crystal can locally be described using a unit vector, $\boldsymbol{n}$, which is referred to as the director. As there is no preferential arrangement in a nematic, $\boldsymbol{n} = \boldsymbol{-n}$ [133].

The key distinction between a nematic and an active nematic is that work is performed by each constituent in the latter, denoted by the activity term ζ. Under the condition $\zeta = 0$, activity ceases and we return to a regular nematic, however, when $\zeta > 0$ the system is considered extensile and for $\zeta < 0$ the system is contractile. Extensile and contractile refer to how the constituents propel themselves. Extensile constituents pull fluid is from their sides and push it along their long axes, whereas the flow around individuals in a contractile system is in the opposite direction [15].

Active nematic theory describes the collective dynamics observed in active matter systems, how-

ever, the movement of individual constituents can differ from that of the bulk. Nematic rod shaped agents exert force along both directions of their long axis, and therefore the alignment of their orientations leads to a nematic description (**Figure 4a**). Polar agents instead exert forces along their axis that are directed in a single direction. A collection of polar agents, however, can be modelled as nematic system if individuals do not align their movement in the same direction, for example because they reverse direction frequently (**Figure 4b**). However, if agents align their movement in the same direction, the collective must be modelled as a polar system (**Figure 4c**) [134].

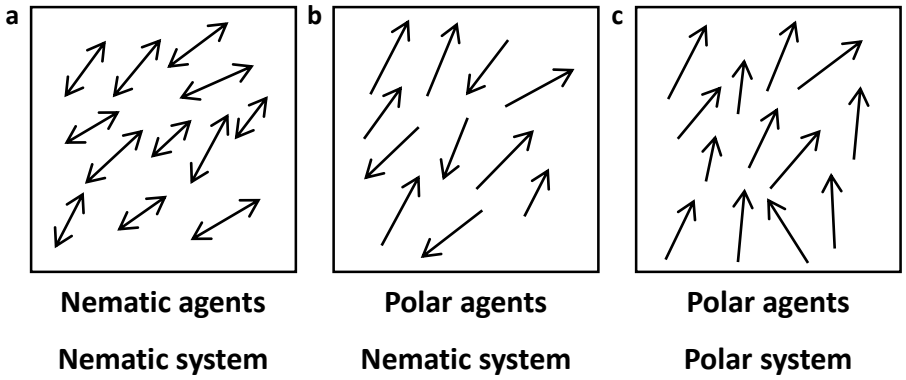

Figure 4: How the properties of a system's constituents dictates its collective behaviour. Arrows indicated the direction in which individuals exert force on one another. Adapted from [134].

Active matter systems are also characterised through the presence of topological defects, which are points in space where domains of agents with different orientations meet one another. The charge of a topological defect is measured by the change of the director field in a closed loop around the defect core [135]. Half integer charged topological defects are observed in active nematic systems, with those of $+\frac{1}{2}$ charge termed 'comets', and those with a $-\frac{1}{2}$ charge termed 'trefoils'. Comets display a head and tail like structure, where as trefoils display threefold symmetry (**Figure 5**).

Due to the activity of the constituents in active matter systems $+\frac{1}{2}$ charged comets propel themselves along the direction of the defect head and display ballistic motion, where as the movement of $-\frac{1}{2}$ charged defects is diffusive [34, 136]. The overall topological charge of a two-dimensional active matter system must be zero, therefore, half integer charged topological defects are generated in pairs of opposing charges through the activity in an extensile system. Like charge defects repel and opposing charges attract one another. If the head of a comet meets inbetween two spokes of a trefoil, the two defects annihilate one another such that the total charge of a system is conserved [137]. In polar systems, full integer charge defects are observed. Therefore, the recent observation of the coexistence of half integer and full integer charged defects in simulated active polar systems is surprising, and highlights the need for future models and experiments to account for this crossover

of behaviours [138].

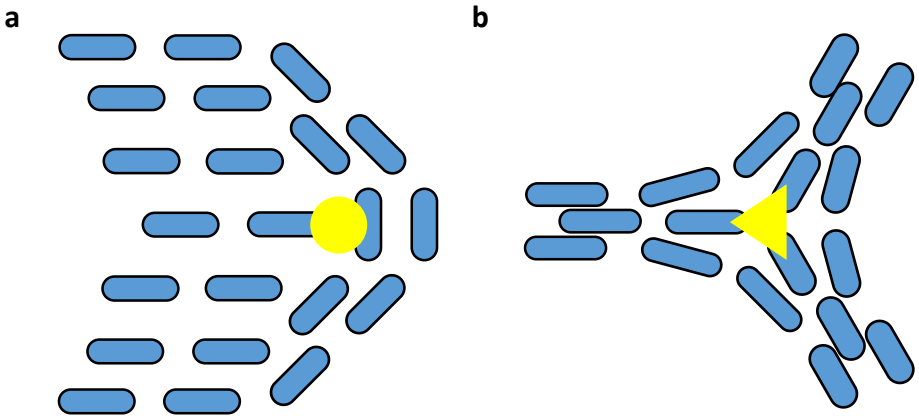

Figure 5: The two types of topological defects commonly found in active nematic systems, (a) comets with a topological charge of $+\frac{1}{2}$ and (b) trefoils, which are $-\frac{1}{2}$ charged. Adapted from [15]

The final property of active matter that we will discuss is that of active turbulence, which exhibits the swirling, vortical patterns that reminiscent of the turbulence found in fluids at much larger length scales. Active turbulence can enhance transport within a collective, which has implications on how compounds are transported by moving bacteria [139]. Through simulations of extensile rod like particles, it was found that the behaviour of topological defects is highly influenced by the amount of friction in a system. In environments with small amounts of friction, active matter systems display active turbulence and the creation and annihilation of half integer charged topological defects. As friction increases defects and vortices become periodically arranged in a lattice, until friction is sufficiently large and no collective dynamics are observed [140].

1.3.2 Biological systems as active matter

With a theoretical understanding of active matter, we can consider how active nematic theory is used to describe collective dynamics in biological systems. We are able to model biological systems as active matter for two reasons: the constituents draw energy from their surroundings to perform work, and display long range orientational order [15]. Here we provide some examples of biological systems modelled as active matter, focusing on how bacterial monolayers comprised of rod shaped agents can be modelled as an active nematic. In particular we highlight the importance of $+\frac{1}{2}$ charged topological defects to various processes across a variety of species.

Mixtures of microtubules and kinesin molecular motors are a classic example of an active nematic system comprised of nematic constituents. When mixed at the interface between water and oil, the kinesin motors bind to the microtubules, which are then sheared by the motors [15]. Topological defects are observed in the microtubule-kinesin system, for which the self propulsion of $+\frac{1}{2}$ charged

comets leads to active turbulence [141]. Growing non-motile *E. coli* microcolonies are also an example of an active nematic system that is composed of intrinsically nematic constituents, as the force exerted due to cell division acts along the long axis of the cell, without a preferred direction. As the microcolony grows, we observe that $-\frac{1}{2}$ charged trefoils remain at the centre of the colony, whilst $+\frac{1}{2}$ charged comets are propelled to the colony edge and facilitate expansion [142].

Bacterial monolayers comprised of twitching rod shaped constituents, in particular those comprised of *P. aeruginosa*, are considered as active nematic systems comprised of polar constituents. The polar nature of each cell arises because twitching motility is often directed from a single pole, however, as it is often assumed that neighbouring cells do not align the direction of their motility, a nematic state arises [15]. Long range orientational alignment of the director field is observed in bacterial monolayers, with the corresponding half integer charged topological defects [34].

Multiple studies have highlighted the importance of topological defects in a variety of systems including the signalling of apoptosis and subsequent extrusion of cells in epithelial sheets, being the site of morphological features in the actin fibres of hydra, and for a diverse range of processes in bacterial monolayers [34, 143, 144]. In subsurface *P. aeruginosa* monolayers $+\frac{1}{2}$ charged defects cause the reorientation of cell bodies out of the two-dimensional plane, a crucial stage in the development of three-dimensional bacterial colonies [34]. In colonies comprised of equal fractions of WT and $\Delta pilH$ cells, the larger force exerting $\Delta pilH$ individuals preferentially accumulate at comet cores. When two comets collide with one another in a head on collision, the cells they are comprised of reorient out of plane if the force is sufficient, overcoming the torque keeping bacteria flat to the surface, forming a $+1$ charged topological defect termed a rosette. The reorientation arrests lateral movement and over time this causes $\Delta pilH$ to be lost from the colony edge and become trapped in the colony's nutrient poor interior [34].

In *M. xanthus* monolayers, both experiments and simulations have shown the importance of half integer charged defects, with cells accumulating around comets, and holes in the monolayer appearing in close proximity to trefoils. Cell accumulation is sufficiently large surrounding comets that multilayer formation occurs through cell-cell interactions reorienting movement out of plane. These multilayered structures are the sites of fruiting body formation, which form when *M. xanthus* experiences starvation conditions [145].

It is evident that collective behaviours are crucial to biofilm development, however we are yet to consider if individual bacterial movement behaviour has a role to play. An example of bacterial movement behaviour is that of a reversal of the direction of twitching motility along the long axis of a cell. Upon initial contact with the surface *M. xanthus* suppresses its reversal rate to find other

cells to cluster together. Once clustered together above a critical local cell density, *M. xanthus* forms one dimensional 'highways', which maintain their stability by the cells increasing their rate of rate of periodic reversal but travelling at the same speed. In comparison ΔFrzE mutants do not reverse and show a lower capability to form these highways [146, 45]. To the best of our knowledge, these are the only studies that investigate how of the movement behaviour of individual cells influences the characteristics of the collective.

Although we have limited experimental examples, theoretical work has been used to understand how the reversal frequency of constituents of active matter systems impacts collective dynamics. Recent simulations have tested how reversal frequency impacts the collective movement of semi-flexible rods along as surface. When the packing fraction is large but below confluency, a relatively small reversal rate allows the rods to exhibit polar movement, which prevents a jammed state from forming. However, when the packing fraction is at confluency (packing fraction is one), more frequent reversals allow the rods to move, a behaviour termed nematic driving, which also prevents a jammed state from forming [147]. This study shows that by varying the rate of reversal rate under different conditions, the constituents of an active matter system can have an influence on collective behaviour. However, it has yet to be seen if bacteria are able to switch between behaviours akin to nematic and polar driving of reversals.

1.3.3 The interface between a biofilm and the environment

The research previously performed to model biofilms as active matter systems is to improve our understanding of how bacterial colonies develop. However, these studies often focus on the monolayer and often do not consider the dynamics at the edge of the colony and how they impact its development. The colony edge is used as a means for studying phenomena at the edge of a biofilm as the dynamics observed are highly repeatable and readily imaged through multiple microscopy techniques. Previous studies performed on the colony edge have focused on how individual cells react to the presence of other bacteria, and how single cells respond to treatment antibiotics as a function of distance from the colony edge [61, 148].

For the purposes of our study, we are interested in the mechanisms that facilitate the expansion of surface-attached colonies. Previous work on interstitial *P. aeruginosa* colonies have shown that expansion through twitching motility is facilitated by groups of 'bulldozer' cells which are aligned both in terms of cell body orientation and direction of travel. As these bulldozers move outwards from the colony, they leave behind a series of interconnecting furrows. Bulldozer groups at the vanguard of the colony are replenished with new cells that travel along these furrows, guided by eDNA. The role of

eDNA in these environments is particularly important, as in the presence of DNaseI the orientational cohesion within the vanguard groups is degraded, as is the replenishment of cells to the edge, causing the colony twitching facilitated expansion to cease [149]. Although this is an illuminating study for the mechanism of colony expansion that twitching *P. aeruginosa* uses, it does not consider how individual bacterial movement behaviour has an impact on colony expansion.

There currently exists a gap in the literature regarding single cell movement behaviour in the context of colony expansion. Both experimental evidence and simulations show that the properties of single cells and their movement behaviour impacts the behaviour of the collective. $\Delta pilH$ *P. aeruginosa* colonies have a reduced long term rate of expansion than the WT, and simulated semi-flexible rods prevent jamming in monolayers of differing fraction by reversing at different rates [34, 147]. As shown by experiments on *M. xanthus*, reversals are essential in maintaining highways, a structure that is of a size much larger than the single cell [45, 146]. Therefore, in this thesis we consider the results of these studies and investigate if *P. aeruginosa* is capable of regulating its movement behaviour by changing its rate of reversal to facilitate colony expansion within groups at the colony edge.

1.4 Thesis Overview

Recent developments in cell tracking algorithms now allow individual cells to be followed in densely packed biofilms [19]. In addition, experiments have shown how pili-based chemotaxis is facilitated by the regulation of reversals in twitching direction [19, 34, 67]. Using massively parallel cell tracking, genetic labelling, high magnification microscopy, and custom analysis algorithms, this thesis investigates both of these strands to resolve novel behaviours. First, we find that individual bacteria are capable of controlling their movement behaviour through preferential deployment of reversals to generate highly polarised collective movement behaviour in expanding colonies. Second, we use individual-based models to understand the role of a novel type of twitching behaviour in which cells actively rotate, rather than reverse, to facilitate chemotaxis. Our findings are spread across three chapters, which are summarised below:

Quantifying polarisation in developing *Pseudomonas aeruginosa* biofilms. We used a custom image analysis pipeline and strain of bacteria that localises fluorescent protein in its leading pole to characterise collective polar behaviour in expanding *P. aeruginosa* colonies. Inspired by recent work on the role of topological defects in bacterial colonies, we developed methods to resolve collective polarisation in the vicinity of topological defects in confluent monolayers and at the very edge of expanding bacterial colonies. In contrast to the nematic alignment that has previously

been assumed, our results show that neighbouring bacteria tend to align their motility in the same direction.

Reversals in the direction of travel contribute to collective polarisation in bacterial monolayers and colony expansion. We investigated how *P. aeruginosa* cells could potentially generate collective polar behaviour through the active regulation of their motility. Building on the custom analysis pipeline used to study collective polar behaviour in bacterial monolayers, we measured reversals of the direction of twitching motility in dense collectives by detecting when a fluorescently-labelled protein associated with pili-based motility was transported from one pole to the other. By combining a large number of these rare events with particle image velocimetry measurements of collective movement, we demonstrate that *P. aeruginosa* actively reverses the direction of its motility more frequently when attempting to twitch against the direction of collective travel. The same behaviour was also observed at the colony edge where it likely drives a strongly polarised state, suggesting that *P. aeruginosa* has evolved this behaviour to enhance colony expansion.

From reversals to twiddles: using an individual based model to understand the how cells generate pili-based chemotaxis. In this chapter we investigate how a novel form of twitching behaviour called 'twiddles' contributes to chemotaxis. By analysing the behaviour of cells in a microfluidic device as they respond to a stable gradients of the chemoattractant succinate, we parameterised a non-dimensional individual based model to understand how both reversals and twiddles to contribute to chemotaxis on surfaces. Our results show that both twiddles and reversals can each drive chemotactic response but they show strong differences in the parameter regimes where they are found to be most effective. Our results indicate that *P. aeruginosa* cells use both types of orientation behaviours to maximise their ability to position themselves around nutrient sources across a wide diversity of different environmental conditions.

2 Experimental methods

The experimental work performed in this thesis investigates either individual or collective movement of surface-attached *P. aeruginosa* driven by twitching motility. Within dense collectives such as bacterial monolayers it is challenging to isolate the movement behaviour of an individual cell due to the influence of its neighbours [15]. To investigate the movement behaviour of individual cells in collectives we used time lapse epifluorescence microscopy to track the distribution of a fluorescently labelled protein FimX, that localises to the cell pole in which twitching motility is directed in [74] and resolved the changes in the localisation pattern of FimX-YFP that occurs on a timescale of seconds.

Twitching motility has been studied using a variety of different assays where bacteria grow either within a microfluidic device, at the interface between agar and air, or between agar and a solid surface [71, 118]. We used subsurface 'sandwich' assays to study the collective movement of surface attached bacteria, where cells are sandwiched between agar and a thin glass coverslip as they can be imaged using oil-immersion objectives [34]. In addition, cells in subsurface assays experience a restoring torque, owing to the elasticity of the agar that keeps cells parallel to the surface and allows them to generate a large confluent monolayer of cells at the edge of colonies [112, 150]. Preventing multiple layers from forming is key from an imaging perspective, as multilayered structures cannot be readily imaged using fluorescence microscopy because the signal from slightly out of focus cells cannot be avoided. Additionally, *P. aeruginosa* must be lying flat on a surface to accurately capture the localisation of FimX-YFP. Therefore, subsurface 'sandwich' assays are ideal for our purposes.

Previous work has highlighted how the properties of an individual influences the characteristics of a collective system. For example, the hyperpilliated $\Delta pilH$ *P. aeruginosa* mutant is capable of propelling itself with a greater amount of force than the WT strain, allowing solitary cells to travel at greater speeds in a subsurface assay. Despite increased speed, monolayers of $\Delta pilH$ mutants expand more slowly over surfaces than the WT, because they are more likely to become oriented out of plane and become trapped in a vertical orientation [34]. Similarly, the subsurface assays used in this thesis contain a co-culture of unlabelled WT cells and WT cells that have been complemented with a FimX-YFP fusion, which could potentially have different properties that differentially affects their motility. As our goal is to understand how individual bacteria behave in dense collectives as found in nature, we must verify that the motility of the FimX-YFP fusions is not impaired relative to that of the unlabelled WT strain.

In this chapter we discuss the methods used in the three experimental conditions examined in this thesis: (i) cells at low density approximately one hour after they have been inoculated onto a surface,

(ii) confluent monolayers approximately 10 hours after cells have been inoculated onto a surface, where the density has increased as a result of cell division, and (iii) at the colony edge approximately 10 hours after cells have been inoculated onto a surface, where groups of aligned cells are observed travelling collectively into virgin agar. The assay preparation, microscopy and cell tracking process is covered in detail, alongside the methods chosen to measure the properties of collective velocity, including particle image velocimetry and single cell tracking [19]. Finally checks are performed on WT and FimX-YFP co-culture assays to ensure that cell length is similar between strains, quantify any velocity difference between the different strains, and ensure that the effects of phototoxicity do not significantly influence the experiments.

2.1 Strain list

All the experiments here were performed have been performed using a *P. aeruginosa* from the Kolter collection (PAO1, [34]) and a fluorescently-labelled mutant constructed in this WT background capable of producing fluorescent FimX-YFP [34].

To visualise FimX localisation, we generated a FimX-YFP protein fusion expressed from a low-expression promoter (BG35) initially characterised in *Pseudomonas putida* [151]. *FimX* was first amplified from the PAO1 chromosome using primers that bind immediately downstream of the *FimX* start codon and ≈ 100 base pairs downstream of the FimX stop codon. The coding sequence of YFP was amplified from plasmid (pEYFP-N1, (Clontech)) using an upstream primer that also introduced the BG35 promoter and a ribosome binding site (designed using automated methodology, see [152]. Here, we also used a downstream primer with a linker [153] designed to separate the functional domains of the two proteins, FimX and YFP. Following amplification, these two fragments were combined by secondary PCR and ligated into the linearized vector pGEM-T (Promega). The resulting plasmid was then transformed via electroporation into *E. coli* S17-1, a broad-host range donor strain. We then used a previously established protocol for using a mini-Tn7 system to insert the construct into the PAO1 chromosome at the chromosomal attTn7 site [154]. The final strain was confirmed by sequencing.

2.2 Bacterial culturing and sample preparation

All cell culture preparation was performed in the same manner for the three experimental environments. For each strain frozen -80 °C stocks were inoculated in 3 ml of 2% liquid LB (Lennox, Fisher) in a 14 ml falcon tube (Corning). Cells were then grown in a 37 °C incubator overnight whilst shaken at 200 rpm. After overnight growth cells are diluted $30-$fold in fresh LB and returned to the incubator at 37 °C under shaking at 200 rpm for a further two hours to obtain cells at exponential phase.

Measurements of OD_{600} were then used to decrease the cell concentration to $OD_{600} = 0.05$, in 3 ml of LB. When mixing together co-cultures of different strains, different volumes of the $OD_{600} = 0.05$ cell solution are combined to obtain the desired ratio of strains.

In the subsurficial 'sandwich assays' we followed the experimental procedures outlined in [34]. We made 0.8% (w/v) LB agar (LBA) by mixing 2% tryptone (BD, Bacto), 1% yeast extract (BD, Bacto), 1% sodium chloride (Fisher Scientific) and 0.8% agar (BD, Difco). We used 0.8% (w/v) LB agar as it is of sufficient stiffness to prevent movement facilitated by flagella, but does not immobilise twitching cells [34]. After autoclaving, 17.5 ml of molten LBA was poured into a 90 mm diameter Petri dish under sterile conditions and allowed to dry for 30 minutes. A fixed volume of LBA is used to generate an agar slab with a consistent thickness, which is essential to ensure that the moisture levels across experimental repeats is conserved. Once the agar has solidified, a slab is cut out and moved carefully onto a cover slip to ensure the flat agar surface is disturbed a little as possible. We pipetted 1 μl of cell culture onto the agar surface (on the side facing the air once poured) and allowed it to dry until the liquid has evaporated, leaving behind a circular 'coffee ring' of cells [155]. The agar is then inverted and carefully placed into a glass bottom dish (Ibidi, 170 μm thickness), ensuring that bubbles do not form as this will destroy the assay. The glass bottomed dish is used rather than a standard microscope slide as it creates a sealed environment, minimising the amount of evaporation that occurs over the course of the experiment. In a low density assay, cells are imaged approximately one hour after they have been inoculated for whereas for the monolayer and colony edge measurements imaging was conduced approximately 10 hours after inoculation. Cells are kept at room temperature (23°C) at all times.

2.3 Microscopy and image processing

All imaging was performed using a Nikon Inverted Ti Eclipse microscope with a SpectraX LED fluorescent light source, a Plan Apo 100× oil immersion objective lens, and an Andor Zyla sCMOS camera. This set up was used to simultaneously record a phase contrast and epifluorescence image at a frame rate of one second, via triggering from a National Instruments timing board. A range of different frame rates were trialed, but 1 fps was found to be sufficient to capture both twitching motility and changes in polar FimX-YFP concentration whilst minimising the effect of YFP bleaching. All of the time lapses were limited to 180 seconds as the YFP signal degrades to a unusable level in timeseries > 180 frames long.

Prior to cell tracking, time lapse images were processed using custom processing macros in FIJI [156]. First, the fluorescence images are bleach corrected using FIJI's built in tool (using an ex-

ponential fit of fluorescence decay) to minimise the changes in YFP signal that occurred over the course of the time lapse. Secondly, a Difference of Gaussian filter was applied to each epifluorescent image. A Difference of Gaussian filter improves the signal to noise ratio of an image by subtracting an image blurred by a Gaussian filter from the same image blurred by a Gaussian filter with a smaller standard deviation. This reduces the magnitude of the noise because it preserves only the spatial information that is between the length scales of the two Gaussians, which have been optimised to preserve objects with the same size as the small puncta of YFP found in the poles of our FimX-YFP cells. For our epifluorescent images, we subtracted each frame blurred by a Gaussian filter with a standard deviation equivalent to 10 pixels (6.4 μm), from the same image blurred by a Gaussian equivalent to one pixel (0.64 μm). The effect of bleach correction and Difference of Gaussian filtering is seen in **Figure 6**.

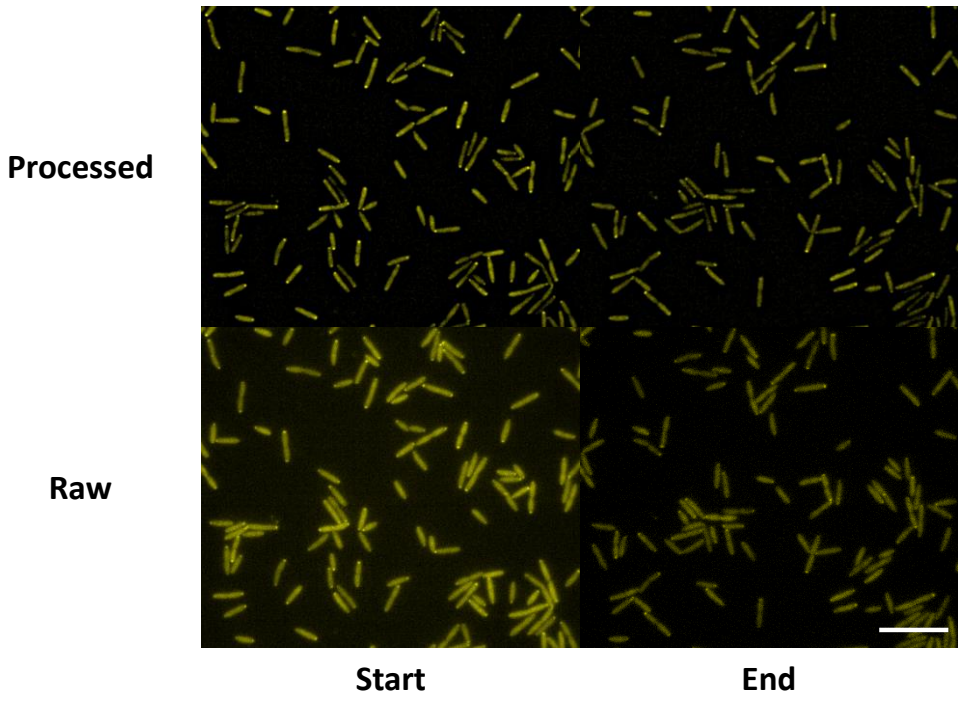

Figure 6: Epifluorescence images of *P. aeruginosa* with intracellular FimX-YFP pre and post bleach correction and application of a difference of Gaussian filter. Images shown are of low density assays containing 100% FimX-YFP cells at the start and end of a three minute long time lapse recorded at one frame per second. Scale bar is 10 μm.

2.4 The three environments

Three types of subsurface assay were used in our analyses (**Section 2.2**). Once the liquid component of our cell solution has evaporated, *P. aeruginosa* cells were observed at greater densities at the edge of the dried spot of inoculum compared to the centre (**Figure 7**) as a result of the coffee ring effect

[157]. At an hour post inoculation, we recorded time lapse videos of bacterial movement within this annulus which by this point exhibited significant twitching motility. Over time cell division results in the formation of a confluent monolayer, that expands outwards into the virgin agar. At the very edge of the colony we observed densely packed groups of aligned cells moving outward in the direction of expansion. We now summarise the purpose of each assay and the challenges that arise during their analysis.

The aim of our experiments is to identify and measure any collective polar movement behaviour that exists in biological active matter. As we cannot infer the direction of twitching motility using phase microscopy alone in densely packed conditions due to the influence neighbours have on single cell movement, we use the asymmetry signal from our fluorescent FimX-YFP fusion to measure the direction and speed of twitching motility. As our FimX-YFP fusion has not previously been used, we must validate that it performs in the same way as other fusions reported in literature, localising in greater concentrations in the leading pole of *P. aeruginosa* performing twitching motility [37]. Cell-cell collisions can skew the correlation between FimX-YFP asymmetry and twitching motility, as a cell that is highly asymmetric can have its motion stopped by a stationary cell. Therefore, we perform assays at low cell densities (**Figure 7c, 6f** and **6i**) to minimise the occurrence of these collisions, and confirm the correlation between FimX-YFP localisation and cell movement. With this correlation proven, we investigate the movement of cells in confluent bacterial monolayers (**Figure 7d, 6g** and **6j**) and at the colony edge (**Figure 7e** and **7h**) using our florescent FimX-YFP reporter to quantify collective polar behaviour, and understand its purpose in the context of colony expansion.

Our first challenge in all three of these assays is ensuring that fluorescent cells with poles in close proximity to one another are not included in analysis as this would skew the measurement of FimX-YFP concentration. To overcome this, we develop a filter that detects when labelled cell poles are in close proximity. Although it is possible to use 100% FimX-YFP cells at low density, if the same were to be done for monolayer or colony edge assays, all cell poles would be excluded by our proximity filter. Therefore, we use co-cultures of unlabelled WT and labelled FimX-YFP cells. This in itself brings up another challenge, as later we will quantify the signal from FimX-YFP surrounding topological effects, and the small proportion of labelled cells used will mean data must be aggregated across many defects to obtain a result. Therefore, and as outlined, it was essential to optimise our assay preparation method. Given the close packing of cells in the monoalyer and colony edge, single cell tracking can occasionally fail, which means measuring the collective velocity by coarse graining the velocity vectors from single cells is not possible. Therefore we must also choose a suitable method of measuring the collective velocity in these densely packed conditions.

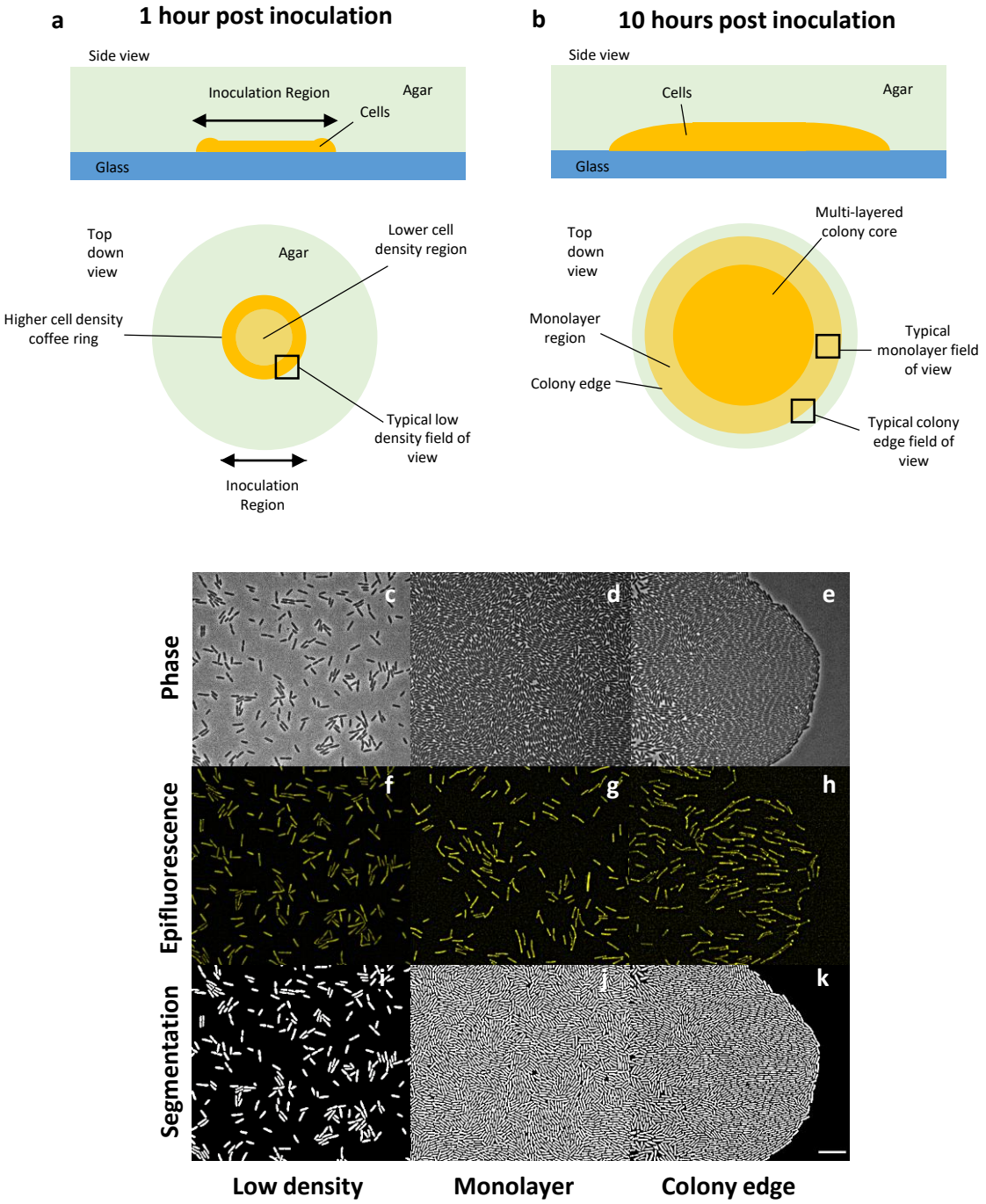

Figure 7: Diagrams (not to scale) of the experimental configurations with accompanying phase and epifluorescence images. (a) The side and top down view of the cell colony 1 hour post inoculation when low density images would be captured. An example of the region in which time lapse images are taken is shown by a black square. (b) The accompanying diagram for 10 hours post inoculation, at which the monolayer and colony edge data would be acquired. Phase images are shown for cells at (c) low density, 100% FimX-YFP cells (d) a $9:1$ WT:FimX-YFP monolayer assay and (e) a $9:1$ WT:FimX-YFP colony edge assay, with accompanying epifluorescence images shown in (f), (g) and (h), and binary segmentations in (i), (j) and (k) for the respective case. The scale bar in (k) is 10 µm.

2.5 Using FAST to track cells

After running the epifluorescence time lapse videos through our custom FIJI processing scripts, we used the corresponding phase images to perform cell tracking. Accurate tracking of single cells in bacterial monolayers has previously been performed using the open source Matlab package, the Feature Assisted Segmenter/Tracker (FAST) [19]. FAST operates in a modular fashion, where the output of each stage is used in the next and in this study we used the Segmentation, Feature Extraction and Tracking modules in sequence [19]. Here we provide a brief overview of each section and the parameters used for cells at low density, in a confluent monolayer or at the colony edge. We will not provide detailed description on the methodology of FAST, these are found in [19].

FAST begins with the Segmentation stage, where the edges of *P. aeruginosa* in the phase channel are identified and used to produce binary objects representing each cell. It was possible to use the same segmentation settings for all experimental conditions, and these values are given in **Table 1**. As seen in **Figure 7i-k**, the parameters used to generate the binary segmentations are able to accurately detect the locations of individual cells in dense collectives. With the binary segmentations obtained, we move onto Feature Extraction, where an ellipse is fitted to each of the binary segmentations to obtain the coordinates, length, width and orientation of each cell. The feature extraction stage also allows for the mean body intensity in the fluorescent channel to be measured, allowing for the categorisation of each cell as unlabelled or labelled. With segmentation and feature extraction complete, we must now perform tracking by linking objects between segmented frames.

Parameter	**Value**
Neighbourhood Size (pixels)	9
Texture Threshold	0
Ridge Scale	50
Ridge Threshold	0.07
Minimum Ridge Area (pixels)	100
Watershed Threshold	3
Object Area Threshold Low (pixels)	500
Object Area Threshold High (pixels)	10000

Table 1: Parameters used in FAST to obtain segmentations.

Unlike the segmentation stage, we changed the value of some parameters to track cells in each experimental condition, as the density and movement in each timelapse was variable. However, we do keep two tracking parameters constant between environments, the first being the Minimum Track Length which sets the minimum time an object must be present for to be included in tracking. Later in **Section 3.1.1**, we check that cell poles of labelled bacteria are sufficiently separated from one another in space. This check requires knowledge of the coordinates of all cells, therefore the set the

Minimum Track Length is set to single frame (one second) so no objects are excluded. The second parameter that was maintained across all timelapses was the Maximum Gap Width, which is the number of time points that a segmentations can be absent for without the track breaking. We set the Maximum Gap Width to two frames (two seconds) which allow a cell to be miss-segmented for a single frame without breaking the trajectory. Increasing the Maximum Gap Width to a value above two frames would could increase the length of trajectories further, but would also increase the likelihood of errors.

To track objects, FAST links objects between frames based on a number of different user defined 'features'. In our case the features we used for tracking were the cooridnates of the cell's centroid, its width, and its orientation. Given we are imaging twitching motility at one frame per second, the position and orientation of each cell should not change significantly, providing reliable measurements to link objects. There are rare occasions when FAST is unable to properly segment two neighbouring, parallel cells in the monolayer or colony edge, which results in a large change in segmentation width over time. Therefore, using the cell width as a feature to allows us to rapidly determine if a miss-segmentation has occurred. FAST uses values named the Inclusion Proportion and Adaptive Detection Threshold which dictate which links are kept in tracking based on their quality. The Inclusion Proportion and Adaptive Detection Threshold used in each experimental condition are summarised in **Table 2**.

Parameter	**Low Density**	**Monolayer**	**Colony Edge**
Inclusion Proportion	0.935	0.910	0.925
Adaptive Detection Threshold	0.003	0.1	0.001

Table 2: Parameters used in FAST for tracking each environment

2.6 Tracking topological defects in bacterial monolayers

Topological defects are points in a bacterial monolayer where domains of cells with different orientations alignments meet one another [138]. This thesis focuses on $+1/2$ and $-1/2$ topological charge defects, termed comets and trefoils respectively. As our assays contain co-cultures of cells with a small proportion of labelled cells, quantification of the polarisation and pole swapping rates of cells around defects (**Section 3.2.1**) required us to collate together data from many defects to enhance the signal.

We used the open source software Defector to detect topological defects using Matlab [34], using phase images of confluent *P. aeruginosa* monolayers. The director field is smoothed by a Gaussian filter prior to detection, with larger standard deviations resulting in smoother director fields, resulting in fewer detected defects. We validated defect detection by overlaying the location of putative defects

on phase images. Once defects are detected in each image, FAST is used to track the movement of defects over time. The Inclusion Proportion was set to 0.8 and the Adaptive Detection Threshold was set to 0.001. We only included defects in our analyses if their trajectories were > 30 seconds long to ensure that ephemeral fluctuations in the director field did not influence our results. This methodology allowed us to reliably track $+\frac{1}{2}$ and $-\frac{1}{2}$ charged topological defects in confluent bacterial monolayers, which was confirmed by visual inspection.

2.7 Using PIVLab to measure bulk velocity in collectives

In **Chapter 3** we will perform analyses that compare the localisation and dynamics of FimX-YFP relative to collective movement, and therefore must quantify the collective velocity of cells moving as a group. One might assume that measuring the collective dynamics in the monolayer is a matter of coarse graining the velocity vectors of neighbouring cells, that are measured through single cell tracking in FAST. However, tracking of individual cells in large cell density environments such as monolayers can fail occasionally due to the close proximity of the bacteria to one another. The velocity of these untracked cells would therefore not be included in the coarse graining to measure collective velocity, which could lead to incorrect measurements of collective movement being returned.

Instead, we utilise particle image velocimetry (PIV) to measure the collective dynamics observed in the monolayer. PIV measures the correlation between a region of pixels in a single frame of a time lapse with the subsequent frame, where the location of the greatest correlation corresponds to an area most similar to the region under investigation, and the distance between the two is be used to calculate a collective velocity [158]. We apply PIV to our monolayer and colony edge time series, using the phase channel to measure collective velocity. We use the open source Matlab package PIVLab to measure PIV, which produces a grid of equally spaced (0.26 μm) velocity vectors along the x and y ($v_{\mathrm{X_{PIV}}}$ and $v_{\mathrm{Y_{PIV}}}$ respectively) axes of each of our time series. To remove spurious results, velocity vectors are restricted to the range -24 μm min$^{-1} < v_{\mathrm{X_{PIV}}} < -24$ μm min^{-1} and 24 μm min$^{-1} < v_{\mathrm{Y_{PIV}}} < 24$ μm min^{-1} [158, 159, 160]. Here, 24 μm min^{-1} is the equivalent of a cell moving one tenth of its length in a second, a reasonable speed for twitching motility [34]. Velocity vectors that are removed by this restriction are replaced using two-dimensional spline interpolation. Before using the filtered fields to calculate collective velocity, we apply a 2D median filter, which converts each vector into the median value of a square shaped 5 μm $\times$ 5 μm window centered on the vector in question and acts to smooth the data spatially. PIV fields were then visually ground truthed by plotting them over top of the phase contrast images. Once we had reliable measurements of $v_{\mathrm{X_{PIV}}}$ and $v_{\mathrm{Y_{PIV}}}$, these velocities were then interpolated at the location of the cell centroids, allowing us

to compare the larges cale movement of the collective (measured using PIV) with that of individual cells (measured using FAST).

2.8 Comparison of unlabelled WT strain with the FimX-YFP fusion

Now that we have explained the methods used quantify the characteristics of *P. aeruginosa* in our three different assays, we used these methods to quantify potential differences between the unlabelled WT and our FimX-YFP fusion strain. Compared to the unlabelled WT strain, our fusion strain has altered amount of functional FimX both because it expresses FimX-YFP from a non-native promoter and because the labelled version of this protein (FimX-YFP) might have impaired function compared to unlabelled FimX. Thus our fusion strain might exhibit altered motility or changes cell length compared to the WT, which ultimately can change how they move as a collective [112]. In this section, we first measure the differences between these two strains at both individual cell level (by comparing their length and speed) and then test whether they move differently at a collective level by measuring whether their relative frequency changes over time as the colony expands across the agar.

Using the trajectories obtained from FAST, cells are assigned as unlabelled or labelled using the mean cell body intensity in the YFP channel, which requires a different manually determined threshold of each time lapse that was chosen by visual inspection (**Figure 15**). **Figure 8a** and **8b** show histograms of WT and FimX-YFP cell length and velocity respectively, with mean values displayed in **Table 3**. To ensure the data included in these analyses was of high quality, we included only trajectories whose aspect ratio was less than 6.5, the minimum track length is 30 seconds long, and removing non-motile cells by only considering trajectories with a mean velocity > 2.7 μm min^{-1} (see **Section 3.1.1** for justifications of filter values). We show filtered data in this section as it is represents the subset of cells used in analysis through this thesis.

Our results show a subtle but consistent difference in cell length, with FimX-YFP cells being on 0.1 μm longer, a difference of approximately 3% (**Figure 8a**). Similar changes in cell length have been observed in other mutants of the Pil-Chp system [34]. We expect that this small difference will not have a significant impact on the behaviour of FimX-YFP cells in dense collectives or the the physical properties of the system such as domain size [112].

A histogram of cell velocity for each strain is shown in **Figure 8b**. In the low density assay, the mean velocity of WT cells, 7.02 ± 0.02 μm min^{-1}, is less than the FimX-YFP strain, 8.63 ± 0.02 μm min^{-1}. A reduced velocity in a low density assay (where cell-cell collisions are rare) therefore implies that the force produced by the FimX-YFP strain is greater than that of the WT. Although

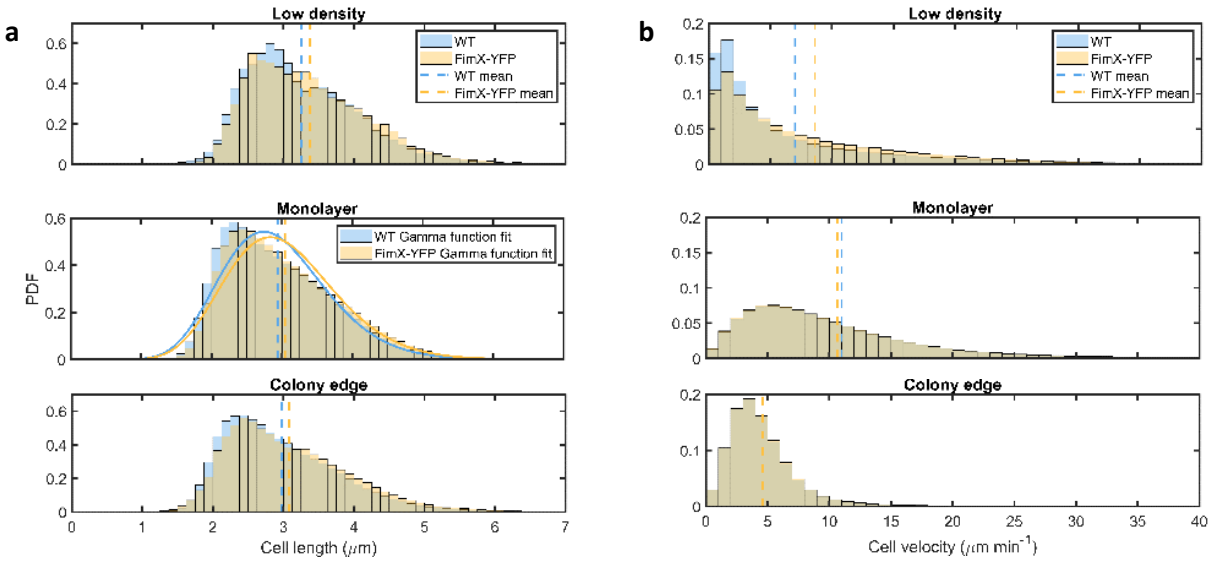

Figure 8: Histograms displaying (a) cell length and (b) velocity for WT and FimX-YFP cells at low density, in monolayers and at the colony edge. Low density, monolayer and colony edge data comes from 16, 15 and 24 experimental time series that are between two and three minutes in length respectively, with the corresponding time of all trajectories shown in **Table 3**. The monolayer cell length plots show fitted Gamma functions used to parameterise a model in **Section 3.2.2**. For (a) bin size is 0.125 μm and for (b) bin size is 1 μm min^{-1}. The ratio of WT:FimX-YFP cells is 1 : 1, 21 : 4, (six 9 : 1 and nine 8 : 2 data sets) and 9 : 1 for low density, monolayer and colony edge data sets respectively.

		Mean Cell Length (μm)		
Environment	**Eligible Time (Days) WT/FimX-YFP**	**WT**	**FimX-YFP**	**Difference**
Low Density	63.7/66.8	3.255 ± 0.002	3.373 ± 0.002	0.1178
Monolayer	1633.5/296.1	2.9366 ± 0.0003	3.0405 ± 0.0008	0.1039
Colony Edge	688.7/115.0	2.9715 ± 0.0005	3.083 ± 0.001	0.1116

		Mean Velocity (μm min^{-1})		
Environment	**Eligible Time (Days) WT/FimX-YFP**	**WT**	**FimX-YFP**	**Difference**
Low Density	63.0/66.1	7.02 ± 0.02	8.63 ± 0.02	1.6068
Monolayer	1614.5/292.9	11.010 ± 0.004	10.676 ± 0.009	0.3336
Colony Edge	680.9/113.8	4.651 ± 0.002	4.602 ± 0.005	0.0483

Table 3: Mean length and velocity of WT and FimX-YFP cells in the three experimental conditions. Error values show the standard error in the mean between all values for each experimental condition. Low density, monolayer and colony edge data comes from 16, 15 and 24 minute long experimental time series between two and three minutes in length respectively. The ratio of WT:FimX-YFP cells is 1 : 1, 21 : 4, (six 9 : 1 and nine 8 : 2 data sets) and 9 : 1 for low density, monolayer and colony edge data sets respectively.

the difference between mean velocity for WT and FimX-YFP cells is similar in the monolayer and at the colony edge, in these assays the movement of each strain in these co-cultures will be impacted by physical interactions with neighbouring bacteria, which will make these two strains behave more similarly to one another.

We have found that at low density, cells containing a FimX-YFP fusion are likely capable of producing larger forces through the retraction of TFP than the unlabelled WT. Previous experiments performed on co-cultures of WT cells and $\Delta pilH$ mutants show that the latter is capable of exerting a greater force than the former, and when density increases such that a monolayer forms, these larger force producing individuals form multilayered structures more readily, and during the early stages of colony development are enriched in concentration at the border, but then become lost over time because they are more likely stand up vertically which arrests their lateral movement [34].

To test whether the faster moving fusion strains might similarly become lost from the colony edge as it expands, we measured the proportion of labelled cells in the monolayer and colony edge to see if it matches the ratio at which the colony was inoculated at. The results, outlined in **Figure 9**, are calculated by measuring the proportion of total time labelled cells are tracked for in each data set. We use the low-density case as a control as imaging takes place an hour post inoculation, and cell division has not caused the density to increase drastically. At low density, our measured proportion of labelled cells matches that of the inoculation ratio, with the same result being the case for the monolayer and colony edge. The median proportion of FimX-YFP cells at the colony edge was above that of the inoculation ratio, which is consistent with faster cells accumulating at the colony

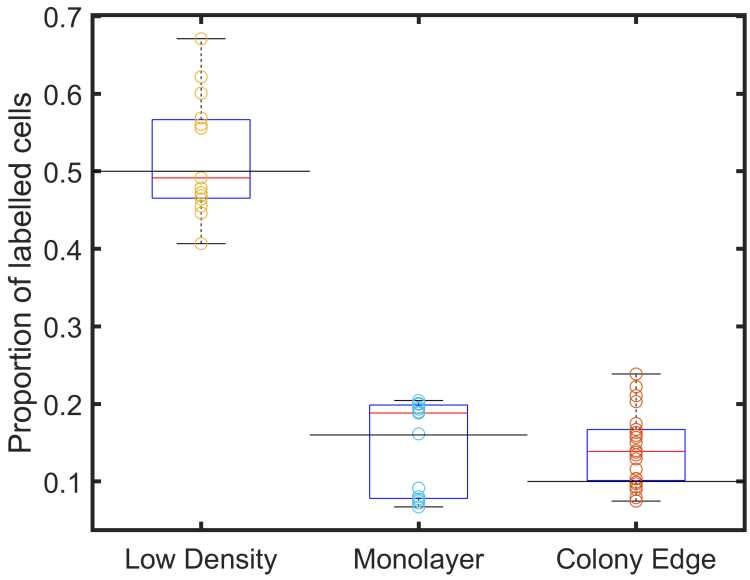

Figure 9: The proportion of WT and FimX-YFP cells in the three experimental environments. Data taken from 16, 15 and 24 experimental time series between two and three minutes in length, taken at one frame per second for cells at low density, in the monolayer and at the colony edge, with each time lapse shown as a circle over the respective box plot. The red line indicates the median and the box represents the interquartile range of proportion values from each experimental time series. Black horizontal lines represent the inoculation proportion of labelled cells for each respective environment, these being 0.5, 0.16 (considering the six $9:1$ and nine $4:1$ WT:FimX-YFP assays used can be equally weighted) and 0.1.

edge. At low density FimX-YFP cells are 22.9% faster than WT cells, where as Δ*pilH* cells have velocities that are approximately twice that of the WT [34]. The relative decrease in velocity between FimX-YFP and Δ*pilH* cells could mean the former has insufficient force to generate the vertical groups of cells in the colony interior that the latter does, and is therefore more likely to be present at the periphery of the colony [34].

Although our cells are faster than the WT, they are still present at the colony border, implying they are not orienting out of plane in the colony interior and becoming immobilised. They are also of a similar length to the WT and will be used in small proportions in our experiments. Therefore, the collective dynamics observed in our experiments should not be drastically affected by cells of differing rod length or force production.

2.9 Quantifying the effect of phototoxicity

When imaging using epifluorescence microscopy, an increase in excitation intensity or imaging frequency accelerates photobleaching and phototoxicity. To investigate if the light used for epifluorescence affects cell motility, we measured how the mean velocity of *P. aeruginosa* cell changes over the course of our time series. Although there is no reason to suggest that excitation illumination will affect WT and FimX-YFP cells differently, they have been analysed separately to check. The results of velocity binning over time is seen in **Figure 10** and summarised in **Table 9**. For all experimental conditions, **Figure 10** shows that velocity decreases over time by approximately 27.9%, suggesting that we cannot extend our experimental measurements for longer than three minutes.

	Mean Cell Velocity (μm min^{-1})					
	WT			**FimX-YFP**		
Environment	**Maximum**	**Minimum**	**Reduction**	**Maximum**	**Minimum**	**Reduction**
Low Density	8.0	6.0	2 (25%)	9.4	7.6	2.2 (23.4%)
Monolayer	11.3	9.9	1.4 (12.4%)	10.7	8.7	2.0 (18.7%)
Colony Edge	5.7	3.6	2.1 (36.8%)	5.6	3.5	2.1 (37.5%)

Table 4: Investigating the effects of phototoxicity on mean velocity for WT and FimX-YFP cells in the three experimental environments. Maximum (minimum) indicates the largest (smallest) mean velocity observed over the time series from **Figure 10**. The reduction indicates the difference in mean velocity between the maximum and minimum value.

In this chapter we have outlined the preparation of the subsurface assay, the microscopy methods, and the image processing and analysis techniques used to quantify the behaviour of solitary and collectively moving *P. aeruginosa* cells. We have also tested whether two strains used in these assays behave differently to one another. The movement speed of cells with a FimX-YFP fusion was found to be larger than that of unlabelled WT cells, however the difference between them was relatively small in high density assays. Likewise, the length of cells with a FimX-YFP fusion was found to is

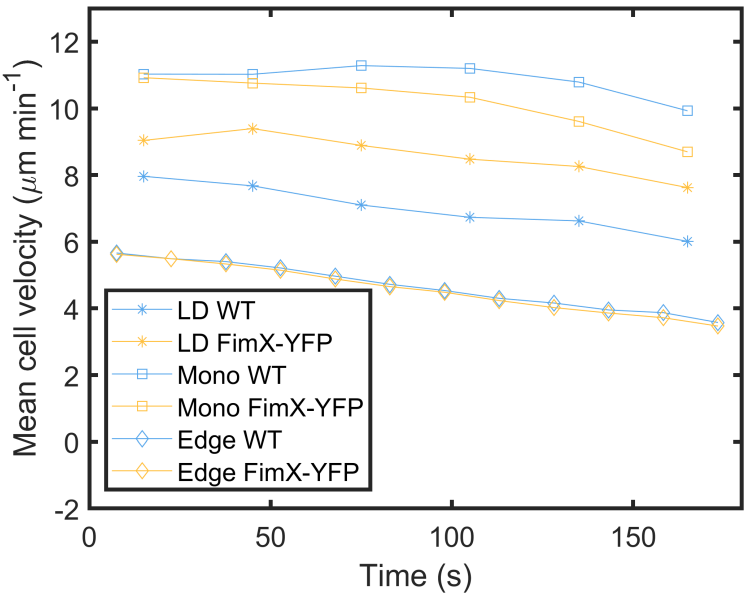

Figure 10: The effects of phototoxicity on mean cell velocity. Mean cell velocity as a function of time for WT and FimX-YFP cells in the low density assay, in the monolayer and at the colony edge. Data taken from 16, 15 and 24 experimental time series respectively. Bin size is 15 seconds.

consistently 0.1 μm larger than that of unlabelled WT cells, but this is only a 3.5% difference. Finally, the effects of bleaching have been investigated and although there is a reduction in velocity, it is not of a size to render any data set unusable. With all appropriate checks in place, it is now possible to proceed with more complex analyses, and investigate bacterial twitching motility in solitary cells and dense collectives.

3 Quantifying polarisation in developing *Pseudomonas aeruginosa* biofilms

Across all scales of life, collective movement is used as a means of improving the reproductive potential for the individual. Schools of fish respond to the presence of a predator, displaying a large degree of alignment in orientation and velocity whilst doing so. Changes in alignment and orientation of an individual can cause its neighbours to follow, and these changes can potentially spread to the entire collective [161]. In the insect kingdom, ants form pheromone based trails leading from the nest to food sources. They will also attack rival colonies by forming interconnected pathways with hundreds of thousands of individuals [128]. Crucially, these collective behaviours only occur once the density of individuals exceeds a certain value [162]. Collective behaviour is also observed at the length scale of unicellular organisms such as bacteria, and again these are only observed above critical population densities [12].

Bacteria commonly live in dense surface-attached collectives called biofilms that are comprised of thousands of individual cells. When living in a biofilm, bacteria produce a range of extracellular polymeric substances, which provide protection from dispersal by flow [97]. Additionally, the effects of some antibiotics on bacteria are lessened in biofilms compared to those in liquid culture, due to the increased cell density reducing the diffusion of antimicrobial molecules [114]. As bacteria live in close proximity to their neighbours in biofilms compared to those in liquid culture, the rate of DNA exchange through horizontal gene transfer increases. As a result, the exchange of genes conferring antibiotic resistance occurs often, and resistant strains commonly arise in biofilms [115]. Due to the increased risk of antibiotic resistant infection, biofilms present a challenge in healthcare and agriculture [115, 116].

The opportunistic pathogen *P. aeruginosa* forms biofilms that are commonly studied at the interface between agar and air, where they form colonies [71]. More recently, interstitial or sub-surface biofilm assays, where bacteria grow at the interface between glass and agar have been used to investigate collective behaviour in *P. aeruginosa* as they can be imaged in detail by high numerical aperture microscopy through a cover slip [34]. When grown at the interface between agar and air, through cell division a torque acts on each individual to reorient its body out of plane and three dimensional structures readily form. In comparison, there is a torque acting in the opposing direction when bacteria are grown in interstitial assays, keeping cell bodies flat at the agar-glass interface, with single layered sheets called monolayers forming as a result [73]. It is often not feasible to track individual bacteria in densely packed three dimensional structure, and therefore a monolayer is preferred for studies at high density when one needs to quantify the behaviour of individuals.

However, even when using high magnification microscopy it is challenging to resolve the motion of each cell in the a monolayer, as the movement of each individual bacterium is highly influenced by the densely packed neighbouring cells surrounding it. Fluorescent protein fusions are often used to quantify temporal information regarding a protein's role in cell motility [77]. At low density, the environmental sensor FimX, has been shown to localise to the leading pole of *P. aeruginosa*, however, to date no studies have been performed using fluorescent fusions to investigate twitching driven collective motility in bacterial monolayers [74].

A bacterial monolayer is an example of active matter, a system that exists outside of thermodynamic equilibrium where individual constituents draw energy from their surroundings to perform work [163]. In the case of *P. aeruginosa* in an interstitial assay, energy is drawn from its surroundings in the form of the agar slab confining the cells to one dimension, and work is performed by TFP, attaching to the substrate, retracting and generating a force to pull the cell body [164]. The equations of active nematics have been used to describe collective and individual behaviour observed within bacterial monolayers, with the presence of long range orienational order and half integer charged topological defects [15]. The constituents of bacterial monolayers are intrinsically polar objects, where a force acts in a single direction. However, nematic equations have been used to describe the behaviour of the collective as through coarse graining of force fields in the monolayer there is no preferential direction of travel [15]. Recently a growing body of evidence suggests that many active matter systems are not purely nematic, and instead exist on a spectrum between nematic and polar, due to coexistence of half integer and full integer topological defects, the latter being a hallmark of polar systems [138]. In this chapter, we seek further evidence that collective polar behaviour exists in a system previously considered as nematic.

Our focus is not restricted to the monolayer, we also investigate collective polar behaviour at the colony edge. The expansion rate of a bacterial colony is used as a measure of fitness as it increases access to nutrients, and as such the fitness of a strain can often be quantified based on how quickly they colonise a surface [148]. For example, one might naively assume that $\Delta pilH$ cells have an increased relative fitness than the WT as on average each cell is fast due to the fact that $\Delta pilH$ are hyperpiliated [22]. However, when considering the expansion rate of the two colonies, the WT is faster than $\Delta pilH$ in the long term, giving it a relative fitness advantage [34] As *P. aeruginosa* forms single layered sheets at the colony edge, the same microscopy techniques used to image the monolayer were used to search for any novel collective movement, identifying large groups of aligned cells moving outward in the direction of colony expansion. We therefore investigate any potential for polar behaviour at the colony edge, and consider the implication of this on colony expansion and

overall collective fitness.

Through the use of simultaneous phase and epiflourescence time-lapse microscopy, high density cell tracking and a custom image analysis pipeline, the following chapter investigates the asymmetry of intracellular FimX-YFP localisation at the cell poles of *P. aeruginosa* at low density, the monolayer, including surrounding $+1/2$ and $-1/2$ defects, and at the colony edge, with respect to the direction of collective velocity. The level of disparity in FimX-YFP concentration, will be referred to as FimX-YFP asymmetry. For example, a cell with a large concentration at one pole, and a small concentration at the other is highly asymmetric. Therefore, any use of the terms polar or polarised will strictly refer to describing the state of collective bacteria behaviour; polar or nematic.

3.1 Does FimX-YFP localisation correlate with individual cell movement?

As shown in **Figure 7**, interstitial 'sandwich' assays are innoculated at the interface between agar and glass, allowing for the acquisition of time-lapse images of WT and FimX-YFP labelled *P. aeruginosa*, and form the focus of this thesis. We use co-cultures of unlabelled and labelled cells as the signal from a pole will always be distorted by its neighbours in a high density 100% FimX-YFP assay. Given that *P. aeruginosa* has been shown to twitch towards the pole with greatest FimX concentration and that $+\frac{1}{2}$ charge defects have been shown to be crucial in many biological processes it was sought to investigate any potential asymmetry in FimX-YFP concentration when bacteria are in close proximity to topological defects [34, 74]. Before investigating the concentration of intracellular FimX-YFP around topological defects, the correlation between asymmetry and cell motility must be confirmed for the strain used in this thesis, as it has not be used previously in literature. In the upcoming sections, the process of FimX-YFP concentration measurement at the cell pole is explained in detail, including the quantification of asymmetry, cell movement and the various filtering processes used.

3.1.1 Quantification of polar FimX-YFP and cell motility in individual cells

Quantifying the concentration of protein at the cell poles is by no means a trivial task, as it requires using appropriate tracking software, an accurate FimX-YFP concentration quantification method, and suitable filtering to ensure accurate data has been obtained. In the upcoming section we outline a generalised process that is applicable to all polar localising proteins, but specifically has been used to quantify intracellular FimX-YFP in *P. aeruginosa* at low density and in packed collectives.

To measure the concentration of FimX-YFP at the cell poles from the epifluorescence images, the coordinates of each pole must be calculated using the corresponding phase contrast image. To determine the pole coordinates, time resolved information of each bacteria's position, orientation

and length must be obtained. If there were only a few cells present in each movie, it would be possible to manually measure the properties of each bacterium. However, even at low density each of our movies contain over a hundred cells in each field of view, across videos between two and three minutes in length. Therefore, the first choice to be made in uncovering the relationship between asymmetry and cell movement, is using the most appropriate tracking software. Any software used must be able to accurately track rod shaped bacteria at low and high densities and resolve them such that neighbouring cells are segmented correctly. The software must also produce time resolved data containing the coordinates, length and orientation of each individual so the positions of both poles can be calculated. The Feature Assisted Segmenter/Tracker is our software of choice as it has been previously used in experiments tracking *P.aeruginosa* in high density environments, outputs the required location, orientation and size information, and allows for the further calculation of additional cell properties such as pole location [19, 34]. A schematic displaying the parameters of each cell that FAST can output is shown in **Figure 11**.

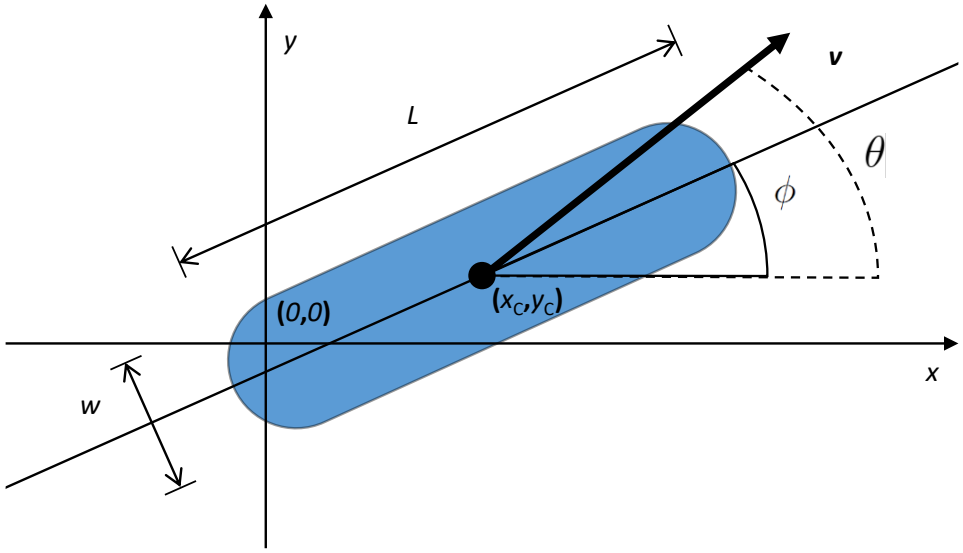

Figure 11: A schematic diagram of the data exported by FAST that is used in further analysis. x_c and y_c represent the x and y centroid of the cell respectively and L and w represent the length and width of the cell respectively. Angles are measured from the positive x direction anti-clockwise. The angle ϕ denotes the orientation of the cell body and the angle θ is the direction of travel of the cell, with the velocity vector shown by $\boldsymbol{v}$.

In **Figure 11**, ϕ is determined by fitting an ellipse to each of the cell segmentations obtained by FAST (see **Section 2.5**) [19]. By convention ϕ is directed from the cell centroid to the pole of the cell that has the greatest x coordinate at the start of tracking. As the cells have the possibility of rotating, we define ϕ from $-\infty < \phi < \infty$.

With ϕ suitably defined, it is now possible to perform measurements of FimX-YFP concentration at each pole of *P. aeruginosa*. Here the calculation of each pole's coordinate will be discussed,

followed by the process, benefits and drawbacks of the first method used to quantify FimX-YFP concentration, the 'ring' method. **Equations 1** and **2** are used to calculate the coordinates of pole 1 and 2 at each time point, which are denoted (x_1, y_1) and (x_2, y_2) respectively,

$$(x_1, y_1) = (x_C + 0.4L\cos(\phi), y_C + 0.4L\cos(\phi)) \quad (1)$$

$$(x_2, y_2) = (x_C - 0.4L\cos(\phi), y_C - 0.4L\cos(\phi)). \quad (2)$$

Here we have multiplied L by 0.4 rather than 0.5 which would yield the coordinates of the very tip of the cell. By visual inspection, multiplication by 0.4 generated a coordinate at the centre of the hemispherical end of our rod shaped cells, where the FimX-YFP signal accumulates, as shown in **Figure 12a**. The mean pixel intensity within a circle of radius 0.4 µm centred at (x_1, y_1) or (x_2, y_2), is used to quantify the FimX-YFP concentration, I_1 and I_2 respectively. As the width of the cell, w, is on average 0.8 µm locating the coordinate of the centre of the hemispherical cap, which is modelled as a circle with diameter 0.8 µm, is essential such that all FimX-YFP localisation is measured (**Figure 12b**).

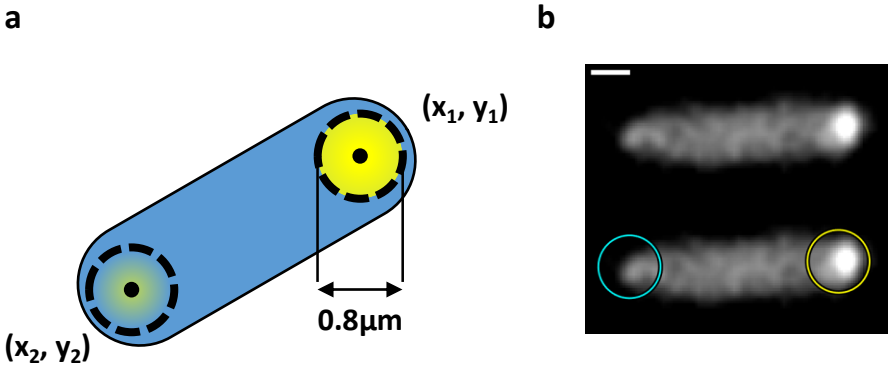

Figure 12: The ring method process of FimX-YFP quantification at the cell poles. (a) Cell body is represented in blue with FimX-YFP in yellow. Cell pole coordinates are shown with black dots and a circle of radius 0.4 µm shown with dashed black lines around the hemispherical caps of the rod-shaped cell. (b) Grayscale image of FimX-YFP signal from a solitary *P. aeruginosa* cell. Top image shows a cell to be analysed with the bottom image showing the same cell with an overlay of the 0.4 µm radius circles with pole 1 in yellow and pole 2 in cyan. The scale bar is 0.5 µm in length.

The ring method provides a relatively simple process of quantifying FimX-YFP concentration at the cell poles using epiflourescence microscopy, however the reliability can vary depending on how accurate the elliptical fit is. As determined through visual inspection, if ellipse fitting is accurate, the center of the cell pole cap is found reliably and an accurate quantification of FimX-YFP is performed.

However, it is often observed that measurements of ϕ and L contain small deviations from the true value, resulting in an incorrect identification of the cell pole cap location (**Figure 13**). When cell pole cap location is incorrect, pixels closer to the centroid or pixels from the image background intensity are incorrectly included in the mean calculations of I_1 and I_2.

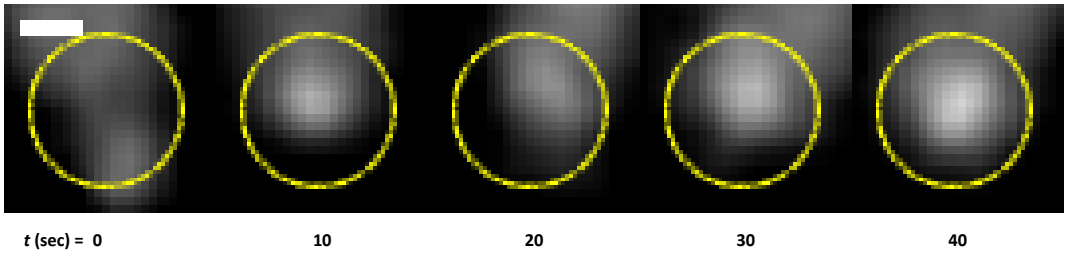

Figure 13: A time lapse of grayscale epifluorecent images showing the 'ring' method of quantifying FimX-YFP concentration, where the yellow ring shows the 0.4 μm radius region where the average value of pixel intensity calculated at the cell poles. It is evident that the ring method often cannot accurately locate the hemispherical poles, owing to inaccurate measurements of ϕ and L from automated ellipse fitting. Scale bar is 0.5 μm.

Given the ring method has inherent inaccuracies as a result of noise in the ellipse fitting in FAST, a new method of quantifying FimX-YFP concentration at the cells poles must be established. The new method still utilises **Equations 1** and **2**, however, an alternate method is used to identity the exact position of the FimX-YFP localisation. Here, the 'spot' method is introduced, the process by which it operates is explained, and the benefits and drawbacks of the method outlined.

The spot method relies on identifying the brightest pixel, or collection of pixels at the cell pole and taking the average value around that coordinate to determine I_1 and I_2. The process begins by only considering pixels within 12.5 pixels (0.38 μm) from the cell pole location, as this decreased the likelihood of noise from the cell body interfering with FimX-YFP quantification. Any pixels outside of this range are excluded from any analysis. We then identify the coordinates of the brightest pixel $(x_\mathrm{B}, y_\mathrm{B})$ and the intensity is calculated as the mean value of all pixels within 2.5 pixels (0.08 μm). This radius was chosen by visual inspection as it included the bulk of the greatest FimX-YFP localisation (**Figure 14**) and also excludes pixels that are more than 0.38 μm from the calculated coordinate of the cell pole. We also check that I_1 and I_2 are above the cell body intensity, I_C, which is calculated by averaging the mean pixel intensities within 0.4 μm of the centroid of the binary segmentation corresponding to that cell. When no FimX-YFP expression was observed at the poles, the cell bodies appeared to have a uniform distribution of fluorescence across their bodies. Therefore, if I_1 or I_2 is smaller than I_C, it implies that one of the poles is not in focus, and therefore we set $I_i = I_C$ as appropriate (where i is pole 1 or 2).

More complex cases when there are more than one pixel at the cell pole with the brightest

intensity will now be considered. These cases include when the pixels with the greatest intensity are isolated from one another, or connect to one another, or if they form multiple groups of connected pixels. If two or more pixels have the largest value, and are adjacent to one another in space they are considered to be a 'pixel island', and (x_B, y_B) is taken to be the mean position of these pixels. I_i is the mean value of pixels within 2.5 pixels (0.805 µm) of (x_B, y_B). If there are two pixel islands with different sizes and the same maximum intensity, the mean position of the pixels in the largest island is set as (x_B, y_B). The same process applies when there is a pixel island and one other single brightest pixel at the cell pole, the mean position of the island is set to (x_B, y_B). When two pixel islands are identified with the same intensity and size, the island closest to the end of the cell is used as the molecular machines that drive twitching motility are typically most abundant at the tip of the pole [64]. When there are two or more pixels islands with the same intensity and size, and equal distance from the cell pole there is no way of distinguishing the two, we exclude these measurements from the further analyses, however this rarely occurs in practise. A comparison of the spot method and ring method is shown in **Figure 14**.

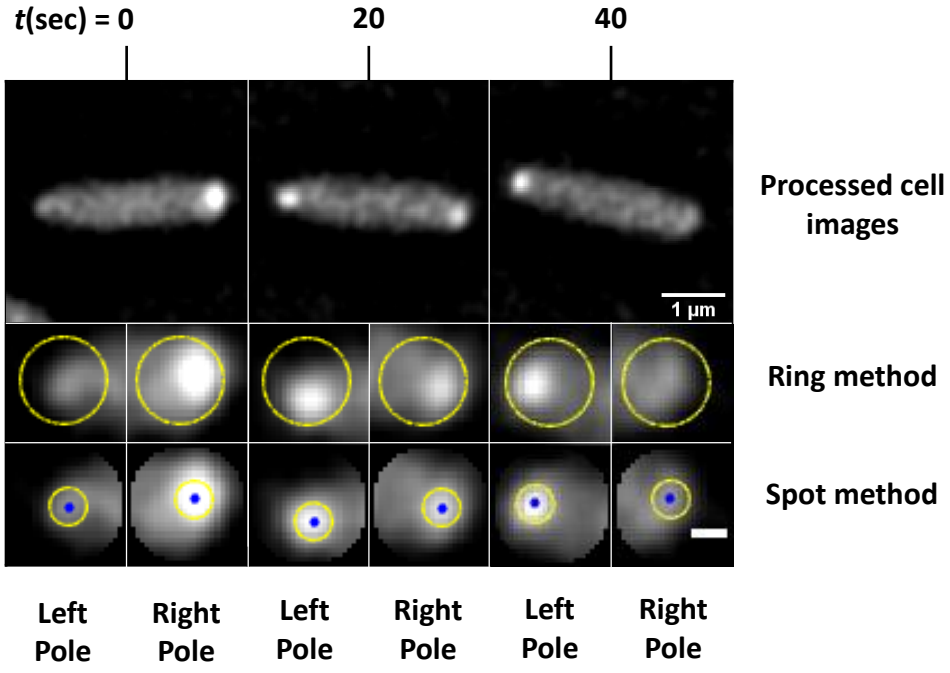

Figure 14: A comparison between the ring and spot methods of quantifying polar FimX-YFP concentration. The upper row shows an example cell at different time points during tracking, with the middle row showing the ring method and the bottom row showing the spot method, where the scale bar is 0.25 µm. In the middle and bottom rows, the left image shows the left hand pole and the right shows the right hand pole. Regions that an average is taken across are displayed in yellow, with the brightest spot in the bottom row shown by a blue marker.

As is no need to quantify the FimX-YFP intensity in the fluorescent channel of unlabelled cells, we must remove them from our analyses. FAST outputs a value of mean intensity for the entire

cell body aggregated over all pixels within the segmentation, which is used to distinguish the cells containing FimX-YFP from unlabelled cells. A PDF of mean cell body intensity is produced using all available data and a threshold manually selected between the two peaks, representing the labelled and unlabelled populations. The threshold is then used to assign every cell as unlabelled or labelled at every time in its trajectory. To account for variability in mean fluorescence intensity between experiments a separate threshold is used for each data set. An example PDF with threshold, and the results of tresholding is shown in **Figure 15**. It is now possible to split the cell population based the mean cell body fluorescence intensity, ensuring that only FimX-YFP cells are used in our analyses when appropriate. The next stage of the processing pipeline is to restrict analysis only to cells with suitable separated poles.

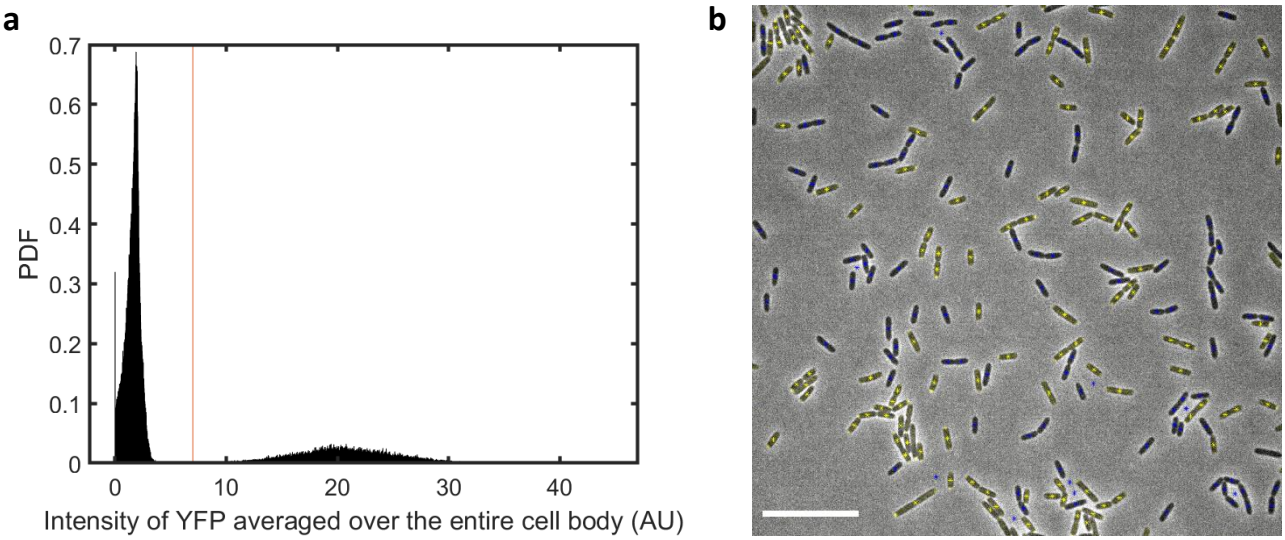

Figure 15: Using mean cell body fluorescence to categorise labelled and unlabelled cells in a low density assay comprised using a 1 : 1 ratio of unlabelled to labelled cells. (a) A PDF of the cell body intensity with the manually set threshold shown as a red line. The distribution is bi-modal with the left peak corresponding to unlabelled cells and the right-hand distribution corresponding to labelled cells. (b) Merged phase and epifluorescence microscopy images with yellow and blue markers overlaid to highlight the labelled and unlabelled cells respectively. An occasional blue marker is seen in empty space due to spurious augmentations however these are removed at later stages of analysis. The scale bar is 15 μm.

As the spot method of FimX-YFP concentration relies on identifying the brightest pixel within a 25×25 pixel (0.805×0.805 μm) region surrounding the cell pole, neighbouring labelled bacteria must be a significant distance away from $(x_{\mathrm{B}}, y_{\mathrm{B}})$, otherwise the signal from a neighbour can interfere with measurement. For example, the brightest pixel can be wrongly identified on a neighbouring cell pole. Without categorising each individual into an unlabelled or labelled population it would not be possible to tell if two labelled cells poles were within close proximity or touching one another. To address this we designed an algorithm called the 'nearest pole neighbour algorithm' to detect when

two labelled poles are too close to one another. The ultimate aim of the algorithm is to indicate if a cell is labelled and if all neighbouring poles are of a reasonable distance away such that FimX-YFP concentration measurement is accurate at each time point in a cells trajectory. If the cell is labelled, the algorithm compares the distance between the pole in question and the five closest neighbouring poles. Five other poles are used rather than all poles within a given time point to save computation time and the five closest poles can include the other pole on the cell in question. We removed any poles from our analysis that have another FimX-YFP pole within 0.8 μm of them (**Figure 16**).

A useful benefit of this algorithm is that it removes dividing cells from analysis. Such nearly separated cells can be resolved individually by FAST's segmentation algorithm, and are therefore considered as two different objects, the poles of the two objects at the division site always fail the nearest pole neighbour algorithm because they are within 0.8 μm of each other, as seen in **Figure 16c**. The nearest pole neighbour algorithm therefore provides a tool to filter the FimX-YFP concentration measurements at the cell poles to remove data that has been potentially contaminated by nearby cells or affected by cell division.

Two additional filters were used and combined with the nearest pole neighbour algorithm so that all points along a cell's trajectory must pass a series of conditions to be included in our analyses. Time points where the aspect ratio $(L/w) > 6.5$ are excluded as these are typically cells that are divided but have incomplete septa so FAST cannot differentiate between them. These cells are removed as their movement is different from those not dividing. As the mean length of *P. aeruginosa* is 4 μm, we exclude any time points in a trajectory where the centroid is within 4 μm of the border of the field of view, to ensure the entire cell is analysed. Therefore, to be included in our analyses, the cell must be labelled, its poles must be distinguishable from any other cell to allow for accurate FimX-YFP measurement, have an aspect ratio less than 6.5 and be beyond 4 μm of the border of the field of view.

It has been previously outlined how the spot method was used to measure FimX-YFP concentration at the cell poles, I_1 and I_2, and the subsequent filters that were used to remove data that was not considered reliable from our analyses. FimX can be unipolar, bipolar or not present at either pole in terms of localisation, and it has previously been shown that it is the asymmetry in FimX distribution between the poles that is correlated with the direction of cell movement [65]. To reliably correlate FimX-YFP localisation and cell movement it is useful to express I_1 and I_2 in a single metric. We express the asymmetry of FimX-YFP concentration between the cell poles using

$$I_{\mathrm{M}} = \frac{I_1 - I_2}{I_1 + I_2}. \tag{3}$$

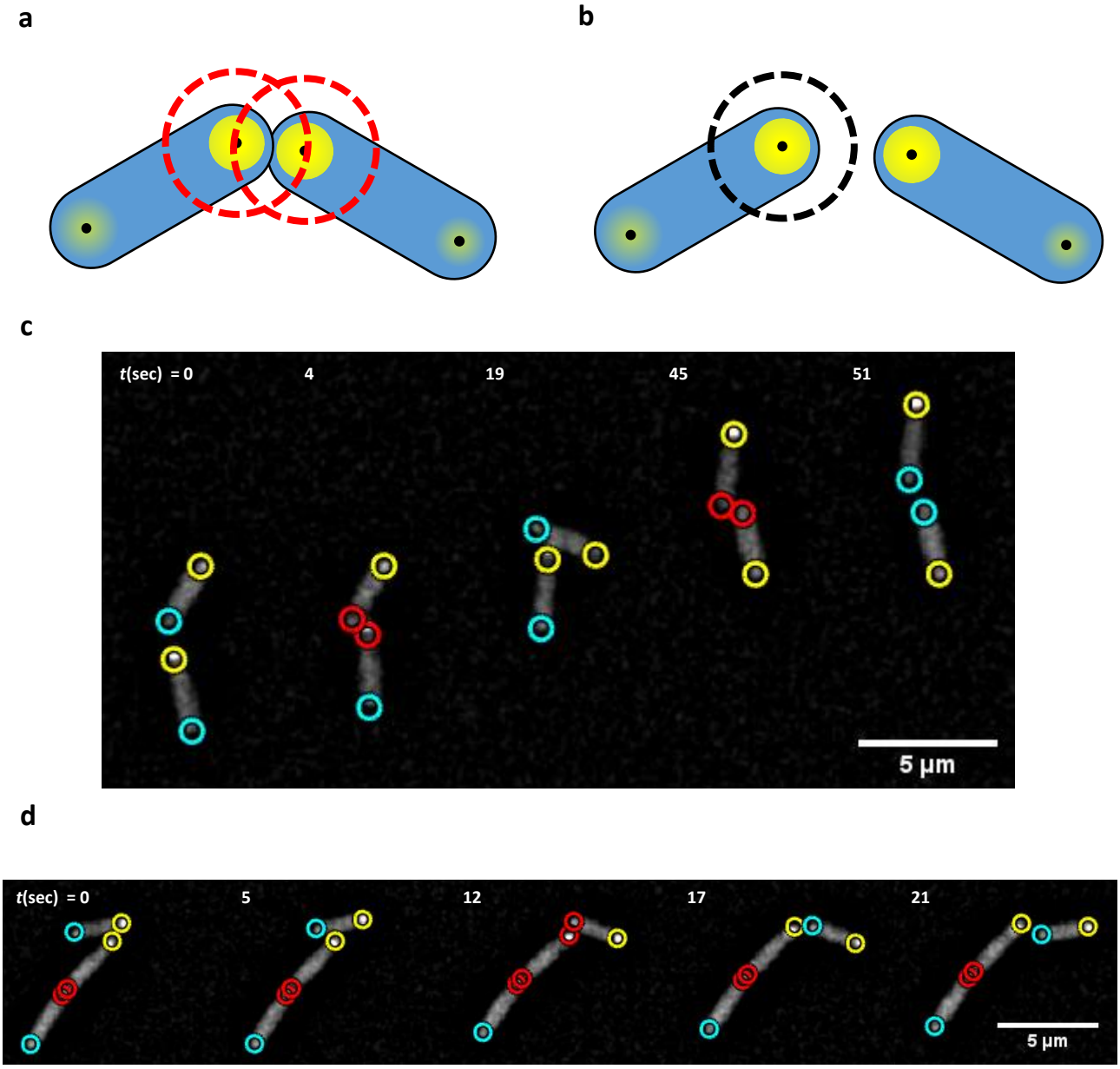

Figure 16: The nearest pole neighbour algorithm removes neighbouring labelled cells with close poles from our analysis (a) The poles of the two labelled cells are too close to one another and would be excluded from analysis as highlighted by the red dashed circles. (b) The two poles are a significant distance from one another and will be used in later data processing. (c) A time lapse showing the nearest pole neighbour algorithm in action. As cell poles are tracked continuously, when passing the algorithm pole 1 and 2 are shown using yellow and cyan rings respectively. If a pole is too close to a neighbouring labelled pole and excluded by the algorithm it is shown in red. (d) The algorithm also excludes cells going through division.

When $I_{\mathrm{M}} = 0$, there is an equal amount of FimX-YFP at each pole. If $I_{\mathrm{M}} > 0$, there is a greater FimX-YFP concentration at pole 1 and if $I_{\mathrm{M}} < 0$ there is a larger concentration at pole 2. Whilst in theory, $|I_{\mathrm{M}}| = 1$ can occur if I_1 has a non-zero value and $I_2 = 0$ or vice versa, however, in practise, as outlined in the description of the spot method, each pole will have the minimum fluorescence of I_{C}, the mean intensity at the centroid of the cell. While we tested other metrics, we found that I_{M},

which can both measure which pole contains more FimX-YFP (by whether it is positive or negative) and measure the strength of the asymmetry (by measuring the absolute value of I_{M}) was best suited for out subsequent analyses.

Beginning with coordinates, lengths and orientations determined by FAST, the process of quantifying FimX-YFP concentration asymmetry at the cell poles has been described. FimX-YFP concentration is measured using the spot method, which identifies the brightest pixel location and takes an average value of the surrounding pixels. Various filters have been outlined that determine if a cell is labelled, if cell poles are sufficiently resolvable in space, its aspect ratio and proximity to the image border, which are used to keep only data points that are reliable. These processes have culminated in the use of a metric, I_{M}, which describes the asymmetry of FimX-YFP concentration at the cell poles as a single number. In the next section, the relationship of I_{M} and cell movement will be investigated further.

3.1.2 Bacteria twitch in the direction of the pole with the largest FimX-YFP signal

Previous studies have shown that *P. aeruginosa* tends to move towards the pole with largest FimX concentration at low density [37, 74]. As the FimX-YFP fusion used in this thesis differs from those previously used in literature the relationship between FimX localisation and the direction of cell movement must be reestablished. Currently, it is unclear if intracellular FimX localisation correlates with twitching motility in the bacterial monolayer, and to separate observed cell movement within dense collectives from the movement generated by the retraction of an individual cell's pili this relationship must be confirmed, as the observed movement of an individual can be highly influenced by interactions with close by neighbours [13]. Therefore, investigating pili facilitated cell movement in dense collectives is not possible using phase microscopy alone, and fluorescent protein fusions must be used to separate a cell's intended movement and observed movement. In this section, we correlate motility and FimX-YFP asymmetry (I_{M}) at low density and then we analyse the behaviour of I_{M} in monolayers where cells are densely packed together.

We first define a metric to quantify bacterial movement. As I_{M} is positive or negative based on which pole has the greatest FimX-YFP concentration, any metric that measures movement should also change signs to reflect if the cell is moving in the direction of its pole 1 or 2. Using the outputs from FAST (**Figure 11**) to measure the direction of cell movement (θ), we can ensure it is in the same frame of reference as ϕ, and therefore make a direct correlation between the velocity vector and I_{M}. We define a new metric, $\boldsymbol{p}.\boldsymbol{v}$, which is the projection of the velocity vector of a cell, $\boldsymbol{v}$, along a unit vector, $\boldsymbol{p}$ in the direction of ϕ,

$$\boldsymbol{p}.\boldsymbol{v} = |\boldsymbol{p}||\boldsymbol{v}| \cos(\phi - \theta) = v_{\mathrm{MAG}} \cos(\beta). \tag{4}$$

Here, v_{MAG} is the magnitude of the velocity vector. Like I_{M}, $\boldsymbol{p}.\boldsymbol{v}$ can either be be positive or negative, representing if the cell is moving in the direction of pole 1 or 2 respectively. **Figure 17a** shows the vectors and angles involved in $\boldsymbol{p}.\boldsymbol{v}$ calculation, where as **Figure 17b** explains when I_{M} and $\boldsymbol{p}.\boldsymbol{v}$ are positive and negative. We note that twitching motility is often directed along a cell's long axis so that $|\cos(\beta)|$ tends to be near one. We can now investigate the correlation between these two variables.

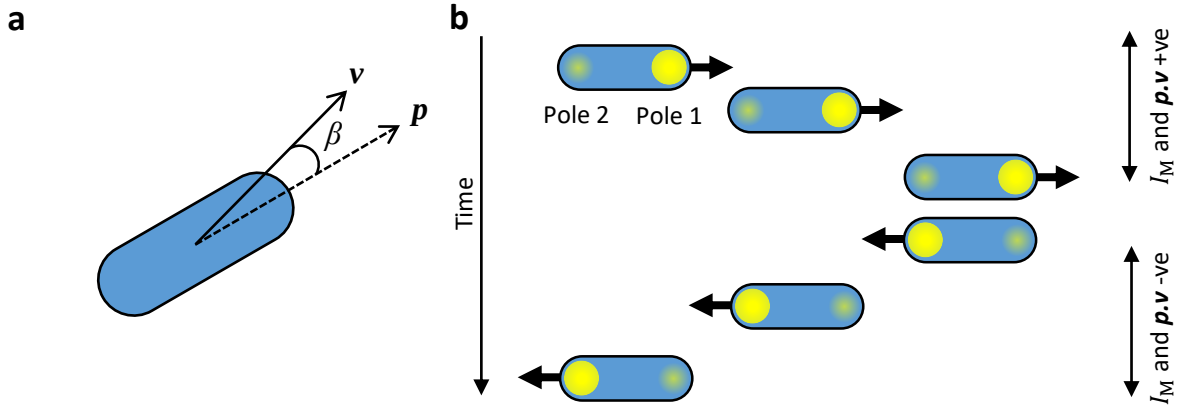

Figure 17: Schematic diagrams highlighting key parameters in $\boldsymbol{p}.\boldsymbol{v}$ quantification and when I_{M} and $\boldsymbol{p}.\boldsymbol{v}$ are positive and negative. (a) The vectors and angles used in $\boldsymbol{p}.\boldsymbol{v}$ calculation. $\boldsymbol{p}$ is the unit vector running along the orientation of the cell, $\boldsymbol{v}$ is the velocity vector and β is the angle separating the two vectors. (b) The signs of I_{M} and $\boldsymbol{p}.\boldsymbol{v}$ for a single cell over time. As cell poles are assigned at the beginning of tracking, I_{M} is positive when more FimX-YFP is localised to pole 1, with the opposite being the case for pole 2, as shown by the yellow spots. The same is true for $\boldsymbol{p}.\boldsymbol{v}$, as shown by the black arrows - when travelling in the direction of pole 1, $\boldsymbol{p}.\boldsymbol{v}$ is positive and when travelling to pole 2 it is negative.

To investigate any potential correlation between I_{M} and $\boldsymbol{p}.\boldsymbol{v}$, every value of $\boldsymbol{p}.\boldsymbol{v}$ has been binned by its accompanying value of I_{M} and an average value taken. The resultant relationship between $\boldsymbol{p}.\boldsymbol{v}$ and I_{M} at low density is shown in **Figure 18a**, highlighting a linear dependence between FimX-YFP concentration asymmetry and cell movement. By assuming that the amount of force produced by *P. aeruginosa* is linearly proportional to its velocity, I_{M} can potentially be used as a proxy for the force produced by the cell, as it is proportional to a cell's velocity. We note that **Figure 18a** shows a linear dependence at all I_{M} values, implying that an increase in the magnitude of I_{M} will always lead to an increase in the magnitude of $\boldsymbol{p}.\boldsymbol{v}$. In **Figure 18b**, it can be observed that as the cell first travels upwards, then changes its localisation and returns in the other direction, displaying that I_{M} changes in sign when FimX-YFP localises at the opposite pole. We have shown that at low density, I_{M} is proportion to cell movement and could potentially be used as a proxy for force. It has not been established however if these relationships hold in the bacterial monolayer.

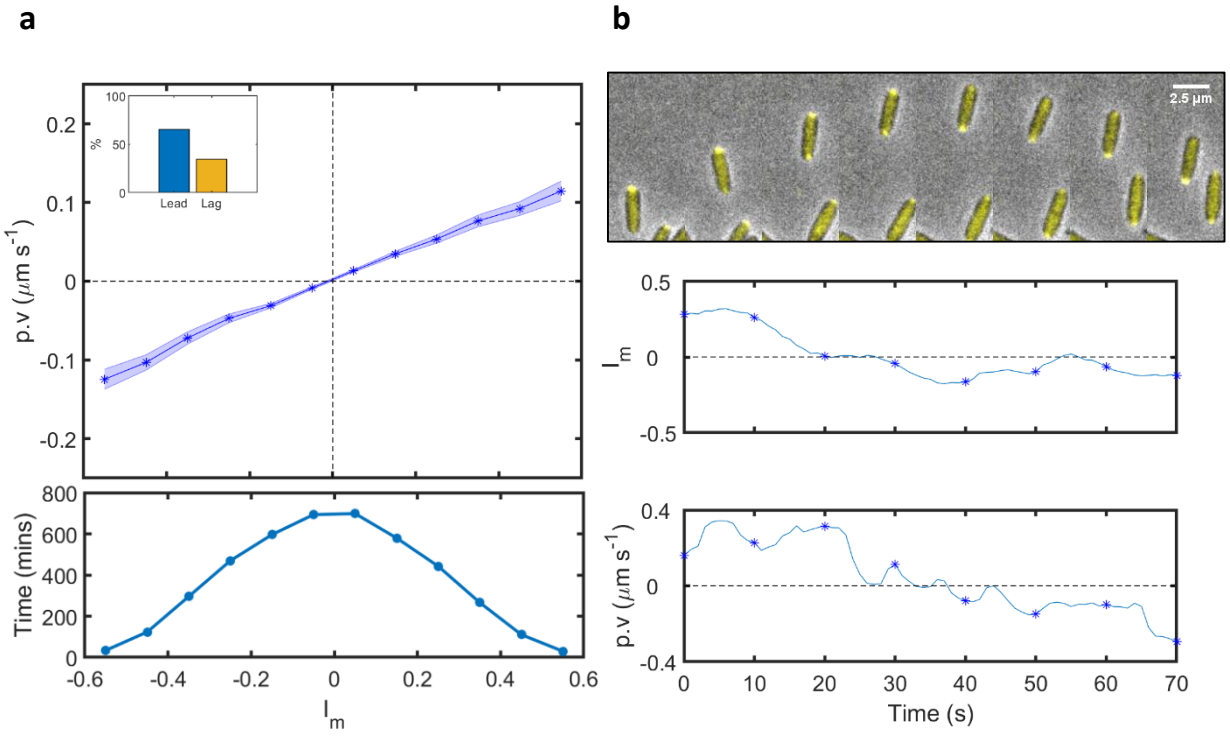

Figure 18: *P. aeruginosa* moves in the direction of FimX-YFP localisation. (a) Mean $\boldsymbol{p.v}$ vs I_{M} for labelled cells. The shaded region represents the standard error between 17 three minute long experimental time series with a total of 72 hours of labelled cell trajectories. I_{M} bin size is 0.1. There is a clear linear relationship between the two parameters. The plot below shows the total time of cell trajectories at each value of I_{M} which decreases as the absolute value of I_{M} increases. Data has been restricted to I_{M} bins that have above five minutes worth of data in the range $-0.6 < I_{\mathrm{M}} < 0.6$. Inset shows percentage of cells with greatest FimX-YFP localisation at the leading or lagging pole. Time points where $I_{\mathrm{M}} < 0.14$ are excluded from the analysis shown in the inset as the FimX-YFP concentration is not asymmetric enough to trigger pole swap detection (see **Section 4.1.1**). (b) A merged phase and epifluorescence time lapse of a single cell with corresponding I_{M} and $\boldsymbol{p.v}$ traces underneath, where blue markers in the plot indicate the corresponding time points in the time lapse. Traces have been smoothed with a five second moving average filter.

Establishing the relationship between I_{M} and $\boldsymbol{p.v}$ in the bacterial monolayer uses the same methods as the low density case. Again, we bin $\boldsymbol{p.v}$ by the accompanying I_{M} value to produce the plot observed in **Figure 19a**, which displays the same relationship as the low density case, however, $\boldsymbol{p.v}$ saturates at large $|I_{\mathrm{M}}|$ values, which could be due to neighbouring cells blocking the movement of the individual cell under investigation. Again, like the low density case there is no preferred pole in terms of direction of travel as shown by the symmetry in the y-axis and the plot passing through the origin. The impact of increased density on the correlation between I_{M} and $\boldsymbol{p.v}$ is seen in **Figure 19b**, as there are times when the two metrics are anti-correlated, and despite FimX-YFP asymmetry being directed towards one pole, the cell is being forced in the opposing direction by its neighbours, for example between 0 and 10 seconds. Despite these anti-correlated occasions, the cell is often able

to move in the direction of largest FimX-YFP concentration. Importantly, our results show that I_M can be used to infer the desired direction of individual movement in a high density environment like the bacterial monolayer where a single cell's motility is strongly influenced by its neighbours [13].

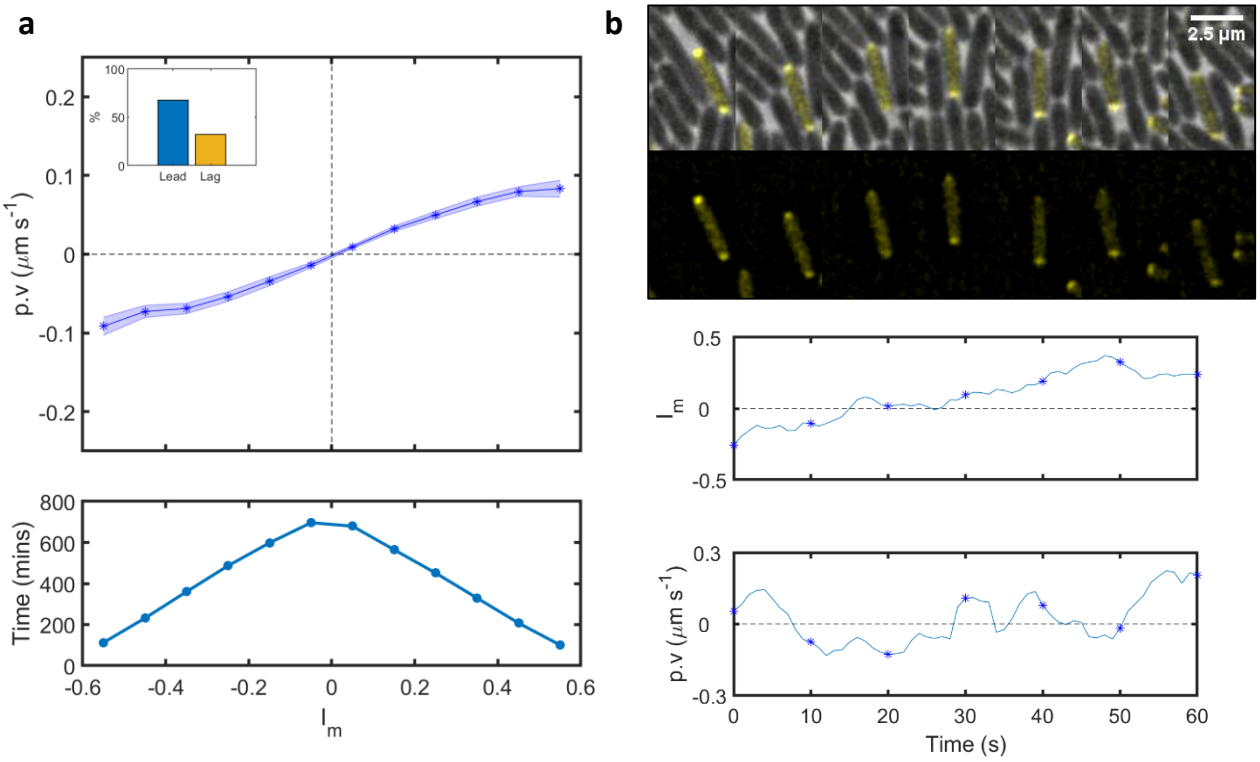

Figure 19: The relationship between FimX-YFP localisation and cell movement within the bacterial monolayer. (a) Plot of mean $\boldsymbol{p.v}$ as a function of I_M for labelled cells that pass all previously outlined analysis filters between 15 experimental time series between two and three minutes in length. I_M bin size is 0.1. The same linear relationship between $\boldsymbol{p.v}$ and I_M is observed at small $|I_M|$ values, although the trend begins to plateau at greater values. Data has been restricted to the same I_M bins as **Figure 18** for comparison. Inset shows percentage of cells with largest FimX-YFP localisation at the leading or lagging pole. Values of $\boldsymbol{p.v}$ corresponding to values of I_M below 0.14 are removed from the analysis shown in the inset as they would not be considered highly localised enough to trigger pole swap detection (see **Section 4.1.1**). (b) A merged phase and epifluorescence time lapse of a single cell with corresponding I_M and $\boldsymbol{p.v}$ traces underneath, where blue markers in the plot indicate the corresponding time points in the time lapse. The influence of neighbouring cells drives large fluctuations in $\boldsymbol{p.v}$. Traces have been smoothed with a five second moving average filter.

In this section, we have first developed a metric to quantify the magnitude and direction of *P. aeruginosa* twitching motility along the cell body, $\boldsymbol{p.v}$. Using the previously defined metric that quantifies FimX-YFP concentration asymmetry at the cell poles, I_M, with appropriate filtering and data processing, a correlation between FimX-YFP asymmetry and single cell movement has been uncovered in low density environments. Using appropriate assumptions, it is reasonable to use FimX-YFP asymmetry to infer which direction an individual wishes to travel in, and the force a cell exerts on the substrate. With the tools to investigate single cell movement in dense collectives

developed, the remainder of this chapter will investigate the asymmetry of FimX-YFP concentration at the cell poles in close proximity to topological defects and at the colony edge.

3.2 FimX-YFP localisation is highly asymmetric in environments where collective motility exists

There exists a building body of evidence that topological defects are crucial to the development of dense bacterial collectives. In *M. xanthus* monolayers, increases in cell density are observed at $+\frac{1}{2}$ charge topological defects, leading to multilayer formation and ultimately fruiting body formation. In contrast, defects with $-\frac{1}{2}$ topological charge exhibit decreases in cell density [145]. In non-motile surface-attached *E. coli* micro-colonies $+\frac{1}{2}$ charged defects move to the colony boundary and facilitate expansion as individual cells divide [142]. Finally, in densely packed *P. aeruginosa* monolayers, cells capable of exerting relatively large amounts of force form $+\frac{1}{2}$ charged defects and collide with another defect of like charge, overcoming the restoring torque from the agar slab to form verticalised, immobile groups [34, 73]. Given the prominence of topological defects in regulating collective phenomena in bacterial colonies, we hypothesised that neighbouring cells might direct their movement in the same direction as a means of enhancing collective movement. As such, this section explains the process of quantifying I_{M} around $+\frac{1}{2}$ and $-\frac{1}{2}$ charge topological defects in densely packed *P. aeruginosa* monolayers, going on to quantify the degree of collective FimX-YFP polarisation in $+\frac{1}{2}$ and $-\frac{1}{2}$ charge topological defects, and comparing the results with a self propelled rod model of a bacterial monolayer [34]. Later, our focus shifts from the monolayer to colony border, where single cell FimX-YFP asymmetry and collective polarisation is again investigated, however this time relative to the direction of colony expansion.

3.2.1 Collecting and processing information from cells surrounding topological defects

When measuring the properties of bacteria near topological defects, such as orientation, it is crucial to average over many defects, as the behaviour of any given cell is highly stochastic. Ideally, a monolayer of 100% labelled cells would be used to gather the maximum amount of information regarding the asymmetry of FimX-YFP concentration, however, as outlined in **Section 3.1.1**, this is not possible as the fluorescent signal of a given pole would become contaminated by that of neighbouring cells. Therefore only a small proportion of labelled cells are used (10-20%), further increasing the importance of defect averaging to obtain enough data to generate a reasonable signal. Utilising the preexisting analysis pipeline in Matlab and Defector, an open sourced topological defect tracking package (see **Section 2.6**), in the following section we describe the process of collating the

properties of bacteria in close proximity to $+\frac{1}{2}$ and $-\frac{1}{2}$ charged topological defects and processing them into heatmaps.

Defector provides the position, orientation and topological charge at every time point for all defects in a field of view. In addition, information on the cells surrounding each defect was collected by using the results of FAST that were previously outlined in **Section 3.1**. Like bacteria, defects are tracked in the lab field of view using Defector [34], with their orientation measured from the horizontal line anti-clockwise. Cell positions and orientations are then recalculated such that they are in the defect frame of reference. This process is outlined in **Figure 20**. Once the labelled cells in the vicinity of defects are put into the same defect centred frame of reference, the data can be averaged across defects, which is described in the next section.

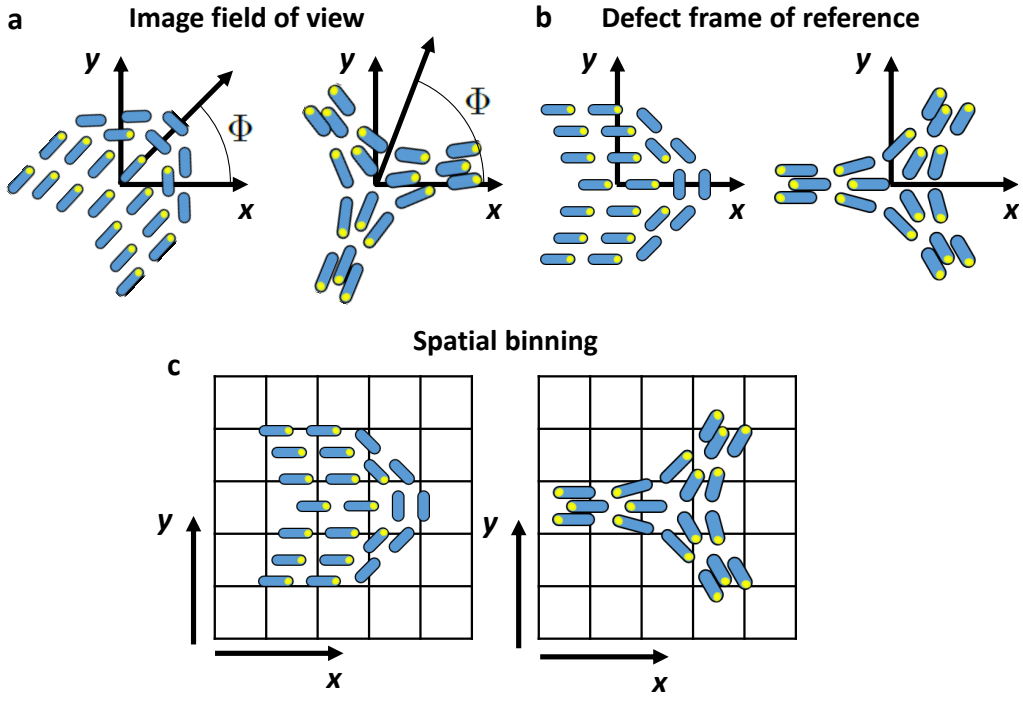

Figure 20: Diagrams showing various stages of comet (left) and trefoil (right) processing (not to scale). Example FimX-YFP spots are shown in yellow on blue cells. (a) The coordinate system used within the image field of view, with the angle Φ shown. (b) The defect frame of reference that is used in (c) to bin the surrounding data.

After we collected data surrounding topological defects, a choice had to be made over two averaging processes; the single defect or pooled method. In the single defect method, the average data field for each defect is taken, and then an ensemble average over all defects is obtained. Although the single defect method is useful for elucidating the flow fields around individual defects, which can vary widely, it is not suitable for processing I_{M}. While the movement of flow fields uses unlabelled cells, here we use a co-culture of unlabelled and labelled cells in experiments so there would be limited I_{M} data in each spatial bin because it can only be measured in labelled cells, leading to a large level

of noise in the ensemble average of a single defect. Instead, the pooled method takes from many defects, performing spatial binning, and then takes an average across all of them. Therefore, going forward the pooled method of averaging data between defects will be used.

With the method of averaging decided, we also face a choice of what cell properties will be investigated, and choosing a suitable bin size. To allow for comparisons with existing literature, orientation and velocity fields will be produced, ensuring that the results obtained are in agreement with existing precedents, then the mean I_{M} field surrounding defects will be determined, to see if any signal emerges. In doing so, a bin size must be chosen and for this 1.6 μm has been picked, which is equivalent to twice the width of a single cell, and allows for a comparison with a simulation that uses the cell width as a scale in **Section 3.2.2** [34]. We have provided details on how data collation is performed between defects of like charges, that the pooled method will be used going forward as it allows for meaningful mean I_{M} fields to be produced, and that the bin size of doing so is twice the cell width or 1.6 μm wide. We will now outline the governing equations that allow for the averaging of information surrounding topological defects.

A conversion needs to be made to the defect frame of reference to allow for averaging to occur. The first conversion to be made is the coordinates of each cell from the lab frame into the defect frame to allow for binning. Assigning the orientation of the defect as Φ, the conversion to the defect frame is made through:

$$x_{\mathrm{D}} = x\cos\Phi - y\sin\Phi \tag{5}$$

for the x coordinate, with the y coordinate converted through

$$y_{\mathrm{D}} = x\sin\Phi + y\cos\Phi. \tag{6}$$

It is now possible to bin data by x_{D} and y_{D}. As the fields for cell orientation and velocity have already been determined these will be considered first, followed by the I_{M} field. When considering the cell orientation, ϕ, the conversion into the defect frame of reference is simply performed through **Equation 7**:

$$\phi_D = \phi - \Phi. \tag{7}$$

To measure the mean velocity field for comets and trefoils, the contribution of x and y velocity in the image frame of reference (v_{X} and v_{X} respectively) is first calculated Then, the contributions of x and y velocity must be converted into the defect frame of reference. To begin, the x and y contributions

of velocity in the image frame of reference are found using **Equations 8** and **9**:

$$v_{\mathrm{X}} = v_{\mathrm{MAG}} \cos(\theta), \tag{8}$$

$$v_{\mathrm{Y}} = v_{\mathrm{MAG}} \sin(\theta). \tag{9}$$

v_{X} and v_{Y} each have their own contribution to x and y velocity in the defect frame of reference ($v_{\mathrm{X_D}}$ and $v_{\mathrm{Y_D}}$), calculated using **Equations 10** and **11**,

$$v_{\mathrm{X_D}} = v_{\mathrm{X}} \cos(-\Phi) + v_{\mathrm{Y}} \sin(-\Phi), \tag{10}$$

$$v_{\mathrm{Y_D}} = v_{\mathrm{X}} \sin(-\Phi) + v_{\mathrm{Y}} \cos(-\Phi). \tag{11}$$

The magnitude of velocity in any given spatial bin surrounding a defect ($v_{\mathrm{MAG_D}}$) is given by:

$$v_{\mathrm{MAG_D}} = \sqrt{(v_{\mathrm{X_D}}^2 + v_{\mathrm{Y_D}}^2)}.$$

The same process is followed for I_{M} however with some few modifications. Both v and I_{M} are now considered as vectors, the former with magnitude v_{MAG} and direction θ, and I_{M} as a vector that acts with magnitude $|I_{\mathrm{M}}|$ in the direction of ϕ or $-\phi$ depending on the sign of I_{M}. To account for this, we introduce $\phi_{I_{\mathrm{M}}}$, where if $I_{\mathrm{M}} > 0$, $\phi_{I_{\mathrm{M}}} = \phi$ and if $I_{\mathrm{M}} < 0$, $\phi_{I_{\mathrm{M}}} = \phi + \pi$. We also denote the direction of the pole with the greatest FimX-YFP concentration from the centre of the cell as the unit vector $\boldsymbol{p}_{\mathbf{FimX}}$. The contributions of I_{M} in the x and y direction in the image frame of reference ($I_{\mathrm{M_X}}$ and $I_{\mathrm{M_Y}}$ respectively) are given by **Equations 12** and **13**:

$$I_{\mathrm{M_X}} = |I_{\mathrm{M}}| \cos(\phi_{\mathrm{I_M}}), \tag{12}$$

$$I_{\mathrm{M_Y}} = |I_{\mathrm{M}}| \sin(\phi_{\mathrm{I_M}}). \tag{13}$$

Therefore, in the defect frame $I_{\mathrm{M_{X_D}}}$ and $I_{\mathrm{M_{Y_D}}}$ are given by **Equations 14** and **15**:

$$I_{\mathrm{M_{X_D}}} = I_{\mathrm{M_X}} \cos(-\Phi) + I_{\mathrm{M_Y}} \sin(-\Phi), \tag{14}$$

$$I_{\mathrm{M_{Y_D}}} = I_{\mathrm{M_Y}} \sin(-\Phi) + I_{\mathrm{M_Y}} \cos(-\Phi). \tag{15}$$

The magnitude of mean vectors in each spatial bin is therefore given by:

$$I_{\mathrm{M}_{\mathrm{MAG}_{\mathrm{D}}}} = \sqrt{I^2_{\mathrm{M}_{\mathrm{X}_{\mathrm{D}}}} + I^2_{\mathrm{M}_{\mathrm{Y}_{\mathrm{D}}}}}.$$

In this section we have described the rationale and mathematical process of binning data from *P. aeruginosa* in close proximity to topological defects within a monolayer, summarised visually in **Figure 20**. This process will be applied to orientation and cell velocity to ensure results previously reported in literature are reproduced, and then applied to I_{M} to investigate any potential change in FimX-YFP localisation when bacteria are close to topological defects. In the upcoming section, the processes outlined will be used to produce heatmaps of cell orientation, velocity and mean I_{M} around $+\frac{1}{2}$ and $-\frac{1}{2}$ charged topological defects, with a subsequent comparison to a self propelled rod model.

3.2.2 Im vector fields are similar to flow fields around defects

We have previously outlined the method of data collection and processing of cells within close proximity of topological defects in bacterial monolayers. Using these equations, in this section we present orientation and velocity fields of half integer topological defects to ensure that our results recapitulate those already found in literature, then compare the velocity flow fields with those measured using I_{M}. Using the I_{M} vector, we go on to use the polar order parameter to make a comparison with a self propelled rod model.

We begin our comparison by investigating mean cell orientation, which is shown in **Figure 21** and matches results previously reported in literature [34]. Both defect charges show that there is only a given radius that orientation alignment holds over, which is particularly pronounced for trefoils, where alignment breaks down 10 cell widths from the defect core. We will now focus on the velocity fields surrounding topological defects to provide an additional check that our data recovers previously reported phenomena.

Mean velocity fields are shown in **Figure 22a** and **22b** and like the orientation plots in **Figure 21** closely match results from existing literature [34]. When broken down into components, it can be seen that a large portion of the comet magnitude plot comes form the x component of velocity, and the y component heat map highlights that before moving through the core, cells converge onto it, with the cells above the horizontal axis having a negative velocity and those below a positive one. For trefoils, a mean velocity magnitude with six 'spokes' is observed, with vortexes observed in between each spoke. The spokes are split equally into two types; inflowing and outflowing, and the vortex direction acts to draw cells in and then move them outward from the defect core. An asymmetry exits in the magnitude of the inward and outward flows, where cells move away from the

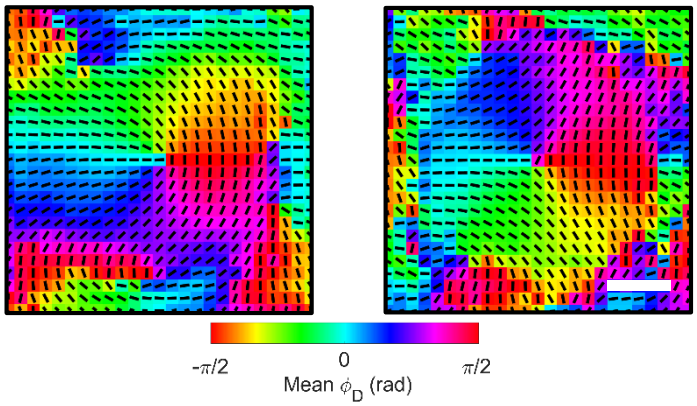

Figure 21: Orientation heat maps for comets (left) and trefoils (right). Bin size is 2 cell widths (1.6 μm) and a 48 × 48 grid is shown (38.4 μm × 38.4 μm), taken from 15 experimental time series, containing 1029 comets and 1051 trefoils. The scale bar is 10 cell widths (8 μm) in length.

defect core with a larger velocity than those moving towards it. With the checks on the velocity flow fields complete, showing that results previously found in literature have been recovered, we can now move onto discussing novel findings in the I_M fields around defects.

When considering the mean I_M heatmaps there are two areas of interest. As previously established in **Section 3.2.1**, cell velocity is proportional to I_M at low density and in the monolayer, giving us a tool to resolve bacterial behaviour in densely packed conditions. For example, take the fields in **Figure 22a**, there is a strong signal at the defect core for both cell velocity and I_M, propelling the cells in the positive x direction. Considering the y components, it can be seen that the cells are trying to twitch towards the defect core before passing through it. Once through the core however, there is little I_M signal in the y component, whereas in the velocity field the y component of velocity is similar for cells that are yet to pass through the defect core, and those that are beyond it. Summarising these findings, for $+\frac{1}{2}$ charge topological defects, in *P. aeruginosa* there is a large degree of collective FimX-YFP polarisation within the defect core, showing that cells are collectively biasing their directing of twitching motility whilst moving through the core but not elsewhere. Considering the trefoils in **Figure 22b**, there is almost no collective FimX-YFP polarisation along the inflowing spokes of the defect, with a strong signal only seen on the outflowing spokes. Looking at the x and y components, the magnitude of the inward flowing velocity fields are not matched by the corresponding I_M fields. Therefore, it appears the cells are passively flowing into the trefoil core, then actively biasing their movement outwards. Here we have shown that in the region surrounding topological defect, *P. aeruginosa* deliberately moves in some areas and appear to be passively advected in others.

Although the behaviour of individual *P. aeruginosa* cells in a bacterial monolayer can be highly polarised, previous modelling has been performed using the equations of active nematics which assumes that there is no preferential direction of travel [135]. More recently simulations have been

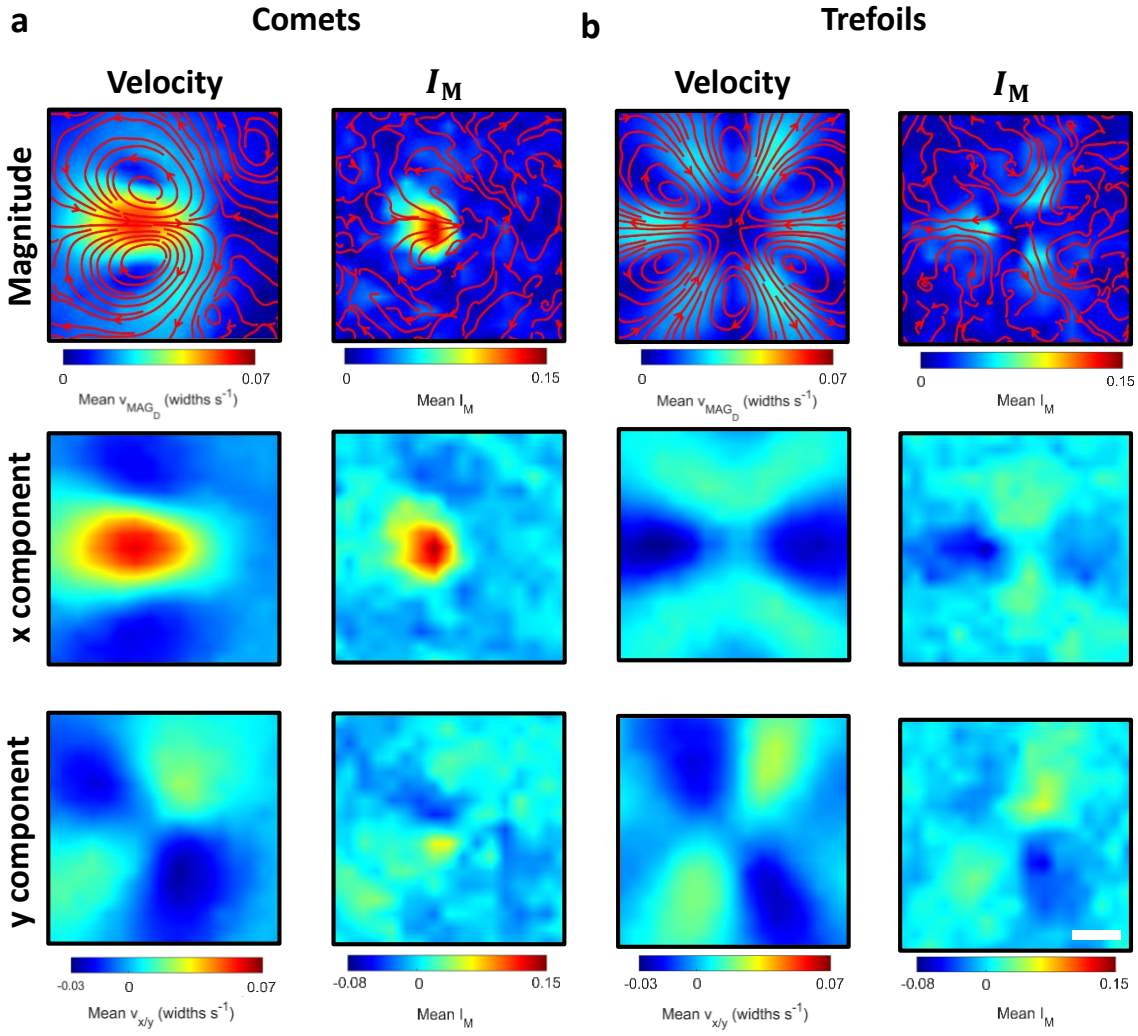

Figure 22: Mean collective velocity and I_M polarisation properties of (a) $+\frac{1}{2}$ comets and (b) $-\frac{1}{2}$ trefoils from bacterial monolayers. Each column displays the mean magnitude, x and y component of velocity or I_M, calculated using the pooled method. Mean velocity and I_M vectors have been shown with streamlines rather than vectors to show the average path a cell would when in close proximity to each defect and which direction FimX-YFP is point in respectively. The magnitude is shown by the heatmap. The plots shown come from 15 experimental time series, containing 1029 comets and 1051 trefoils. Bin size is 2 cell widths (1.6 μm) showing a 48 × 48 cell width grid (38.4 μm × 38.4 μm). Scale bar is 10 cell widths (8 μm).

performed that support the coexistence of collective nematic and polar behaviour, which our results are consistent with [138, 147]. If collective FimX-YFP polarisation were to be nematic, there would be no preferential direction of localisation in close proximity to half integer topological defects, and the mean I_M heatmaps displayed in **Figure 22** would be zero valued at all positions in space, as individual I_M vectors in each bin would cancel each other out, which is not the case, and we show collective polar behaviour instead. We also considered if the polar behaviour observed could arise by purely physical means, rather than there being any biological influence. Prior work performed by the Durham group has used an individual based, self propelled rod (SPR) model of a two dimensional

bacterial monolayer to better understand collective bacterial motility [34]. The model is comprised of individual agents that exert a constant of force acting along the long axis of the cell to generate movement. Unlike our experimental work, the model does not include reversals of direction along the long axis of the cell, which have been observed experimentally (see **Figure 19**). Overlapping of individuals is prevented by repulsive forces between the rod segments, causing orientational alignment to occur between neighbouring cells.

To directly compare the experimental results and simulations, the parameters of the latter need to be matched as best as possible. As cell aspect ratio has a large impact on the physical interactions between constituents of active matter systems, we use the distribution of rod lengths from experiments and use them as inputs for the SPR model [112]. A gamma function was fitted to the distribution of FimX-YFP cell lengths in the monolayer plot in **Figure 8** returning a shape and scale parameter of 14.18 and 0.296 μm respectively. We used the FimX-YFP cell lengths as we can only measure the force produced from these cells and not the WT, which is important for making comparisons with simulations (**Figure 23**). We are now comparing an experimental scenario with reversals, and an equivalent simulation that lacks them. In addition, cells in experiments are able to exert variable levels of force, whereas the self propelled rods all produce the same amount of force. Therefore, we only consider the sign of I_{M} to make a comparison with the polar order parameter, P. By measuring the alignment of I_{M} vectors in a spatial bin, or the force vectors in the SPR simulation, P provides a single valued measure of how polar a system is. If the system is nematic, $P = 0$ and tends to 1 as polarisation becomes stronger. P is calculated using

$$P = |\frac{1}{N}\sum_{k=1}^{N} \exp i\eta_k| \tag{16}$$

where N is the number of cells and η_k represents the angle of the direction of the pole with greatest FimX-YFP concentration, given by:

$$\eta = \tan^{-1}\left(\frac{I_{\mathrm{M}_{\mathrm{Y_D}}}}{I_{\mathrm{M}_{\mathrm{X_D}}}}\right).$$

With a suitable metric identified to allow for the comparison of FimX-YFP concentration asymmetry in *P. aeruginosa* in close proximity to topological defects and the force vectors in a SPR model, the resultant polar order parameter heatmaps are shown in **Figure 23**.

As there are non-zero values in the polar order heatmaps shown in **Figure 23a**, collective polar behaviour is present in close proximity to topological defects within bacterial monolayers comprised of rod shaped individuals. Given the similarities between the polar order heatmaps, and I_{M} plots

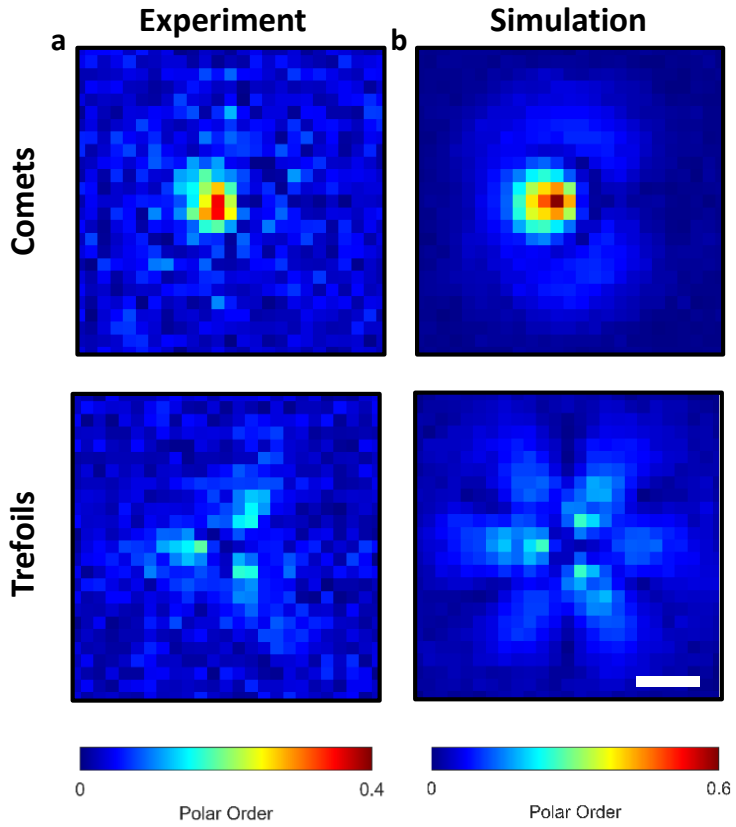

Figure 23: Polar order parameter heat maps comparing (a) experimental and (b) simulated SPR data. Bin sizes for both plots are 2 cell widths (1.6 μm) and a 48 × 48 cell width grid is show (38.2 μm × 38.2 μm). Experimental results are taken from 15 experimental time series between two and three minutes in length, containing 1029 comets and 1051 trefoils respectively. Simulated data contains 4308 comets and 4319 trefoils comprised of 11744 rods. Scale bar is 10 cell widths (8 μm).

in **Figure 22**, we can conclude that the polar order arises from *P. aeruginosa* actively biasing its movement when near defects. For comets this is observed just behind the defect core, propelling individuals along direction of defect travel, and for trefoils the movement is along the outflowing spokes. When considering the results from the SPR model for trefoils in **Figure 23b**, an increase in polar order is observed. The increase in polar order is likely due to the absence of reversals in the SPR simulation, as semi-flexible filaments have been shown to increase polarity when decreasing their rate of reversal [147]. Therefore, if it were possible to remove reversals experimentally, we would likely observe an increase in polar order if reversals are random. Overall, the increase in polar behaviour shows that if we were to remove reversals experimentally, we should expect to see increased polar order in the vortexes returning *P. aeruginosa* from the defect front to back, and along the inflowing spokes of trefoils. Ultimately, although it is possible for collective polarisation of twitching motility to occur through purely physical means as shown by the SPR model, our experimental results show that the presence of random reversals of direction, a biological factor, can influence the amount of

collective polarisation present in close proximity to topological defects.

To ensure that the defects in our co-culture assay reproduce the orientation and velocity flow fields surrounding $+\frac{1}{2}$ and $-\frac{1}{2}$ topological defects in a *P. aeruginosa* monolayer reported in literature, we have combined single cell tracking in FAST and defect tracking using Defector [19, 34]. Having validated these fields, the degree of collective FimX-YFP polarisation surrounding topological defects was investigated, reporting similarities to the velocity fields but with some distinct differences, showing that in some regions *P. aeruginosa* is deliberately moving with the flow fields and in other regions they appear to be passively advected by neighbours. In both scenarios, we have shown that polar behaviour exists in a system previously described using the equations of active nematics [15]. By making a comparison between experimental bacteria capable of reversing and a model of non-reversing self propelled rods, we have shown that collective polar behaviour can be generated through purely physical means, however the presence of reversals can have an influence on the degree of collective polar behaviour present. With our studies complete on the collective polarisation of bacterial movement behaviour surrounding topological defects, we examined other regions of the colony where collective polar behaviour might be present.

3.2.3 Cells at the colony edge have highly polarised FimX-YFP

As before, we are limited to imaging intracellular FimX-YFP in regions where multilayering does not occur, as measurements of the FimX-YFP concentration in one cell could be distorted by another that is out of the focal plane. The colony edge fulfils both these criteria; it is comprised of aligned, single-layered groups expanding into previously unexplored surface. When located at the colony edge, individual cells have the benefit of having the earliest access to any nutrients that arise whilst exploring the surface. However, there are also risks of being at the edge and cells at the border experience the maximum effect of any antimicrobial treatments and are often the first in a colony to be the victims of any attacks from rivalling strains [118, 148, 165]. In interstitial *P. aeruginosa* biofilms, it has been shown previously that colony expansion is facilitated by the alignment of cells to form rafts, requiring a constant replenishment of new contributors to continue expansion. Without this replenishment, colony expansion is severely inhibited [107]. In non-motile *E. coli* colonies, colony expansion is facilitated by $+\frac{1}{2}$ topological defects generated through cell elongation and subsequent division [142]. Given that alignment is already observed in groups of cells at the edges of the colony and strong polarisation of FimX-YFP is observed within $+\frac{1}{2}$ topological defects, could polar behaviour also exist at the colony border? In this section, we combine the use of single-cell tracking and a custom made colony border identification system to investigate the properties of *P. aeruginosa*

within close proximity to the edge of a bacterial colony.

The first stage in analysing the properties of bacteria near the colony border is having a clear understanding of the dynamics of the collective in this region. **Figure 24** shows an example of how a colony expands over time, in a finger-like manner. The colony border is not flat and instead has undulating curvature to it, permeated by groups of cells that align their bodies and movement toward the direction of expansion. In these groups, cell density is extremely large and FimX-YFP asymmetry appears to be oriented toward the direction of colony expansion. At the back of these groups there is often a region of decreased cell density, where individuals have more freedom to rotate and FimX-YFP localisation is not as static. At the border between the colony and untouched surface, there is a layer, often just one cell deep, of individuals orientated orthogonal to those deeper within the group. As shown in **Figure 24**, colony expansion is facilitated by the group moving outward in a single direction. Therefore, to allow for the analysis of individuals in close proximity of the colony border, we must first be able to follow the location of the border as it moves over time.

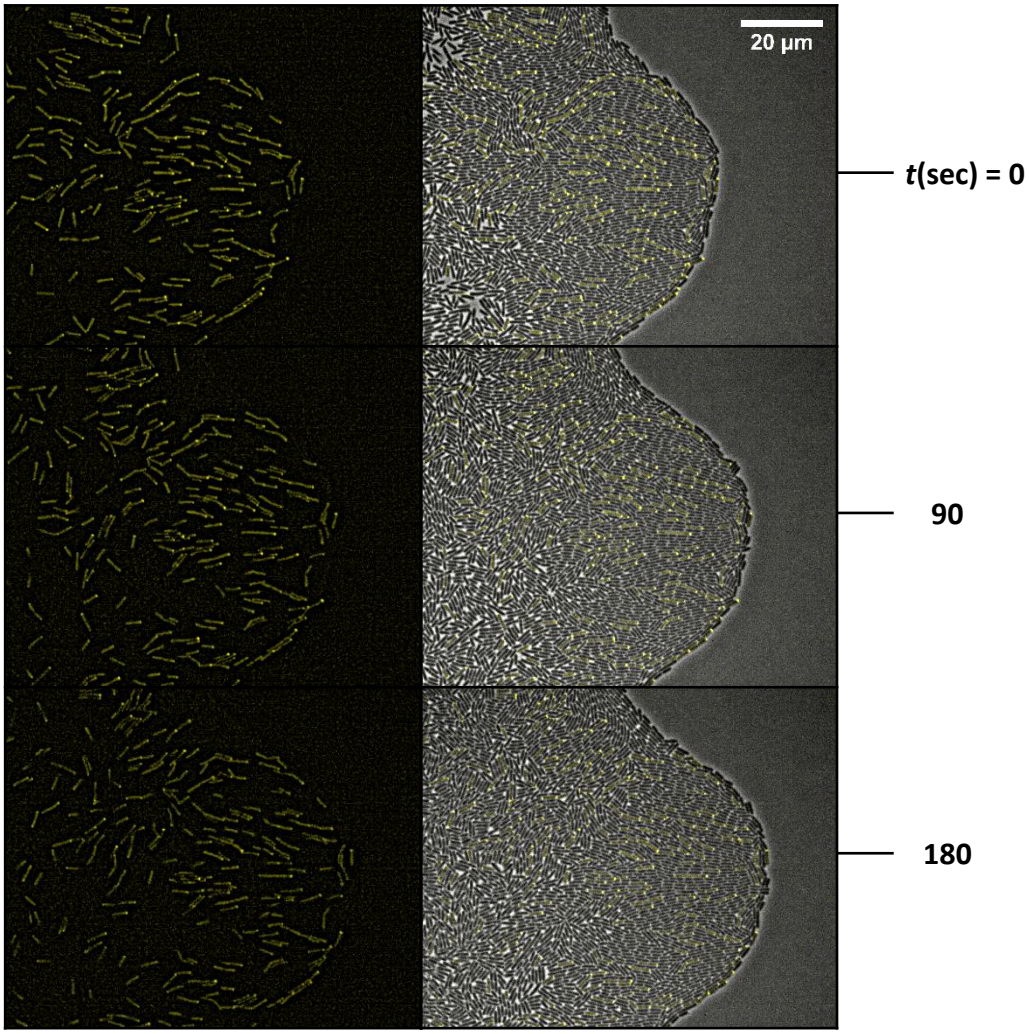

Figure 24: The expansion of the colony border over time. Images show a co-culture of 9 : 1 WT:FimX-YFP cells.

In a single-frame, it would be relatively simply to manually identify the location of the colony border, however, our data set is comprised of 24 time-lapse series, each 181 frames in length, presenting a time–consuming process. Instead we have developed an automated border recognition system using the binary output of FAST [34]. The process, shown in **Figure 25**, begins by filling the gaps between objects in the binary segmentation's produced by FAST, to produce a single large 'on' region representing the group. The identification system searches for regions where the binary segmentation turns from off-to-on and fills in any gaps between objects. This results in only one final location where the binary segmentation turns from off-to-on: the colony border. To search for the off-to-on off-to-on binary change, all images are rotated such that colony expansion is towards the top of the image field of view, allowing for a scan across the x axis to find the off-to-on off-to-on coordinate in y. The amount of rotation is assigned through visual inspection and is dictated by the direction of colony expansion within the image field of view, $\theta_{ROT_{CB}}$. Once identified in the rotated frame of reference, the coordinates are translated back into the original image frame. As our interest lies purely in the edge of colony group, we place limits on the minimum and maximum x and y coordinate for which the border is identified. Any coordinates of the border that are outside of these limits are ignored during analysis. With the process of colony border identification outlined, we can move onto how the properties of cells in close proximity to the border are processed to allow us to assign data according to a cell's orientation relative to the border and its distance from it.

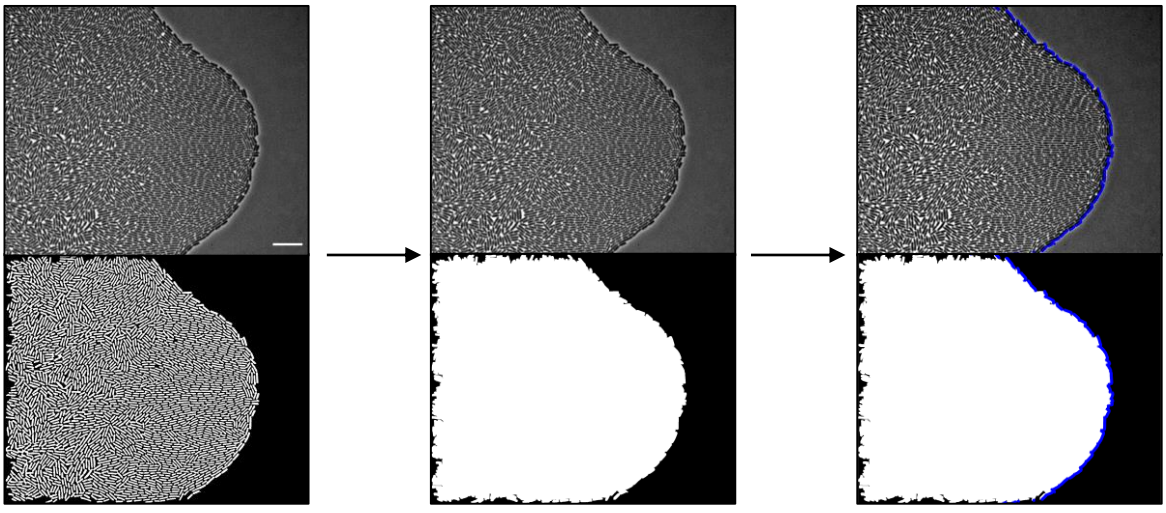

Figure 25: The process of identifying the colony border. (a) The binary segmentations have any gaps filled and it is checked that only one large object remains in the field of view. Scale bar is 10 μm long. The border is then identified at the border of the large binary object.

When investigating how bacteria behave at the colony edge relative to their orientation and

position within the collective, it is important to consider what the angle and coordinates of a cell are being measured relative to. We have decided to measure cell orientation relative to the direction of colony expansion and measure cell coordinates as a distance from the border. It is simplest to measure the angle that an individual cell makes with the direction of expansion, ϕ_{CB}, and the distance from the border, d_{CB} in the rotated frame of reference, where colony expansion is always upward in the field of view. We calculate the coordinates of any property of the cell in frame of reference of colony expansion using

$$x_{\mathrm{ROT_i}} = x_{\mathrm{i}} \cos\theta_{ROT_{CB}} - y_{\mathrm{i}} \sin\theta_{ROT_{CB}} \tag{17}$$

for the x cooridnates, and

$$y_{\mathrm{ROT_i}} = x_{\mathrm{i}} \sin\theta_{ROT_{CB}} + y_{\mathrm{i}} \cos\theta_{ROT_{CB}} \tag{18}$$

for the y coordinates. Here, the suffix i is used to denote the cell centroid, pole 1 or 2 using 'C', 'P1' and 'P2' respectively. Using the centroid and cell pole locations, along with the coordinates of the colony border in the rotated frame, ($x_{\mathrm{ROT_{CB}}}$, $y_{\mathrm{ROT_{CB}}}$), the distance of the cell and its poles from the colony border is calculated using **Equations 19 - 21**,

$$d_{CB} = y_{\mathrm{ROT_{CB}}} - y_{\mathrm{ROT_C}} \tag{19}$$

$$d_{CB_{P1}} = y_{\mathrm{ROT_{CB}}} - y_{\mathrm{ROT_{P1}}} \tag{20}$$

$$d_{CB_{P2}} = y_{\mathrm{ROT_{CB}}} - y_{\mathrm{ROT_{P2}}}. \tag{21}$$

As we are quantifying FimX-YFP asymmetry relative to the direction of colony expansion, and taking an average between many different time-series, a change in the allocation of pole 1 and pole 2 must be applied. The example shown in **Figure 25** is of a colony expanding towards the right-hand side of the image field of view, however, it is equally likely that a similar group exists travelling towards the left-hand side field of view. Currently pole 1 is assigned at the beginning of tracking as the pole with the greatest x coordinate, however, in the case of **Figure 25**, this would result in a purely positive I_{M} signal, assuming FimX-YFP is orientated in the direction of colony expansion. For the example group travelling towards the left-hand side, the I_{M} signal would be negative, and an average of the two cases would cancel each other out, resulting in a null signal which is visually not the case. To overcome this averaging issue, we ensure that if $d_{\mathrm{CB_{P1}}} < d_{\mathrm{CB_{P2}}}$ the assignment is kept, whilst

if $d_{\mathrm{CB_{P2}}} < d_{\mathrm{CB_{P1}}}$ the pole coordinates are swapped such that $d_{\mathrm{CB_{P1}}}$ is always closest to the colony border. I_{M} is then recalculated with the corresponding intensity values. Once reassignment of the pole locations has taken place, the orientation of the cell relative to the colony border is calculated using **Equation 22**,

$$\phi_{\mathrm{CB}} = \tan^{-1}\left(\frac{y_{\mathrm{ROT_{P1}}} - y_{\mathrm{ROT_{P2}}}}{x_{\mathrm{ROT_{P1}}} - x_{\mathrm{ROT_{P2}}}}\right). \tag{22}$$

We now have the mathematical framework in place to assign cells according to their orientation, ϕ_{CB} and distance from the colony border d_{CB}, (**Figure 26a**). **Figure 26b** goes on to show ϕ_{CB} on an example edge of colony group with each contour representing 10 μm intervals from the border. **Figure 26c** and **26d** additionally show merged phase and epifluorescence images, which visually suggest that FimX-YFP within individual cells often aligns in the direction of colony expansion. Finally, **Figure 26e** shows a binary image colour-coded to ϕ_{CB}, which shows that cell body orientation is highly correlated in the direction of colony expansion until approximately 40 μm from the colony border, where the orientational alignment breaks down. This most likly occurs due to a decrease in density, allowing cells to turn more freely. Therefore, going forward we will restrict our analusis to cells that are within 40 μm of the colony border. Through the use of our custom colony border identification method, the binary segmentations and tracking data from FAST have been used to identify the coordinates of the colony border and describe the orientation and position of individual cells relative to the border. Using this information, we will now quantify the visually observed variability in cell body orientation and FimX-YFP asymmetry in the direction of colony expansion.

Initially, we will focus on the physical properties of the cells at the colony border, these being cell orientation relative to the direction of expansion and the amount of freedom each individual has to rotate. Following these physical properties, we will investigate the degree of similarity in FimX-YFP localisation between neighbouring cells. As cell position relative to the colony border is defined by d_{CB} and orientation relative to colony expansion, ϕ_{CB}, cell trajectory data is binned using these measurements. We begin describing the physical properties of *P. aeruginosa* at the colony border by measuring velocity parallel and perpendicular to the direction of colony expansion. Parallel and perpendicular velocities ($v_{||}$ and $v_{\perp}$) are calculated using $y_{\mathrm{ROT_{CB}}}$ and $x_{\mathrm{ROT_{CB}}}$ respectively, and the distribution of values for all cells at all time points is given in **Figure 27a** which displays $\log_{10}$ of the PDF of velocity values. The zero valued mean of $v_{\perp}$ is anticipated, as there is minimal cell movement in the direction perpendicular to colony expansion (**Figure 24**) and we calculate that the movement parallel to the direction of colony expansion ($v_{||}$) has a mean value of 3.3 μm min^{-1}.

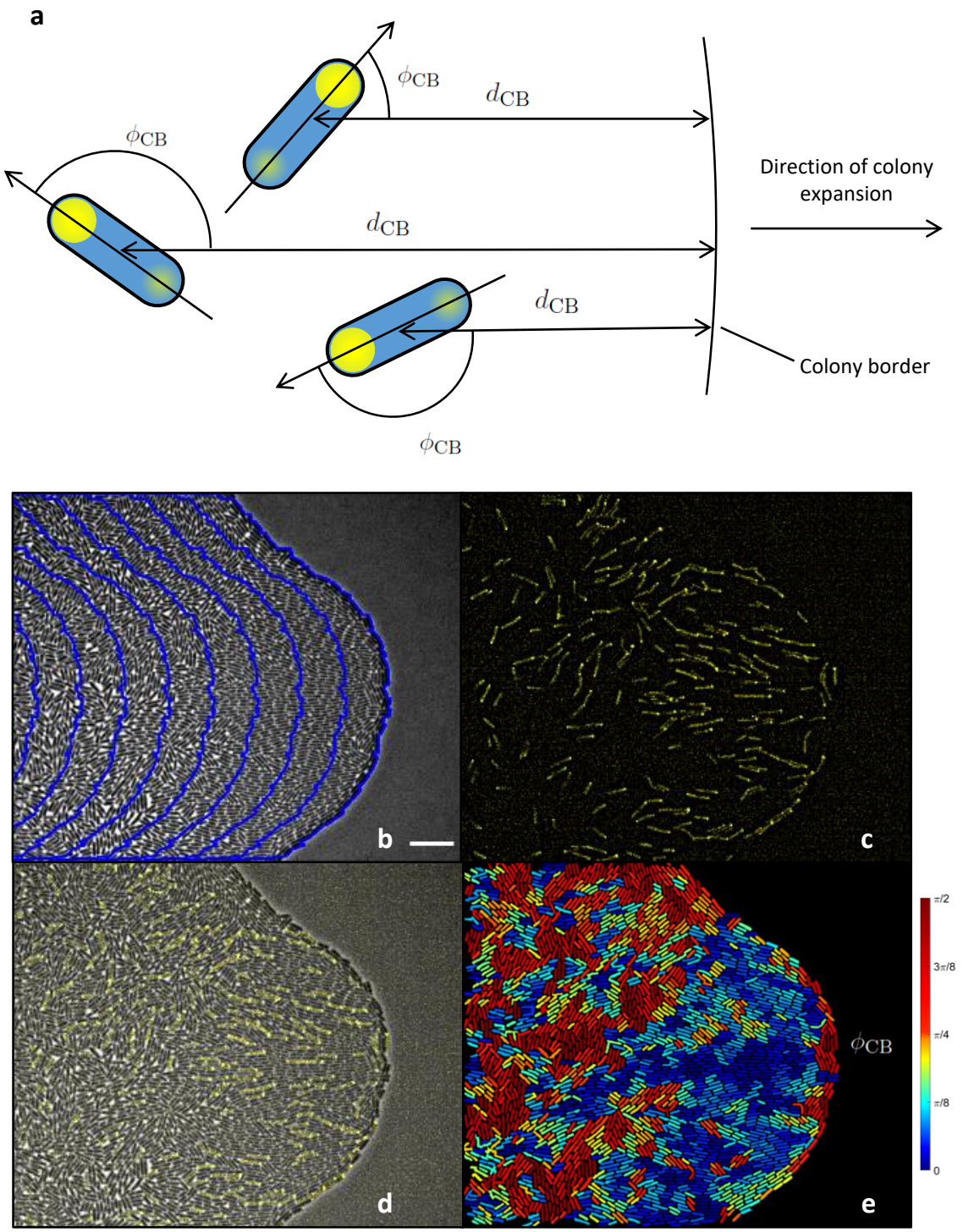

Figure 26: Properties of cells relating to the colony border with images displaying their application. (a) Diagrams showing the distance from colony border, d_{CB}, and the angle subtended by the cell and the colony border in the direction of colony expansion, ϕ_{CB}. (b) The same phase image as **Figure 25** overlaid with contours showing d_{CB} in 10 µm graduations. Scale bar is 10 µm (c) Fluorescent YFP image of (b). (d) Merged phase and YFP image of (b). (e) The binary corresponding binary segmentation for (b), with segmented cells coloured according to ϕ_{CB}.

Figure 27b shows how cell orientation changes at increasing distances from the colony edge. These findings reflect what is visually observed in **Figure 26e** in that the greatest proportion of cells

oriented orthogonal to the direction of colony expansion is found at the smallest d_{CB} value. Across each d_{CB} bin, the number of cells orientated in the direction of colony expansion then increases until $d_{\mathrm{CB}} = 20$ μm, above which it begins to fall slightly. The decrease in alignment when $d_{\mathrm{CB}} = 20$ μm is most likely due to a fall in density, allowing each cell more rotational freedom. The increase in rotational freedom is shown in **Figure 27c**, as $\log_{10}(\mathrm{RMS}\Delta\phi)$ as a function of $\log_{10}(\tau)$ increases in ascending d_{CB} bins. Here, $\mathrm{RMS}\Delta\phi$ is calculated using **Equation 23**,

$$\mathrm{RMS}\Delta\phi(\tau) = \sqrt{\frac{1}{N}\sum_{i=1}^{N}\left(\phi_{\mathrm{i}}(t) - \phi_{\mathrm{i}}(\tau)\right)^2}, \tag{23}$$

where τ is the time-lag and N is the number of measurements for a given time lag. To ensure accuracy in each d_{CB} bin, only cells that remain within the limits of a single bin at all times during tracking are considered. We have shown that, aside from individuals that are closest to the colony border, at all values of d_{CB} , the majority of cells are aligned with the direction of expansion. The proportion of cells aligned to the direction of expansion falls slightly once beyond 20 μm, which we attribute to the increase in rotational diffusion. With the physical properties of *P. aeruginosa* at the colony border defined, we now discuss FimX-YFP localisation relative to the direction of expansion.

FimX-YFP localisation is represented by I_{M} and at the colony edge, is defined such that when it is positive, the greatest concentration of FimX-YFP is at the pole closest to the direction of expansion, and when negative, it points in the opposite direction. It is therefore simple to count the number of positive and negative I_{M} values in each d_{CB} bin and calculate the percentage of cells aligned with the direction of colony expansion, as done so in **Figure 27d**, which shows that at all values of d_{CB}, more cells have a larger concentration of FimX-YFP aligned in the direction of colony expansion. As d_{CB} increases from 0 μm to 20 μm, there is a rapid increase in the number of cells aligned with the direction of colony expansion, 12.5%, reflecting that there is an increase in orientation in the direction of colony expansion over this range of d_{CB}. When the percentage of FimX-YFP alignment is then binned by d_{CB} and ϕ_{CB} (**Figure 27e**), it is seen that even at the colony border, aligned cells are more likely to have their FimX-YFP oriented in the direction of colony expansion, with the percentage reducing with increasing ϕ_{CB}. From **Figures 27d** and **27e**, it appears therefore that there is a correlation between alignment and FimX-YFP localisation, however it is not possible from the current analysis to determine which property leads the other. We observed that FimX-YFP alignment in the direction of colony expansion is greatest not at the border, but further back into the group. This is similar to how FimX-YFP concentration asymmetry in $+\frac{1}{2}$ topological defects does not peak at the core, but just behind it. Given the location of largest FimX-YFP alignment in the

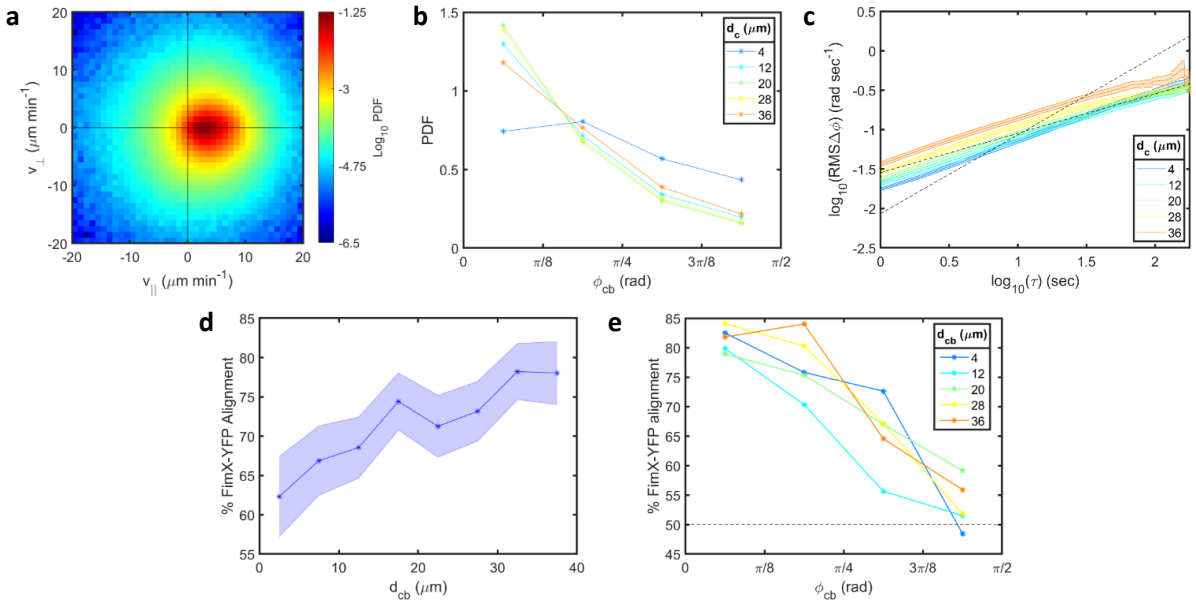

Figure 27: *P. aeruginosa* aligns its body and FimX-YFP distribution with the direction of colony expansion. Data shown is comprised of 24 experimental time series. (a) $\log_{10}$PDF of $v_{||}$ and $v_{\perp}$. Bin size is 1 μm min^{-1}. (b) PDF of cell body orientation and ϕ_{CB} binned by distance from colony border. Angular bin size is $\frac{\pi}{4}$ rad. d_{CB} bin size is 8 μm. (c) $\log_{10}$ RMS$\Delta\phi$ as a function of $\log_{10}\tau$, binned by d_{CB}. d_{CB} bin size is 8 μm. Shaded region shows the standard error of the mean taken between the 24 three minute experimental time lapses time lapses. Dashed lines show a gradient of $\frac{1}{2}$ and 1. (d) Percentage of cells with FimX-YFP aligned to direction of colony expansion as a function of d_{CB}. d_{CB} bin size is 5 μm and the shaded region shows the standard error of the mean between experimental time lapses. (e) Percentage of cells with FimX-YFP aligned to direction of colony expansion binned by d_{CB} and ϕ_{CB}. d_{CB} bin size is 8 μm and ϕ_{CB} bin size is $\frac{\pi}{4}$ rad.

colony edge, this implies that the driving force for expansion comes from the behind the colony edge, and that cells at the border are mostly being pushed from behind. However, despite the similarity in the collective polarisation of FimX-YFP, we were unable to detect $+\frac{1}{2}$ topological defects at the colony border. We have shown that FimX-YFP is aligned in the direction of colony expansion in a similar manner to cell body orientation. As FimX-YFP localisation is used as an indicator of pili activity and therefore active movement in *P. aeruginosa*, the alignment in the direction of expansion implies that cells at the colony border are actively biasing their movement, rather than passively expanding outwards.

Through developing a method that automatically identifies the border of an expanding bacterial colony in every frame of a time-lapse, we have been able to measure the distance from the border and orientation relative to the direction of expansion for every cell tracked in the densely packed outwardly moving group. After mathematical quantification of cell orientation relative to the border, we then determined the percentage of cells that have FimX-YFP within the cell pole oriented in the direction of colony expansion. We found that the proportion of cells with FimX-YFP pointing in the direction of colony expansion increases with distance away from the border. Furthermore, we found that the

asymmetry of FimX-YFP localisation also increases as cell bodies are increasingly aligned with the direction of colony expansion. These trends are similar to those observed in $+\frac{1}{2}$ topological defects, where FimX-YFP polarisation is not greatest at the defect core or colony edge, and is in fact largest just behind the core or further into the colony. Ultimately, the existence of FimX-YFP polarisation at the colony border implies that active and directed motility is involved in driving colony expansion.

3.2.4 Motility properties of cells in different sub-surface environments

In this chapter thus far, we have first shown that at low density there is a correlation in FimX-YFP localisation and the direction of cell movement, and utilised this relationship to investigate bacterial motility in dense collectives where movement can be highly influenced by physical interactions with neighbours [139]. In both the bacterial monolayer and the periphery of the colony, we reveal novel polar behaviour, where *P. aeruginosa* deliberately directs its movement in the direction of travel of $+\frac{1}{2}$ defects, and in the direction of colony expansion in highly aligned groups at the colony edge. Active behaviour here is generated by TFP exerting a force on the substrate by retracting to pull individual cells along the surface. As all phenomena described in this chapter are the result of TFP action, here we compare common properties of each system to provide a complete overview of the three environments.

We will first focus on the properties of bacterial motility by looking at both translational and rotational diffusion, followed by the polarisation of FimX-YFP in each environment. We measure translational diffusion by calculating RMSD at each time lag using

$$\mathrm{RMSD}\,(\tau) = \sqrt{\frac{1}{N}\sum_{i=1}^{N}\Big((x_{\mathrm{i}}\,(t) - x_{\mathrm{i}}(\tau))^2 + (y_{\mathrm{i}}\,(t) - y_{\mathrm{i}}(\tau))^2\Big)}. \tag{24}$$

Figure 28a displays the mean value of RMSD averaged across our data sets, for each environment. The values of each line correspond with the results in **Figure 8b**, that cells at the colony edge move the slowest, followed by those in low density assays, resulting in cells in the monolayer travelling the furthest distance in the shortest amount of time. These results occur as twitching speed is limited in single cells at low density, then increases as many cell twitch coherently in a monolayer. At the colony edge many cells twitch together, but are doing so into unexplored surface where the agar has not yet been burrowed out, so movement is slower. By extracting the gradient of these lines through linear fitting, we find values of 0.760 ± 0.002 μm s^{-1}, 0.807 ± 0.003 μm s^{-1} and 0.9015 ± 0.0007 μm s^{-1} (errors represent a 95% confidence interval) for the low density, monolayer and colony edge experiments. These values imply that twitching motility in all environments is closer to ballistic (τ) than it is diffusive ($\tau^{\frac{1}{2}}$), and confirm visual observations that the movement at the colony edge is the

most directed in a single orientation.

The comparison of RMS$\Delta\phi$, calculated using **Equation 23** and averaged across our data sets, is shown in **Figure 28b** and displays similar trends to those shown in **Figure 28a** for RMSD. At low density, physical cell-cell interactions that cause turning are rare, and therefore any rotational diffusion arises from the retraction of pili or their stochastic detachment from the surface [166]. In the monolayer, through physical interactions between cell bodies, bacteria form domains in space where all individuals have similar alignments and the rotation caused by pili retraction or stochastic

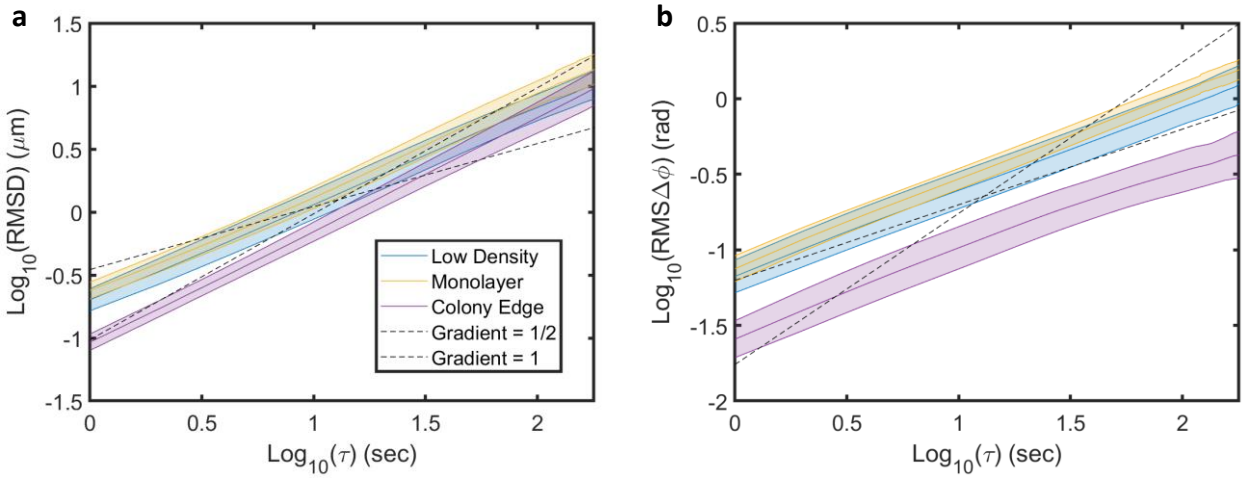

Figure 28: Comparing bacterial movement in the three experimental conditions. Plots showing (a) mean RMSD and (b) mean RMS$\Delta\phi$ on logarithmic axes. Data has been taken from 17, 15 and 24 experimental time series each between two and three minutes in length for low density, monolayer and edge of colony samples respectively. Shaded regions indicate the standard error between the time lapses.

detachment is blocked by neighbouring cells. Instead, rotation occurs through the mixing of separate domains, where physical cell-cell interactions drive turning [139]. The gradient of the low-density slope in **Figure 28b** is slightly lower than that of the monolayer, 0.56 ± 0.02 rad sec^{-1} and 0.5787 ± 0.0009 rad sec^{-1} (errors represent a 95% confidence interval from linear fitting of the lines in **Figure 28b**), and therefore the rotation is diffusive. When considering the case of cells in highly aligned groups at the colony edge, there is a large drop in the amount of rotational diffusion which confirms visual observations that cells at the colony border turn less. The gradient of the line however is similar to the low density and monolayer experiments (0.501 ± 0.001 rad sec^{-1}), meaning rotation here is also diffusive. The decrease in the amount of rotational diffusion arises from the highly aligned state, as unlike in the monolayer, there are few other domains of differing orientations present, and therefore physical cell-cell interactions mostly occur with other individuals already of a similar alignment, generating a reduced amount of rotation relative to the other environments. With a comparison of the physical properties of cell movement described, we now consider FimX-YFP polarisation in the

different environments.

We measure FimX-YFP polarisation through two different metrics: plots of $\boldsymbol{p.v}$ as a function of I_{M} (**Figures 18a** and **19b**) and by comparing the mean epifluorescence intensity profiles along the cells along axis, oriented in the direction of twitching motility, found at low-density, in the monolayer and at the colony edge. As previously shown in **Figures 18a** and **19b**, $\boldsymbol{p.v}$ as a function of I_{M} shares similar properties at low-density and in the monolayer, aside from the saturation that occurs at large $|I_M|$ values at high density. We observe the same linear relationship between $\boldsymbol{p.v}$ and I_{M} for cells at the colony edge, however with a lower gradient, implying that a much larger increase in force is required to generate the equivalent amount of movement seen at low density and in the monolayer. The decrease in gradient is likely caused by cells having to expand into previously untouched agar, which provides a greater resistance to movement compared to individuals that can move in surface regions already colonise by other cells [149]. Additionally, **Figure 27c** shows that FimX-YFP polarisation is greatest not at the colony edge, but instead increases with increasing distance from the border. Cells just behind the colony edge can experience additional resistance because they push cells that are closer to the border. **Figure 18a** also has a negative $\boldsymbol{p.v}$ axis intercept, which likely occurs due to individuals with FimX-YFP aligned against the direction of colony expansion being pushed in the opposite direction to their FimX-YFP polarisation.

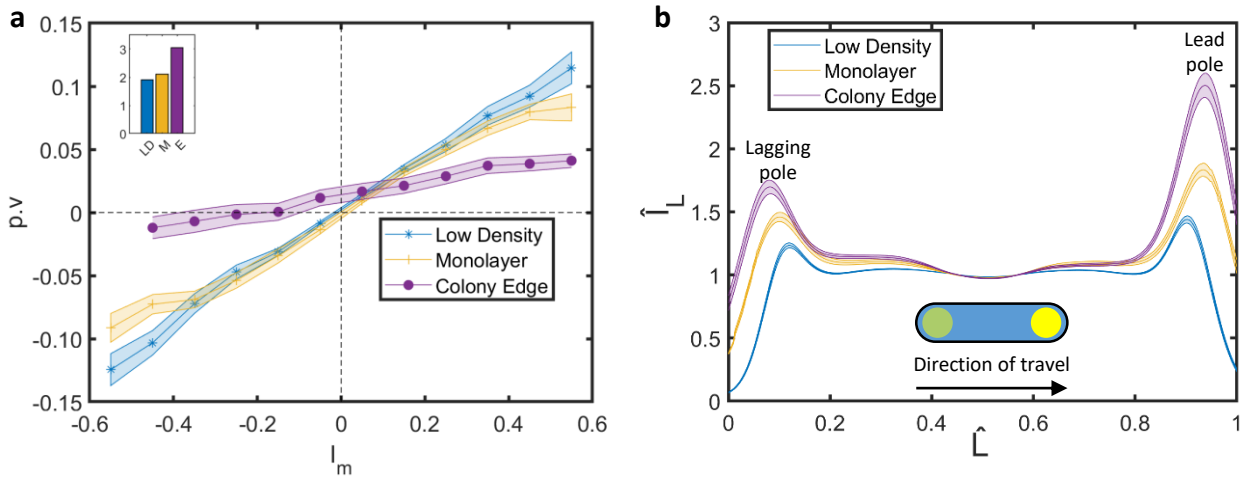

Figure 29: Comparing FimX-YFP polarisation in the three experimental conditions. The low density, monolayer and edge of colony plots are comprised of 17, 15 and 24 experimental time series each between two and three minutes in length. Shaded regions indicate the standard error between the mean value from each time lapse. (a) Mean $\boldsymbol{p.v}$ as a function of I_{M} for all experimental conditions. Inset shows the ratio of the percentage of time when $\boldsymbol{p.v}$ and I_{M} are correlated and anti-correlated. I_{M} bin size is 0.1. (d) $\hat{I}_L$ as a function of $\hat{L}$ for the three experimental conditions. Shaded region shows the standard error in the mean between the repeats of each experimental condition.

Finally, the extent of FimX-YFP production in each environment is considered, through a normalised mean cell intensity line profile, $\hat{I}_L$. At each suitable time point, a line profile is taken from

the lagging to the leading pole of the cell as defined by the sign of $\boldsymbol{p.v}$. As cell length is variable, we measured a normalised cell length, $\hat{L}$ by dividing the position in the line profile by the cell length. We then perform linear interpolation to generate an interpolated line profile with 501 data points. Interpolated line profiles are then normalised by the cell body intensity to account for any changes in epifluorescence signal, taking cell body intensity to be the mean value of the interpolated line profile in the range $0.4 \leq \hat{L} < 0.6$, giving the normalised mean cell intensity line profile, $\hat{I}_L$. For each data set, the mean value of $\hat{I}_L$ at each $\hat{L}$ for all time points is considered, then an ensemble mean is taken for each experimental condition, the results of which are seen in **Figure 29b**. We show that FimX-YFP production increases with density, as the low-density scenario sees the lowest values of $\hat{I}_L$. Additionally, FimX-YFP is produced in greater concentrations at the colony edge than in the monolayer. We can measure the degree of FimX-YFP polarisation from **Figure 29b** by taking the ratio of maximum $\hat{I}_L$ at the leading and lagging pole, giving 1.17, 1.25 and 1.47 at low density, in the monolayer and at the colony edge respectively, agreeing with visual inspection.

Here we have provided an overview of the properties of movement and FimX-YFP polarisation of *P. aeruginosa* within the three environments investigated in this chapter. The results found agree with visual inspection and the results outlined in **Section 3.2.3**, (i.e. that the greatest degree of FimX-YFP polarisation is found at the colony edge, yet the movement of individuals here is the least diffusive).

3.3 Discussion

Using genetic labelling, phase and epifluorescence microscopy, combined with cell and defect tracking and a custom analysis pipeline, we have investigated the pili-mediated twitching motility of *P. aeruginosa* in dense collectives at the interface between glass and agar. We began by mathematically quantifying FimX-YFP concentration at the cell poles, a protein known to localise predominantly towards a twitching cell's leading pole, using the metric I_{M} [74]. Subsequently, we also quantified bacterial movement as $\boldsymbol{p.v}$, the projection of cell velocity along the long-axis of the cell. We established that FimX-YFP leads pili-based movement at low density within our own strain, allowing us to infer the desired direction of travel within labelled individuals in dense collectives, where cell motility is highly influenced by neighbours [15]. We then used the relationship between FimX-YFP and cell movement to test the hypothesis that increased levels of polarisation occurs within topological defects due to their defined flow fields and importance in biological processes [34, 142, 145, 167]. We observe increased levels of polarisation within $+\frac{1}{2}$ topological defects behind the defect core in the direction of defect travel, with the mean I_{M} heat maps around comets possessing some similarity

to the velocity heat maps. The similarity between velocity and I_{M} heat maps suggests that there is a biological component to the movement of bacteria surrounding topological defects, where the cells are actively biasing their movement rather than the system being governed by purely physical processes. We also observed polarisation along the outflowing spokes of the trefoil, correlating with the velocity fields. However, the same correlation was not observed in the inflowing fields implying that *P. aeruginosa* passively drifts towards the core of trefoils, and then biases its movement away. Furthermore, large amounts of FimX-YFP polarisation have been found in groups of aligned cells at the colony edge, expanding out into uncolonised agar. In similar fashion to $+\frac{1}{2}$ defects, FimX-YFP localisation at the colony edge is greatest at the pole pointing to the direction of colony expansion, and increases with distance from the border, implying that expansion is facilitated by aligned cells biasing their movement away from the colony. The polarisation measured in these dense collectives implies that polar behaviour exists within close proximity to half integer defects and facilitates the process of colony expansion. This degree of polarisation is not currently recognised in the field and it has several important implications for the manner in which bacterial monolayers are modelled.

Bacterial monolayers are classified as a form of active matter, a system that exists outside of thermodynamic equilibrium with constituents that draw energy from their surroundings to perform work [163]. In the case of *P. aeruginosa*, nutrients are drawn from the agar that they are confined by and the cells perform work through the retraction of pili at their poles to generate force on a substrate to drive twitching motility. As movement is often directed from a single pole, individual cells in a bacterial monolayer are described as having head-tail asymmetry, or exhibit polar behaviour. Despite the polar behaviour of individuals, bacterial monolayers are commonly modelled using the equations of nematic liquid crystals, as it was assumed that there was no preferential direction of collective travel and due to the presence of half integer topological defects, which are intrinsic to a system with nematic symmetry [15, 138]. Recent studies have shown that rather than a system being either nematic or polar, there is in fact a cross over between the two types of behaviour. Previously, whole integer defects were thought to be present in polar systems, yet recent evidence shows that +1 charged topological defects arrest bacterial movement in monolayers, a system modelled as nematic, and half and full integer defects coexist within actomyosin assays [34, 168]. We build upon this growing body of evidence for polar and nematic coexistence by showing that FimX-YFP, and therefore cell movement, is highly polarised just behind the core of comets in the direction of defect travel, and along the outflowing spokes of trefoils, providing the first evidence of collective polar behaviour within close proximity to half integer topological defects. The collective polar behaviour observed in close proximity to topological defects will inform how to model collective systems going forward. It is

important to model the behaviour of topological defects accurately, especially $+\frac{1}{2}$ charged defects, as they play crucial roles in many biological processes, such as multi-layer formation in *M. xanthus* monolayers, which form the sites of fruiting body formation, and the development of 3D structures in *E. coli* and *P. aeruginosa* colonies [34, 45, 112, 145, 169]. It is not just in the bacterial monolayer that novel collective polar behaviour has been identified; cells at the colony periphery also display greater FimX-YFP concentration in the pole pointing in the direction of expansion. Here we have highlighted for the first time that colony expansion appears to be facilitated by the alignment of cell bodies and an active biasing of bacterial movement.

Although we have added to the evidence that nematic and polar dynamics coexist within active matter systems, here we have found no rationale for the source of collective polarisation, be it from the clustering of highly polar individuals during monolayer formation, or bacteria coming in close proximity to topological defects and becoming polarised by some mechanism. One potential source of polarisation could be through mechanosensing, as *P. aeruginosa* has been shown to sense mechanical forces through the Pil-Chp system and reverse its direction of travel at low density [37]. However, to our knowledge, no research has been performed to investigate this phenomena at large cell densities. We have also only reported on the collective polar properties of wild-type *P. aeruginosa* and it would be instructive in future studies to examine polar behaviour in different knockouts. For example, Δ*pilH* mutants are known to generate larger forces and move at greater velocities than the WT but also reverse direction of travel at increased frequencies [34]. It is unclear if collective polar behaviour increases due to the increased force exerted, or if it would decrease due to lack of coordination in movement due to the elevated reversal rate.

The same issue is present at the colony edge: although we have quantified the polarisation, there is no evidence to suggest what might be driving this polarisation. We often observed that individual cells behind the group of highly aligned cells at the colony edge move very rapidly and therefore could not be tracked easily. As no data on these rapidly moving cells is obtainable, we have been unable to outline how *P. aeruginosa* joins the collective, and if this has any influence on polarisation. Additionally, due to the relatively rapid rate of bleaching of the fluorescent signal, any future analysis on how individuals join the collective and subsequently move within it would need to record phase images at a larger rate, and epifluorescence images at a reduced rate [152]. We were also unable to identify the facilitation of colony expansion through $+\frac{1}{2}$ defects as observed in developing non-motile *E. coli* colonies [149]. However, the polarisation of FimX-YFP at the colony edge that increases with distance from the border, displayed similarities with $+\frac{1}{2}$ defects where collective polar order is greatest just behind the defect core, where cell bodies are most highly aligned.

There are several other future directions in which the work here could be expanded. We have developed a robust analysis pipeline capable of reliably measuring polar protein concentration and quantifying polar order surrounding topological defects in bacterial monolayers. The pipeline is generalised to a sufficient extent that by adjusting various filters, the same process that is applied to FimX-YFP can be performed on any other labelled protein that localises to the poles of *P. aeruginosa* such as those in the Pil-Chp system [64]. Performing such analyses could yield further information on the role of each protein in the Pil-Chp system and the relationships between them. Another potential area of further research is how collective polarisation at the colony border and in close proximity to topological defects might potentially alter in the presence of DNaseI. eDNA is essential to biofilm growth, and when degraded using DNaseI, even mature biofilms grown over several days will disperse [107]. The impact of DNaseI is not limited to biofilm growth; collective movement is also disrupted. Colony expansion requires a constant supply of new cells to replenish those at the border, and expansion ceases when the supply is not refreshed, and coherence of orientation and velocity is diminished [149]. If polar order were to be reduced in the presence of DNaseI, therefore reducing the rate of expansion, it would provide further support for the role of collective polarisation in colony development.

Through the work described in this chapter, we have measured the localisation of FimX-YFP at the cells poles of *P. aeruginosa* in a bacterial monolayer, producing the mean polarisation field surrounding topological defects. The FimX-YFP polarisation fields provide the first evidence of collective polar behaviour in close proximity to half integer topological defects, highlighting the need for future models of active systems to incorporate the coexistence of nematic and polar behaviour. Novel polar behaviour is not exclusively found within the bacterial monolayer, and we find that bacteria deliberately bias their movement in highly aligned groups at the colony edge in the direction of colony expansion. To further our understanding of novel polar behaviour, we must uncover its mechanism of origin and maintenance

4 Reversals in the direction of travel contribute to collective polarisation in bacterial monolayers and colony expansion

Movement is one of the most ubiquitous aspects of life across all spatial scales of living organisms and the mechanisms that facilitate motion are hugely varied. For example, bacterial motility is found in both planktonic and surface-associated cells [31]. The movement of individual swimming bacteria has classically been studied by tracking cells using small cell densities[2, 74]. However, bacteria spend the majority of their life cycle in surface-attached, high-density biofilms, where motility is much harder to follow because cells are tightly packed together. Recently, improvements in cell tracking algorithms and software have started to address this challenge [19, 113]. As such, the role of collective movement within biofilms has begun being explored, showing that the motility of aligned groups of bacteria within dense collectives varies as a function of the characteristics of their constituents, for example, by the number of pili they produce and their length [34, 73]. However, it is often assumed that within collectives that cells cannot actively modify their behaviour, but rather their properties are fixed and governed purely by physics [34].

Recently, microfluidic studies of twitching motility in surface-attached *P. aeruginosa* have shown that individual cells are able to navigate chemical gradients by reversing their direction of travel along their long axis. In a gradient of nutrient, cells increase their reversal rate when they are moving towards smaller concentrations of nutrient, which leads to a net bias of motility towards greater concentrations [67]. *M. xanthus* has also been shown to suppress its reversal rate when encountering increasing chemical gradients, leading to a net movement towards increased nutrient concentrations [170]. Reversals of direction have also been identified in less well understood motility systems such as gliding in *F. johnsoniae*, although the stimulus that causes a change in direction is yet to be identified [42]. Given that reversals occur across multiple species of bacteria and that they play important roles in the formation and maintenance of collectives in *M. xanthus*, we hypothesised that they also serve a purpose in developing *P. aeruginosa* biofilms [45].

It has been shown that at low density *P. aeruginosa* directs twitching motility through mechanotaxis, specifically using the Chp chemotaxis like system to regulate the forward motion or reversal of an individual. During a 'T-bone' like collision, where a cell collides with another cell at a right angle, the cell will often reverse its direction of twitching motility [37]. Such T-bone collisions are found in the core of $+\frac{1}{2}$ topological defects with one group of aligned cells colliding with another at right angles. One therefore might hypothesise that we would observe an elevation in reversal rate at the defect core relative to the rest of the monolayer. The core of $+\frac{1}{2}$ defects is often characterised by a greater density of cells than the rest of the monolayer [145, 171], which in dense *M. xanthus*

collectives is the site of multilayer formation which seed the production of three-dimensional fruiting bodies. On the other hand, $-\frac{1}{2}$ charge defects trigger a localised region of low cell density [145]. We hypothesised that the decrease in cell density could also impact reversal rates. For instance, increased cell densities might promote reversals if they play a role in preventing jamming [146, 172]. These possibilities will be investigated over the course of this chapter.

Both in our low density and densely packed monolayer experiments, the previous chapter has established FimX-YFP as an indicator of the direction of twitching motility in individual cells, showing that *P. aeruginosa* twitches in the direction of the pole with the greatest FimX-YFP concentration. We found that *P. aeruginosa* displays highly polarised collective FimX-YFP alignment within topological defects in monolayers, and for groups of aligned cells at the colony border expanding into virgin territory. Active nematic theory offers explanations for how the alignment of rod-shaped particles (in this case twitching cells in a monolayer) could arise through purely physical effects [15]. However, we hypothesised that deliberate movement behaviour changes in *P. aeruginosa*, like reversals, have the ability to increase polarisation of neighbouring individuals and increase their rate of travel.

The challenge with detecting reversals in dense collectives is that changes in a cell movement direction can be driven either by either a reversal or by forces exerted on a cell by its neighbours. It is thus not possible to resolve a cell's behaviour from following its movement alone. However, our time-lapse images of FimX-YFP cells at low density demonstrate that FimX-YFP can swap from one pole to the other and this 'pole swap' is often correlated with a reversal of movement direction. These reversals of direction are observed to persist for time scales longer than the stochastic detachment of a pilus would cause [36], and therefore can be considered as deliberate action of the cell [32]. Since we use FimX-YFP as a reporter for the direction of twitching motility, and pole swaps appear to accompany reversals, we will use pole swaps to identify reversals originating from individual bacterial movement behaviour rather than the action of neighbours in densely packed monolayers.

In this chapter, the role of intracellular FimX-YFP pole swaps as a proxy for reversals in movement direction is investigated. The process of pole swap and reversal detection are outlined, along with the appropriate filters developed. The link between FimX-YFP pole swaps and reversals is established further to build upon previous anecdotal published evidence [37]. We then use this information to investigate if we could identify if particular conditions trigger pole swaps. Finally, pole swaps at the colony border are investigated, along with how reversing potentially benefits individual cells.

4.1 Reversal in twitching direction are associated with polar re-localisations of FimX

In **Chapter 3** we presented evidence that in densely packed bacterial monolayers, *P. aeruginosa* displays large amounts of collective FimX-YFP polarisation when in close proximity of half integer charged topological defects. Bacterial monolayers have previously been modelled as nematic systems, where neighbouring cells are equally likely to direct their motility along either axis, however, the presence of collective FimX-YFP polarisation when in close proximity to half integer charged topological defects show the existence of polar behaviour [15, 34, 147]. When comparing the experimentally determined collective polarisation to an equivalent model of self-propelled rods comprised of individuals that produce identical amounts of force but cannot reverse, we observe an increase in polar order.

Given that the amount of polar order observed in our simulations that are devoid of reversals was larger than in our experiments, we sought to understand if *P. aeruginosa* uses reversals to influence the amount of collective polar behaviour in active matter systems. To investigate the relationship between the rate of reversal and the amount of collective polar behaviour, we must first build a robust detection system for both pole swaps and reversals that is capable of accurately quantifying both of these behaviours. Additionally, as our strain differs from those reporting correlations between pole swaps and reversals in the literature[37], we must prove this relationship again. It is crucial to establish this relationship as in dense collectives individual movement is highly influenced by neighbouring cells and an observed reversal could be the result of collective movement rather than the desired change of direction by a bacterium that a pole swap indicates [15]. In the following section, we outline our pole swap and reversal detection and filtering pipeline, and how cross correlation is used to investigate the relationship between the two processes.

4.1.1 Detection of pole swaps and reversals

Before a relationship between pole swaps and reversals can be established, we must first detect each type of event, requiring us to calculate both the concentration of FimX-YFP at either pole and the direction *P. aeruginosa* twitching motility over time. We have already presented metrics, I_{M} and $\boldsymbol{p.v}$, that respectively allow us to automatic detect pole swaps and reversals . In this section we outline the methods that are used to identify these events, along with the accompanying filters that are used to prevent false positives that result from idiosyncratic conditions.

To recap, a pole swap occurs when the region of a cell with the greatest FimX-YFP concentration

switches from one of a cell's poles to the other. A pole swap is be observed in two forms: a cell pole with no FimX-YFP increases in concentration and the opposing previously localised pole loses all FimX-YFP or both poles are already abundant in FimX-YFP yet the pole with largest concentration swaps. A reversal is considered as a change in direction of travel along the long axis of the cell. The key element to both processes is that they must be sustained changes in either FimX-YFP localisation or direction of travel. Sustained changes in FimX-YFP polarisation are more commonly observed in our experiments, as due to the jerky nature of twitching motility (caused in part by the stochastic detachment of pili), multiple rapid changes of direction on a short time scale can occur, which are not related to pole swaps and that we do not want to include in analyses [39]. Therefore, we will design an automatic pole swap and reversal system that identifies sustained temporal changes in FimX-YFP concentration and direction of travel using the metrics I_{M} and $\boldsymbol{p.v}$. Automatic detection is crucial in establishing the correlation between pole swaps and reversals, as thousands of cells can occupy one field of view for each of the 15 time lapses movies used in our analyses (each 181 frames long), posing an impossible task without automatic detection.

Detection of pole swaps and reversals relies on first identifying where I_{M} and $\boldsymbol{p.v}$ time series pass through zero. We begin by smoothing these metrics using a five second moving average filter to minimise the effect of rapid, noisy changes in FimX-YFP concentration asymmetry or cell movement. In **Figure 30a** and **30b** we show time lapses of cells undergoing simultaneous pole swaps and reversals in low density and in the monolayer experiments respectively, with the accompanying smoothed I_{M} and $\boldsymbol{p.v}$ traces, with the initially detected pole swaps and reversals, and those events that remain after our custom filtering pipeline is applied (shown in the I_{M} and $\boldsymbol{p.v}$ traces as vertical blue dashed lines).

As observed in **Figure 30**, a robust filtering process is needed to remove false positive pole swaps and reversals from our subsequent analyses. Below we document the various filters that are used in analysis:

- Removing events at the start/end of trajectories – We exclude pole swaps and reversals that occur within five seconds of the start or end of a trajectory because subsequent filters use data that is obtained from before and after putative events. As this information is not available for events that occur close to the beginning and end of a trajectory, they are removed from our analyses.

- Testing whether zero crossings of I_{M} and $\boldsymbol{p.v}$ are robust - We want to identify events which mark a sustained change in the direction FimX-YFP concentration asymmetry and cell travel,

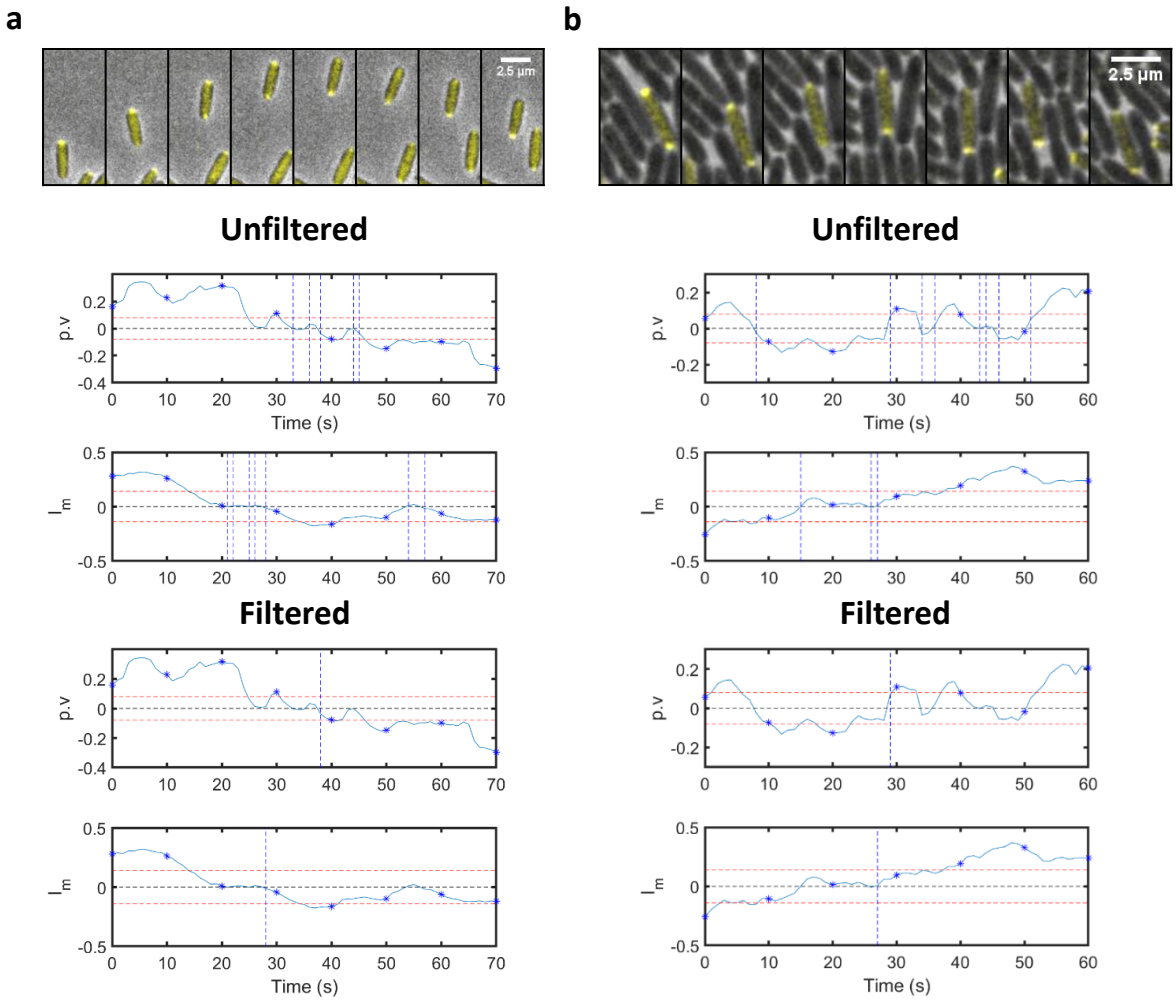

Figure 30: Unfiltered and filtered pole swap and reversal detection at low density and in the monolayer. (a) A merged phase and epifluorescence image of a FimX-YFP labelled cell undergoing a pole swap and reversal. Underneath are the I_{M} and $\boldsymbol{p.v}$ traces showing unfiltered and filtered pole swap and reversal detection, with events shown as vertical blue dashed lines along the corresponding time series. Blue stars along the trace represent the time points shown in the montage whereas horizontal red dashed lines show the minimum values of I_{M} and $\boldsymbol{p.v}$ used in the filtering process. I_{M} and $\boldsymbol{p.v}$ traces have been smoothed across five seconds using a moving average filter. (b) The same process as (a) but for a cell in a monolayer. Despite the influence of this cell's neighbours it can be observed that the relocalisation of FimX-YFP still results in a change of direction of this cell's travel.

however, I_{M} and $\boldsymbol{p.v}$ can also change sign if it randomly fluctuates about zero. To distinguish sustained changes from the more ephemeral zero crossings, we test whether I_{M} and $\boldsymbol{p.v}$ exceeds a threshold value both before and after the putative event. More specifically, we test if the absolute value of I_{M} and $\boldsymbol{p.v}$ exceeds 0.14 and 0.08 µm s^{-1} respectively (illustrated in **Figure 30** as dashed red lines) in the time period both and after each zero crossing. This analysis considers the sign of the event - for example, if I_{M} goes from negative to positive during a zero crossing, then we must observe that $I_{\mathrm{M}} < 0.14$ for at least one timepoint before the putative event, and $I_{\mathrm{M}} > 0.14$ for at least one time point after the putative event for it to be retained. The exact values of these thresholds were obtained by visual inspection of many

putative events. The absolute value of I_M and $\boldsymbol{p.v}$ must exceed the above threshold within the period that extends from the previous event (or from start of the trajectory if no other events precede it) to the event under question. Likewise, the absolute value of I_M and $\boldsymbol{p.v}$ must exceed the threshold within the period that extends to the event under question to the subsequent event (or to the end the trajectory if no other events occur after it). As potential events are removed during this process (which can then change the time period that we interrogate both before and after a putative event), this process is repeated iteratively - if a putative event is removed the process begins again on those that remain. Although described checks are a useful step in filtering if a single track is 180 seconds long and for example there are pole swaps at 10 and 170 seconds, it seems unreasonable to compare all of the values between these two events as they are separated so far apart in time. Considering the time difference, a window of 30 seconds either side of an event is then checked to ensure that for a single time point, the I_M and $\boldsymbol{p.v}$ thresholds have been passed, or if an event is close to the start or end of the track as wider window as possible is used. Although this can mean different amounts of data can be checked before and after an event, the thresholds are often surpassed within 30 seconds, as confirmed through visual inspection of I_M and $\boldsymbol{p.v}$ traces. If a single time point has not surpassed the thresholds pre and post event, the pole swap or reversal is rejected.

- Ensuring cells are below a minimum aspect ratio - for each pole swap or reversal, the five seconds before or after an event are checked to confirm a series of properties regarding the cell. For the first check, we ensure that within this window that all values of aspect ratio are below 6.5. Through visual inspection, we found that once above an aspect ratio of 6.5, cells appear to be elongated such that they begin division. As septa have not completely formed, FAST is unable to distinguish between daughter cells, therefore, we reject any events where an aspect ratio in the window around an event is above 6.5.

- Removing cells in close proximity to the edge of the field of view - to ensure that the entire cell is within the image field of view and therefore accurate quantification of FimX-YFP concentration asymmetry is achieved, a pole swap or reversal is rejected if five seconds prior or after an event that cell is within 4 μm of the image border.

- Resolving FimX-YFP concentration at the cell pole - as FimX-YFP asymmetry and the direction of twitching motility is correlated, we need accurate I_M and $\boldsymbol{p.v}$ traces to perform reliable detection. Therefore, if the nearest pole neighbour algorithm (**Figure 16**) deems cell poles are not separated within five seconds before or after an event, the event is rejected. This filter is

especially important for I_{M}, as if two cell poles are within close proximity to one another the fluorescent signal is distorted, and can result in inaccurate detection of pole swaps.

- Only analysing labelled cells - as we are searching to infer reversals in the direction of twitching motility from pole swaps, the cells must be labelled to allow for pole swap detection.

It can be observed in **Figure 30** that these filters are effective in removing spurious pole swaps and reversals, with the remaining events accurately marking those which can be observed by eye in the corresponding experimental images. In this section we have outlined our method of detecting FimX-YFP pole swaps, and reversals in movement direction. In the following section we investigate the relationship between these events.

4.1.2 Cross correlation analysis reveals the relationship between pole swaps and reversals

Our experimental images indicate that the FimX-YFP concentration asymmetry is a good indicator of the direction of travel for our labelled strain of *P. aeruginosa*, and that it is consistent with previous literature that used a different fluorescent fusion construct [37]. Quantifying I_{M} and $\boldsymbol{p.v}$ has allowed us to accurately detect individual pole swap and reversal events. Given I_{M} and $\boldsymbol{p.v}$ are correlated with one another when cells are at low density, we seek to prove the correlation between pole swaps and reversals, through cross correlation to infer the movement behaviour of *P. aeruginosa* cells when they are in dense collectives.

Rather than using discrete events, our cross correlation analysis uses all of I_{M} and $\boldsymbol{p.v}$ values obtained over the course of a trajectory. Cross correlation is the process of calculating the correlation between a stationary signal, and another signal that is shifted in time by a lag, τ. In the case of our experiments, I_{M} is our stationary signal and $\boldsymbol{p.v}$ is the lagging signal. If two metrics were not correlated with each other, then we would expect to observe that the cross correlation would be approximately zero. However, if a correlation was present, we would expect to observe a non-zero peak in correlation over the range of lag times which the two signals are correlated, with the sign of the cross-correlation indicating if the two signals are either positively or negatively correlated with one another. Furthermore, this analysis can also determine which signal 'leads' the other e.g. if the peak of the cross correlation occurs at a non-zero lag time it would imply that one sign precedes the other by the timescale at which the peak occurs..

We hypothesised that trajectories in which pole swaps or reversal occurred might exhibit a larger dynamic range and therefore a larger crosscorrelation than trajectories that did not, so we calculated the cross correlation of I_{M} and $\boldsymbol{p.v}$ traces separately for trajectories containing at least one pole

swap, trajectories containing at least one reversal, and trajectories neither a pole swap or reversal. As the maximum track length is 180 seconds, cross correlation is performed to time lags of -90 to 90 seconds. If a track is under 180 seconds long and there is no remaining data large time lags, so a zero value is returned. Once cross correlation is performed, we take the median value of cross correlation at corresponding time lags across all trajectories, and exclude zero valued results as these would bias our result. For completeness, we also calculated the autocorrelation, which quantifies the duration over which signal stays correlated with itself. By definition the autocorrelation is one at a zero time lag, it enables us to check that our analyses are operating as expected. The process and results of cross and auto correlation analysis are shown in **Figure 31**.

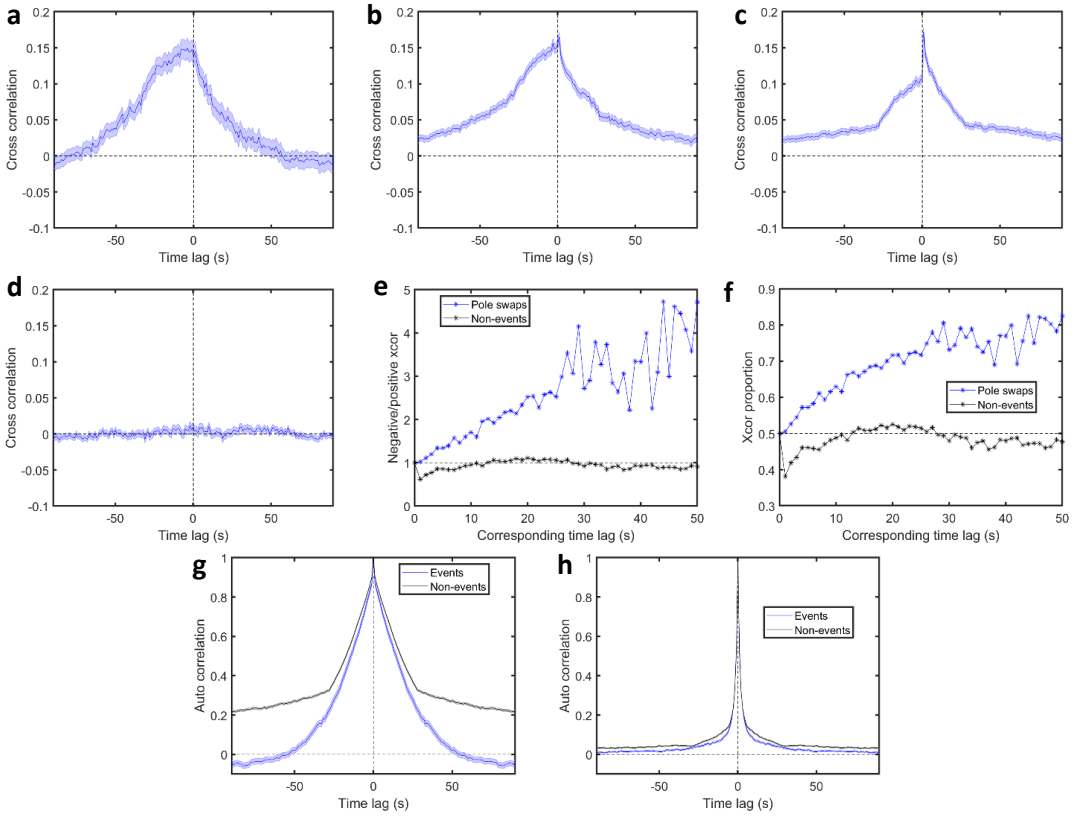

Figure 31: Crosscorrelation analysis shows that I_{M} and $\boldsymbol{p.v}$ are highly correlated with one another when cells are at low density. Crosscorrelation for (a) tracks with at least one pole swap (b) tracks with at least one reversal (c) tracks with neither a pole swap or reversal. The shaded region in all plots is the standard error in the median. (d) The result of crosscorrelation of I_{M} with a randomised $\boldsymbol{p.v}$ series. (e) The ratio of cross correlation values corresponding to a negative time lag compared to those that correspond to a positive time lag. (f) The proportion of the total cross correlation that values corresponding to negative time lags possess compared to the sum of the cross correlation at the negative and positive value. The auto correlation of (g) I_{M} and (h) $\boldsymbol{p.v}$ for tracks with and without pole swaps and reversals. These analyses used a total of 7039 trajectories containing 402 tracks that contained at least one pole swap, 3762 tracks that contained at least one reversal, and 5351 trajectories with neither a pole swap or a reversal. Shaded regions show the standard error in the median.

Our results, which all were obtained using time lapses of *P. aeruginosa* twitching at low density,

indicate that I_{M} and $\boldsymbol{p.v}$ are positively correlated with one another for a period of approximately 100 seconds. Interestingly, in our measurements of the cross correlation from tracks with pole swaps (**Figure 31a**) we observe that peak cross correlation occurs at a time lag of -4 seconds, implying that on average, a pole swap occurs four seconds before a reversal. However for trajectories with at least one reversal, the maximum occurs at a time lag of zero (**Figure 31b**). Both however, have a strong asymmetric shape indicating that prior to a pole swap the localisation of FimX-YFP and cell movement is likely correlated for a longer period of time than after the pole swap. When there are no pole swaps or reversals in a trajectory (**Figure 31c**) the zero time lag arises as on average FimX-YFP asymmetry and the direction of twitching motility are correlated. We can be confident that the results observed are real, as we also run our analysis with the original I_{M} values from a trajectory, but the corresponding $\boldsymbol{p.v}$ time series has a randomised order (**Figure 31d**). As expected, the cross correlation of approximately zero at all time lags indicates that there is no correlation between the original FimX-YFP localisation signal, and that of the randomised cell movement. To highlight the degree of asymmetry in the positive and negative time lags for cross correlation arising from tracks with pole swaps, we plot the ratio of negative to positive time lag values and the proportion of negative values in **Figures 31e** and **31f**. These plots show that at all time lags, the value of negative cross correlation is larger than the positive for pole swap events. As a comparison, the value for tracks with no events are nearly always equal. Finally, in **Figures 31g** and **31h** we consider the auto correlation of I_{M} and $\boldsymbol{p.v}$ respectively. In both cases we see that tracks without pole swaps or reversals consistently have increased auto correlations, for time lags greater than or smaller than zero, arising as pole swaps and reversals cause I_{M} and $\boldsymbol{p.v}$ respectively to change sign, reducing auto correlation as both metrics before and after the event are anti-correlated. The auto correlation curves for I_{M} are much wider than those for $\boldsymbol{p.v}$, which likely arises from the jerky nature of twitching motility resulting so that $\boldsymbol{p.v}$ exhibits more random fluctuations compared to I_{M}. Thus I_{M} is a more temporally stable measurement of the persistence of twitching motility than $\boldsymbol{p.v}$, which can be affected by spontaneous detachment of pili which causes rapid movement [166].

Previous studies on the role of FimX in twitching motility have described anecdotally that pole swaps coincide with a reversal of direction of travel, however there existed no accompanying analysis to link the two events [37]. By splitting the metrics defining FimX-YFP concentration asymmetry and bacterial movement into those with pole swaps, those with reversals and those with neither, and performing cross correlation using the metrics I_{M} and $\boldsymbol{p.v}$, we have shown that pole swaps can be used as proxies for reversal detection in dense collectives. As such we now investigate potential stimuli that trigger reversals in dense collectives.

4.2 Investigating potential stimuli of intracellular bacterial pole swaps

As a result of the work performed in **Section 4.1**, we have confirmed that FimX-YFP pole swaps occur alongside a reversal in the direction of twitching motility in *P. aeruginosa* at low density. During biofilm development, cell density becomes sufficiently large that collective behaviours emerge and an individual's movement becomes strongly influenced by neighbouring cells, however we are able to detect reversals that are caused by the deliberate retraction of pili in individual cells through pole swaps. In the upcoming section we seek to determine stimuli that trigger FimX-YFP pole swaps.

Our search for the driving forces behind bacterial reversals is motivated from the novel collective polar behaviour identified in bacterial monolayers in **Chapter 3**. Although monolayers of *P. aeruginosa* are comprised of polar agents, they have been be described using active nematic theory which can be derived by coarse graining length scales containing many cells [15]. The polar behaviour we have identified surrounding half integer topological defects highlights the need for modelling of bacterial monolayers to allow for the coexistence of nematic and polar behaviour, an emerging area of interest in recent literature [168]. Additionally, we show that collective polarisation surrounding defects increases in a self-propelled model of the bacterial monolayer, that is similar to that observed in our experiments but lacks reversals. However, we wondered whether if *P. aeruginosa* might use stimuli to actively regulate reversals to generate polarisation, as cells moving in the same direction would likely collectively move more rapidly than if they moved in opposite directions.

In the following sections, we investigate how different properties of the bacterial monolayer impact the rate of reversal. We begin by building upon the analysis pipeline described in **Chapter 3**, first investigating the effect of cell density and proximity to topological defects in a monolayer impact reversal rate, and then subsequently testing if individual movement relative to that of the collective impacts its reversal rate. Lastly, we test if reversals drive the collective polarisation of FimX-YFP at the colony edge, which could potentially help facilitate colony expansion and thus enhance a colony's evolutionary fitness.

4.2.1 Cell density

Previous studies have highlighted the importance of cell density to multilayer formation in *M. xanthus*, as high density regions go on to seed fruiting body formation [145]. Additionally, *M. xanthus* employs periodic reversals of the direction of twitching motility to ensure a collective holds together during fruiting body formation[45]. Given the importance of density and reversals in fruiting body formation in *M. xanthus* we considered the possibility that density is crucial in the triggering of *P. aeruginosa* reversals in a monolayer.

To quantify cell density we considered multiple methods of measurement. The first method we tried relied on the binary segmentations produced by FAST [19]. Here, we take the number of pixels corresponding to cells within a given radius of the focal cell and then divided this by the area of the circle. The issue with this method is that the binary segmentations do not always represent the true area of the cells, and an underestimate is often obtained. Also, there are gaps in the binary segmentations that do not appear in the phase images, and it is unknown if these gaps are uniform in size across each image. The second method we tried also relied on using a circle centered on each focal cell, and we would count the number of centroids of the neighbouring cells that fell within this area. The main issue with this method is that a centroid might be just beyond the radius of the circle so it would not be included, but a large portion of the cell body would be, making this measure very noisy. In addition, this method was highly dependent on the cell size. Moreover, both methods also involve the use of a user defined threshold, which we tried to avoid where possible. We therefore searched for a method to calculate cell density calculation that did not involve any user defined thresholds.

We decided to use Voronoi diagrams as they enable density measurement without requiring user defined inputs. In a Voronoi diagram, a set of locations in a plane, commonly referred to as seeds, are split into domains with a given area. Each domain is defined by the coordinates within, which are closest to a particular seed than any other, meaning the borders are locations within the plane that are equidistant to two or more seeds [173]. As tracking in a bacterial monolayer is highly accurate, and we are able to detect all domains in a field of view at every time point, we define our set of seeds as the centroids of the domains identified by FAST (**Figure 32a** shows an example Voronoi tessellation from an image of the bacterial monolayer). We note that domains at the edge of the plane are unbound and therefore have infinite area, and must be excluded from the analysis. We define cell density, D, as

$$D = \frac{1}{A}$$

where A is the area of a Voronoi domain and **Figure 32b** shows a histogram of D that was aggregated over a large number of experimental data sets.

As we are using pole swaps as proxies for bacterial reversals in a dense collective, we must now calculate pole swap rate as a function of cell density. Quantifying the pole swap rate as a function of another variable is done many times over in the rest of the chapter, and we will describe the method of calculation each time as there can be some differences in methodology depending on

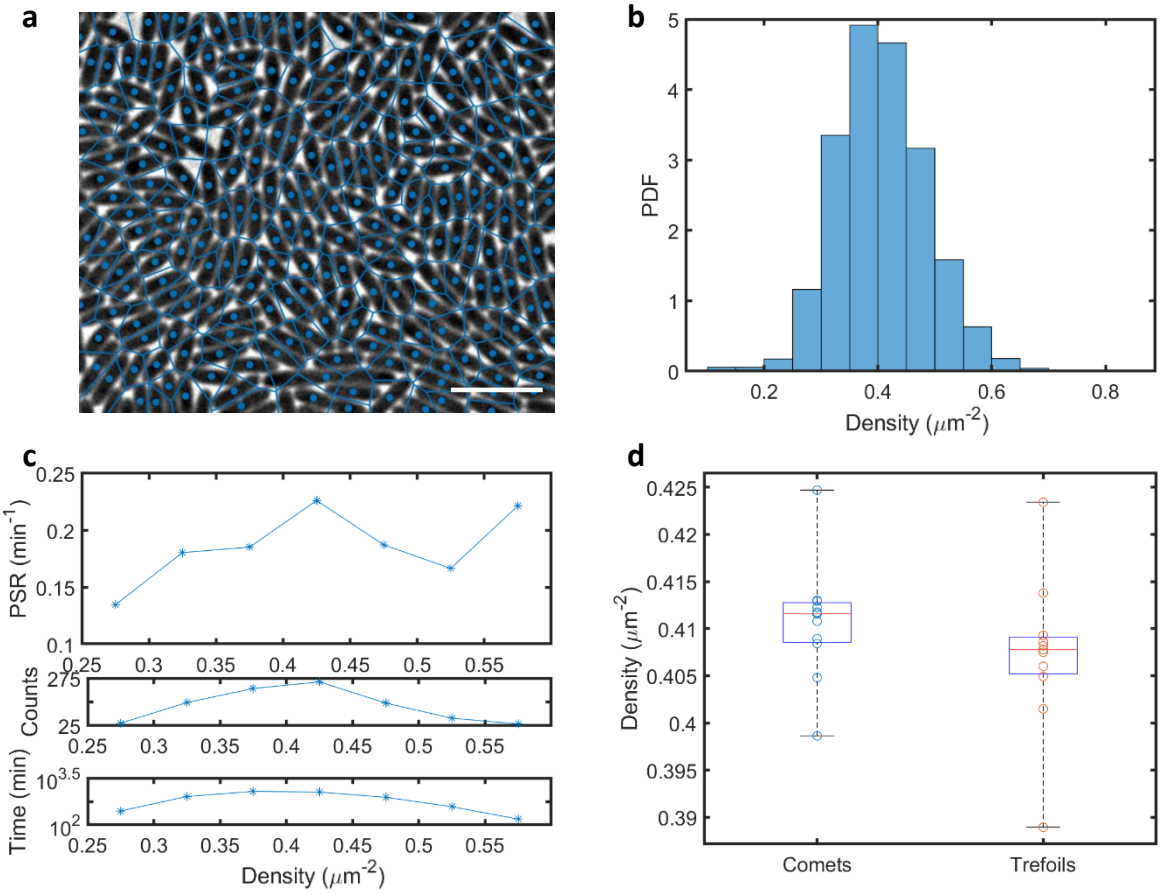

Figure 32: Measuring the pole swap rate as a function of cell density. (a) A Voronoi tessellation generated from the locations of *P. aeruginosa* centroids in a bacterial monolayer. Centroid locations are shown as blue spots and areas are indicated by blue lines. The image shown here is the central $\frac{1}{4}$ of a single field of view. Scale bar is 10 μm. (b) PDF of cell density for data pooled over 15 experimental time series each between two and three minutes in length. (c) Pole swap rate as a function of cell density. Bin size is 0.05 cells μm^{-2}. Bins with less than 30 minutes worth of trajectory data have been removed from this analysis. (d) Box plots showing the mean density around comets and trefoils for each data set. The red line is the median and the bounds of the boxes represent the 25th to 75th percentile of data. Each circles show the mean density value around surrounding topological defects from each experimental time series. Values below 1.5× the interquartile range minus the 25th percentile and above the 1.5× the interquartile range plus the 75th percentile are considered outliers and therefore removed.

the variable under investigation. In the case of cell density, we bin our trajectories based on their instantaneous measurements of D. In each cell density bin, we calculate both the number of pole swap events that occur within the bin and total amount of time that cells spend within over which they could have potentially performed a pole swap. The pole swap rate in a bin is then simply the number of pole swaps observed divided by the total time that trajectories spend in that bin. The relationship between pole swap rate and cell density is shown in **Figure 32c**, and there appears to be no correlation between the two variables.

It is also known that in *M. xanthus* monolayers, $+\frac{1}{2}$ charge topological defects are associated with increases in cell density see increases in density, and those with $-\frac{1}{2}$ charge are associated with

decreased cell density [145]. Therefore, we sought to measure the density around topological defects in our *P. aeruginosa* monolayers. Using Voronoi tessellations, we calculated the mean cell density within 10 μm of each defect core for both $+\frac{1}{2}$ and $-\frac{1}{2}$ defects in each experimental time series (**Figure 32d**). We observed that the cell density around the core for both comets and trefoils is similar to one another, which stands in contrast with previous reports for *M. xanthus* [145].

Next, we measured the spatial distribution of cells around the core of defects to understand if either cell type preferentially accumulates at the core of topological defects, or if there is a depletion. To do this we calculated the cumulative time that cells spend about each type of defect and then normalised this by the total amount of time each defect was observed for. Calculating a normalised amount of time is important as we track each defect type for different amounts of time. Therefore, we normalised the total number of cells observed in the vicinity of a defect by the amount of time that each type of defect is tracked for.

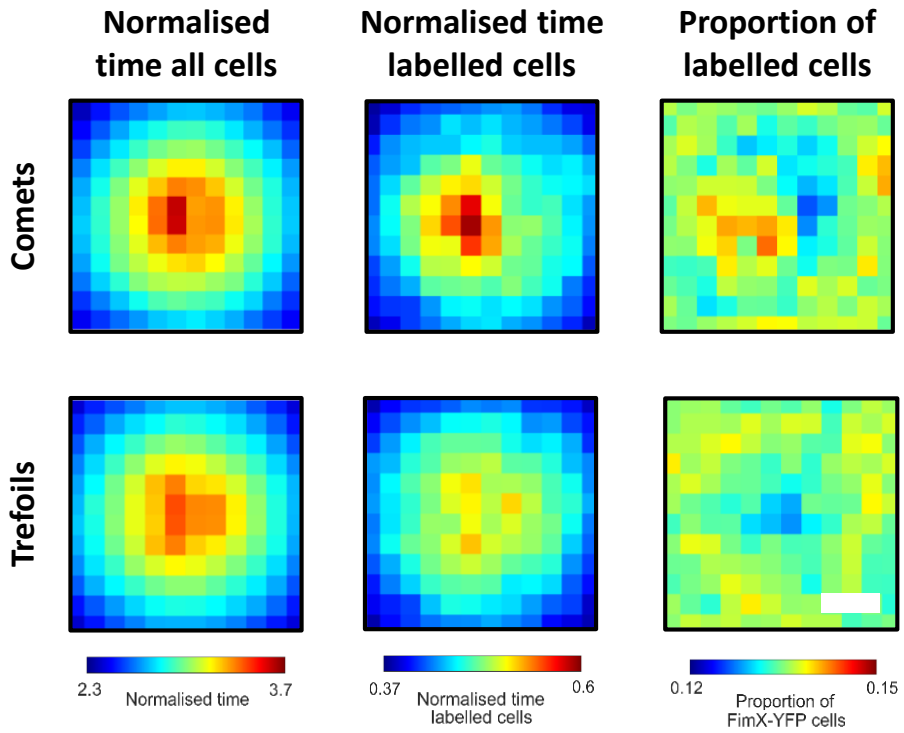

Figure 33: Normalised time measurements in close proximity to topological defects. Displayed is the normalised time for all cells, FimX-YFP labelled cells, and the proportion of FimX-YFP labelled cells. Data shown is a 48 × 48 cell width (38.4 × 38.4 μm) window surrounding each topological defect with a bin size of 4 cell widths (3.2 μm), scale bar is 12 cell widths (9.6 μm). Data shown here has been pooled from 15 experimental time series each between two and three minutes in length, containing 1029 and 1051 comets and trefoils.

Figure 33 shows the normalised time of all cells and of labelled cells and we can see that the difference between the total normalised time of comets and trefoil is negligible, which stands in contrast with previous work that shows accumulations in comets, and a depletion of cells around

trefoils [145]. However, we do observe an enrichment of labelled FimX-YFP cells just behind the core of comets whereas in the core of trefoils they are depleted, which is in agreement with previous work showing that cells capable of exerting larger amounts of force accumulate in $+\frac{1}{2}$ charged defects [34].

Although the normalised time plots are useful indicators for the accumulation of bacteria surrounding topological defects, we cannot completely rely on the conclusions that come from them as if a defect is close to the image border some bins will not collect data, which overall reduces the amount of normalised time. This might be responsible for the trend of normalised time decreasing radially from the defect core for comets and trefoils, for all cells and labelled cells only. However, we can still investigate the accumulation of labelled cells surrounding topological defects by measuring the proportion of time labelled cells are tracked for in close proximity to a defect. By dividing the normalised time of labelled cells by the normalised time of all cells, we observe two distinct spatial distributions around each defect type. For comets, we observe an enrichment of labelled cells behind the core and a depletion infront, implying that the greater force producing cells are first depleted and then accumulate as a comet passes through an area. At the core of trefoils, we observe only a depletion of labelled cells. We also measured the mean proportion of time labelled cells spend around topological defects for **Figure 33**, with both comets and trefoils returning 0.14, consistent with the results that the density of cells surround comets and trefoils is very similar (**Figure 32d**). Therefore, we conclude that topological defects appear to have no influence on local cell density in *P. aeruginosa* monolayers, however they do cause spatial patterning of cells capable of exerting greater amounts of force.

Although we were unable to identify a clear trend in the relationship between pole swap rate and local cell density, we have shown that the greater force producing FimX-YFP cells accumulate at greater concentrations in $+\frac{1}{2}$ charged comets, than $-\frac{1}{2}$ charged trefoils. Additionally, albeit over a small range, we see a depletion of FimX-YFP cells in front of the core of comets and at the centre of trefoils, then at larger concentrations behind the comet core. Given we see increased polarisation of FimX-YFP behind the core of $+\frac{1}{2}$ defects (**Figure 22a**), could this be driven by a reduction in pole swap rate in this region? To answer this, we will next measure how the pole swap rate varies around defects.

4.2.2 Topological defects

Not only were we motivated to investigate how pole swap rate varies surrounding topological defects by the enrichment and depletion of FimX-YFP cells, topological defects also play a crucial role in many biological processes [169]. Recent literature has shown that pole swaps occur at low density

when two cells undergo a 'T-bone' collision, with the colliding cell reversing direction after it makes contact [37]. The alignment of cells at the core of $+\frac{1}{2}$ charged topological defects (**Figure 21**), are reminiscent of the aforementioned T-bone collision, albeit at a much larger cell density. One could therefore hypothesise that reversals might be enriched at the defect core. Here we probe how pole swap rate varies with position relative to half integer charged topological defects, to investigate whether spatial trends might be observed.

First, we will measure how pole swap rate varies with distance from the defect core, r_{D}, and angular position, θ_{D}, measured from the orientation of the defect counter clockwise. Half integer charged topological defects each have lines of symmetry, meaning data can be combined about these to enhance the signal given that pole swaps are relatively infrequent. For $+\frac{1}{2}$ comets, the line of symmetry runs horizontally (**Figure 22a**), splitting the defect core in half. By setting the x axis in the comet frame of reference as this line of symmetry, such that data with a negative y value can have its sign swapped and combined with the data with a positive y value. The case with trefoils is slightly more complex as there are three lines of symmetry running along each inflowing spoke of the velocity field (**Figure 22b**). There are thus three identical domains about θ_{D}: $-60° \leq \theta_{\mathrm{D}} < 60°$, $60° \leq \theta_{\mathrm{D}} < 180°$ and $180° \leq \theta_{\mathrm{D}} < 300°$. We subtract 120° from θ_{D} in the second domain, and 240° in the third to collate the data. We calculate r_{D} and θ_{D} using

$$r_{\mathrm{D}} = \sqrt{x_{\mathrm{D}}^2 + y_{\mathrm{D}}^2} \quad \text{and} \quad \theta_{\mathrm{D}} = \tan^{-1}\left(\frac{y_{\mathrm{D}}}{x_{\mathrm{D}}}\right)$$

with the resultant plots shown in **Figure 34**.

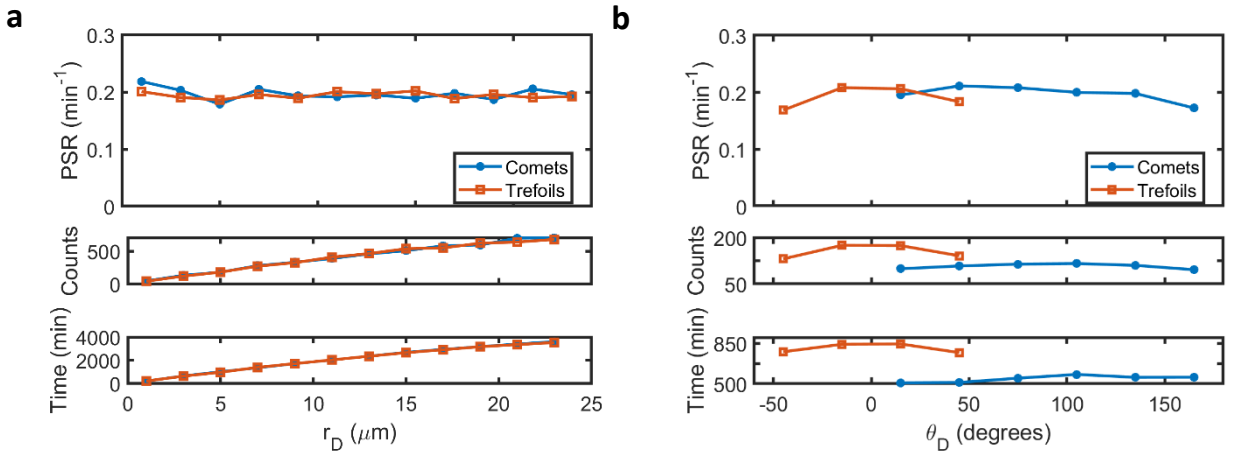

Figure 34: Pole swap rate at different positions around the defect core. Data is pooled from 15 different experimental time series containing a total of 1029 and 1051 suitable comets and trefoils respectively. (a) Pole swap rate as a function of r_{D} with the accompanying number of pole swaps and time available in each radial bin. Bin size is 2 μm. (b) Pole swap rate as a function of θ_{D} with the accompanying number of pole swaps and time available in each angular bin. Values shown have $r_{\mathrm{D}} < 12$ μm and bin size is 15°. Data shown is from the 'folded over' analysis.

As shown in **Figure 34a**, there are only very small differences in pole swap rate between comets and trefoils for all values of r_{D}. It is worth noting also that at large values of r_{D} some of the pole swaps and the amount of eligible time could potentially be counted twice when defects are in close proximity to other. Thus, we set a limit of 12 μm when investigating pole swap rate as a function of θ_{D}. As observed in **Figure 34b** the changes in pole swap rate relative to θ_{D} are very small.

As no clear trend can be identified plotting pole swap rate against distance from the defect core or the angle from the direction of defect travel, we next sought to spatially resolve pole swap rate in the area around topological defects. Following the same process used to generate the pole swap rates shown in **Figure 33**, we divided the number of pole swaps observed in each spatial bin around a defect by the total amount of eligible time in which a pole swap could occur, with the results shown in **Figure 35**.

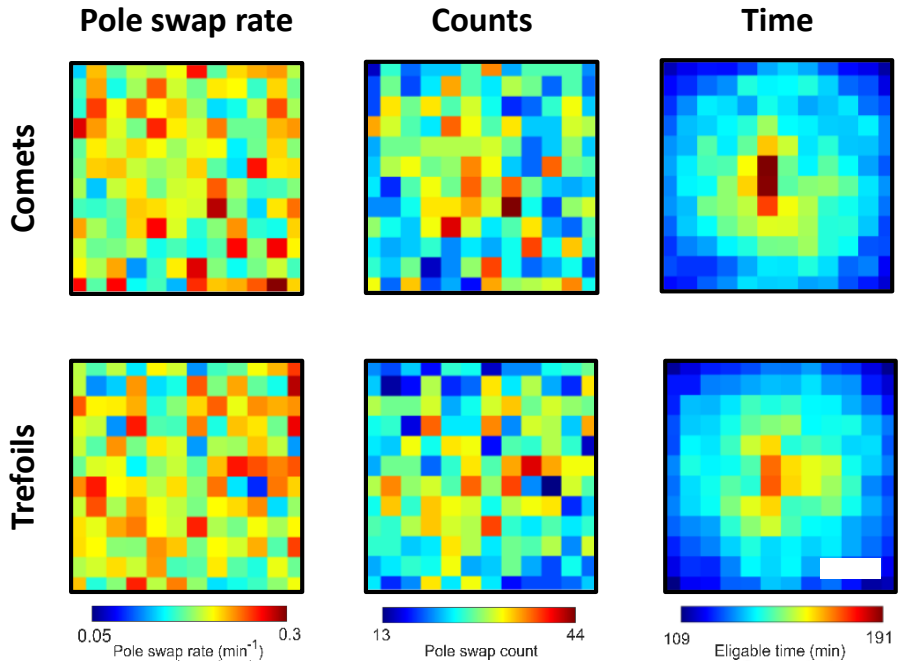

Figure 35: Resolving pole swap rate in the area surrounding topological defects for (a) $+\frac{1}{2}$ comets and $-\frac{1}{2}$ trefoils. Data displayed is the pole swap rate, pole swap count and time count. Defects are oriented in the same manner as in **Figure 21**. Plots contain data pooled across 15 different experimental time series containing 1029 and 1051 comets and trefoils respectively. Data displayed in the same bins used in our SPR model with a bin size corresponding to 4 cell widths (3.2 μm). Heatmaps show a region corresponding to a 48×48 cell widths (38.4×38.4 μm). The scale bar is 12 cell widths (9.6 μm).

As can be seen in **Figure 35**, there is no clear relationship between pole swap rate and the location surrounding a defect, the signal is too noisy for any trend to be identified. Partly, the noise could be due to the relatively small number of pole swaps found in some bins. Regardless, we cannot use these plots to draw any conclusions on the effects topological defects may have on the rate of reversal of bacteria in confluent monolayers. Instead, we considered how pole swaps might be

stimulated via alternate properties of the monolayer.

4.2.3 Individual bacterial response to collective direction of travel

A *P. aeruginosa* monolayer is comprised of rod-shaped individuals that align their orientations in the same direction as their neighbours [34]. Upon closer inspection of epifluorescence time lapses of bacterial movement in these dense collectives, it became apparent that the localisation of FimX-YFP was aligned with the direction of group travel in majority of cells (i.e. cells had the most FimX-YFP in the pole oriented in the direction of the collective movement), however, significant variability was observed and in some individuals the opposite was observed. We therefore considered the hypothesis that *P. aeruginosa* is reversing to travel with the collective, facilitating collective polar behaviour.

The first step of investigating the reversal response to collective travel is to measure bulk velocity of the collective, which we accomplished via Particle Image Velocimetry (PIV), outlined in **Section 2.7**. We then interpolated the PIV field at the location of a cell at each time point. To test if FimX-YFP does indeed accumulate more in the cell pole corresponding to the direction of collective travel, we first measured θ_{DIFF}, the angle between the orientation of FimX-YFP, $\phi_{I_{\mathrm{M}}}$, and the direction of collective travel, θ_{PIV} (**Figure 36a**). We define $\phi_{I_{\mathrm{M}}} = \phi$ when $I_{\mathrm{M}} > 0$, and $\phi_{I_{\mathrm{M}}} = \phi + \pi$ when $I_{\mathrm{M}} < 0$, where ϕ is the orientation of the cell. We then calculate θ_{PIV} using

$$\theta_{\mathrm{PIV}} = \tan^{-1} \frac{v_{\mathrm{PIV_Y}}}{v_{\mathrm{PIV_X}}},$$

where $v_{\mathrm{PIV_Y}}$ and $v_{\mathrm{PIV_X}}$ are the x and y component of collective velocity interpolated at the location of the cell. As such, it is possible to calculate the angle subtended by θ and θ_{PIV}, θ_{DIFF} as

$$\theta_{\mathrm{DIFF}} = \theta - \theta_{\mathrm{PIV}},$$

and designate each labelled cell at each time point as either aligned ($\cos(\theta_{\mathrm{DIFF}}) > 0$) or anti-aligned ($\cos(\theta_{\mathrm{DIFF}}) < 0$), relative to the direction of collective travel (**Figure 36b**). It should be noted that if $\cos(\theta_{\mathrm{DIFF}}) = 0$ at that given time the cell cannot be designated as aligned or anti-aligned and is excluded from our analyses.

With the necessary tools in place to measure FimX-YFP alignment to collective velocity, we calculate the proportion of time spent aligned to the direction of travel, binned by $|I_{\mathrm{M}}|$ and θ_{DIFF}. We bin by $|I_{\mathrm{M}}|$ rather than I_{M} since the assignment of the two cell's two poles is arbitrary at the start of tracking. The results of this analysis is shown in **Figure 36c** and **36d**. In the former, we calculate the proportion of time spent aligned to the direction of collective travel in an individual

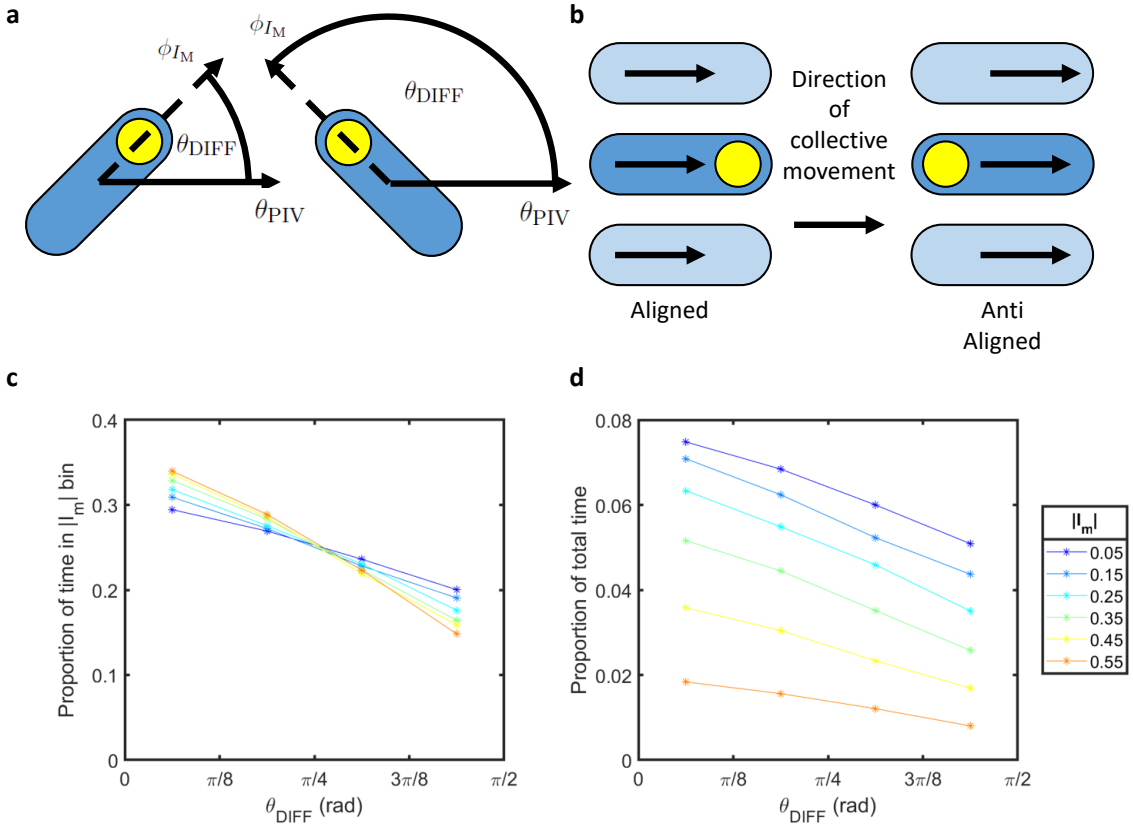

Figure 36: FimX-YFP tends to accumulate in a cell's pole that is pointed to the direction of collective travel in monolayers. Diagrams showing (a) the angles used in assigning FimX-YFP concentration asymmetry as aligned and anti-aligned and (b) when a cell is an aligned and anti-aligned state. (c) The proportion of time cells spend in each $|I_M|$ bin as a function of θ_{DIFF}. The sum of each line shown is one. (d) The proportion of time cells spend in each $|I_M|$ compared to the overall time available. The sum of all lines shown is one. Plots contain data pooled from 15 experimental time series each between two and three minutes in length. The bin size is $\frac{\pi}{8}$ radians.

$|I_M|$ bin, showing that for all values of $|I_M|$, FimX-YFP is more likely to be aligned to the orientation of bulk velocity. As $|I_M|$ increases the degree of alignment becomes greater, as the proportion of time spent aligned in small θ_{DIFF} bins ($\theta_{DIFF} < \frac{\pi}{4}$) grows. In **Figure 36d** we show the same trends but with the proportion of total time. Overall, these results imply that the stronger the FimX-YFP asymmetry, the more likely an individual is to be aligned with the direction of collective travel.

We have now quantitatively proven that the cells align their direction of travel with that of the collective, and now we will investigate whether there is any difference in pole swap rate when a cell is aligned or anti-aligned depending on its FimX-YFP polarisation relative to the direction of collective travel. In **Figure 37a**, we show an example of a *P. aeruginosa* cell in a monolayer whose FimX-YFP is initially anti-aligned to the direction of collective travel. It can be observed to perform a pole swap so that it becomes aligned with the movement of the group. As seen in the time series of θ_{DIFF} in **Figure 37b**, a pole swap as expected causes a large change in θ_{DIFF}. We can categorise pole swaps as being either aligned or anti-aligned depending on the cell's FimX-YFP localisation before the pole

swap. Aligned pole swaps occur when $\cos\theta_{\mathrm{DIFF}} > 0$ before the pole swap, whereas anti-aligned pole swaps occur when $\cos\theta_{\mathrm{DIFF}} < 0$. The aligned and anti-aligned pole swap rate can thus calculated by counting the number of pole swaps of either type, and dividing by the total eligible time that cells spend moving in either an aligned or anti-aligned state. We have processed each time lapse separately and shown the bulk, aligned and anti-aligned pole swap rate in **Figure 37c**. These box plots indicate that the aligned pole swap rate is suppressed relative to that of the bulk (which includes all cells in both aligned and anti-aligned states), and the anti-aligned rate is elevated relative to that of the bulk. The mean bulk, aligned and anti-aligned pole swap rates are 0.19 ± 0.01 min^{-1}, 0.16 ± 0.01 min^{-1} and 0.24 ± 0.01 min^{-1} respectively (error values are the standard error of the mean between the experimental time series), showing a 51.4% difference between the aligned and anti-aligned states. Here we have presented the first evidence that *P. aeruginosa* deliberately biases its reversal rate to move in the direction of collective movement. However, the relationship between cell orientation and pole swap rate can be probed further.

We now seek to move away from the discrete nature of aligned and anti-aligned states, and instead analyse how the pole swap rate continuously varies with θ_{DIFF}. Therefore, we bin the amount of eligible time and the number of pole swaps by $\cos\theta_{\mathrm{DIFF}}$ in the pooled data sets. We find that the pole swap rate decreases linearly with $\cos\theta_{\mathrm{DIFF}}$ (**Figure 37d**), suggesting that cells become progressively more likely to reverse as the direction of the FimX-YFP localisation rotates away from the direction of collectively motility. Here we have shown that pole swap rate varies continuously with $\cos\theta_{\mathrm{DIFF}}$, but this does not consider the magnitude of collective velocity which also could potentially affect the pole swap rate.

By measuring the projection of collective velocity in the direction of FimX-YFP asymmetry, we will be able to consider when cell movement is with the group or against it, depending on if the projection of collective velocity ($\boldsymbol{p}_{\mathbf{FimX}} \cdot \boldsymbol{v}_{\mathbf{PIV}}$) is positive or negative respectively. To completely describe this phenomenon, we will also investigate the projection of single cell velocity in the direction of FimX-YFP localisation ($\boldsymbol{p}_{\mathbf{FimX}} \cdot \boldsymbol{v}_{\mathbf{CELL}}$). $\boldsymbol{p}_{\mathbf{FimX}} \cdot \boldsymbol{v}_{\mathbf{CELL}}$ and $\boldsymbol{p}_{\mathbf{FimX}} \cdot \boldsymbol{v}_{\mathbf{PIV}}$ are calculated through **Equations 25** and **26**

$$\boldsymbol{p}_{\mathbf{FimX}} \cdot \boldsymbol{v}_{\mathbf{CELL}} = v_{\mathrm{MAG}} \cos\left(\phi_{I_{\mathrm{M}}} - \theta\right), \tag{25}$$

$$\boldsymbol{p}_{\mathbf{FimX}} \cdot \boldsymbol{v}_{\mathbf{PIV}} = v_{\mathrm{PIV}_{\mathrm{MAG}}} \cos\left(\phi_{I_{\mathrm{M}}} - \theta_{\mathrm{PIV}}\right), \tag{26}$$

where $\boldsymbol{p}_{\mathbf{FimX}}$ donates a unit vector pointing along the direction of $\phi_{I_{\mathrm{M}}}$, and the magnitude of collec-

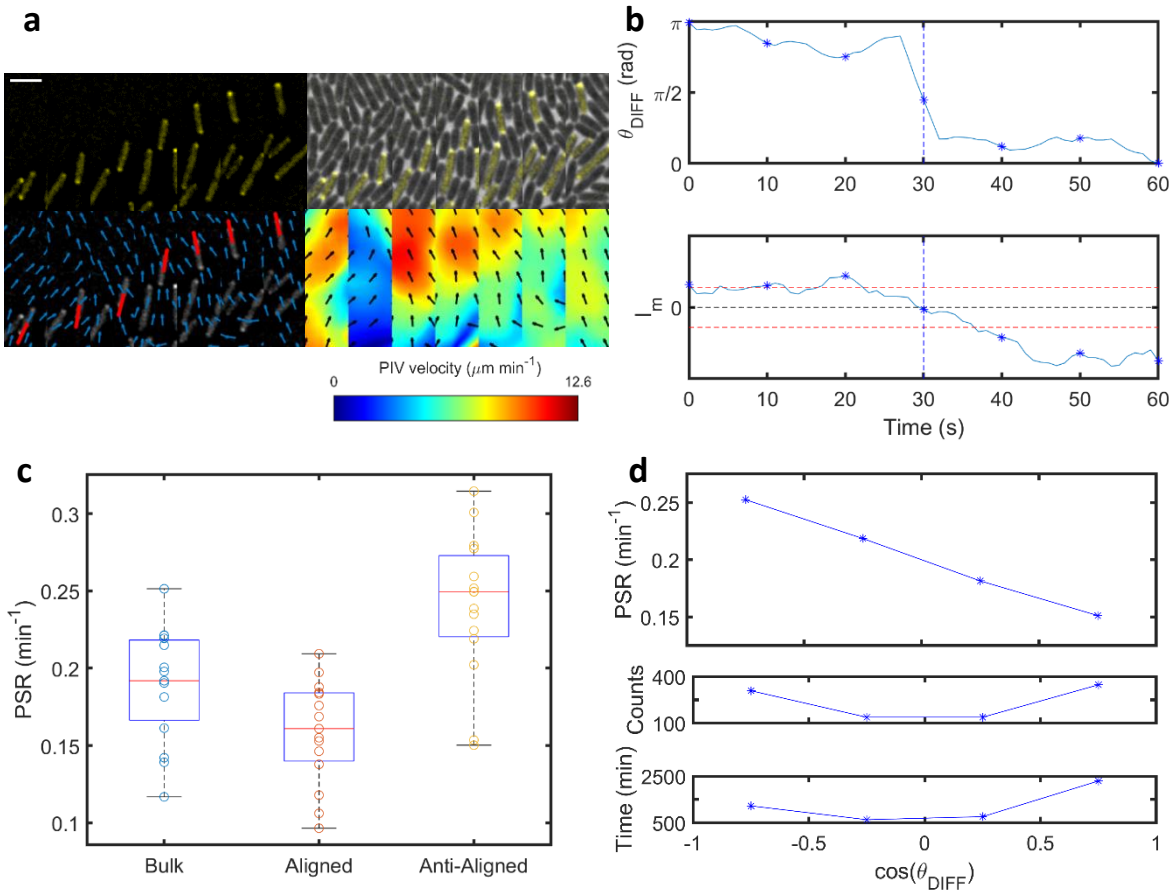

Figure 37: FimX-YFP pole swaps align bacterial movement with the direction of collective travel. (a) Images show the (top left) epifluorescence channel (scale bar is 3 µm), (top right), a merge epifluorescence and phase image, (bottom left) epifluorescence channel overlaid with blue arrows interpolated at cell locations showing PIV direction with a large red marker highlighting the FimX-YFP orientation for the cell under examination, (bottom right) colours indicate the magnitude of PIV field shown and black arrows indicating PIV direction interpolated over a 2 µm spaced grid. (b) Time series of θ_{DIFF} and I_{M} for images shown in (a). The pole swap is shown as a vertical dashed blue line and I_{M} thresholds are shown with red dashed horizontal lines. Blue markers along the time series are at the time points shown in the above montage in (a). (c) Box plots displaying the bulk, aligned and anti-aligned pole swap rates. Data comes from 15 different experimental time series with each circle representing one time lapse. The red line is the median and the bounds of the boxes represent the 25th to 75th quartile. A paired t-test that compares the aligned and anti-aligned pole swap rates rejected the null hypothesis that there is no difference in rate between the two states with $p = 2.99 \times 10^{-7}$. (d) Pole swap rate as a function of θ_{DIFF} with the accompanying number of pole swaps and available time for labelled cells. Bin size is 0.5.

tive velocity, $v_{\mathrm{PIV_{MAG}}}$, can be calculated from the x and y components of the PIV field:

$$v_{\mathrm{PIV_{MAG}}} = \sqrt{v_{\mathrm{PIV_x}}^2 + v_{\mathrm{PIV_y}}^2}.$$

Intuitively, when $\boldsymbol{p}_{\mathbf{FimX}} \cdot \boldsymbol{v}_{\mathbf{CELL}} > 0$, we expect that a cell already is pulling itself towards its pole with the greatest FimX-YFP concentration, whereas when $\boldsymbol{p}_{\mathbf{FimX}} \cdot \boldsymbol{v}_{\mathbf{CELL}} < 0$ it is moving in the opposite direction. Analogously, for $\mathbf{p}_{\mathbf{FimX}} \cdot \mathbf{v}_{\mathbf{PIV}} > 0$, the individual cell is pulling itself with the

direction of collective velocity, and against it for $\boldsymbol{p}_{\mathbf{FimX}} \cdot \boldsymbol{v}_{\mathbf{PIV}} < 0$. We observe that $\boldsymbol{p}_{\mathbf{FimX}} \cdot \boldsymbol{v}_{\mathbf{CELL}}$ is typically larger in magnitude than $\boldsymbol{p}_{\mathbf{FimX}} \cdot \boldsymbol{v}_{\mathbf{PIV}}$ (see **Figure 38a**), because individual cells tend of jiggle back and forth as they move, but the movement of the collective is much more steady in time. However the PDF of both velocity projections is biased towards positive values, as collective FimX-YFP asymmetry is pointed towards the direction of collective travel (**Figure 36**) and that cells twitch towards their pole with the largest FimX-YFP concentration (**Figure 29**), therefore, $\cos(\phi_{I_M} - \theta)$ and $\cos(\phi_{I_M} - \theta_{\mathrm{PIV}})$ have an increased probability of being positive than negative.

With the two velocity projections defined, we calculate pole swap rate by counting the number of pole swaps and dividing by the amount of eligible time in each velocity projection bin, pooling data across all 15 experimental time lapses (**Figure 38b**).

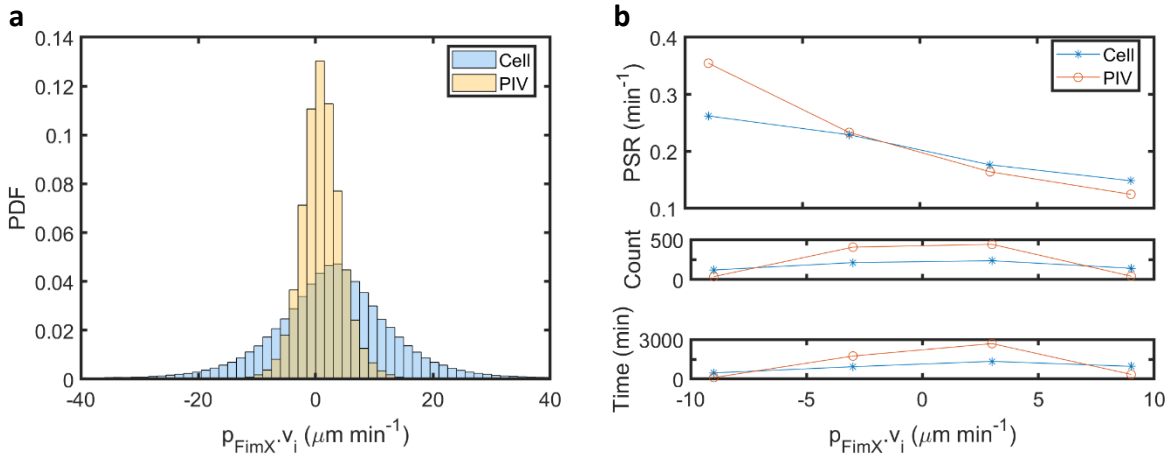

Figure 38: *P. aeruginosa* increases pole swap rate when moving against the direction of collective travel. (a) Histogram showing the PDF of velocity projection for cell and PIV velocity. Bin size is 1.5 μm min^{-1}. (b) Pole swap rate as a function of the cell and PIV velocity projection, along with the accompanying pole swap count and eligible time plots. Data shown has been pooled across the 15 experimental time series each between two and three minutes in length. All bins displayed contain more than 20 minutes of data. Bin size is 6 μm min^{-1}.

We observe similar trends for both $\boldsymbol{p}_{\mathbf{FimX}} \cdot \boldsymbol{v}_{\mathbf{CELL}}$ and $\boldsymbol{p}_{\mathbf{FimX}} \cdot \boldsymbol{v}_{\mathbf{PIV}}$ in **Figure 38b**, which are consistent with our previous observations that that *P. aeruginosa* tends to bias its movement so that it tends to move in the same direction of the collective. We observe that an increase in the positive values of $\boldsymbol{p}_{\mathbf{FimX}} \cdot \boldsymbol{v}_{\mathbf{PIV}}$ result in increased suppression of pole swap rate, and as $\boldsymbol{p}_{\mathbf{FimX}} \cdot \boldsymbol{v}_{\mathbf{PIV}}$ becomes more negative, the pole swap rate increases rapidly. Our results indicate that *P. aeruginosa* cells increase their likelihood of reversing direction as the proecjtion of collective velocity along the axis of their pole with the most FimX-YFP decreases. This suggests they use mechanosensing to actively sense their differential movement relative to their neighbours.

We began this section with visual evidence that *P. aeruginosa* appears to move with the collective direction of travel obtained by inspecting the orientation of intracellular FimX-YFP asymmetry in a

bacterial monolayer. The orientation of individual twitching motility can change drastically through a reversal of direction along the long axis of a cell, and coincides with FimX-YFP pole swaps. By categorising the orientation of FimX-YFP concentration asymmetry relative to the direction of collective travel, we were able to categorise each cell into two states: aligned or anti-aligned. We found that on average *P. aeruginosa* spends more time with FimX-YFP aligned rather than anti-aligned with the collective. Furthermore, we determined the pole swap rate for these two discrete categories, finding that relative to the bulk, the anti-aligned rate was elevated more than the suppression seen for the aligned case. We sought to investigate any potential continuous relationship that exists, and determined the pole swap rate as a function of θ_{DIFF}, which shows a linear relationship, where the rate of reversal decreased with $\cos\theta_{\mathrm{DIFF}}$. Finally, we incorporated an essential component to this process, the collective velocity, by calculating the pole swap rate relative to the projection of bulk speed along the orientation of FimX-YFP asymmetry. Here we see the same suppression and elevation when the cell is aligned or anti-aligned, where the extent of reversal rate increase is larger than the decrease, resulting in a non-linear relationship. Ultimately, these results show that *P. aeruginosa* uses reversals to ensure it travels with the direction of collective movement, by increasing reversal rate when moving against the group and suppressing it when migrating with the flow. Here we have shown that collective polar behaviour can be driven by a biological process that appears to be stimulated by a physical property of the system.

4.2.4 Pole swaps at the colony edge

In **Section 3.2.3** we showed that *P. aeruginosa* cells at the colony border from groups that exhibit alignment of their cell bodies and velocity whilst expanding into previously untouched surface. Cells in these groups exhibit collective polarisation of FimX-YFP in the direction of expansion. Therefore, we considered if biased reversals are also used in this region of the growing biofilm as a means to drive collective polar behaviour and possibly, expansion.

First, we measure the collective velocity using PIV and determine how the alignment of FimX-YFP localisation varies as a function of alignment to collective velocity, and FimX-YFP asymmetry. As done previously in **Section 3.2.3**, only cells within 40 μm of the edge are considered for analysis. We restrict our analysis to this distance into the colony as beyond this cells move more rapidly and in many different directions, whereas closer to the edge nearly all cells move in the direction of colony expansion (see the left-hand side of phase images in **Figure 25**). **Figure 39a** highlights the velocity field obtained by PIV for the section of the colony border that is analysed (**Figure 25**). An example of a pole swap at the colony border, and the corresponding θ_{DIFF} time series is shown in **Figure**

39b and **c** respectively. In **Figure 39d**, we investigate the proportion of time cells spend aligned to θ_{PIV}, and we find greater degrees of alignment of $\phi_{I_{\mathrm{M}}}$ with θ_{PIV} than in the monolayer, as the gradient of each line is steeper. When comparing time in each $|I_{\mathrm{M}}|$ bin, we see the same trend as the monolayer where cells spend most of their time at small values of θ_{DIFF}. When considering the proportion of total time cells spend at different strengths of FimX-YFP polarisation (**Figure 39e**), we can conclude that cells at the colony edge are in a more polarised state in the monolayer, as a greater proportion of time is spent at large $|I_{\mathrm{M}}|$ values. In general, we observe that *P. aeruginosa* is in a more polarised state at the colony border compared to that observed in the monolayer. Next we investigate how pole swap rate varies with the projection of collective velocity in the direction of FimX-YFP polarisation.

We will employ the same methodology that we used in the monolayer to determine the bulk, aligned and anti-aligned pole swap rates, the relationship between the rate of reversal and θ_{DIFF}, and how the projection of collective velocity along $\phi_{I_{\mathrm{M}}}$ can influence pole swap rate. Additionally, by identifying the position of the colony border and the coordinates of each cell within that frame of reference, the rate of reversal as a function of distance from the colony border will be quantified.

The overall bulk, aligned and anti-aligned pole swap rates are shown in **Figure 40a**. The same trends identified in the monolayer are also found in the colony edge, the aligned rate is suppressed relative to the bulk, but the frequency of anti-aligned reversals is increased, resulting in mean values of 0.10 ± 0.01 min^{-1}, 0.08 ± 0.01 min^{-1} and 0.16 ± 0.02 min^{-1}. Although the absolute rates are reduced, the percentage difference between the aligned and anti-aligned rate is 97.1%, which is approximately twice as large as the difference observed in the monolayer. We will discuss potential mechanisms behind this larger difference in **Section 4.2.5**. Considering the relationship between pole swap rate and θ_{DIFF}, we also observed the same trend identified in the monolayer, namely that as $\cos\theta_{\mathrm{DIFF}}$ increases from -1 to 1, pole swap rate decreases. Given we visually observe a decrease in the cohesion of cell body orientation with increasing distance from the colony border, we sought to determine the pole swap rate as a function of distance from the colony border, d_{CB} (**Figure 40c**). To determine the pole swap rate, the number of pole swaps and the total eligible time within each d_{CB} bin was counted, subsequently the former divided by the latter. We are able to split the number of pole swaps and eligible time into aligned and anti-aligned based on the orientation of FimX-YFP relative to the direction of collective travel, that is often oriented in the direction of colony expansion (**Figure 40a**). If a pole swap is termed aligned it occurs when a cell's FimX-YFP distribution if most concentrated toward the direction of expansion, and vice versa for the anti-aligned pole swaps. Aligned time is the amount of time cells spend with FimX-YFP asymmetry oriented towards colony expansion, and

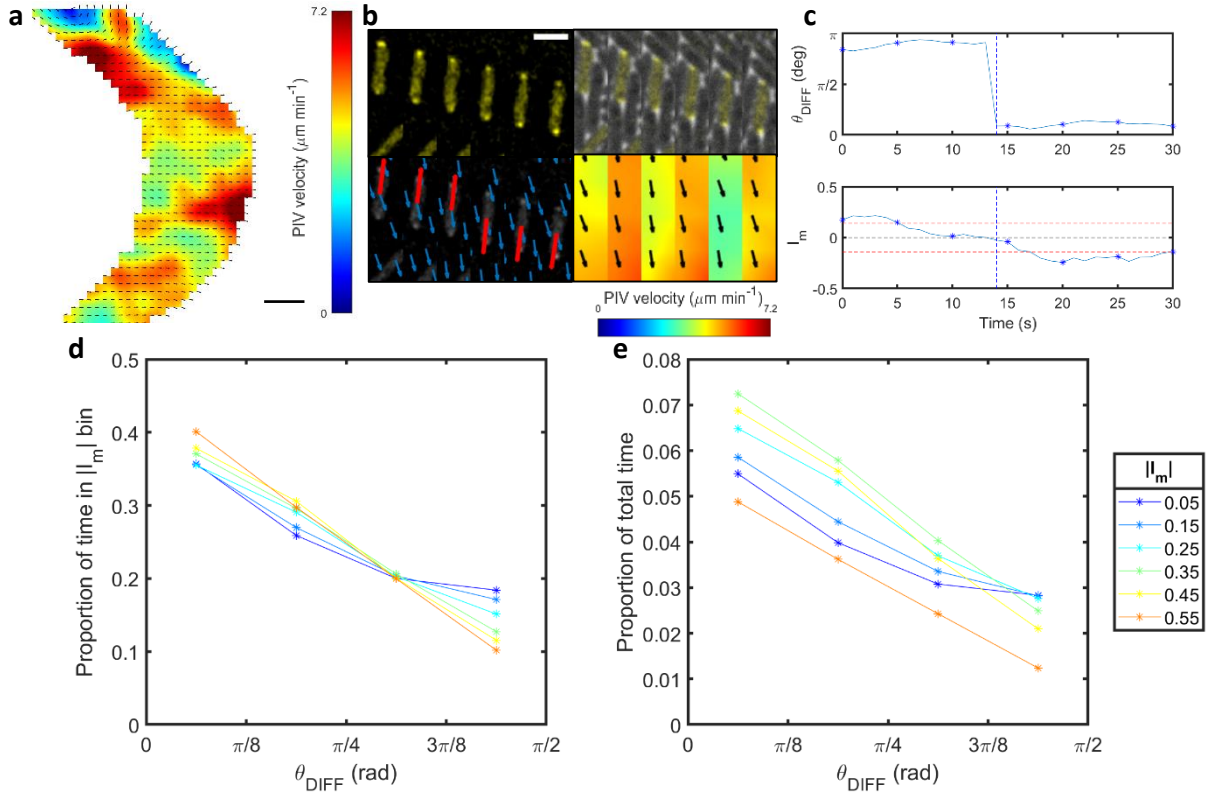

Figure 39: Pole swaps occur at the colony edge which is highly polarised in the direction of colony expansion. (a) Heatmap displaying the magnitude of collective velocity within 30 μm from the colony border, with arrows indicating the direction of group travel. Scale bar is 10 μm. (b) Montages showing a cell undergoing a pole swap and PIV direction and magnitude properties at the colony edge. Images show the (top left) epifluorescence channel (scale bar is 2 μm), (top right), a merged epifluorescence and phase image, (bottom left) epifluorescence channel overlaid with blue arrows interpolated at cell locations showing PIV direction with a large red marker highlighting the FimX-YFP orientation for the cell under examination, (bottom right) colours indicate the magnitude of PIV field shown and black arrows indicating PIV direction interpolated over a 2 μm spaced grid. (c) Time series of θ_{DIFF} and I_{M} as a function of time time for the cell in (b). (d) The proportion of time cells spend with FimX-YFP polarisation aligned in the direction of collective movement within each $|I_{\mathrm{M}}|$ bin, binned by θ_{DIFF}. Bin size is $\frac{\pi}{8}$ rad. Data shown is taken from 24 three minute long experimental time series. The sum of each line shown is one. (e) The proportion of time cells spend with FimX-YFP polarisation aligned to the direction of collective movement overall, binned by binned by θ_{DIFF}. The sum of all lines shown is one. Angular bin size is $\frac{\pi}{8}$ rad.

anti-aligned time is the opposite. We observed a relatively constant rate of reversal through the group at the colony border, with the anti-aligned rate of reversal being consistently greater than those considered aligned.

Finally, we explore how pole swap rate is influenced by the projection of collective velocity in the direction of FimX-YFP asymmetry for bacteria moving in tightly packed groups at the colony border (**Figure 40d**). We observed similar results to that found in the monolayer, with pole swap rate decreasing as the projection of collective velocity increases from negative to positive. Again, these results show that *P. aeruginosa* is actively biasing its rate of reversal to travel in the direction of

group motion, depending on if it is moving with against the collective, and the speed of the collective movement.

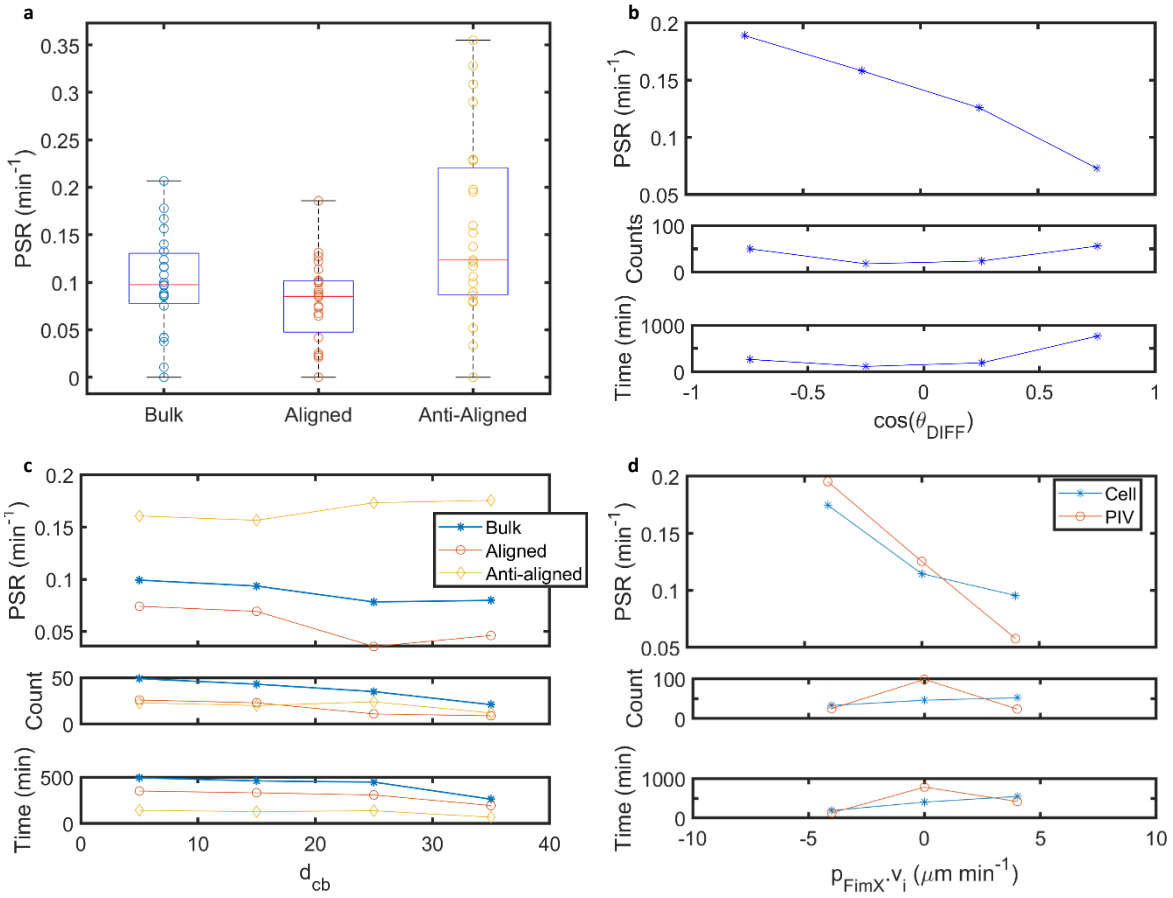

Figure 40: Pole swaps at the colony edge align twitching motility to the direction of expansion. (a) Box plots of bulk, aligned and anti-aligned pole swap rate calculated from θ_{DIFF} where each circle represents one time lapse series. The red line is the median and the box represents the interquartile range of bulk, aligned and anti-align pole swap rate measured in experimental time-series. Data comes from 24 experimental time series. Values below 1.5× the interquartile range minus the 25th percentile and above the 1.5× the interquartile range plus the 75th percentile are considered outliers and therefore removed. A paired t-test that compares aligned and anti-aligned rates rejected the null hypothesis that there is no difference in rate between the two states with $p = 3.2 \times 10^{-4}$. (b) Pole swap rate as a function of θ_{DIFF}. Bin size is 0.5. (c) Pole swap rate as a function of d_{CB} pooled across the time lapses. Data has been split into a bulk rate, aligned and anti-aligned categories with a bin size of 10 µm. Data 40 µm from the colony border is included. (d) Pole swap rate as a function of $\boldsymbol{p}_{\mathbf{FimX}} \cdot \boldsymbol{v}_{\mathbf{CELL}}$ and $\boldsymbol{p}_{\mathbf{FimX}} \cdot \boldsymbol{v}_{\mathbf{PIV}}$. Data has been pooled across the time lapses and a bin size of 3 µm min^{-1} has been used. Only bins containing more than 30 minutes worth of data are shown.

Here we have presented three different methods of measuring the rate of reversal of *P. aeruginosa* using intracellular FimX-YFP pole swaps whilst travelling in densely packed monolayers, and at the colony edge. By calculating the angle that subtends the orientation of I_{M} and the direction of collective travel, we were able to calculate the pole swap rate as a function of whether the cell is aligned or anti-aligned with the direction of collective travel. We found that the reversal rate is suppressed relative to the bulk when FimX-YFP polarisation is aligned, and elevated when anti-aligned with the

direction of the collective. We go on to develop a continuous relationship between pole swap rate and FimX-YFP orientation relative to collective movement, showing that an increased angle of separation causes an increase in pole swap rate. Finally, the magnitude of collective velocity experienced by the cell is considered, with anti-aligned individuals in regions of rapid bulk movement reversing direction of travel at a much larger rate then those in the equivalent aligned region. Ultimately, we have shown that in both the monolayer and colony edge, *P. aeruginosa* reverses its direction of travel to move with its neighbours, or to 'go with the flow', facilitating polarisation of the collective. In the upcoming section, we will directly compare the relationships outlined previously between the monolayer and colony edge.

4.2.5 Pole swap rate comparison between different experimental scenarios

In this chapter, we investigated how *P. aeruginosa* uses biased reversals to align twitching motility with the direction of collective travel in densely packed monolayers and groups at the edge of colonies. As previously alluded to in **Section 4.2.4**, we see a decrease in the overall rate of pole swaps at the colony edge relative to the monolayer, but an increase in the percentage change between the aligned and anti-aligned rate. Here, we directly compare the properties that underpin the relationship between pole swap rate and collective velocity projection on the cell. Our rationale behind presenting these results side by side is to glean a better understanding of what causes the differing trends in pole swap rate between the two densely packed environments.

Before delving into our results it is worth noting that chemotaxis is unlikely to be a cause of the increased polarisation or elevation in aligned and anti-aligned rate percentage change seen in the monolayer relative to the colony edge. The colony, of which only a small proportion at the centre is multilayered, is growing at the interface between glass and an approximately 2 mm thick slab of LB agar, the contains a vast amount of nutrients. Therefore, the nutrient gradients that exist at the periphery of more mature biofilms [174] likely do not arise in the monolayer or the colony edge observed here.

First, we consider how the pole swap rate varies between the two environments as a function of the angle subtended between the direction of FimX-YFP polarisation and direction of collective movement. In **Figure 41a**, we see that at all values of θ_{DIFF}, that the monolayer pole swap rate is above the corresponding value at the colony edge. Additionally, as $\cos\theta_{\mathrm{DIFF}}$ decreases, the rate of reduction in pole swap rate in both environments is similar aside from the largest bin for the colony edge. A similar trend is observed for the trends in pole swap rate as a function of $\boldsymbol{p}_{\mathbf{FimX}} \cdot \boldsymbol{v}_{\mathbf{PIV}}$ in **Figure 41c**, the rate of pole swapping is larger in the monolayer, however, cells at the colony edge

exhibit a larger range of pole swap rates, which can be observed as an increase in the slope.

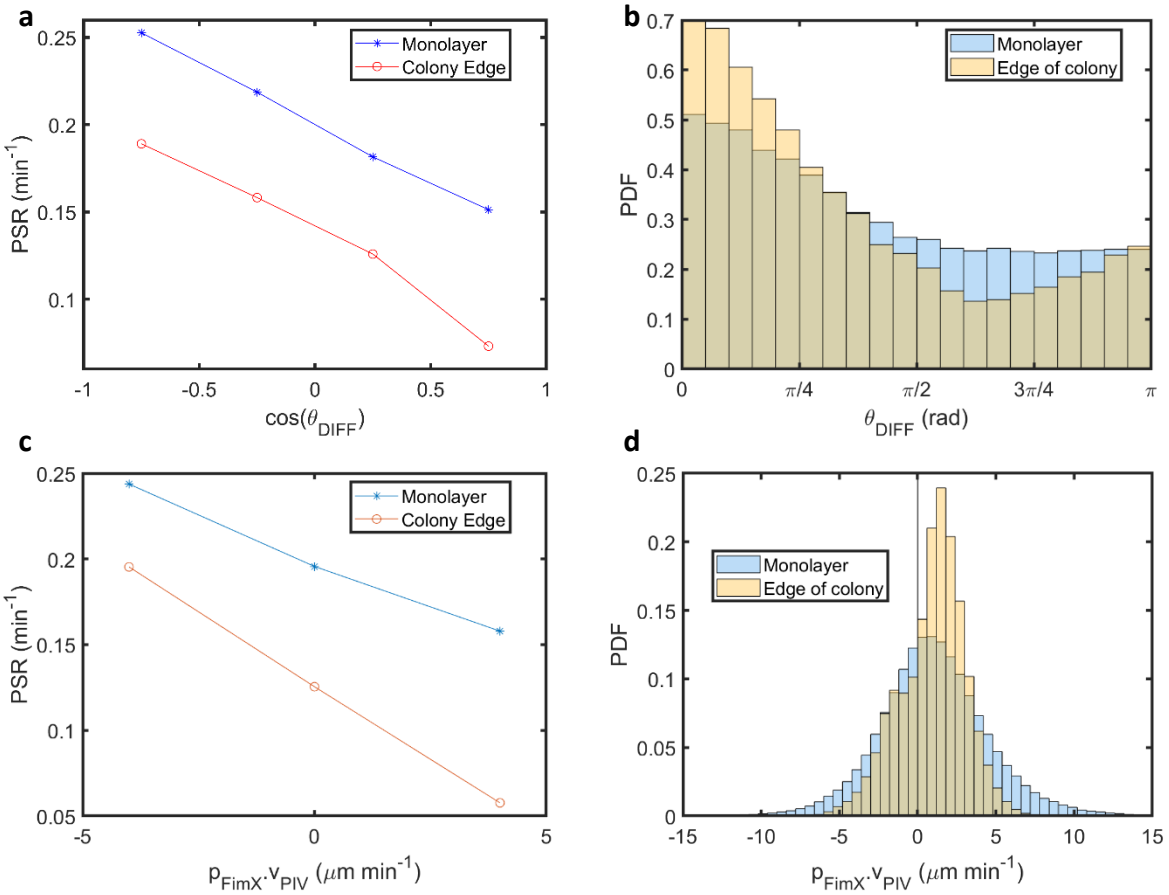

Figure 41: A comparison of the pole swap rate in the monolayer and colony border using θ_{DIFF} and PIV velocity projection. Monolayer and colony edge data comes from 15 and 24 experimental time series respectively. (a) Pole swap rate as a function of $\cos\theta_{\mathrm{DIFF}}$. Bin size is 0.5 and the shaded region indicates the standard error across the 15 and 24 time lapses respectively. (b) PDF histogram of θ_{DIFF}, bin size is 0.05π radians. (c) Pole swap rate as a function of $\boldsymbol{p_{\mathbf{FimX}}} \cdot \boldsymbol{v_{\mathbf{PIV}}}$. Bin size is 3 μm min^{-1}. (d) PDF histogram of PIV velocity projection values, bin size is 0.6 μm min^{-1}. The black line indicates where the projection equals zero.

Although there may be other factors that influence the rate of pole swapping, our explanation for the elevation in pole swap rate in the monolayer compared to the colony edge is due to the constant mixing of cells with differing orientations in the former. When domains of cells with like orientations collide with one another the physical interactions between cells causes their bodies to turn. The presence of domain mixing in the monolayer means rotational diffusion is increased compared to the colony edge (**Figure 28b**), which leads to a flatter distribution of θ_{DIFF} (**Figure 41b**). Although translational movement is more ballistic at the colony edge compared to the monolayer (**Figure 28a**), cells in the monolayer move at larger speeds (**Figure 8b**). The reduced speed and more directed movement at the colony edge leads to a larger mean value of $\boldsymbol{p_{\mathbf{FimX}}} \cdot \boldsymbol{v_{\mathbf{PIV}}}$ (**Figure 41d**), however cells in the monolayer are more likely to have extreme values of $\boldsymbol{p_{\mathbf{FimX}}} \cdot \boldsymbol{v_{\mathbf{PIV}}}$ due to their increased velocity, which leads to an increased rate of pole swapping. We propose that the increased

probability of cells in the monolayer experience entering the regime where $\boldsymbol{p}_{\mathbf{FimX}} \cdot \boldsymbol{v}_{\mathbf{PIV}} < 0$ more frequently, is due to the greater chance of a cell entering a domain that is moving in the opposing direction of twitching motility, or a cell at the interface between two domains travelling in opposing directions.

4.2.6 Do individuals benefit from reversing in dense collectives?

Throughout **Section 4.2** we have focused on how *P. aeruginosa* regulates its movement behaviour and how this effects collective polar behaviour in a bacterial monolayer and at the colony edge. We anticipate that polarised movement enables colony expansion to occur more rapidly, allowing cells to benefit from increased access to both space and nutrients [147]. Having proposed a benefit that biased reversals of direction can have on the collective, we sought to understand how they might be advantageous for individual cells to use.

We can calculate the projection of cell movement in the direction of collective travel, to investigate if an individual benefits from moving with the collective. We expect that cells deliberately twitching in the direction of collective movement will enhance the spread of colonies. If twitching in the opposite direction, an individual runs the risk of moving towards the centre of the colony which, at later times, will be depleted of nutrients. To investigate how the cell velocity in the direction of collective movement changes before and after a pole swap. We calculate the projection of cell velocity in the direction of collective movement at each time point in a cells trajectory,

$$\boldsymbol{p}_{\mathbf{PIV}} \cdot \boldsymbol{v}_{\mathbf{CELL}} = v_{\mathrm{MAG}} \cos\left(\theta_{\mathrm{PIV}} - \theta\right), \tag{27}$$

where $\mathbf{p}_{\mathbf{PIV}}$ is a unit vector pointing in the direction of group travel interpolated at the cell.

As each pole swap has a corresponding value of $\boldsymbol{p}_{\mathbf{FimX}} \cdot \boldsymbol{v}_{\mathbf{PIV}}$, we bin values of $\boldsymbol{p}_{\mathbf{PIV}} \cdot \boldsymbol{v}_{\mathbf{CELL}}$ that occur 15 seconds before and after the pole swap according to $\boldsymbol{p}_{\mathbf{FimX}} \cdot \boldsymbol{v}_{\mathbf{PIV}}$, and subsequently take the average. We have chosen a window of 15 seconds before and after a pole swap is detected as by visual inspection the relocalisation of FimX-YFP is complete in this time. Additionally, increasing the timescale of this window would reduce the number of events eligible for analysis because we want to have a full 15 seconds before and after a pole swap, and increasing this window would mean a larger proportion of pole swaps close to the start and end of the 180 second experimental time lapse would not be included in our analyses. The results of averaging $\boldsymbol{p}_{\mathbf{PIV}} \cdot \boldsymbol{v}_{\mathbf{CELL}}$ pre and post pole swap as binned by $\boldsymbol{p}_{\mathbf{FimX}} \cdot \boldsymbol{v}_{\mathbf{PIV}}$ are shown in **Figure 42a**. If $\boldsymbol{p}_{\mathbf{FimX}} \cdot \boldsymbol{v}_{\mathbf{PIV}}$ is negative when a pole swap occurs it is considered as correct, as it causes an anti-aligned cell to align its direction of twitching motility with the collective. Similarly if $\boldsymbol{p}_{\mathbf{FimX}} \cdot \boldsymbol{v}_{\mathbf{PIV}}$ is positive when a pole swap happens it is

considered incorrect, and causes a cell previously twitching with the direction of collective movement to now move against it.

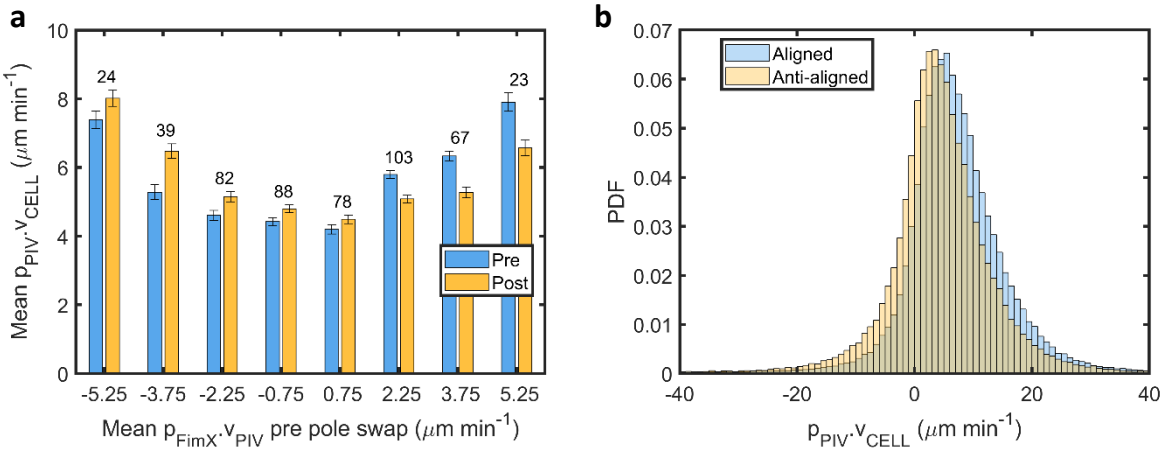

Figure 42: *P. aeruginosa* is rewarded and punished by reversing correctly and incorrectly respectively. Data shown comes from 15 experimental time series of confluent monolayers. (a) Mean cell velocity projection in the direction of the collective vs bulk velocity projected along ϕ_{I_M} ($\boldsymbol{p_{PIV}} \cdot \boldsymbol{v_{CELL}}$ as a function of $\boldsymbol{p_{FimX}} \cdot \boldsymbol{v_{PIV}}$) pre and post pole swap. The number of pole swaps is shown above each bar, with the accompanying standard error in each $\boldsymbol{p_{FimX}} \cdot \boldsymbol{v_{PIV}}$ bin shown. Bin size is 1.5 µm min^{-1} within the range -6 µm min$^{-1} \leq \boldsymbol{p_{FimX}} \cdot \boldsymbol{v_{PIV}} \leq 6$ µm min^{-1}. This range has been chosen as the number of pole swaps is limited as $|\boldsymbol{p_{FimX}} \cdot \boldsymbol{v_{PIV}}|$ increases. (b) Velocity of the cell projected in the direction of collective movement for aligned and anti-aligned cells based on the orientation of largest FimX-YFP concentration. Bin size is 1 µm min^{-1}.

The main result from **Figure 42a** is that correct pole swaps are rewarded by moving more rapidly and incorrect pole swaps are penalised by experiencing a decrease in their velocity. The increases in $\boldsymbol{p_{PIV}} \cdot \boldsymbol{v_{CELL}}$ after a correct pole swap are often smaller than the decreases that occur due to an incorrect pole swap, implying that there is a larger penalty for making the incorrect choice than being rewarded for acting correctly. It is worth noting however, that even though there is a decrease in $\boldsymbol{p_{PIV}} \cdot \boldsymbol{v_{CELL}}$ for bacteria reversing direction to twitch against the collective, cell velocity is still aligned to the direction of collective movement as shown by the positive $\boldsymbol{p_{PIV}} \cdot \boldsymbol{v_{CELL}}$ values post pole swap for all $\boldsymbol{p_{FimX}} \cdot \boldsymbol{v_{PIV}}$. As $\boldsymbol{p_{PIV}} \cdot \boldsymbol{v_{CELL}}$ is positive this means on average the cells will still move with the collective, arising from the fact that a single cell twitching against its neighbours is not able to exert enough force move in a direction opposite to that of its neighbours [175].

As these mean values have obscured finer details on the behaviour of single cells pre and post pole swap, we plot a histogram of all $\boldsymbol{p_{PIV}} \cdot \boldsymbol{v_{CELL}}$ values split into two populations, aligned and anti-aligned according to when $\boldsymbol{p_{FimX}} \cdot \boldsymbol{v_{PIV}}$ is positive and negative, as seen in **Figure 42b**. Here we observed that both aligned and anti-aligned cells have positive mean values of $\boldsymbol{p_{PIV}} \cdot \boldsymbol{v_{CELL}}$, 6.9 µm min^{-1} and 4.4 µm min^{-1} respectively, which is to be expected as cells twitching in the opposing direction to collective movement will still be swept along with the bulk. The key difference is that

those anti-aligned cells are more likely to be twitching against the collective and actually moving against it, as shown by the greater proportion of cells with negative $\boldsymbol{p}_{\mathbf{PIV}} \cdot \boldsymbol{v}_{\mathbf{CELL}}$ in the anti-aligned population. In fact, if a cell is anti-aligned relative to the direction of collective movement, it is 65% more likely to be travelling in the opposite direction of its neighbours than those that are aligned. Given cells with FimX-YFP anti-aligned to the direction of collective movement are more likely to be travelling in the opposing direction to their neighbours, or more slowly, we conclude that these results are consistent with reversals allowing cells to collectively move faster in the monolayer. Faster collective moment facilitates nutrient transport through active turbulence, benefiting the colony and individual through a more even nutrient destitution throughout the colony [147].

4.3 Discussion

In **Chapter 3** we show that surface-attached *P. aeruginosa* cells tend to twitch towards their pole with largest FimX-YFP concentration in both low cell densities and in densely packed collectives. Rod shaped bacterial monolayers contain half integer charged topological defects, in which we observed collective FimX-YFP polarisation in the direction of travel of comets, and along the outflowing spokes of trefoils [34]. FimX-YFP localises at greater concentrations in the pole of *P. aeruginosa* closest to the colony edge when in groups of cells displaying large degrees of orientational alignment near the border, which expand outward into untouched surface. As we are using FimX-YFP localisation as a proxy for cell movement, its bulk polarisation in topological defects and at the colony edge is evidence of collective polar behaviour. Bacterial monolayers have previously been thought of as an active matter system comprised of agents that are modelled using the equations of active nematics, assuming that cells cannot preferentially exert a force in the same direction as their neighbours [15, 138]. As **Chapter 3** presents evidence of FimX-YFP polarisation in densely packed conditions, we sought to investigate whether polar behaviour could be triggered by bacteria actively regulating their movement behaviour.

Having built a robust analysis pipeline to investigate collective FimX-YFP polarisation in dense collectives, we expanded on this through the addition of FimX-YFP pole swap and bacterial reversal detection and filtering. Our work in **Chapter 3** has already shown that FimX-YFP concentration asymmetry can be used as a proxy for the direction and speed of twitching motility, and we show through cross correlation analysis that a pole swap is correlated with a change of direction of travel along the long axis of the cell, building upon previous visually described evidence [37]. As an individual cell's movement behaviour is highly influenced by neighbours in dense collectives, pole swaps are used as proxies for reversals in densely packed conditions. Having detected pole swaps,

we searched for the potential triggers of bacterial reversals beginning with cell density. We were unable to identify a clear trend between pole swap rate and local cell density, therefore, due to their importance in many biological processes, we investigated the topological defects. However, no clear trends in the pole swap rate could be identified around either type of half integer charged defect [145, 169, 176]. We therefore had to consider other stimuli that triggers bacterial reversals.

We hypothesised that bacterial reversals could be stimulated by the movement of neighbouring cells. To probe this, we first measured collective bacterial movement in confluent monolayers and at the colony edge using PIV [160]. We first identified that when FimX-YFP was localised in an anti-aligned state, with the largest concentration at the pole pointing in the opposite direction of collective travel, the rate of pole swapping is greater than if FimX-YFP is aligned with collective movement. This analysis calculated the projection of collective velocity in the direction of greatest FimX-YFP concentration, showing that reversals occur most frequently when *P. aeruginosa* is trying to twitch against a rapidly moving collective. The rate of reversal then decreases as the projection of collective velocity decreases. These trends were found in both in the monolayer and at the colony edge. We can therefore conclude that a source of polar behaviour in densely packed *P. aeruginosa* collectives is the increased reversal rate when bacteria twitch in the opposing direction of collective travel.

We also considered how a single cell could benefit from employing biased reversals in dense collectives by comparing the projection of cell velocity in the direction of group movement pre and post pole swap. Although there was a increase in velocity when pole swapping correctly and a decrease when an incorrect pole swap was performed, the overall mean values were still positive, which was to be expected as single cells are rarely observed moving in a direction opposite to that of their collectively moving neighbours [175]. Instead we split the populations according to FimX-YFP alignment with the direction of collective travel and found that anti-aligned cells are more likely to move in the opposing direction of group movement than those that are aligned. We therefore conclude that employing biased reversals to twitch with the collective prevents individual *P. aeruginosa* cells from falling behind the collective, increasing its potential to acquire nutrients that lie further afield, outside the colony [147].

The results we have obtained show that *P. aeruginosa* is capable of altering its movement behaviour through biasing its rate of reversal in response to physical stimuli in dense collectives, ultimately driving collective polar behaviour. It is collective polar behaviour that appears to drive colony expansion through twitching motility, complementing work done previously showing that coordination is essential in facilitating colony expansion [45, 149]. Bacterial reversals have also been

shown to be important in other dense collectives, for example, *M. xanthus* employs timed reversals to maintain relatively large local cell density during fruiting body formation [45]. Multilayer formation in *M. xanthus* has been shown to occur around $+\frac{1}{2}$ charged topological defects [145] and although we observed polarisation within topological defects in *P. aeruginosa* monolayers, we do not have evidence that suggests that this polarisation is driven by the active regulation of pole swaps. More broadly however, biased reversals present a method of driving and sustaining the polarisation of cell movement in active matter systems. Recent studies have highlighted the need for future modelling of active matter systems to incorporate the coexistence of collective nematic and polar behaviour [138]. We have provided further evidence that rod shaped bacterial monolayers comprised of polar agents must be modelled to facilitate the coexistence between nematic and polar behaviour.

Even though this study has uncovered novel information on the movement behaviour of *P. aeruginosa* in dense collectives, there are limitations to the conclusions drawn. The analysis performed has shown that biased reversals occur in dense collectives and act to drive group polar behaviour. Increased polar behaviour would be expected to result in each individual exerting a force in the direction of travel of the collective, increasing the overall distance travelled, particularly enhancing the amount of colony expansion [147]. Although it would be expected that the ensemble force from an increasing number of aligned individuals results in greater rates of expansion, we have not definitively proved it in this study. We have determined the relationship between reversal rate and collective movement through the use of FimX-YFP, however, a number of different proteins have been found to localise in the leading pole of *P. aeruginosa* which could similarly be used in the analysis pipeline presented here. For example, the retraction motors PilT and PilU localise to the leading pole of *P. aeruginosa*. In addition, it would be instructive to investigate mutation in the Pil-Chp system, for example Δ*fimX*, Δ*pilU* or the hyperpilliated Δ*pilH* mutant appears to reverse more frequently than the WT (only through visual inspection) [34, 37, 64]. By putting strains with different labelled proteins or mutants through this analysis pipeline, we might improve our knowledge on how the Pil-Chp system is used to regulate collective motility.

Although we have demonstrated that *P. aeruginosa* employs biased reversals to generate collective polar behaviour, the stimulus and signalling pathway that triggers the change of direction of travel remains unknown. Due to the number of cell-cell interactions that occur in the monolayer, it is possible that mechanosensing through the cell envelope protein PilY1 has a role to play in triggering bacterial reversals, as it has been known to sense shear and shares structural similarities to known mechanically sensitive domains [69]. Alternatively, force sensing through the pilus may play a role, as when under force a pilus becomes elongated through a conformational change, which can potentially

be sensed by the Pil-Chp system [68]. It stands to reason that when a cells is anti-aligned to the direction of collective travel, its pili are more likely to stretch and undergo a conformational change compared to when it moves in the direction of collective movement. Such stimuli might prompt cells to increase their poleswap rate, allowing them to reverse direction to move with the collective. If this hypothesis is correct, it would explain the greater rate of pole swapping observed in the monolayer (**Figure 41**) relative to the colony edge, as the greater speeds in the monolayer would cause a large conformational change in pili when anti-aligned, as the pili anchored to the substrate are stretched by the body being rapidly moved by its neighbours.

Recent modelling on semi-flexible agents (rather than rod shaped) has highlighted how the reversal rate can influence the amount of movement in a densely packed system [147]. As the time reversal rate decreases and the system is found to become more polar. This is because reversals are assumed to be random and occur at equal rates in cells in the aligned and anti-aligned state. An increase in polar behaviour results in increased RMSD and a decrease in the amount of jamming in the system. It is also reported that as the cell density approaches confluence that increasing the reversal rate or employing nematic driving of reversals aid in preventing jamming. Preventing jamming within active systems allows the maintenance of active turbulence which potentially allow nutrients to be mixed into the interior of the colony via collective movement [147]. We therefore propose that *P. aeruginosa* has evolved the ability to respectively elevate and suppress its rate of reversal when travelling with and against the collective, to facilitate a behaviour like observed in simulations of semi-flexible agents. A polar approach is used when cells are aligned (relatively infrequent reversals) and a nematic approach is taken when an individual is anti-aligned (relatively frequent reversals) and cell bodies come into close contact with one another, increasing local density. As shown by simulations, this behaviour increases RMSD and assists in facilitating active turbulence, which facilitates a more equal distribution of nutrients throughout a colony [147]. While we do not currently have the means to vary the rate of reversal when travelling with or against the group, future molecular work on the Pil-Chp system might ultimately provide us with the means to do so.

In terms of next steps, as mentioned in **Section 3.3**, the robust analysis pipeline developed to detect, filter and understand pole swaps should be utilised to investigate the function of other polar localising proteins such as PilB, PilT and PilU [37, 64]. Cross correlation analysis could then be utilised to elucidate in which order other proteins are recruited to the cell pole during the reversal process, potentially providing information on how different proteins in the Pil-Chp system interact with one another [22]. The other extension of this work would involve constructing a model of a bacterial monolayer, comprised of rod shaped agents that exert a force in a single direction and can

reverse, flipping the orientation of this force to align with the direction of collective travel. Although it might be computationally expensive to run the simulation whilst simultaneously quantifying group movement, it would allow different simulations to be run with varying reversal rate biases. Through measurement of RMSD, it would then be possible to quantify the benefits of regulating reversals. If there was no reversal rate bias, we would observe a more nematic system, whereas at the opposite end of the spectrum if agents only reverse when anti-aligned, we would expect the system to become highly polarised. By tuning the reversal rate bias we could probe at which point in the cross over from nematic to polar behaviour generates the most robust collective movement.

Through this study, we have used a fluorescent protein that localises to the leading pole of *P. aeruginosa* as a proxy for bacterial movement behaviour in dense collectives. We previously showed novel collective polar behaviour within topological defects in confluent bacterial monolayers and in groups of aligned individuals at the colony edge expanding outward into untouched surface. Now, we show that *P. aeruginosa* employs reversals to align twitching motility with the direction of collective travel. These reversals occur more frequently when *P. aeruginosa* tries to move against the direction of collective travel, and are suppressed when moving with neighbours. Our results provide the first experimental evidence of bacteria modifying their movement behaviour to increase polar behaviour, which appears to facilitate colony expansion, benefiting both the individual at the edge and the collective overall through the acquisition of nutrients. These results provide insight into the mechanism of how polarisation of cell movement in dense collectives is generated and sustained but also raises many interesting new challenges such as uncovering the mechanism causing biased reversals, discovering to what degree do the reversals boost or hinder polarisation and to what extent reversals affect the rate of colony expansion.

5 From reversals to twiddles: using an individual based model to understand the role of a newly observed twitching behaviour

Subsurface assays are excellent tools for investigating novel surface-based bacterial movement behaviours in both solitary cells and dense collectives [34, 149]. They are particularly useful for studying the physical and biological processes that influence motility in dense collectives of bacteria, as cells are forcibly restrained to the substrate in a monolayer which makes microscopy more accessible [73]. Although useful, it is not possible to probe the effects of fluid flow in a subsurface assay or easily manipulate chemical gradients. Instead, experiments studying cells at the interface between liquid and glass in microfluidic devices are used [87]. Microfluidic flow chambers generate stable, well-defined and reproducible flow patterns, and allow the investigation of the effects that chemoattractants and other chemical treatments such as antibiotics have on surface-attached cells and developing biofilms [67, 81, 177, 178]. Flow chambers are also used to continuously provide cells with fresh nutrients in order to study the long term growth of individual bacteria and collectives [118]. Chambers with more complex geometries are also be used to study different natural environments, such as soil pores [122]. As cells are no longer restricted to two dimensions in flow chambers, multilayer formation occurs frequently, resulting in three-dimensional biofilms forming [121]. As well as differences in collective behaviour, individual cell motility is different in flow chambers compared to subsurface assays. For instance in *P. aeruginosa*, twitching speed decreases significantly in flow chambers due to the lower number of pili expressed when cells are not confined, and the rate of bacterial reversals changes drastically, with the characteristic time between reversals increasing from an order of minutes to hours [34, 67].

Recent research in our group has observed a novel form of twitching motility in *P. aeruginosa* at the interface between glass and liquid termed twiddling, which we have not observed in subsurface assays. A twiddle involves a twitching cell rotating around its centre, with both cell poles turning as would a propeller on a boat or aircraft, differing from if the turn was focused around one pole, like the hands of a clock. At the end of a twiddle, rotation ceases and the cell resumes travelling in the direction of its long-axis from either cell pole. Rather than being an instantaneous process like a reversal, twiddles occur over the course of tens of minutes. We have observed twiddles in multiple *P. aeruginosa* strains including PA01, PA07, PA09, and PA11. Twiddles are also observed in a strain without a functioning flagellum (a $\Delta motABCD$ knockout mutant that lacks the flagella stators), which suggests that the behaviour is facilitated by pili and not flagellum rotation. Furthermore, in preliminary experiments using a strain expressing fluorescently labelled PilT-YFP (the pilus retraction motor), equal levels of PilT-YFP were found at each cell pole during a twiddle, indicating that

the behaviour might be generated by the retraction of pili from each pole at the same time. Taken together, our data thus far suggests that twiddles are a newly identified behaviour used by twitching cells as they travel across surfaces under flow [179].

Preliminary results indicate that the entry and exit rate of twiddles are fixed in the presence or absence of a chemoattractant gradient. To investigate if twiddles are a chemotactic behaviour the proportion of cells exiting twiddles in the direction of an increasing or decreasing chemoattractant gradient (succinate) was measured and compared to a case with no gradient. When there is no gradient, the proportion of twiddle exits in either direction was equal, but in the presence of a gradient the proportion of exits towards elevated levels of nutrient concentrations was increased. These results indicate that twiddle exits are biased and could potentially contribute to chemotaxis, but do not give a conclusion on the if the entire twiddling process helps or hinder chemotaxis [179].

Alongside twiddles, *P. aeruginosa* cells have been shown to reverse their direction of twitching motility along their long axis to facilitate chemotaxis towards nutrients and other chemicals including antibiotics [67, 81]. Specifically, cells reverse direction more frequently when moving away from chemoattractants, which act to direct them up gradients. From our experiments, it is not clear whether twiddles simply perform a similar role to reversals or whether twiddles contribute to chemotaxis in an entirely different manner [179].

Investigating the relative contribution of reversals and twiddles towards chemotaxis is experimentally challenging, as the two behaviours occur simultaneously in microfluidic experiments [179]. Ideally, it would be possible to simply switch off twiddles or reversals experimentally, perhaps through genetic manipulation, however, we have not be able to identify any genes that specifically effect either type of twitching behaviour. The most likely candidates are genes in the Pil-Chp system, but manipulating their expression would likely have other unintended consequences for twitching motility [32]. Instead, we sought to develop a mathematical model to represent twitching cells in a chemotattractant gradient. Utilising a model would firstly allow the experimental scenario to be stripped back to its essential components to allow for changes of properties such as the strength of the chemical gradient or cell speed to show under which conditions twiddles and reversals best contribute to chemotaxis. Secondly, a simulation would allow for the independent modelling of twiddles and reversals, effectively allowing either behaviour to be switched off at any time. By switching off twiddles and reversals independently, the contribution of each behaviour to chemotaxis can be determined.

Over the course of the following chapter, the process of developing a non-dimensional model of twiddles and reversals is documented. First the properties of twiddles and reversals are quantified using experimentally measured data. Second, the non-dimensional model is outlined and the necessary

equations are derived. We go on to establish a base case scenario, performing appropriate validations on the simulated output to ensure the movement and response of simulated agents to a chemical gradient represents our experimental observations. Finally, the results of parameters sweeps are discussed, revealing potentially independent roles for reversals and twiddles in chemotaxis in different regions of parameter space.

5.1 Measuring properties of twiddles and reversals to build a model

Non-dimensional models are useful tools for understanding biological phenomena as they allow the reduction of the number of physical parameters that require investigation. To ensure that the model best reflects nature, parameters used to govern bacterial movement and chemotaxis are extracted from experiments. In this section, we present the experimental configuration used to measure properties of *P. aeruginosa* twitching in a microfluidic device, along with the rationale and governing equations of an individual based model simulating chemotaxis facilitated by biased twiddle exits and reversals.

The first step to developing such a model is having a clear understanding of the experimental conditions being investigated. To investigate the properties of *P. aeruginosa* twitching at the liquid-glass interface we use a dual-inlet BioFlux^{TM} device to generate a stable chemical gradient (**Figure 43a**). A chemical gradient is generated by flowing growth medium into one channel and a growth medium supplemented with a chemoeffector into the other. Our experiments use tryptone broth (TB) as the growth medium and succinate (at a maximum concentration of 2 mM) as the chemoeffector and therefore we will present experimental results from TB-only and 'succinate-only' (TB supplemented with succinate on both sides of the channel so cells experience a uniform 2 mM concentration of succinate all over the device) controls, and compare these to the case when a succinate gradient is present in the background of TB medium [67].

To perform an experiment that allows the quantification of chemotaxis, the device is first filled with growth medium and inoculated with *P. aeruginosa* at low density ($OD_{600} = 0.25$) on both sides of the channel, and left without flow for 10 minutes to allow for surface attachment. Subsequently, to remove any planktonic or weakly adhering cells, media was flowed through the channel at 40 $\mu l\ h^{-1}$. Once imaging begun, the flow rate was set to 4 $\mu l\ h^{-1}$ for the duration of the experiment [67]. Images were taken at one frame per minute for over 10 h, however, the continued cell division increases the cell density in the channels making it progressively more challenging to distinguish individual cells and the channels eventually become clogged. Therefore only the first 300 min of each time series is considered for analysis. Images were captured at the point where the two inlet channels meet as here the steepest chemoeffector gradients are present, and therefore chemotaxis should be at its largest.

To investigate chemotaxis, we wanted to measure the concentration and concentration gradient of succinate at the location of each bacterium. To quantify the concentration field, a pilot experiment was first performed using flourescein in place of succinate and the normalised concentration of fluorescein was visualised across the width of the channel (**Figure 43b**), see [67]. The normalised concentration field was then modelled using an analytical model of diffusion (**Figure 43c**) and differentiated to obtain the normalised concentration gradient (**Figure 43d**). As we now possess a clear picture of the experimental set up including the concentration and gradient fields of succinate, we must now consider how *P. aeruginosa* uses reversals and twiddles to generate chemotaxis.

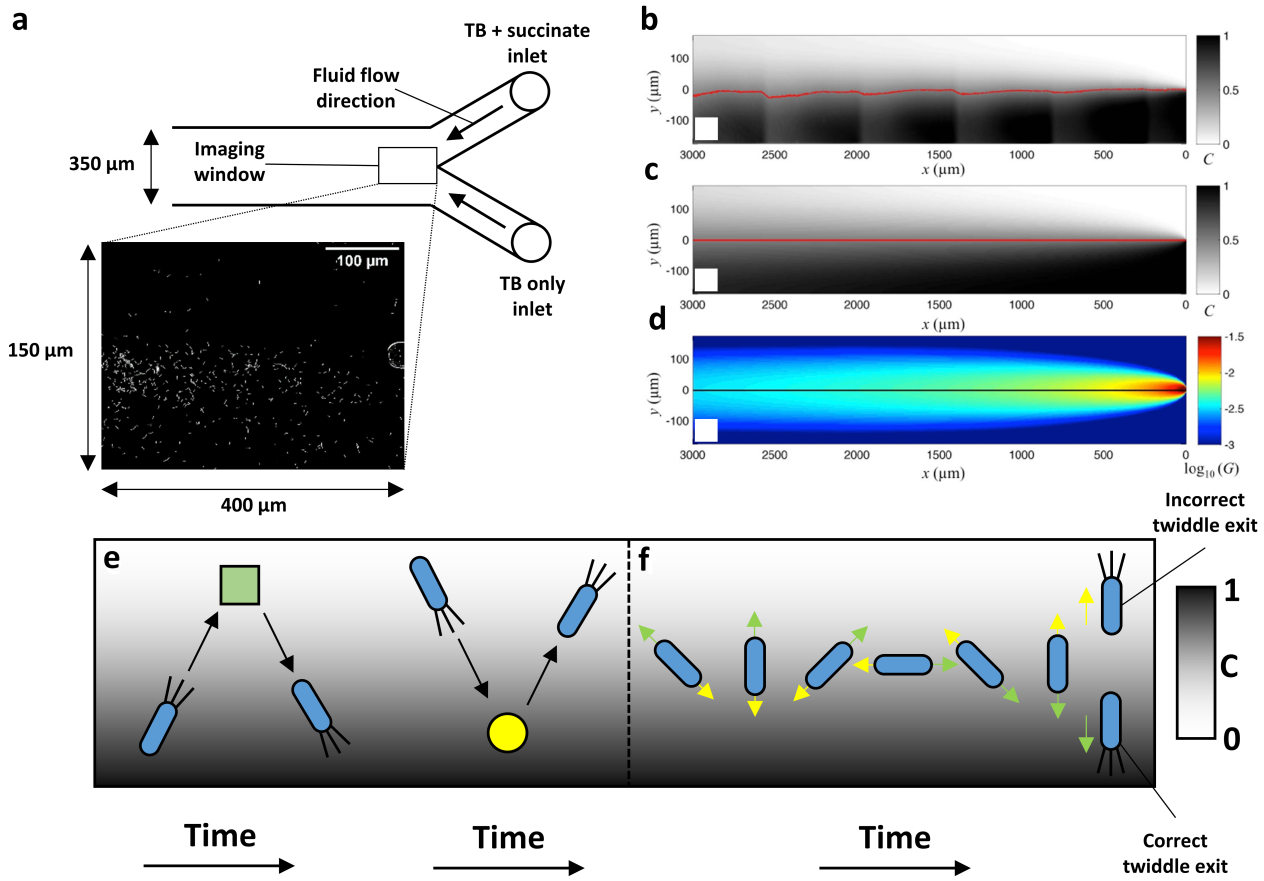

Figure 43: *P. aeruginosa* performs reversals of twitching direction and twiddles in a chemical gradient. (a) A schematic diagram of the BioFlux^{TM} device and experimental set up with an accompany binary segmentation image of the experiment taken 10 hours post channel inoculation. (b) The normalised concentration of fluorescence in the device which is then converted into (c) an analytical model of the normalised concentration which is subsequently differentiated into the (d) normalised concentration gradient field, G ($G = \frac{1}{C_{\mathrm{MAX}}}\frac{dC}{dy}$ where C_{MAX} is the maximum concentration of succinate). (b-d) used with permission from [67]. (e) A diagram of a twitching cell undergoing a correct and incorrect reversal, shown as a green square and yellow circle respectively. Black arrows show the direction of twitching motility. (f) A diagram of a cell undergoing a twiddle, with poles distinguished by yellow and green arrows. At the end of the event the cell leaves a twiddle correctly or incorrectly by moving towards greater or smaller nutrient concentrations respectively.

P. aeruginosa is capable of performing two twitching behaviours whilst moving at the interface

between liquid and glass: a reversal or a twiddle. Reversals, as shown in **Figure 43e**, involve a change in the direction of travel of π radians, with the leading pole becoming the lagging pole of the cell, and vice versa [67]. Reversals are considered correct or incorrect if they reorient the cell towards or away from increased nutrient concentrations respectively. Twiddles are a newly observed twitching behaviour and arise due to pili retraction at both poles, causing the cell body to rotate, as shown in **Figure 43f** [179]. Whereas reversals involve an instantaneous change of direction, twiddles take place over a longer time span, with rotation persisting for on average between 20 to 40 min. Upon completion of a twiddle, the cell moves towards or away from increased nutrient concentrations allowing exits to be classified as correct or incorrect respectively [179]. Therefore, both of these behaviours have the potential to contribute towards chemotaxis but it remains unclear whether they play similar or different roles in surface navigation.

5.1.1 Quantifying chemotaxis from twiddles and reversals

Although we possess a description of the reversing and twiddling process, we need to develop a method to detect twiddles and reversals, and quantify their potential chemotactic properties. Given that any meaningful result will require the averaging of many time-lapse data sets, an automatic method of detecting reversals, twiddle entries and exits must be developed. In our assays *P. aeruginosa* cells are automatically tracked using the Trackmate plugin for Fiji and an image processing pipeline developed previously [67, 179, 180]. We must then combine this tracking data with the concentration gradient field to elucidate any potential trends regarding chemotactic behaviour [179]. In this section, we describe the automatic detection of reversals and twiddles, along with their categorisation as correct and incorrect depending on if the events drive cells towards or away from increasing succinate concentrations. Finally, we quantify how the chemotactic effect of twiddles and reversals vary with the concentration gradient strength the cells experience.

Before any analysis is performed, reversals, twiddle entries and exits are detected. We follow a previously established method of reversal detection [67]. Twitching motility is driven by stochastic pili dynamics and therefore an inherently noisy form of movement in terms of cell position and orientation [4]. Therefore, we first smooth the direction of cell movement, θ, using a moving average filter to give θ_{M} (data taken every minute smoothed over 10 minutes). A reversal of direction of travel occurs when the leading pole of the cell changes. The leading pole is defined as the pole whose orientation subtends the smallest angle with θ_{M}. The angle of reversal, $\theta_{\mathrm{R_M}}$, is determined by taking the mean value of $\sin\theta$ in the 5 min before the reversal occurs (and therefore reversals in the first and final five frames of a trajectory are excluded from the analysis). We also use θ_{M} to quantify the

total time cells spend moving towards and away from greater succinate concentrations. By dividing the number of correct reversal by the amount of time cells spend moving away from succinate (i.e the total time that cells could theoretically undergo a correct reversal), we calculate the correct reversal rate, whilst dividing the number of incorrect reversals by the amount of time cells spend moving towards succinate (i.e the total time that cells could theoretically undergo an incorrect reversal) to calculate the incorrect reversal rate. Finally, false positives occur as the result of cell division and so the subsequent 7 min post reversal are checked for separations, and any reversals that are associated with cell divisions are excluded from our analysis [67]. By visual inspection the method described reliably detects reversals, enabling the resulting data to be used to calibrate our model.

Twiddle detection relies on measuring the rate of change in the orientation of the cell body, denoted as the angle ϕ. Like θ, ϕ is also smoothed due to the jerky nature of twitching motility, and is done so using a Savitzky-Golay filter over 20 min. Once smoothed, putative twiddles are considered to be at any time points where $|\frac{d\phi}{dt}| > 0.05$ rad min^{-1} and are disregarded if: they are less than 10 min long, change direction of rotation, or if the mean $|\frac{d\phi}{dt}| < 0.1$ rad min^{-1} when averaged across the entire twiddle. Twiddle entry angle, $\phi_{\mathrm{TE_M}}$, is calculated in the same manner as $\theta_{\mathrm{R_M}}$ (so as with reversals), therefore, any twiddles that occur within the first five frames of a trajectory are disregarded. Determination of twiddle exit angle, $\phi_{\mathrm{TX_M}}$, using the five frames prior to a cell returning to normal twitching motility proved unreliable in comparison to manual measurement. Therefore, each trajectory was reversed in time, allowing twiddle exits to be detected as twiddle entries. One additional filter is then applied, where any twiddle exits in the first frame of the reversed time series are removed as it is not possible to know if the twiddles actually end at this point in normal time or if they persist beyond the time of image acquisition. We are now able to automatically detect twiddles and reversals reliably and perform further analyses on them.

To ensure that the simulation accurately reflects the behaviour of non-twiddling and twiddling cells, a set of common filters has been put in place to correlate the properties of a tracked individual and its environment. We start with a complete exclusion of data recorded 300 min after chamber inoculation, as often the channel becomes so crowded due to cell division that is not possible to separate the movement of an individual from that which is imposed by its neighbours. Second, any time points where an individual's speed is below 0.08 μm min^{-1} are removed, as these cells are considered stationary [67]. Data points are also excluded if the aspect ratio is below 1.4 to remove tracked objects that are not actually cells. The final overall filter is only applied to data sets with succinate gradients present, when data is only considered if a cell is tracked in a region where the normalised gradient exceeds 0.003 μm^{-1} and by doing so, we are only investigating the behaviour of

P. aeruginosa when they are most likely to be able to detect the gradient, as opposed to including trajectories in regions of the device where the gradient is negligible.

Before creating a model of *P. aeruginosa* using biased reversals and twiddles to generate chemotaxis, we must first quantify the parameters that govern this behaviour. In previous experiments using a different chemoeffector (dimethyl sulfoxide, DMSO), it was found that cells use a pessimistic reversal rate strategy whereby cells increase their rate of reversals when moving away from DMSO but reverse at the basal rate when moving towards it [67]. To establish that this behaviour persists in newer experiments that use succinate as the chemoeffector, the rate of correct and incorrect reversal was determined and compared to the basal rates in the absence of gradients. The rates of twiddle entry and exit must also be measured and correlated with the presence or indeed the strength of succinate gradients. Finally, an array of accompanying parameters must also be determined, including mean cell velocities and twiddle rotation rate. We will now explain how the parameters that govern the individual based model are measured experimentally, documenting any relevant filters that are applied.

We begin will cell velocity, using this method of analysis as the framework for other parameters. As *P. aeruginosa* has been shown to vary its velocity in response to the media it is grown in, we compared tracking data from time lapses recorded in TB-only, succinate-only, and succinate gradient conditions to measure any potential change in speed [179]. It is clear that cells move more rapidly in the presence of succinate (**Figure 44a**), an effect we wanted to consider in our individual based model. Additionally, we split cell velocity values into correct or incorrect according to whether cells were moving up or down the succinate gradient (or simply up and down the channel width in the control cases) using θ_{M}. **Figure 44a** shows no difference in mean velocity for the TB-only and succinate-only data sets, however, when a gradient is present there is a small but significant difference in mean velocity with cells moving more rapidly towards increasing succinate concentrations (a response known as orthotaxis [67]). However, as our study focuses purely on the impact of twiddles and reversals, and not the impact of orthotaxis, we decided to set cell velocity, $v_{\mathrm{C}} = 0.6$ μm min^{-1} for the individual based model, a value taken from the succinate-only control.

With v_{C} determined, we consider the reversal rates when cells are travelling up or down the succinate gradient. The individual and mean values across multiple biological replicates are displayed for the TB-only, succinate-only and gradient case in **Figure 44b**. Rather than a pessimistic response as has been seen previously with DMSO, *P. aeruginosa* shows a bi-bias response, where relative to succinate-only control, its rate of reversal is suppressed when travelling up the chemical gradient and, elevated when moving down [67].

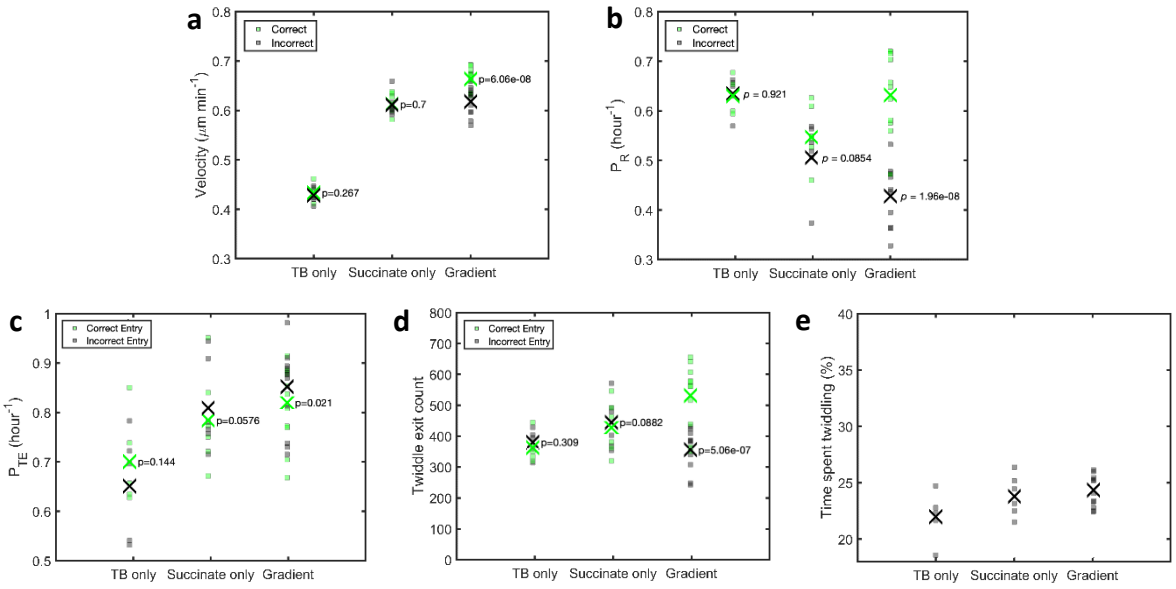

Figure 44: Quantification of twitching velocity, reversal rate, twiddle entry rate, twiddle exit bias, and the percentage of time spent twiddling. For all plots the mean value from each replicate experiment is represented with a square, and a cross for the overall mean. Data is split into correct and incorrect values for (a) velocity, (b) reversal rate (c) twiddle entry rate and (d) the number of twiddle exits. Data shown comes from five TB-only, six succinate-only and eleven gradient data sets, with p-values calculated from paired T tests which test the null hypothesis that the correct and incorrect values are the equal. The final plot (e) shows the percentage of time cells spend twiddling, which is used to calculate the twiddle exit rate.

Before investigating if a similar bi-bias response is present for twiddle exits we first determined the overall rate of twiddle entry (P_{TE}) and exit (P_{TX}) to quantify any differences. We calculate P_{TE} by dividing the number of detected entries by the amount of time a cell could enter a twiddle (the time not spent twiddling). There are small differences in P_{TE} between the correct and incorrect gradient case and twiddles occur more frequently in the presence of succinate (**Figure 44c**). When comparing the amount of twiddle exits, we see similar numbers of correct and incorrect events when there is no gradient present (in these controls the direction of correct and incorrect is arbitrary). However, in the presence of a chemoattractant gradient we observe a bi-bias response similar to that observed for reversal rates (**Figure 44d**). Here incorrect twiddle exits are suppressed, and correct exits are elevated in the presence of a gradient relative to if there was not one, a strategy that is be referred to as a bi-bias strategy. We are unable to directly measure the rate of twiddle exit, as we cannot assign lead and lag-pole polarity during a twiddle. Furthermore, twiddles, can last for over 30 min and tracking could fail in this time. We also cannot pair twiddle entries and exits for this reason. Instead, we estimate P_{TX}, using the proportion of time spent twiddling, P. We directly count the amount of time cells spend twiddling and not twiddling, with results shown in **Figure 44e**, and then calculate P_{TX} using

$$P = \frac{P_{\mathrm{TE}}}{P_{\mathrm{TE}} + P_{\mathrm{TX}}}.$$

Figure 44e shows that cells spend 23%, 25% and 26% of their time twiddling in the TB-only, succinate-only and gradient scenarios respectively.

So far, we have outlined what value cell velocity will take in our simulations, shown that reversals and twiddle exits have a bi-bias, and that it is possible to determine the twiddle exit rate from P_{TE} and the proportion of time spent twiddling. After careful consideration, we decided to focus our study on how the process of each twitching behaviour influences how an individual cell navigates towards increased concentration regions. In doing so, using the experimental results as a guide, we decided to set the rate of reversal, P_{R} and the rate of twiddle exit, P_{TE}, to be the same, at 0.5 event h^{-1} cell^{-1}. In doing so, P_{TX} becomes 1.5 h^{-1} cell^{-1} to ensure that cells spend 25% of their trajectories twiddling. Given that these behaviours occur at fixed rates, we must now implement a method for reversals and twiddle exits to generate chemotaxis by employing a bi-bias strategy, which first involves measuring the strength of the response.

As *P. aeruginosa* has been shown to alter its reversal rate in response to a chemical gradient and can change direction before it has travelled a single cell length, it has been proposed that it adopts a spatial strategy of sensing chemical gradients, where comparisons in chemical concentration are made between the cell poles [67]. We therefore considered that there are two different factors that can affect chemotactic sensing: the gradient strength $\frac{dC}{dy}$ (where C is the normalised concentration gradient, and y is the vertical position of the cell in the channel), and ρ is the orientation of the cell relative the direction of the gradient. We include ρ as a cell orthogonal to the gradient will not be able to sense any change in concentration between its poles, where as one parallel will have maximum sensing capabilities. As ρ is defined from the horizontal axis of the channel in the clockwise direction, we use $\sin\rho$ to calculate the projection of the gradient along the cell length. Therefore, at each time point in tracking, the concentration gradient experienced by each cell, $\frac{dC}{dy}_{\mathrm{EXP}}$, is given by **Equation 28**, where

$$\frac{dC}{dy}_{\mathrm{EXP}} = \frac{dC}{dy}\sin\rho. \tag{28}$$

We are now able to calculate $\frac{dC}{dy}_{\mathrm{EXP}}$ at each time point along a cell's trajectory. We use this to count the number of correct and incorrect reversals and twiddle exits, and the amount of time spent twitching towards and away from greater nutrient concentrations, by binning in $\frac{dC}{dy}_{\mathrm{EXP}}$. Within each bin, we calculate the bias in correct and incorrect reversal rate by dividing the former by the latter

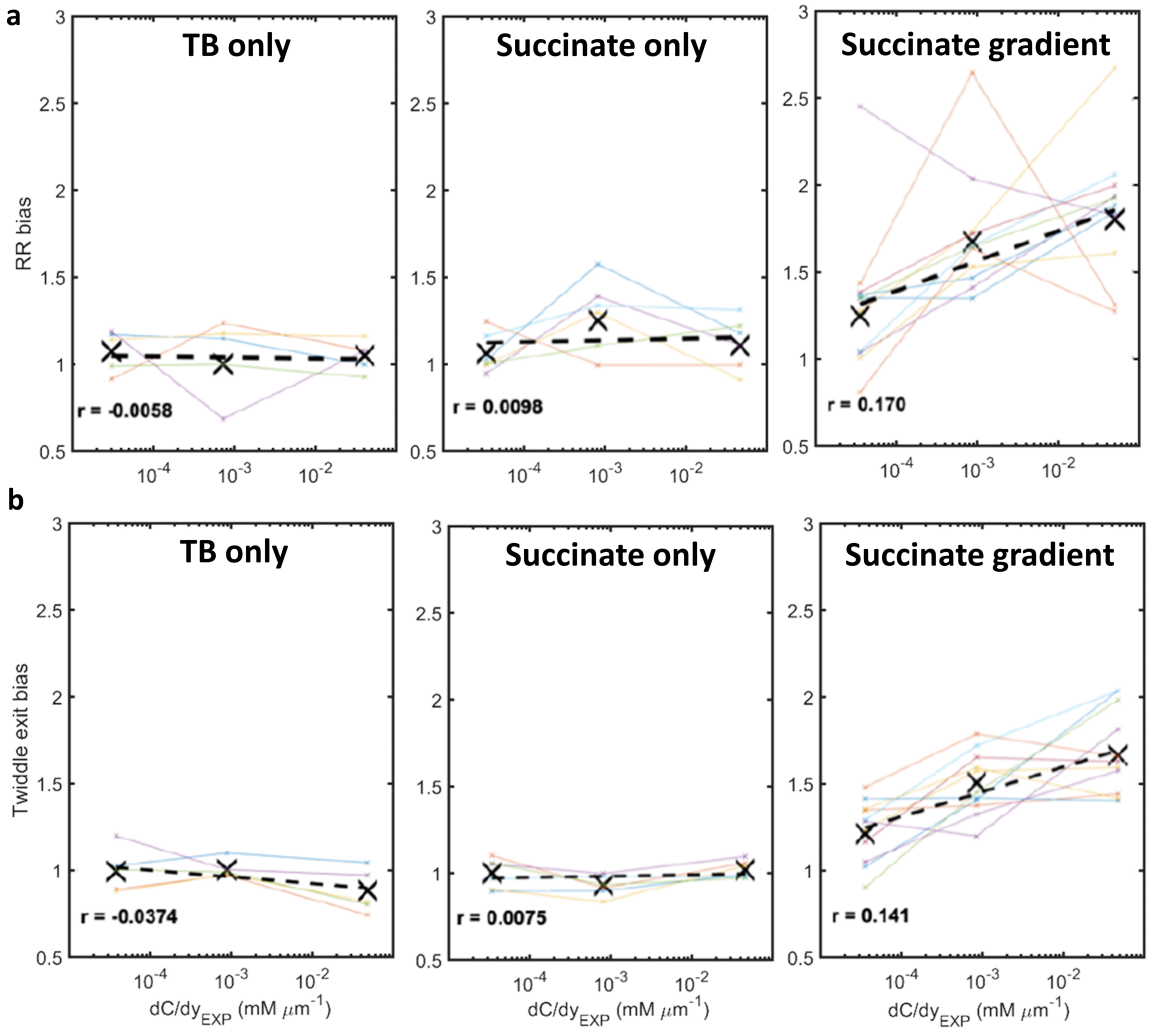

Figure 45: *P. aeruginosa* increases its twiddle exit and reversal chemotactic bias in response to sensing stronger gradients. Plots showing (a) reversal rate bias (correct reversal rate/incorrect reversal rate) and (b) twiddle exit bias (number of correct twiddles/number of incorrect twiddles) as a function of $\frac{dC}{dy}\sin\rho$. Bin edges are set such that each bin contains a similar amount of data, $0, 7.5\times10^{-5}$, 1.875×10^{-3}, and 0.2, with r (the gradient of each line) values calculated via least squares regression. Data shown comes from five TB-only, six succinate-only and eleven gradient experimental time series. Repeat experimental time series are shown as coloured lines, the mean of each bin with a black cross and the subsequent linear fit as a dashed black line.

and apply the same process to the number of correct and incorrect twiddle exits. **Figures 45a** and **45b** show a linear dependence of the bias for both correct reversal rates and correct twiddle exits on $\frac{dC}{dy}_{\text{EXP}}$, showing that cells exhibit a greater chemotactic response when they sense larger chemical gradients. Given *P. aeruginosa* uses a bi-bias chemotaxis strategy, one would anticipate that when $\frac{dC}{dy}_{\text{EXP}}$ increases, the rate of correct behaviour increases, and the incorrect rate is decreases. The plots from TB-only and succinate-only experiments serve as a control case where there is no chemotaxis, which is reflected in the near zero-gradient measured between $\frac{dC}{dy}_{\text{EXP}}$ and the bias for both the rate of reversal and the number of twiddle exits. We have now quantified the chemotactic response of *P. aeruginosa*, and use the information to construct the chemotactic element of an individual based

model.

Using cell tracking and custom analysis scripts, we have quantified some of the physical parameters needed to describe simulated agent behaviour in an individual based model of *P. aeruginosa* undergoing chemotaxis by employing biased twiddle exits and reversals. By using a bi-bias strategy, the cell suppresses incorrect choices and elevates the rate of correct chemotactic decisions to guide chemotaxis. However, we are yet to consider how our simulation agents will rotate outside of and during a twiddle.

5.1.2 Measuring the rotation rate of twiddling and non-twiddling *Psuedomonas aeruginosa* cells

Twiddling and non-twiddling *P. aeruginosa* cells display distinct forms of rotation. During a twiddle, the rotation of the cell body is persistent in one direction, where as outside of a twiddle cell movement is not directed in a single direction, but instead a cell diffuses away from its original position. Given these two distinct forms of movement, in this section we outline the methods used to determine the average twiddle rotation rate, how the rotation of non-twiddling cells are modelled as particles undergoing Brownian rotational diffusion, and how the equivalent diffusion coefficient was extracted. At the end of this section, we will possess all necessary parameters to construct our model.

Before performing analysis, we first filter our data to remove tracks that have a net to gross displacement ratio (NGDR) below 0.15. The relatively small value of NGDR has been chosen so that we remove any cells that are simply jiggling back and forth and inherently do not travel far [179]. Like the previous analysis, we also remove any time points 300 min post chamber-inoculation, as increased cell density will cause cell-cell collisions that will influence the rate of rotation whether twiddling or not.

As we are able to detect twiddle entries and exits, we split each track into twiddle and non-twiddle events. Any events that are below 10 min in length are removed to ensure reliability of the data. We apply the same minimum normalised concentration gradient strength filter as used previously to ensure that when we are analysing events in a chemical gradient, and as before we exclusively investigate the central region of the device where the cells are experiencing a significant succinate gradient. Objects with an aspect ratio below 1.4 are also removed, as discussed above.

With all relevant filters applied, we seek to determine a rotation rate for twiddling cells, T_{R}, and a rotational diffusion coefficient, D_{R}, for non-twiddling cells. When considering these values, the cell body orientation (ϕ) will be used as twitching motility is often oriented in the direction of the cell body [164]. All values of ϕ have been edited such that they are continuous (by 'unwrapping' the angle so that there are no 2π jumps when the cell passes through the origin) ensuring there are no

large changes when calculating angular velocity or RMS$\Delta\phi$.

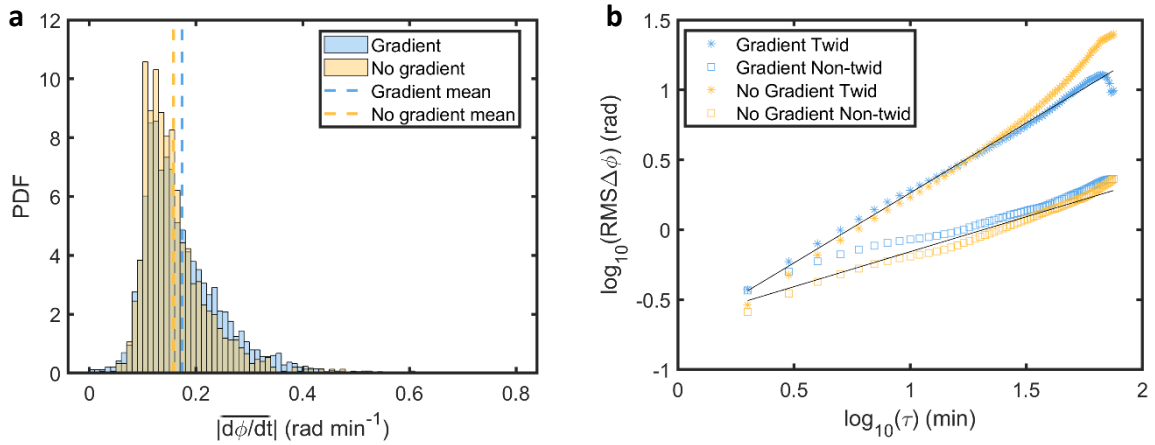

Figure 46: Quantifying the rotation of twiddling and non-twiddling cells. (a) PDF histograms of $|\frac{\bar{d\phi}}{dt}|$ for cells twiddling in the presence of a succinate concentration gradient, and in the succinate-only control. Bin size is 0.01 rad min^{-1}. Vertical dashed lines indicate the mean value in the presence and absence of a chemical gradient. (b) RMS$\Delta\phi$ as a function of τ for twiddling and non-twiddling cells in the presence of a succinate concentration gradient, and the succinate only control. Black lines of gradient 1 and $\frac{1}{2}$ to show ballistic and diffusive rotation respectively. Data shown comes from six succinate-only and eleven succinate gradient experimental time series.

To determine T_{R}, we considered two methods. The first involves calculating the mean absolute rotation rate for each twiddle $|\frac{\bar{d\phi}}{dt}|$, and the using this to calculate the mean or median of this data set. We used the absolute value of rotation rates here as twiddles were found to have an equal probability of rotating clockwise or counter-clockwise. Alternatively, we could consider pooling all $|\frac{d\phi}{dt}|$ values from all data sets together and calculate the mean or median, which would weight longer twiddles more. In our simulation, twiddles have a set average length that matches the distribution of experimentally measured events, and so we applied the same rationale to obtaining T_{M} from experimental data and opted for the former method. **Figure 46a** shows the PDF of $|\frac{\bar{d\phi}}{dt}|$ values for cells in the presence and absence of a gradient. We consider the case with no gradient to measure T_{M} to remove any impact the succinate gradient has on increasing cell velocity or rotation rates, and find mean and median values of $|\frac{\bar{d\phi}}{dt}|$ equating to 0.158 ± 0.004 rad min^{-1} and 0.143 ± 0.005 rad min^{-1} respectively, with uncertainties calculated through the standard error of the mean or median. The mean and median values of $|\frac{\bar{d\phi}}{dt}|$ equate to one rotation every 39.7 or 43.9 minutes respectively, therefore we consider the order of magnitude of these values and set $T_{\mathrm{R}} = 0.157$ rad min^{-1} or one rotation per 40 minutes in our model.

The focus now shifts to non-twiddling cells [181]. Cells not undergoing a twiddle will be modelled as particles undergoing Brownian rotational diffusion, and a value of rotational diffusion coefficient, D_{R} , was calculated. We note that cells undergoing pili-based movement are physically attached to a

surface and are not affected by Brownian motion. However, the stochastic actuation of pili introduces small changes to their orientation, which gives rise to rotational diffusion over long time scales. To determine RMS$\Delta\phi$, we used the same pre-processed data that was used to calculate T_{R}, except that now we use only the time in between twiddles. The calculation of RMS$\Delta\phi$ investigates the difference between ϕ at time t and at subsequent later time points, generating a value of RMS$\Delta\phi$ at a given time lag, τ. The sum of RMS$\Delta\phi$ across all cells at each τ is calculated then divided by the number of data points at each τ, N, calculated using **Equation 29**,

$$RMS\Delta\phi\left(\tau\right)=\sqrt{\frac{1}{N}\sum_{i=1}^{N}\left(\phi_{\mathrm{i}}\left(t\right)-\phi_{\mathrm{i}}(\tau)\right)^{2}}. \tag{29}$$

Here, $\phi(t)$ indicates the value of ϕ at the time point in question and $\phi(\tau)$ is the reference value of ϕ.

To ensure that the motion of the cells can be modelled as Brownian rotational diffusion, we must validate that $\log_{10}(\mathrm{RMS}\Delta\phi)$ as a function of $\log_{10}(\tau)$ is linear and has a gradient of $\frac{1}{2}$. **Figure 46b** shows the results of $\log_{10}(\mathrm{RMS}\Delta\phi)$ as a function of $\log_{10}(\tau)$ analysis for both twiddling and non-twiddling cells in the presence and absence of a gradient. As seen in **Figure 46b**, the gradient of the $\log_{10}(\mathrm{RMS}\Delta\phi)$ as a function of $\log_{10}(\tau)$ plot is approximately 1 up until larger values of $\log_{10}(\tau)$ for twiddling cells. For the non-twiddling cells both in the presence and absence of a gradient, the data plots do not always have a gradient of $\frac{1}{2}$ and therefore a selection must be made on the subset of points to fit to. As such, data points in the range $\log_{10}(15)\leq\tau\leq\log_{10}(35)$ have been chosen for fitting. A straight line with gradient $\frac{1}{2}$ is fitted to the subset of data points and the intercept found. Once the intercept has been found, the equation to calculate D_{R} must be derived, beginning with **Equation 30**,

$$\mathrm{RMS}\Delta\phi(\tau)=\sqrt{2D_{\mathrm{R}}\tau} \tag{30}$$

$$\log_{10}(\mathrm{RMS}\Delta\phi(\tau))=\frac{1}{2}\log_{10}(2D_{\mathrm{R}}\tau)$$

$$\log_{10}(\mathrm{RMS}\Delta\phi(\tau))=\frac{1}{2}\log_{10}(\tau)+\frac{1}{2}\log_{10}(2D_{\mathrm{R}}). \tag{31}$$

Which is analogous to y = mx + c, taking $\frac{1}{2}\log_{10}(2D_{\mathrm{R}})$ as the y intercept from $\log_{10}(\mathrm{RMS}\Delta\phi)$. Once the intercept has been acquired D_{R} is calculated using

$$c = \frac{1}{2}\log_{10}(2D_{\mathrm{R}})$$
$$D_{\mathrm{R}} = \frac{1}{2}10^{2c}. \tag{32}$$

In **Equation 32**, c is the intercept obtained from fitting $\log_{10}(\mathrm{RMS}\Delta\phi)$. D_{R} was found to be 0.0299 ± 0.0002 rad^2 min^{-1} and 0.0207 ± 0.0006 rad^2 min^{-1} in the presence and absence of the gradient respectively, with errors representing 95% confidence intervals. Moving forwards into the simulation, D_{R} will be set to 0.02 rad^2 min^{-1}, using data from the succinate-only control to negate any effect of increased speed from a chemoattractant gradient (**Figure 44a**).

Now a complete set of parameters has been extracted from the experimental data, with the remaining values of T_{R} and D_{R} being acquired by considering the mean and median value of $|\frac{d\bar{\phi}}{dt}|$ and through analysis of $\log_{10}(\mathrm{RMS}\Delta\phi)$ as a function of $\log_{10}(\tau)$ respectively. The remainder of this section will focus on the formulation of the simulation, with a list of all parameters used at the end.

5.1.3 Development of the simulation

Now that all the relevant experimental parameters have been estimated, the equations that define our model of *P. aeruginosa* performing surface-attached chemotaxis through biased twiddles and reversals can now be described. As chemotaxis is purely facilitated by twiddle exits and reversals, the movement of simulated agents whilst freely twitching and in a twiddle will be outlined first, followed by a description of the $2D$ nutrient concentration field and the subsequent concentration gradient fields that are used in simulations. We assume that the consumption of nutrients by cells is negligible, and do not include growth in our simulations. Next, the model of gradient sensing will be outlined, followed by how this impacts the bias of twiddle exits and reversals up or down a gradient. The following section will outline the operation of the model at any given time point and provide a description of how the simulation is initialised.

At each time point, t, each simulated agent has coordinates, (x, y), and orientation, ϕ. Here the orientation is the direction of movement which for twitching cells is directed along the long axis of the cell [164]. When not performing a twiddle, simulation agents are modelled as particles that move at a constant speed along its long axis whilst undergoing Brownian rotational diffusion (**Equations 33 - 35**) [182]. For each agent the first operation is to update ϕ prior to the change in coordinate, then position using

$$\phi(t) = \phi(t - dt) + \mathcal{N}\sqrt{2D_{\mathrm{R}}dt}, \tag{33}$$

$$x(t) = x(t - dt) + v_{\mathrm{C}}\cos(\phi(t))dt, \tag{34}$$

$$y(t) = y(t - dt) + v_{\mathrm{C}}\sin(\phi(t))dt. \tag{35}$$

For **Equations 33 − 35**, dt is the time-step of the simulation and $\mathcal{N}$ is a value sampled from a normal distribution with a mean of zero and unit standard deviation. Whilst performing a twiddle, the coordinates do not change however the orientation is updated by T_{R},

$$\phi(t) = \phi(t - dt) \pm T_{\mathrm{R}}dt, \tag{36}$$

$$x(t) = x(t - dt), \tag{37}$$

$$y(t) = y(t - dt). \tag{38}$$

In **Equation 36** the ± arises as each agent has a 50% chance of twiddling clockwise or anti-clockwise as decided at the beginning of the twiddle. With the description of cell motion complete, the chemical gradient and cell sensing will be outlined.

Rather than using a 1D nutrient field that runs from the top of a domain to the bottom (as is the case in our experiments), a 2D shape will be used to represent a nutrient source as one might occur in natural environments [183]. The nutrient field will be described using a two dimensional Gaussian,

$$C(r, \sigma) = C_{\mathrm{MAX}} \exp\left(\frac{-r^2}{2\sigma^2}\right). \tag{39}$$

As chemotaxis operates by sensing the gradient of this field, the derivative of the concentration with respect to radial position r can be calculated as

$$\frac{dC}{dr} = \frac{rC_{\mathrm{MAX}}}{\sigma^2} \exp\left(\frac{-r^2}{2\sigma^2}\right) \tag{40}$$

In **Equations 39** and **40**, σ is the standard deviation of the Gaussian used to model the nutrient source and has been set such that it is sufficiently larger than the distance a cell travels between twiddle or reversal events. C_{MAX} is the maximum value of the Gaussian shaped concentration field. Note that we have defined $\frac{dC}{dr}$ as the absolute value of the radial gradient in order to simplify notation.

The functions presented in **Equations 39** and **40** are shown in **Figure 47a** and **47b** respectively.

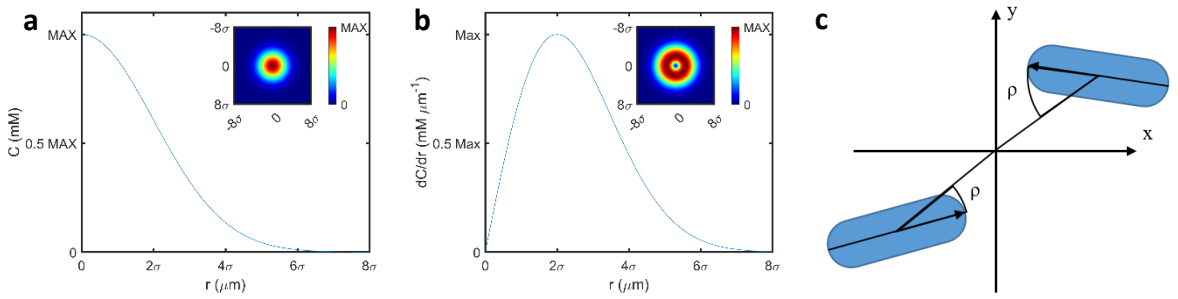

Figure 47: Generalised nutrient concentration field and concentration gradient field used in the model and how the concentration gradient is sensed by simulated agents. (a) The concentration field was modelled as a two dimensional Gaussian. Inset: A bird's eye view showing the nutrient concentration within a $8\sigma \times 8\sigma$ region. (b) The corresponding concentration gradient . Inset: A bird's eye view showing the nutrient concentration gradient within a $8\sigma \times 8\sigma$ region. (c) A representation of the angle subtending the cell orientation relative to the radial gradient field, ρ. Black arrows indicate the direction of cell travel, however, the value of ρ for each agent would be the same, as it is independent of the direction of travel.

Although $\frac{dC}{dr}$ is calculated at the coordinates of an agent, it would not fully represent the gradient experienced by *P. aeruginosa* as we are hypothesising that chemotactic sensing is performed spatially along the cell body [179]. Spatial sensing involves comparing concentration values between the two cell poles (i.e along the long axis of the body) and this means that the greater the angle subtended by the cell body orientation and gradient direction, the smaller the stimuli a bacterium experiences [179]. We represent this angle in our simulations as ρ, which is the angle subtended by the orientation of the cell pole closest to the nutrient source and the nutrient source, which in our simulations is at the origin. As such, ρ may take any value in the range $0 \leq \rho \leq \frac{\pi}{2}$. ρ is shown in **Figure 47c** and is calculated using **Equation 41**.

$$\rho(t) = \phi(t) - \tan^{-1}\left(\frac{y(t)}{x(t)}\right). \tag{41}$$

The resulting concentration gradient experienced by each agent, $\frac{dC}{dr}_{\text{EXP}}$, is shown in **Figure 48a** and is determined using **Equation 42**,

$$\frac{dC}{dr}_{\text{EXP}} = \frac{dC}{dr}\cos\rho = \frac{rC_{\text{MAX}}}{\sigma^2}\exp\left(\frac{-r^2}{2\sigma^2}\right)\cos\rho. \tag{42}$$

Similar to **Equation 40**, here we present the absolute value of the radial gradient to simplify notation.

We have outlined how a simulated agent experiences a chemical gradient, and we now define how this signal is translated into chemotaxis. Before delving into how chemotaxis is modelled, we must first describe how a reversal and twiddle entry is initiated. At each time-step an agent enters a twiddle or begin a reversal with the experimentally derived probabilities P_{R} and P_{TE} respectively.

We draw a random number from a uniform probability distribution ($\mathcal{U}_{\mathrm{R}}$ for reversals, $\mathcal{U}_{\mathrm{TE}}$ for twiddle entries and $\mathcal{U}_{\mathrm{TX}}$ for twiddle exits) at each time-step and if the following inequality is satisfied

$$\mathcal{U}_{\mathrm{R}} \leq P_{\mathrm{R}} dt \tag{43}$$

the agent begins reversing. Likewise, if

$$\mathcal{U}_{\mathrm{TE}} \leq P_{\mathrm{TE}} dt \tag{44}$$

holds, the agent begins twiddling. Once in a twiddle, an agent cannot reverse. There is of course the chance that both conditions are satisfied at once. In such cases a weighted coin toss is used, using another number drawn from a uniform probability distribution, where if the following is satisfied

$$\mathcal{U}_{\mathrm{CP}} < \frac{P_{\mathrm{R}}}{P_{\mathrm{R}} + P_{\mathrm{TR}}},$$

the agent begins a reversal, otherwise a twiddle is initiated. The scenario is comparatively simpler considering twiddle exits, as when the following inequality is fulfilled a twiddle exit occurs,

$$\mathcal{U}_{\mathrm{TX}} < P_{\mathrm{TX}} dt. \tag{45}$$

Now that the first step in modelling when twiddle exits and reversals occur has been outlined, we describe the second step where chemotaxis is generated. Upon a twiddle exit the cell has two choices, to either twitch in the direction of increasing or decreasing concentration, a correct or incorrect decision respectively. Likewise, when the opportunity to reverse arises, the cell has two choices, to either reverse or to suppress the reversal, choices that are correct or incorrect depending on the original direction of travel relative to the concentration gradient. As we have shown experimentally that *P. aeruginosa* follows a bi-bias chemotaxis strategy (**Figure 45**) and since we are modelling twiddle exits and reversals in as similar way as possible, the same method of chemotaxis will be implemented for both behaviours. We have also seen that the proportion of 'correct' behaviours increases with $\frac{dC}{dy}_{\mathrm{EXP}}$ (**Figure 44**). The probability that a cell makes a correct or incorrect chemotactic decision depends on the value of $\frac{dC}{dy}_{\mathrm{EXP}}$ that is currently experiences. We denote these probabilities as P_{C} and P_{I} respectively, and we use these to model the bi-bias response.

Since we are interested in developing a generalised, non-dimensional model (see **Section 5.2.6**), we only need to consider the form of the relationships in **Figures 48a** and **48b**, rather than directly

measuring the chemotactic response of *P. aeruginosa* to a particular chemical gradient. Twiddles and reversals occur at fixed rates in our simulation (defined by P_{TE}, P_{TX} and P_{R} respectively), therefore, we will model a chemotactic bias by calculating the proportion of correct chemotactic decisions a cell makes for any given value of concentration gradient experienced. To do so, we must determine the probability that an agent makes the correct (P_{C}) and incorrect (P_{I}) decision at any value of $\frac{dC}{dr}_{\mathrm{EXP}}$. We calculate P_{C} (the blue line in **Figure 48a**) using

$$P_{\mathrm{C}} = m\frac{dC}{dr}_{\mathrm{EXP}} + K_{\mathrm{C}}, \tag{46}$$

and P_{I} (the red line in **Figure 48a**) using

$$P_{\mathrm{I}} = -m\frac{dC}{dr}_{\mathrm{EXP}} + K_{\mathrm{I}}. \tag{47}$$

In **Equations 46** and **Equations 47**, K_{C} and K_{I} are intercepts on the y axis of a plot of $P_{\mathrm{C/I}}$ as a function of $\frac{dC}{dr}_{\mathrm{EXP}}$ (**Figure 48**a) and are therefore rates. K_{C} and K_{I} are calculated using

$$K_{\mathrm{C}} = P_{\mathrm{B}} - m\chi \tag{48}$$

and

$$K_{\mathrm{I}} = P_{\mathrm{B}} + m\chi \tag{49}$$

respectively. Here, P_{B} represents the basal rate of correct behaviour, which is set as $P_{\mathrm{B}} = P_{\mathrm{R}}$ such that once converted to a non-dimensional form (see **Section 5.2.1**) its value is one, χ represents the minimum value of chemical gradient sensed needed to generate a chemotactic bias, and m represents the chemotactic sensitivity of a cell, i.e. its ability to respond to a chemical gradient, and is the gradient of the lines seen in **Figure 48a**. The correct and incorrect rates of behaviour are expressed graphically in **Figure 48a**. At the point where P_{I} is zero, we have the saturation point of the agents, S, which represents the largest chemical gradient that a cell can sense before before its response saturates. Therefore, an agent can sense a chemical gradient provided it is in the range $\chi < \frac{dC}{dr}_{\mathrm{EXP}} < S$, which is illustrated in **Figure 48b**.

To simplify our modelling, we calculate the proportion of correct chemotactic decisions, B, using **Equation 50**,

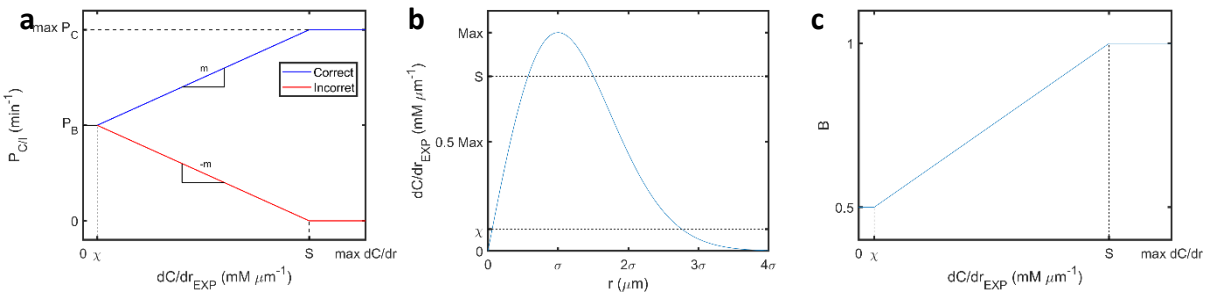

Figure 48: Implementing the experimental reversal rate bias and twiddle exit bias as a function of $\frac{dC}{dr}_{\text{EXP}}$ into a model of chemotaxis. (a) The rate of correct and incorrect chemotactic behaviour changes as a function of concentration experienced. (b) The concentration gradient experienced by each agent as a function of distance from the nutrient source. The values of χ and S are indicated with dashed lines, which represent the minimum value of concentration gradient sensed that can cause a chemotactic bias, and the the value where the response is saturated. (c) The proportion of correct chemotactic decisions as a function of concentration gradient experienced, the resultant relationship from **Equation 50**.

$$
\begin{aligned}
B &= \frac{P_{\text{C}}}{P_{\text{C}} + P_{\text{I}}} \\
B &= \frac{m\frac{dC}{dr}_{\text{EXP}} + K_{\text{C}}}{m\frac{dC}{dr}_{\text{EXP}} + K_{\text{C}} - m\frac{dC}{dr}_{\text{EXP}} + K_{\text{I}}} \\
B &= \frac{m\frac{dC}{dr}_{\text{EXP}} + K_{\text{C}}}{K_{\text{C}} + K_{\text{I}}}.
\end{aligned} \tag{50}
$$

B varies with $\frac{dC}{dr}_{\text{EXP}}$ as shown in **Figure 48c**. When $\frac{dC}{dr}_{\text{EXP}} \leq \chi$, $B = 0.5$, meaning there is an equal probability of a reversal being correct or incorrect. When $B = 0.5$, a twiddle exit has an equal probability of reorienting the movement of an agent towards or away from greater nutrient concentrations. In either case, twiddles and reversals do not contribute to chemotaxis when $B = 0.5$. In the range $\chi < \frac{dC}{dr}_{\text{EXP}} < S$, B increases, meaning the probability of an agent making the correct chemotactic choice increases, until $\frac{dC}{dr}_{\text{EXP}} \geq S$, at which point $B = 1$ such that the response is always correct. To decide if a chemotactic decision is correct, we draw another distinct number from a uniform distribution, $\mathcal{U}_{\text{B}}$, and test it using the following the following inequality,

$$
\mathcal{U}_{\text{B}} < B,
$$

which if fulfilled, means the twiddle exit direction orients an agent towards increased nutrient concentrations, suppresses a reversal if the agent is already travelling up the gradient, or reorients the agent if moving away. Otherwise, the decision will be incorrect.

Practically, B has an influence over an agent's orientation, ϕ, post reversal or twiddle. If a cell is

moving towards greater nutrient concentrations and a correct reversal event is triggered, ϕ remains the same. If an incorrect event is triggered, the agent orientation becomes $\phi + \pi$. In the case of a cell moving towards smaller nutrient concentrations, an incorrect reversal would suppress a change in orientation here, and a correct event would add π radians to the agents orientation. Twiddle exits are less complicated as they do not depend on the original orientation of the agent. A correct twiddle exit will set $\phi = \rho$ and an incorrect event will set $\phi = \rho + \pi$.

We have now summarised the two-step process that we use to model chemotaxis. The overall rate of reversals and twiddle entries is fixed, with the proportion of correct reversals and twiddle exits changing according to the chemical gradient sensed. The set-up of the simulation domain and initialisation will now be discussed.

Our simulations are run within a domain of size $16\sigma \times 16\sigma$, where σ is the standard deviation (100 μm) of a $2D$ Gaussian shaped concentration field at the middle of our domain at $x = 0$, $y = 0$. The Gaussian has a maximum concentration, C_{MAX}, of 2 mM. We define L as the shortest distance from the origin to the edge of the domain, which in this case $L = 8\sigma$ (meaning the domain size is $2L \times 2L$). We initialise cells within a square $8\sigma \times 8\sigma$ region centred on the origin, such that the majority of cells are capable of sensing the gradient when the simulation begins. We define I as the shortest distance from the origin to the edge of the initialisation region, therefore in this case $I = 4\sigma$ (meaning the initialisation size is $2I \times 2I$). Cells in our simulation navigate towards greater nutrient concentration regions by chemotaxis generated by the regulation of twiddles exits and reversals, which is balanced at steady state by diffusion of the agents that arises from the randomness of their movement direction. To fully determine the impact of these opposing processes, the simulation will be run with and without periodic boundary conditions, modelling two scenarios: the case where there is an infinite lattice of equally spaced nutrient sources, or a single nutrient source appears in an otherwise barren region of space, allowing agents to drift off and become 'lost'. Therefore, these simulations will test both the chemotactic ability of twiddles and reversals, but also their ability to prevent cells from accidental wandering away from a nutrient patch.

Agents are initialised into the $2I \times 2I$ region with periodic boundaries using a random distribution in x and y, with a ϕ randomly drawn from a unit circle. The purpose of the initialisation stage is to reproduce the conditions that would occur prior to the appearance of the nutrient source. During the initialisation period $B = 0.5$, such that twiddle exits and reversals are unbiased in their direction. At the first time point of initialisation all agents are in the non-twiddling state, and therefore the simulation must reach a steady state where the number of agents twiddling matches our experimental measurement of the number of cells twiddling at any time, 25% (see **Figure 44**). Once complete,

the final time point of the initialisation period becomes the first time point of the main simulation and periodic boundary conditions are extended to the range denoted by L if the simulation is being run with boundary conditions, or removed if the simulation is being run without them.

The process of modelling *P. aeruginosa* using twitching motility to climb a chemical gradient using appropriately biased twiddle exits and reversals has been outlined in this section, using experimentally derived parameters in all cases possible. In the upcoming sections of this chapter, the process of converting these equations into a non-dimensional form will be outlined, and the results of parameter sweeps of non-dimensional parameters discussed. A summary of the dimensional parameters values and equations used are given in **Table 5**.

Parameter	**Notation**	**Value used in model**
Cell velocity	v_{C}	0.3 μm min^{-1}
Rotational diffusion coefficient	D_{R}	0.02 rad^2 min^{-1}
Twiddle entry probability	P_{TE}	1/120 min^{-1}
Twiddle exit probability	P_{TX}	3/120 min^{-1}
Twiddle rotation rate	T_{R}	$\pi/10$ rad min^{-1}
Reversal probability	P_{R}	1/120 min^{-1}
Chemotactic sensitivity	m	20 μM min^{-1} mM^{-1}
Gradient detection limit	χ	0.002 mM $\mu\mathrm{m}^{-1}$
Basal correct behaviour rate	P_{B}	1/120 min^{-1}
Domain size	L	$-800 : 800$ μm
Initialisation size	I	$-400 : 400$ μm
Maximum concentration	C_{MAX}	2 mM
Standard deviation	σ	100 μm

Table 5: Parameters used in the dimensional model of chemotaxis facilitated by twiddles and reversals.

5.2 A non-dimensional model reveals the role of twiddles in bacterial chemotaxis

In the previous section, we have comprehensively outlined how experimental data was used to construct a model of twitching *P. aeruginosa* performing chemotaxis in a microfluidic device. Rather than restricting our analysis to scenarios that match the experimental configuration, we seek to understand how twiddles and reversals influence bacterial chemotaxis across a variety of scenarios. As such, we have converted our model into a non-dimensional form to reduce the number of parameters. Over the course of this section, we first derive the non-dimensional equations required to run the model, and use a base case run using experimentally derived parameters to validate agent behaviour. We then go on to discuss the results of our parameter sweeps, uncovering further information on the role of twiddles.

5.2.1 Development of non-dimensional equations

Creating non-dimensional equations requires converting each of the experimentally derived parameters into values that have no units by dividing by intrinsic scales of the system, for example a key length scale such as the mean run length between a run and tumble in swimming *E. coli* [27]. Once we convert our equations into a non-dimensional form, they yield non-dimensional groups that fully define the system.

Our model has three intrinsic dimensions: length, time and chemical concentration. The standard deviation of the Gaussian shaped distribution used to model the nutrient field, σ, is the characteristic length scale, the inverse of the reversal rate, P_{R}^{-1}, is the chosen as the characteristic time scale and the maximum concentration used in the microfluidic flow chamber, C_{MAX}, gives the characteristic chemical concentration. An agent's radial position, chemical concentration and time can thus be non-dimensionalised as:

$$\tilde{r} = \frac{r}{\sigma}, \qquad \tilde{t} = tP_{\mathrm{R}}, \qquad \tilde{C} = \frac{C}{C_{\mathrm{MAX}}},$$

where the presence of a tilde over a parameter indicates a non-dimensional value.

Beginning with the equations of cell movement using the change in ϕ position as an example, the non-dimensional substitutions are made

$$\begin{aligned}
\phi(t) &= \phi(t - dt) + \mathcal{N}\sqrt{2D_{\mathrm{R}}dt}, \\
\phi(\tilde{t}) &= \phi(\tilde{t} - d\tilde{t}) + \mathcal{N}\sqrt{\frac{2D_{\mathrm{R}}}{P_{\mathrm{R}}}d\tilde{t}}, \\
\phi(\tilde{t}) &= \phi(\tilde{t} - d\tilde{t}) + \mathcal{N}\sqrt{2\alpha d\tilde{t}}.
\end{aligned} \tag{51}$$

Where, ϕ is an angle and by definition already non-dimensional. The first of three non-dimensional groups is contained in this equation, α,

$$\alpha = \frac{D_{\mathrm{R}}}{P_{\mathrm{R}}}, \tag{52}$$

which specifies the rotational diffusion normalised by the reversal rate. The second non-dimensional group is identified using the equations dictating the change in position of each agent,

$$
\begin{aligned}
\frac{dx}{dt} &= v_{\mathrm{C}}\cos(\phi(t)), & \frac{dy}{dt} &= v_{\mathrm{C}}\sin(\phi(t)),\\
\sigma P_{\mathrm{R}}\frac{d\tilde{x}}{d\tilde{t}} &= v_{\mathrm{C}}\cos(\phi(\tilde{t})), & \sigma P_{\mathrm{R}}\frac{d\tilde{y}}{d\tilde{t}} &= v_{\mathrm{C}}\sin(\phi(\tilde{t})),\\
\frac{d\tilde{x}}{d\tilde{t}} &= \frac{v_{\mathrm{C}}}{\sigma P_{\mathrm{R}}}\cos(\phi(\tilde{t})), & \frac{d\tilde{y}}{d\tilde{t}} &= \frac{v_{\mathrm{C}}}{\sigma P_{\mathrm{R}}}\sin(\phi(\tilde{t})),\\
\frac{d\tilde{x}}{d\tilde{t}} &= \beta\cos(\phi(\tilde{t})), & \frac{d\tilde{y}}{d\tilde{t}} &= \beta\sin(\phi(\tilde{t})).
\end{aligned} \tag{53}
$$

The second non-dimensional group is β,

$$\beta = \frac{v_{\mathrm{C}}}{\sigma P_R}, \tag{54}$$

which specifies the non-dimensional velocity normalised by the product of the standard deviation of the nutrient concentration field represented as a Gaussian distribution, and the reversal rate. Considering the case when a cell is undergoing a twiddle, **Equations 37** and **38** simply become

$$\tilde{x}(\tilde{t}) = \tilde{x}(\tilde{t} - d\tilde{t}) \tag{55}$$

and

$$\tilde{y}(\tilde{t}) = \tilde{y}(\tilde{t} - d\tilde{t}), \tag{56}$$

however, **Equation 36** requires further modification:

$$
\begin{aligned}
\phi(\tilde{t}) &= \phi(\tilde{t} - d\tilde{t}) \pm \frac{T_{\mathrm{R}}}{P_{\mathrm{R}}}d\tilde{t}\\
\phi(\tilde{t}) &= \phi(\tilde{t} - d\tilde{t}) \pm \tilde{T}_{\mathrm{R}}d\tilde{t}
\end{aligned} \tag{57}
$$

where

$$\tilde{T}_{\mathrm{R}} = \frac{T_{\mathrm{R}}}{P_{\mathrm{R}}} \tag{58}$$

represents the non-dimensional twiddle rotation rate.

All components of cell motion have now been converted into a non-dimensional form, therefore we now consider the chemical gradient sensing mechanism. Beginning nutrient concentration field in **Equation 39**, we convert to a non-dimensional form by

$$C_{\mathrm{MAX}}\tilde{C}(r) = C_{\mathrm{MAX}}\exp\left(\frac{-r^2\sigma^2}{2\sigma^2}\right)$$
$$\tilde{C}(r) = \exp\left(\frac{-r^2}{2}\right). \tag{59}$$

The non-dimensional concentration gradient field experienced by a cell is therefore given by

$$\frac{C_{\mathrm{MAX}}}{\sigma}\frac{d\tilde{C}}{d\tilde{r}}_{\mathrm{EXP}} = \frac{\tilde{r}\sigma C_{\mathrm{MAX}}}{\sigma^2}\exp\left(\frac{-r^2\sigma^2}{2\sigma^2}\right)\cos\rho$$
$$\frac{d\tilde{C}}{d\tilde{r}}_{\mathrm{EXP}} = \tilde{r}\exp\left(\frac{-r^2}{2}\right)\cos\rho. \tag{60}$$

As an increase in concentration experienced by a cell leads to a greater number of correct chemotactic reorientations, **Equation 50** must be converted into a non-dimensional form. When calculating B the conversion of

$$\tilde{K}_{\mathrm{C/I}} = \frac{K_{\mathrm{C/I}}}{P_{\mathrm{R}}} \tag{61}$$

is used as $K_{\mathrm{C/I}}$ is a rate. B is calculated using

$$B = \frac{m\frac{d\tilde{C}}{d\tilde{r}}\frac{C_{\mathrm{MAX}}}{\sigma} + \tilde{K}_{\mathrm{C}}P_{\mathrm{R}}}{\tilde{K}_{\mathrm{C}}P_{\mathrm{R}} + \tilde{K}_{\mathrm{I}}P_{\mathrm{R}}},$$
$$B = \frac{P_{\mathrm{R}}\left(m\frac{d\tilde{C}}{d\tilde{r}}\frac{C_{\mathrm{MAX}}}{\sigma P_{\mathrm{R}}} + \tilde{K}_{\mathrm{C}}\right)}{P_{\mathrm{R}}\left(\tilde{K}_{\mathrm{C}} + \tilde{K}_{\mathrm{I}}\right)},$$
$$B = \frac{m\frac{C_{\mathrm{MAX}}}{\sigma P_{\mathrm{R}}}\frac{d\tilde{C}}{d\tilde{r}} + \tilde{K}_{C}}{\tilde{K}_{\mathrm{C}} + \tilde{K}_{\mathrm{I}}},$$
$$B = \frac{\omega\frac{d\tilde{C}}{d\tilde{r}} + \tilde{K}_{C}}{\tilde{K}_{\mathrm{C}} + \tilde{K}_{\mathrm{I}}} \tag{62}$$

yielding another non-dimensional group,

$$\omega = m\frac{C_{\mathrm{MAX}}}{\sigma P_{\mathrm{R}}}. \tag{63}$$

Here, ω represents non-dimensional cell sensitivity to the chemical gradient experienced, and which can be obtained by considering the equation for $P_{\mathrm{C/I}}$. Starting from (**Equation 46** or **47**)

$$\tilde{P}_{\mathrm{C/I}}P_{\mathrm{R}} = \pm m\frac{d\tilde{C}}{d\tilde{r}}\frac{C_{\mathrm{MAX}}}{\sigma} + \tilde{K}_{\mathrm{C/I}}P_{\mathrm{R}},$$
$$\tilde{P}_{\mathrm{C/I}} = \pm m\frac{C_{\mathrm{MAX}}}{\sigma P_{\mathrm{R}}}\frac{d\tilde{C}}{d\tilde{r}} + \tilde{K}_{\mathrm{C/I}},$$
$$\tilde{P}_{\mathrm{C/I}} = \pm\omega\frac{d\tilde{C}}{d\tilde{r}} + \tilde{K}_{\mathrm{C/I}}, \tag{64}$$

where ω arises again. Finally $\tilde{\chi}$ must be determined, representing the minimum value of $\frac{d\tilde{C}}{d\tilde{r}}_{\mathrm{EXP}}$ that chemotaxis can occur. As χ is a value of chemical gradient

$$\tilde{\chi} = \chi\frac{\sigma}{C_{\mathrm{MAX}}} \tag{65}$$

and for completeness, when substituted into **Equation 48** or **49** gives

$$\tilde{K}_{\mathrm{C/I}}P_{\mathrm{R}} = \tilde{P}_{\mathrm{B}}P_{\mathrm{R}} \mp \frac{\omega\sigma P_{\mathrm{R}}}{C_{\mathrm{MAX}}}\frac{C_{\mathrm{MAX}}\tilde{\chi}}{\sigma},$$
$$\tilde{K}_{\mathrm{C/I}} = \tilde{P}_{\mathrm{B}} \mp \omega\tilde{\chi}. \tag{66}$$

Finally the the equations that govern reversals, twiddle entries and exits must be converted to a non-dimensioanl form. The same methods outlined in **Equations 43, 44 and 45** are used yielding,

$$Pdt = \tilde{P}P_{\mathrm{B}}\frac{d\tilde{t}}{P_{\mathrm{B}}} = \tilde{P}d\tilde{t}.$$

Here, P represents any probability. Therefore reversals, twiddle entries and exits are triggered when the inequalities

$$\mathcal{U}_{\mathrm{R}} < \tilde{P}_{\mathrm{R}}d\tilde{t},$$
$$\mathcal{U}_{\mathrm{TE}} < \tilde{P}_{\mathrm{TE}}d\tilde{t},$$

and

$$\mathcal{U}_{\mathrm{TX}} < \tilde{P}_{\mathrm{TX}}d\tilde{t}$$

are fulfilled respectively (the latter assuming the agent is already undergoing a twiddle). Reversals and twiddle entries can potentially be triggered in the same time-step in the non-dimensional model,

and therefore the weighted coin toss shown changes to

$$\mathcal{U}_{\mathrm{CP}} < \frac{\tilde{P}_{\mathrm{R}}}{\tilde{P}_{\mathrm{R}} + \tilde{P}_{\mathrm{TR}}}$$

for reversal to be triggered, otherwise the agent begins a twiddle. For completion, correct chemotactic decisions are made when

$$\mathcal{U}_{\mathrm{B}} < B$$

holds, otherwise the cell will move in the incorrect direciton.

All equations required to describe a non-dimensional model of chemotaxis facilitated by biased twiddle exits and reversals have been described. The non-dimensional parameters used in the simulation derived from experimental measurement are summarised in **Table 6**.

Parameter	**Notation**	**Value**
Rotational diffusion	α	2.4
Cell velocity	β	0.72
Twiddle entry probability	$\tilde{P}_{\mathrm{TE}}$	1
Twiddle exit probability	$\tilde{P}_{\mathrm{TX}}$	3
Twiddle rotation rate	$\tilde{T}_{\mathrm{R}}$	6π
Reversal probability	$\tilde{P}_{\mathrm{R}}$	1
Chemotactic sensitivity	ω	2.1983
Gradient detection limit	$\tilde{\chi}$	0.0303
Basal correct behaviour rate	$\tilde{P}_{\mathrm{B}}$	1
Domain size	$\tilde{L}$	$-8:8$
Initialisation size	$\tilde{I}$	$-4:4$

Table 6: Parameters used in the non-dimensional model of chemotaxis facilitated by twiddles and reversals.

5.2.2 Validation of non-dimensional equations

As non-dimensional equations describing twitching facilitated chemotaxis in *P. aeruginosa* have been developed, it must now be proven that when converted back to a dimensional form, the inputs match their experimentally derived counterparts. If there are disparities between the physical inputs and the non-dimensional conversions, simulation results will not give a true representation of reality. In this section we show that for the parameters $\tilde{C}$, $\frac{d\tilde{C}}{d\tilde{r}}$, and $\tilde{P}_{\mathrm{C/I}}$ that the non-dimensional curves match those with physical units. As B is calculated using $\tilde{P}_{\mathrm{C/I}}$ and is already dimensionless, it will not be included in these analyses, as if $\tilde{P}_{\mathrm{C/I}}$ accurately returns to physical units so will B.

Conversion testing will begin with $\tilde{C}$, which is converted using the previously defined $\tilde{C} = \frac{C}{C_{\mathrm{MAX}}}$.

Converting back to a dimensional chemical gradient is performed using: We calculate $\frac{d\tilde{C}}{d\tilde{r}}$ using

$$\frac{dC}{dr} = \frac{C_{\mathrm{MAX}}}{\sigma}\frac{d\tilde{C}}{d\tilde{r}}.$$

As shown in **Figure 49a-f**, the non-dimensional values for $\tilde{C}$ and $\frac{d\tilde{C}}{d\tilde{r}}$ map back to their dimensional counterparts. Shifting focus to $\tilde{P}_{\mathrm{C/I}}$, conversation back to a dimensional form occurs through

$$P_{\mathrm{C/I}} = \tilde{P}_{\mathrm{C/I}} P_{\mathrm{R}}^{-1}$$

As shown in **Figure 49g-i**, $\tilde{P}_{\mathrm{C/I}}$ and $P_{\mathrm{C/I}}$ match upon conversion.

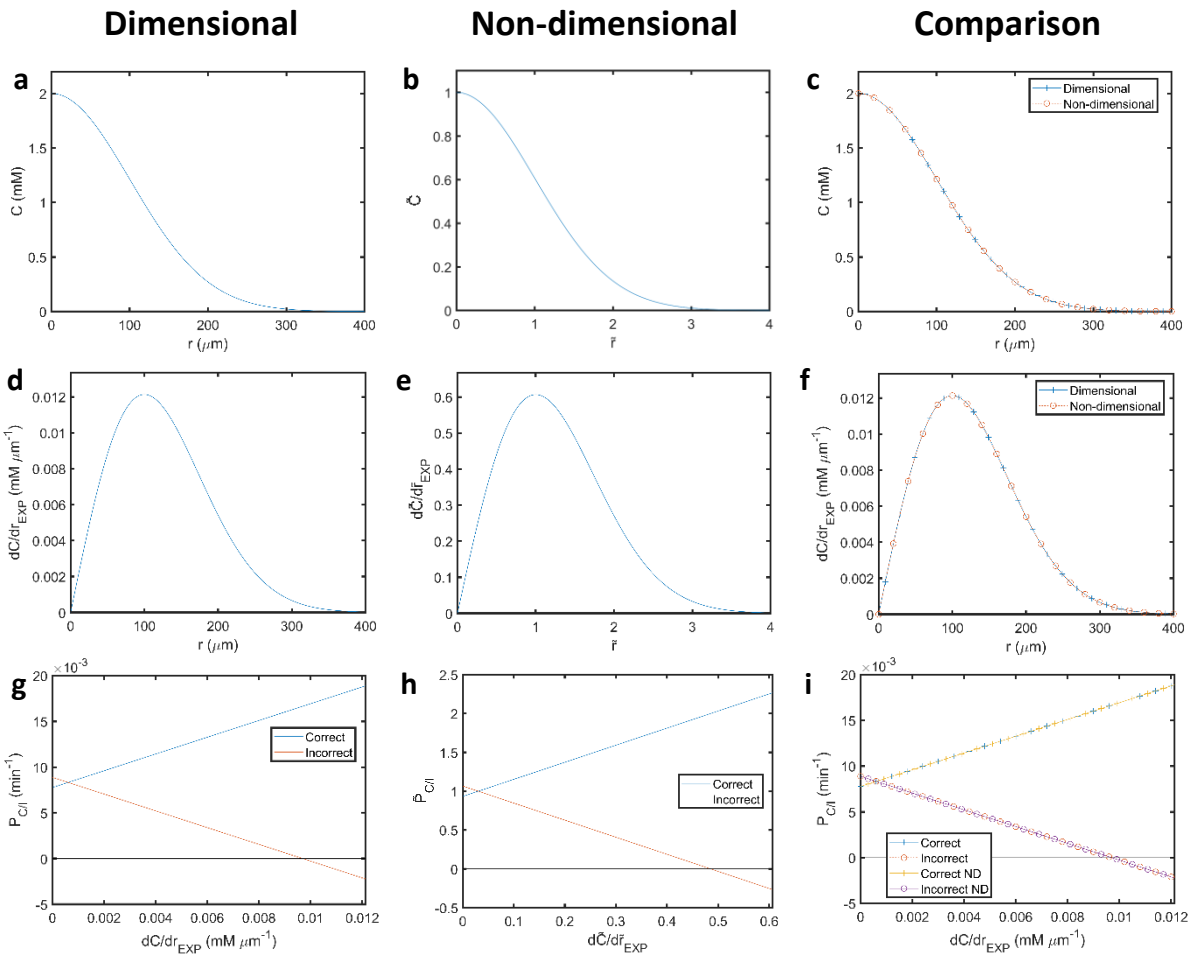

Figure 49: Conversion between dimensional and non-dimensional simulation inputs is accurate. The dimensional (a,d,g), non-dimensional (b,e,h) and the comparison between the dimensional and converted non-dimensional inputs (c,f,i). We show the concentration (a-c) and concentration gradient (d-f) as a function of distance from the source, and probability of making a correct or incorrect chemotacic decision as a function of concentration gradient experienced (g-i).

We have shown that the non-dimensional values representing nutrient concentration, gradient strength and the probability of making a correct or incorrect chemotactic choice convert back to physical dimensions accurately. These checks have ensured that results discussed in **Section 5.2.6**

are suitable for drawing conclusions about the physical system being modelled.

5.2.3 Convergence testing

A complete description of governing equations and parameters, simulation methodology and conversion to a non-dimensional form has been provided. In the following section, we show the process for choosing an appropriate time-step, $d\tilde{t}$, and total agent number, N, using both simulations that use the 'base case' of experimentally estimated parameters in addition to simulations run with more extreme values of the non-dimensional parameters. $d\tilde{t}$ must be small enough to accurately simulate cell movement, and if the time-step is too large the simulations will not reach numerical convergence, whereas a time step that is too small leads to wasted computational effort. As each agent in our simulation exhibits stochastic behaviour, we must also run our simulations with a suitable number of agents to resolve how they are distributed. As such, we discuss the set-up of a simulation base case to test these factors before parameter sweeps.

The simulated base case has been run using the parameters in **Table 6**. These simulations have been run for a total non-dimensional time ($\tilde{T}$) of $50,000{\tilde{P_{\mathrm{R}}}}^{-1}$, using 25,000 agents. We have chosen $50,000{\tilde{P_{\mathrm{R}}}}^{-1}$ as it will allow simulations to reach a steady state and is five weeks in length once converted to dimensional units, which is a reasonable time-scale for mature biofilm formation [184]. At each time point, an agent will experience a nutrient concentration, $\tilde{C}$, calculated using **Equation 59**. At each time time-step, we calculate the mean value of concentration experienced by all agents, $\tilde{C}_{\mathrm{M}}$, indicating the average fitness of a cell in a given environment. As small changes occur at each time-step, we sample data every $100d\tilde{t}$ for further analysis in post-processing. We compare three time-steps to test for convergence, $0.5\tilde{P}_{\mathrm{R}}^{-1}$, $\tilde{P}_{\mathrm{R}}^{-1}$ and $2\tilde{P}_{\mathrm{R}}^{-1}$, measuring $\tilde{C}_{\mathrm{M}}$ over non-dimensional time with periodic boundary conditions applied. One would anticipate that as $d\tilde{t}$ decreases, $\tilde{C}_{\mathrm{M}}$ will converge, such that an even smaller time step would not change our results. We see that convergence has already occurred at $2\tilde{P}_{\mathrm{R}}^{-1}$ (**Figure 50a**), therefore to ensure that the simulation runs accurately, we use $d\tilde{t} = \tilde{P}_{\mathrm{R}}^{-1}$ as our time-step. We must also ensure that we simulate an appropriate number of agents chosen as having a too few agents will lead to noisy results. In **Figure 50b**, we calculate $\tilde{C}_{\mathrm{M}}$ using an increasing number of simulated agents. As the number of agents increases, the noise decreases, until at $\mathrm{N} = 10,000$ the simulation converges and therefore, to minimise noise further we use 25,000 agents for our simulations. In **Figure 50c**, we show $\tilde{C}_{\mathrm{M}}$ measured over the simulation for 10 repeats of the simulated base case with $d\tilde{t} = \tilde{P}_{\mathrm{R}}^{-1}$ and $\mathrm{N} = 25,000$. Given the random placement of cells at the start of simulation, rotational diffusion, and the randomness in the twiddles and reversals (which both follow a Poisson distribution), we expect that there will be an element of variability

between two different runs of the same simulation. Repeated runs of our simulation yielded nearly the same results (**Figure 50c**), indicating that our results are highly robust and can be used to draw conclusions from our simulations about the behaviour of *P. aeruginosa* in this environment.

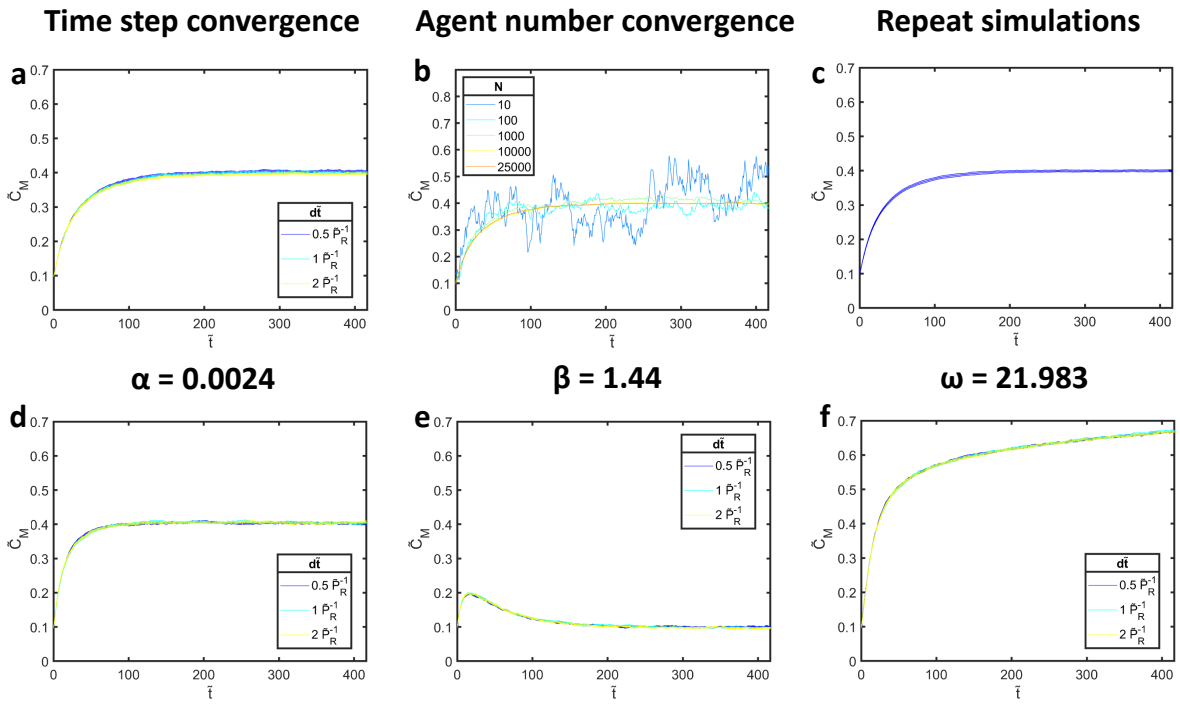

Figure 50: Determination of the simulation time-step and the number of agents to be used in parameter sweeps. Each line contains data from 25,000 agents and the shaded region shows the standard error unless specified otherwise. (a) Plotting $\tilde{C_{\mathrm{M}}}$ as a function of $\tilde{t}$ to investigate time step convergence. (b) Plotting $\tilde{C_{\mathrm{M}}}$ as a function of $\tilde{t}$ to test convergence in the number of agents used. Here each line is coloured according to how many agents are used. (c) Running 10 iterations of the base case simulation with 25,000 agents to measure the amount of noise in each simulation run. (d-f) Testing time-step convergence by measuring C_{M} as a function of $\tilde{t}$ for relatively small α, large β and large ω simulations.

Despite being able to draw conclusions on the behaviour of chemotaxing bacteria in our experimentally derived base case, it is currently unclear if the simulation can be relied upon to produce meaningful results at extreme values of the parameter sweeps that will be performed. To test this, we have run the time-step checks seen in **Figure 50a** at extreme values of α, β and ω, to test the movement and chemotactic ability of agents. We are most interested in the movement properties of our agents here, as if the simulation time-step is not suitably large at small values of α ($\alpha = 0.0024$) and large values of β ($\beta = 1.44$) we will incorrectly simulate the twitching behaviour of *P. aeruginosa*. **Figures 50d**, **50e** and **50f** show small values of α and large values of β and ω respectively. In all cases, we observe convergence at a time step of $\tilde{P}_{\mathrm{R}}^{-1}$, indicating that our simulations conducted using this step step can be trusted even when our parameters are at extreme values.

In this section we have shown that our base case simulation converges for all time-steps tested and for an appropriate number of agents, choosing suitable values for N and $d\tilde{t}$. Additionally, we have

validated these choices for more extreme values of simulation parameters that govern physical and chemotactic properties of agents. Now, we will validate that the physical and chemotactic behaviour of our agents matches simulated inputs.

5.2.4 Agent behaviour validation

To ensure that the simulation is running correctly we used the model's output to see if we could recover the same parameters that were used as model inputs. Therefore, in the coming section we ensure that B is recovered from simulations that were run with the base case set of parameters, along with $\tilde{P}_{\mathrm{R}}$, $\tilde{P}_{\mathrm{TE}}$ and $\tilde{P}_{\mathrm{TX}}$. We then move onto recovering α, which subsequently leads to an investigation into how different chemotactic strategies influence rotational and translational diffusion.

We begin our series of behaviour validations with B, which represents the chance an agent has of making a chemotactic choice that drives itself towards larger nutrient concentrations depending on $\frac{d\tilde{C}}{d\tilde{r}}_{\mathrm{EXP}}$. At each twiddle exit or reversal, we record the value of $\frac{d\tilde{C}}{d\tilde{r}}_{\mathrm{EXP}}$ and keep a count of the correct (N_{C}) and incorrect (N_{I}) chemotactic decisions in terms of twiddle exits and reversals, allowing the calculation of B through

$$B = \frac{N_{\mathrm{C}}}{N_{\mathrm{C}} + N_{\mathrm{I}}}.$$

We are then able to bin N_{C} and N_{I} for twiddle exits and reversals by $\frac{d\tilde{C}}{d\tilde{r}}_{\mathrm{EXP}}$ and compare the results to the simulation input as shown in **Figure 51a**, which displays a strong match between B defined by $\tilde{\chi}$ and ω, and measured B. For completion, we show that the chance of undergoing a correct chemotactic decision is greater when ρ is near zero and decreases as ρ approaches $\frac{\pi}{2}$ (**Figure 51b**). We must now confirm that the rate of reversal, twiddle entry and exit match the values defined to run the simulation. To do so, the number of reversals, twiddle entries and exits are counted for each agent and divided by the amount of time available to perform each operation, then a mean is taken. The time available to reverse is equal to the time a cell spends not twiddling, and the time available to enter a twiddle is the same time minus a time-step for each reversal, as each behaviour cannot occur concurrently. The time available to exit a twiddle is the amount of time spent twiddling, with one time-step removed for each twiddle, as a cell cannot exit a twiddle on the same time-step it enters a twiddle. For $\tilde{P}_{\mathrm{R}}$, $\tilde{P}_{\mathrm{TE}}$ and $\tilde{P}_{\mathrm{TX}}$, we measure 1.00, 1.00 and 2.98 respectively, which are all suitably similar to the initially defined values.

Having validated the chemotactic behaviour, we seek to recover α from our simulation. To do so, we must measure RMS$\Delta\phi$, as done using **Equation 29**, but for our simulated results. To retrieve α, we must perform measurements on agents that do no twiddle or reverse, as each behaviour type

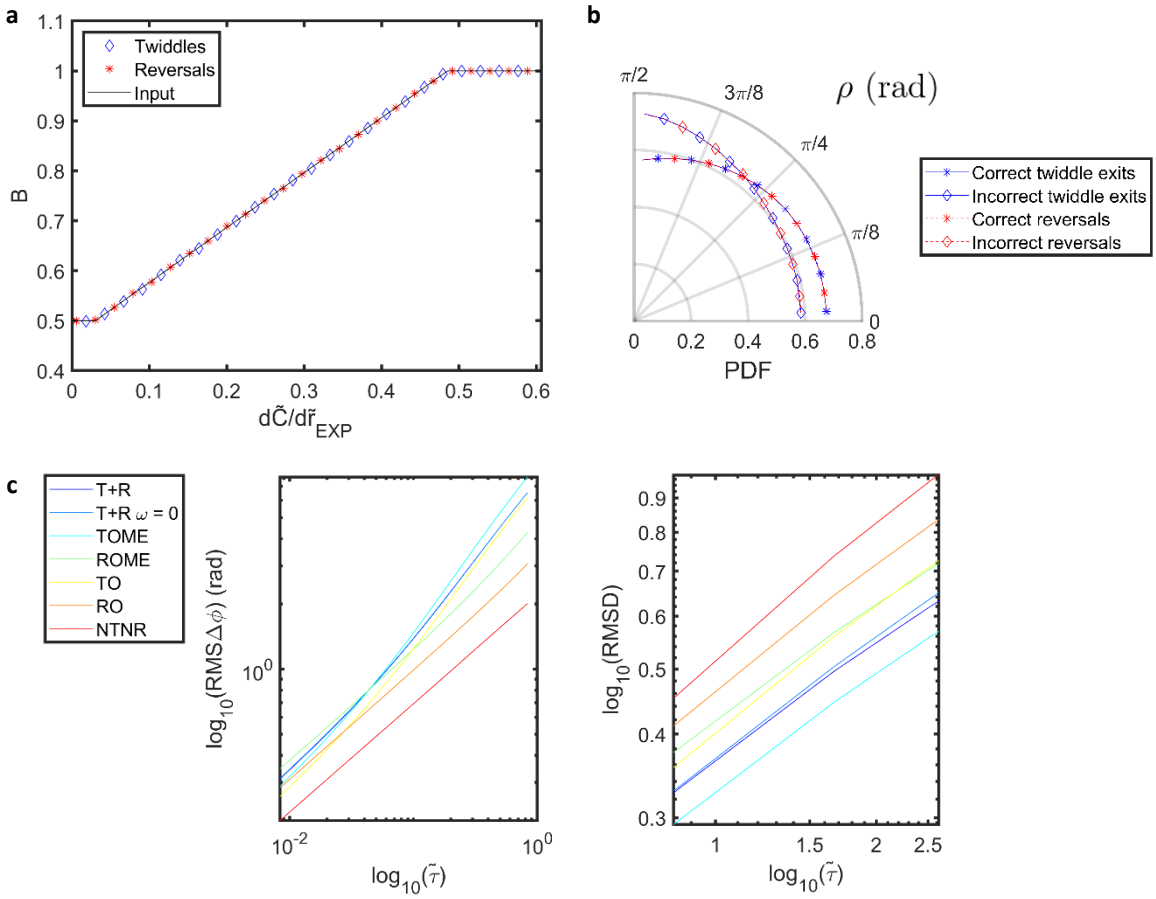

Figure 51: Measuring the chemotactic properties and movement of simulation agents to match the defining parameters. Plots presented are run without boundaries and show the results for 25,000 agents. (a) The proportion of correct twiddle exits and reversals as a function of $\frac{d\tilde{C}}{d\tilde{r}}_{\text{EXP}}$ matches the defined behaviour rate. Data shown is for agents that twiddle and reverse. Bin size is 0.0121. (b) The probability of exiting a twiddle or reversing correctly or incorrectly as a function of ρ. Data shown is for agents that twiddle and reverse. Bin size is $\frac{\pi}{32}$ rad. (c) RMS$\Delta\phi$ as a function of $\log_{10}(\tilde{\tau})$ for different agent behaviours. Modelling the non-twiddling non-reversing cells allows RMS$\Delta\phi$ line fitting to return the experimentally derived value of α. (d) RMSD as a function of $\log_{10}(\tilde{\tau})$ for different agent behaviours.

acts to increase the change in ϕ over the same time period. Therefore, we perform the same RMS$\Delta\phi$ analysis used to measure D_{R} of non-twiddling and non-reversing cells on our simulated agents to obtain α. We found that using sampled data gave inaccurate results, therefore we use the first 100 time-steps of our simulation for all agents rather than sampled data, obtaining $\alpha = 2.4$, matching the experimentally derived value.

In this section we have shown that both the physical and temporal parameters set to define agent behaviour in the simulation are recovered through measurment. These checks are important to ensure that the simulation is running correctly and allows for the extraction of results that have meaning in the context of understanding the purpose of biased twiddles and reversals in twitching chemotaxis.

5.2.5 Quantifying translational and rotational diffusion in different chemotactic strategies

We sought to quantify the rotational and translational diffusion of other behaviour types that we can simulate and use in our parameter sweeps to compare the effectiveness of different chemotactic strategies. To isolate the different role that reversals and twiddles play in pili-based chemotaxis, as well as identify potential synergies, we will use simulations with the following characteristics:

- T+R: Twiddles and reversals: agents twiddle and reverse at the rate dictated by $\tilde{P}_{\mathrm{R}}$, $\tilde{P}_{\mathrm{TE}}$ and $\tilde{P}_{\mathrm{TX}}$.
- T+R $\omega = 0$: Twiddles and reversals with no chemotaxis: The rates described in the T+R case still apply, however reversals and twiddle exits are unbiased in their direction.
- TOME: Twiddles only matching events: No reversals, and the number of twiddle exits matches the total number of chemotactic events in the T+R case. $\tilde{P}_{\mathrm{R}} = 0$, $\tilde{P}_{\mathrm{TE}} = 2\tilde{P}_{\mathrm{TE}_0}$ and $\tilde{P}_{\mathrm{TX}} = \tilde{P}_{\mathrm{TX}_0}$, where $\tilde{P}_{\mathrm{TE}_0}$ and $\tilde{P}_{\mathrm{TX}_0}$ represents the twiddle entry rate and twiddle exit rate from the T+R case respectively.
- ROME: Reversals only matching events: No twiddles, and the number of reversals matches the number of chemotactic events in the T+R case. $\tilde{P}_{\mathrm{R}} = 2\tilde{P}_{\mathrm{R}_0}$, $\tilde{P}_{\mathrm{TE}} = 0$, where $\tilde{P}_{\mathrm{R}_0}$ represents the rate of reversal from the T+R case.
- TO: Twiddles only - reversals are switched off. Twiddle entry and exit rates are dictated by $\tilde{P}_{\mathrm{TE}}$ and $\tilde{P}_{\mathrm{TX}}$ and $\tilde{P}_{\mathrm{R}} = 0$.
- RO: Reversals only - twiddles are switched off. Reversals occur with rate $\tilde{P}_{\mathrm{R}}$, and $\tilde{P}_{\mathrm{TE}} = 0$.
- NTNR: no twiddles and no reversals - all chemotactic behaviour is removed and agents act as particles undergoing Brownian rotational diffusion.

For the TOME and ROME cases, we multiply the rate of remaining behaviour (twiddle entry and reversal rate respectively) by two to ensure the same number of chemotactic events (twiddle exits and reversals) occur as in the T+R case. We are able to multiply by two since their rates of occurrence as measured experimentally are the same. By doing so, we compare the effectiveness of each chemotactic strategy rather than the number of events occurring.

We calculate RMS$\Delta\phi$ for all the above behaviour types, as shown in **Figure 51c**. As anticipated, over the long-term, any behavioural type that involves twiddling has an increased RMS$\Delta\phi$ compared

to those that do not twiddle. We find that TOME agents have the most rotational diffusion, which is unsurprising as they spend the most time twiddling.

What is perhaps more interesting is the effect that each behaviour type has on the translational diffusion of the simulated agents, as this will impact an individuals ability to navigate towards nutrient sources and climb chemical gradients. We calculated RMSD using **Equation 24** for all behaviour types and display the results in **Figure 51d**. Although TOME cells have the largest RMS$\Delta\phi$, they have the smallest RMSD, which arises as cells spend more time stationary (the cell centroid remains fixed in place whilst they are twiddling) as they twiddling at twice the frequency of T+R agents. We then observe that T+R and T+R $\omega = 0$ agents have the next largest RMSD, then ROME and TO cells. Cells that spend more time twiddling experience the smallest amount of translational diffusion, and this effect is increased when doubling their rate of occurrence (e.g. comparing TOME with TO). We also see an increase in translational diffusion when moving from the RO to ROME strategy. Increasing translational diffusion can help a cell find a nutrient patch, however it can also cause an individual to more like to wander away from a patch it has already found.

In this section we have shown that the output from our simulations recovers the same parameters that were used to run the model. These checks are important to ensure that the simulation is running correctly. We have begun to probe how the frequency and type of chemotactic behaviour influences diffusion. These relationships will be investigated further through parameter sweeps.

5.2.6 Results of parameter sweeps

Having validated the behaviour of our simulated agents, we now run parameter sweeps to investigate the conditions under which twiddles and reversals help or hinder chemotaxis. Before doing so, we discuss how the fitness of each parameter sweep is measured using the base case (using parameters from **Table 6**) as an example. By plotting a subset of simulated agents, we show how chemotaxis from biased twiddle exits and reversals drives cells to increased concentration regions at the centre of the domain (**Figure 52a**). An accumulation of agents develops at the centre of the domain when periodic boundary conditions are applied and when there are no boundaries to the simulation. The accumulation at the domain centre appears to be of greater density in the periodic boundary case than without. Additionally the density of agents appears to be larger at distances in the range $4 \leq \tilde{r} < 8$. One would anticipate that the density is increased when periodic boundaries are applied, as an agent cannot become 'lost' like when the simulation borders are removed. To validate this claim, we calculate the probability an agent has of appearing at a given $\tilde{r}$ (**Figure 52b**). We plot the distribution of agents at the beginning of the simulation to ensure that the same starting

conditions are present. At the simulation end, we see a marginally larger density of agents at the centre of the simulation when periodic boundaries are applied.

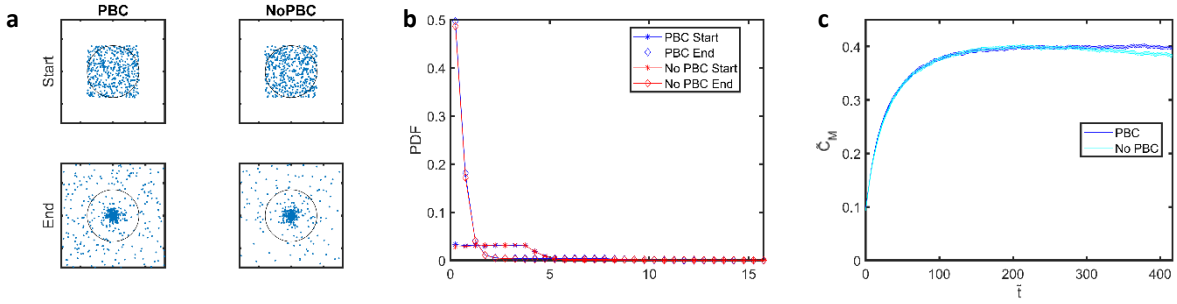

Figure 52: Results from the simulation base case with and without periodic boundary conditions. (a) Start and end positions of simulation agents with and without periodic boundary conditions. A subset of 500 agents is shown, each as a blue spot. Each box is $2\tilde{L} \times 2\tilde{L}$ (16×16) in size, equalling the domain size when periodic boundary conditions are applied. The black circle indicates a radius of 4. (b) PDF of radial agent positions at the start and end of the simulation normalised by annulus area. Bin size is 0.5. (c) Mean concentration experienced of all simulation agents with and without periodic boundary conditions. The shaded region indicates the standard error in $\tilde{C}_{\mathrm{M}}$ between $25,000$ agents.

We probe how each behaviour type influences agent fitness by measuring how $\tilde{C}_{\mathrm{M}}$ changes over time (**Figure 52c**). Each parameter sweep uses a set of values like those defined in **Table 6**, and to compare sweeps we will need to represent $\tilde{C}_{\mathrm{M}}$ as a single value. Therefore, we will measure the mean value of $\tilde{C}$ that all cells experience within a given time period, $\tilde{C}_{\mathrm{MM}}$, as means of comparing the effectiveness of twiddles and reversals at facilitating chemotaxis. Most simulations have an early phase where cells climb the gradient, then a later phase, where the change in $\tilde{C}_{\mathrm{M}}$ is small or it is stable. As our simulations run for a non-dimensional time equivalent to five weeks, over which a mature biofilm can form [185], we measure $\tilde{C}_{\mathrm{MM}}$ for the first and final 15% of the simulation, referred to as the early and late phase respectively.

For the base case, in the early time period we measured $\tilde{C}_{\mathrm{MM}}$ with and without periodic boundaries to be 0.268 ± 0.002, and in the late stage as 0.395 ± 0.003 and 0.384 ± 0.002 with and without periodic boundaries respectively (errors calculated using the standard error in the mean). These are extremely small differences, arising most likely from cells in the non-periodic boundary case only just starting to drift beyond where the boundaries would be in the equivalent case. Once differing values of the parameters are used to run the simulation, we anticipate seeing an increased difference in $\tilde{C}_{\mathrm{MM}}$ between the two boundary conditions. With validation of chemotaxis occurring and an explanation of our fitness measurement in place, we now discuss the results of the parameter sweeps performed.

We begin with α, non-dimensional rotational diffusion, with results shown in **Figure 53**. A common feature of all conditions with increased rotational diffusion ($\log_{10}(\alpha/\alpha_0) \geq 2$), is a convergence

of $\tilde{C}_{\mathrm{MM}}$ to a relatively small value ($\tilde{C}_{\mathrm{MM}} \leq 0.1$). One would anticipate that in these conditions rotational diffusion is so large that agents become restricted to moving within a small region of space in the domain, essentially becoming fixed in place as there is no movement in one persistent direction. In the early phase, the case with and without periodic boundary conditions is nearly identical, and the benefit is seen for TO cells when $\log_{10}(\alpha/\alpha_{\mathrm{o}}) < -0.5$ and for TOME cells when $\log_{10}(\alpha/\alpha_{\mathrm{o}}) < -1.5$ over those that which reverse. In the late phase of the simulation, all agent behaviour types perform similarly when periodic boundary conditions are applied, until α is very small at $\log_{10}(\alpha/\alpha_{\mathrm{o}}) < -2$,

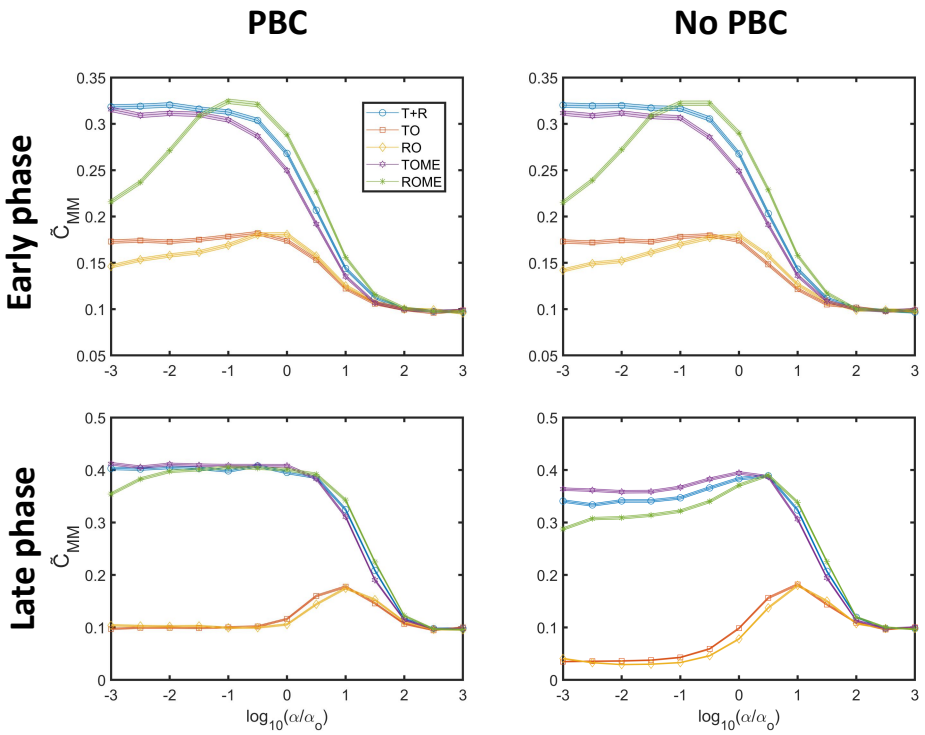

Figure 53: Results of the α parameter sweep for the early and late phase of the non-dimensional simulation. The shaded region indicates the standard error in $\tilde{C}_{\mathrm{MM}}$ between 25,000 agents.

where T+R and TOME agents begin to outperform ROME cells. Twiddles display the greatest benefit during the late phase of the simulation when periodic boundary conditions are removed, and agents become lost. Here, TOME agents begin to outperform all others when $\log_{10}(\alpha/\alpha_{\mathrm{o}}) < 0.5$. We also observe T+R cells outperforming ROME agents in this range.

The results shown in **Figure 53** display a common trend observed in nearly all other parameter sweeps, that agents which perform a greater number of chemotactic events (e.g ROME agents perform more reversals than RO agents), experience greater concentrations of nutrient on average. Additionally, we typically see an increase in $\tilde{C}_{\mathrm{MM}}$ when periodic boundaries are applied. The increase arises as cells are unable to become lost from the nutrient patch and therefore have a greater probability of encountering increased nutrient concentration regions again. Although these are obvious conclusions,

we have commented on them during our first parameter sweep and will not on subsequent sweeps, unless these trends change.

We attribute the relative increase in chemotactic performance of agents able to twiddle in conditions with reduced rotational diffusion to their capability to turn the cell. When rotational diffusion is sufficiently small, an agent is unable to turn without twiddling, resulting in straight lined trajectories. Given the concentration field is radial, and the paths are straight, this means there is a maximum value of $\tilde{C}$ each agent can reach. A twiddle therefore enables a cell to reach increased nutrient concentrations under conditions where turning through normal twitching motility is restricted (which is investigated further in **Figure 61** after the discussion of parameter sweeps performed in experimentally derived conditions).

Parameter sweeps for non-dimensional velocity, β, are shown in **Figure 54**. A key feature of all plots here is the improved performance of reversing cells at decreasing values of β/β_o. Reversing cells continue to perform the best until β/β_o approaches zero, where all conditions perform equally. The equal performance arises due to the uniform random placement of cells at the simulation start, where they remain for the entire duration when $\beta = 0$. In the early phase, we see ROME agents out compete all others until a cross over at $\beta/\beta_o = 1.67$ for both boundary conditions. Once beyond this

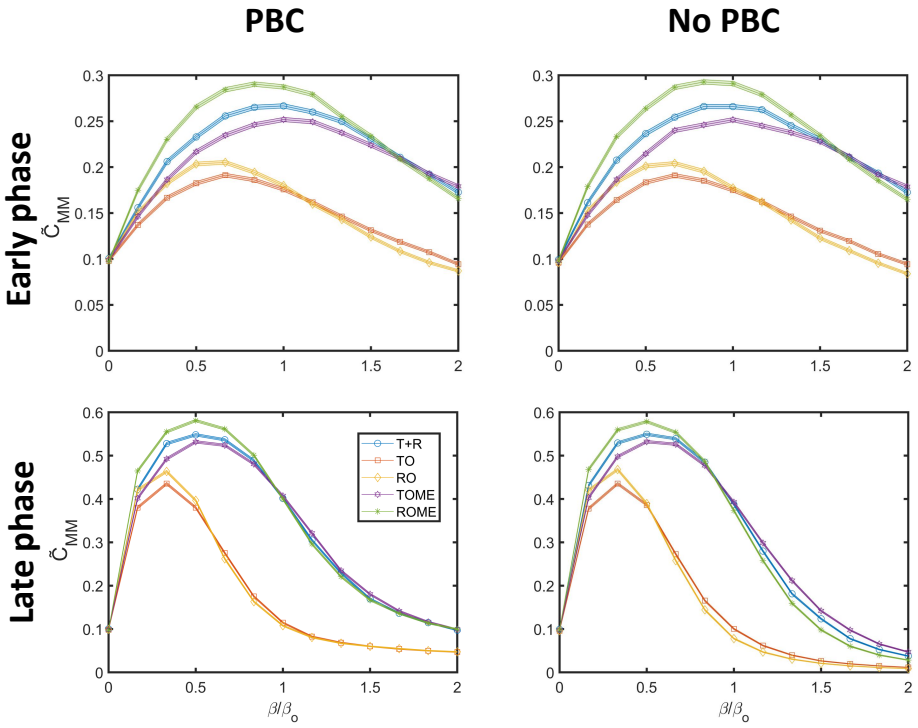

Figure 54: Results of the β parameter sweep for the early and late phase of the non-dimensional simulation. The shaded region indicates the standard error in $\tilde{C}_{\mathrm{MM}}$ between 25,000 agents.

value, TOME cells perform best, however the increase is not large at the maximum value of our

sweep. A similar crossover also exists for TO and RO cells, occurring at $\beta/\beta_o = 1.17$. Once the simulation reaches the late phase, the cross over is extremely small when periodic boundary conditions are applied, however, it persists above $\beta/\beta_o = 0.833$ when periodic boundaries are removed. During twitching motility, twiddles act to pause cell movement (cells rotate while their centroid remains stationary), giving *P. aeruginosa* a greater opportunity of experiencing increased nutrient concentrations if already in a high concentration region, or if quickly moving away from the source.

As velocity decreases, each agent will travel shorter distances in between reorientation events. In the case where a cell either twiddles or reverses but not both (TO and RO strategies), the RO strategy performs better than the TO strategy because the reorientation of the direction of travel towards increased nutrient concentrations is instantaneous. The instantaneous turn means whilst other cells are twiddling and remain stationary, those only capable of reversing travel towards larger nutrient concentrations. However, if cell velocity is too great, agents risk overshooting the chemical source or even becoming lost. Therefore, when cells travel at relatively large velocities, twiddling causes them to pause in high concentration regions, acquiring more nutrients whilst doing so.

For cells at the same orientation and position in the simulation, twiddle exits and reversals have equal probabilities of making the correct chemotactic decision. When moving with large velocities, the pauses in translational movement twiddles generate allow our agents to experience larger nutrient concentrations on average, as at increased velocities diffusion acts to drive agents away from the nutrient source at a faster rate. As there appears to be an interplay between cell velocity, and the amount time of agents spend stationary by rotating in a twiddle, which we investigate further in **Figure 62**.

To better understand how the length of a pause in movement caused by a twiddle influences the fitness of *P. aeruginosa*, we run parameter sweeps varying $\tilde{P}_{\mathrm{TX}}$ (**Figure 55**). In all cases we have run scenarios with RO and ROME agents (in which RO has half the reversal rate of ROME) to ensure the simulation is functioning correctly, and to provide a comparison for very long and instantaneous twiddles. In all cases, when $\log_{10}\left(\tilde{P}_{\mathrm{TX}}\right)$ is suitably large, twiddles become instantaneous and are effectively reversals, hence the convergence to RO and ROME like performance. It is therefore expected that in the early phase, as $\log_{10}\left(\tilde{P}_{\mathrm{TX}}\right)$ decreases, the performance of twiddling cells drops, as the response to the gradient becomes slower as the amount of time between a twiddle entry and exit increases. For the late phase, as found at large α values ($\log_{10}\left(\tilde{P}_{\mathrm{TX}}\right) \leq -3$), behaviour types with a greater number of twiddles and reversals (T+R and TOME strategies) perform similarly to those with a reduced amount (TO and RO strategies). When $\log_{10}\left(\tilde{P}_{\mathrm{TX}}\right) \leq -3$, cells enter a twiddle and do not leave as they have an extremely small probability of doing so. The similarity in $\tilde{C}_{\mathrm{MM}}$ in

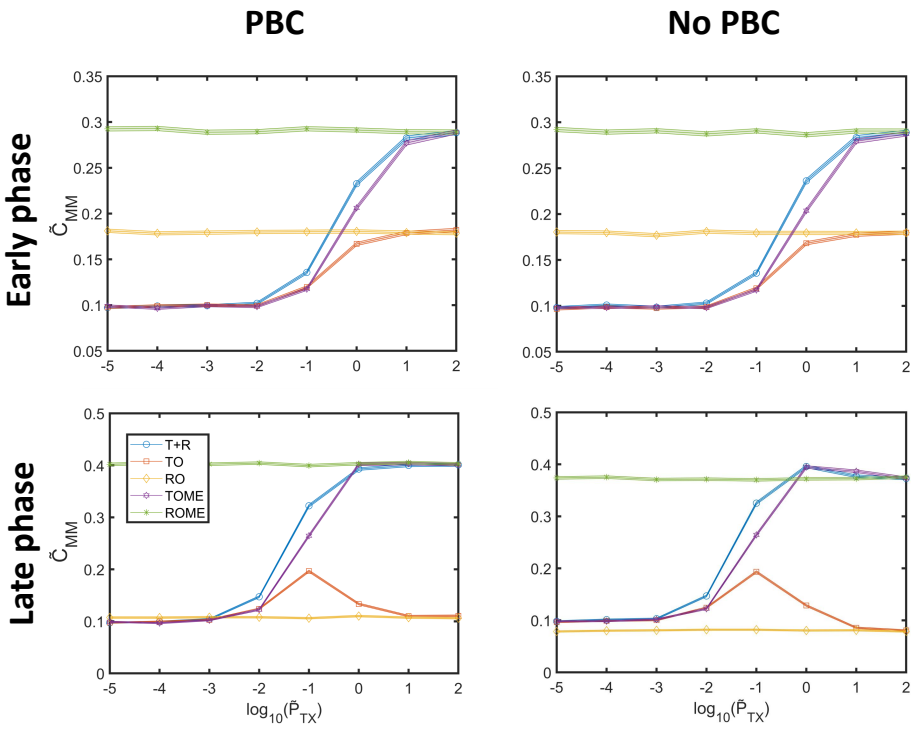

Figure 55: Results of the $\tilde{P}_{\mathrm{TX}}$ parameter sweep for the early and late phase of the non-dimensional simulation. The shaded region indicates the standard error in $\tilde{C}_{\mathrm{MM}}$ between 25,000 agents.

between T+R, TOME, TO and RO agents with boundaries applied implies that entering a twiddle and never leaving is just as effective as a strategy for acquiring nutrients as performing reversals at a reduced rate ($0.5\tilde{P}_{\mathrm{R}}$). The improvement arises in the case without periodic boundaries when agents can become lost to the source if they do not enter a never ending twiddle.

Mainly included for completeness, parameter sweeps for varying $\tilde{T}_{\mathrm{R}}$, are shown in **Figure 56**. These sweeps effectively represent the base case however where agents are able to sample the angles in a twiddle at a faster rate. As the angle of a cell has no bearing in over when a twiddle exit occurs, the rate of sampling has no impact on the fitness of any behaviour type.

We now consider the gradient strength sensing parameters, beginning with ω (**Figure 57**), which represents the sensitivity of a bacterium to the chemical gradient. When ω is small ($\omega \leq 2$), the agents respond weakly to a chemical gradient, meaning there is a reduced bias in twiddle exit and reversal direction. As ω ($2 < \omega$) increases, the agents respond more accurately to a chemical gradient, increasing their chemotactic bias. The increase in bias is reflected in rising $\tilde{C}_{\mathrm{MM}}$ as ω increases in all scenarios. During the early phase ROME cells outperform all other behaviour types by a large amount, most likely because they are able to quickly respond to the chemical gradient in comparison to twiddles, which cause the cells to pause in one position. When ω is sufficiently large, the chemotactic decision will nearly always be correct, and therefore, reversals provide each agent with the

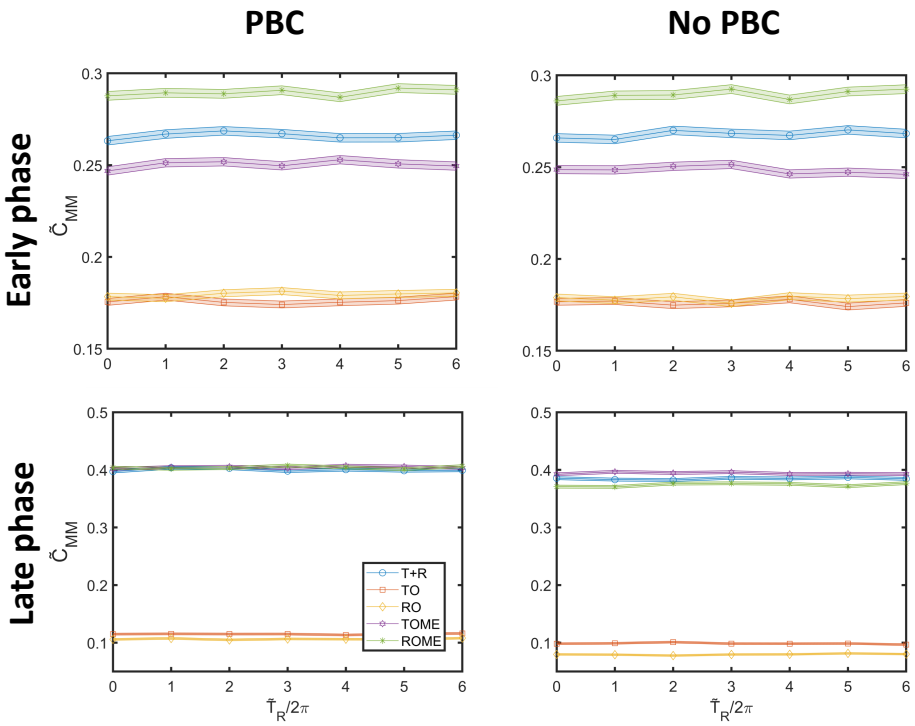

Figure 56: Results of the $\tilde{T}_{\mathrm{R}}$ parameter sweep for the early and late phase of the non-dimensional simulation. The shaded region indicates the standard error in $\tilde{C}_{\mathrm{MM}}$ between 25,000 agents.

opportunity to always drive themselves instantaneously towards increased nutrient concentrations. We see in **Figure 51c** that when chemotactic behaviour is present, reversing cells have the largest RMSD, and therefore explore the surface at the fastest rate. If a cell is exploring the surface at a fast rate and always making correct chemotactic decisions, it will likely navigate towards regions of greater nutrient concentration rapidly, which explains why we see an increased performance in agents that do not twiddle at large ω. In contrast, twiddles cause a cell to pause and reduce translational diffusion relative to reversals. As ω decreases and the probability of making a correct chemotactic decision falls, ceasing movement allows an individual to experience greater nutrient concentrations for longer on average. Cells that are paused remain in regions with a large nutrient concentration, whilst those only able to chemotax poorly continue to drift away due to diffusion. The increased performance of reversing behaviour is present for large ω in all cases, then as ω decreases the benefit of twiddling is seen in the late phase with no boundaries applied.

The second sensing parameter is $\tilde{\chi}$, representing the minimum value of chemical gradient sensed that generates a chemotactic bias. As $\tilde{\chi}$ gets larger, the minimum gradient required to perform chemotaxis increases, until at one we are simulating the case with no chemotaxis. We observe that as $\tilde{\chi}$ tends to one, the average concentration experienced decreases (**Figure 58**). In the early phase at large $\tilde{\chi}$, we observe a tiny increase in the performance of agents that twiddle over ones that

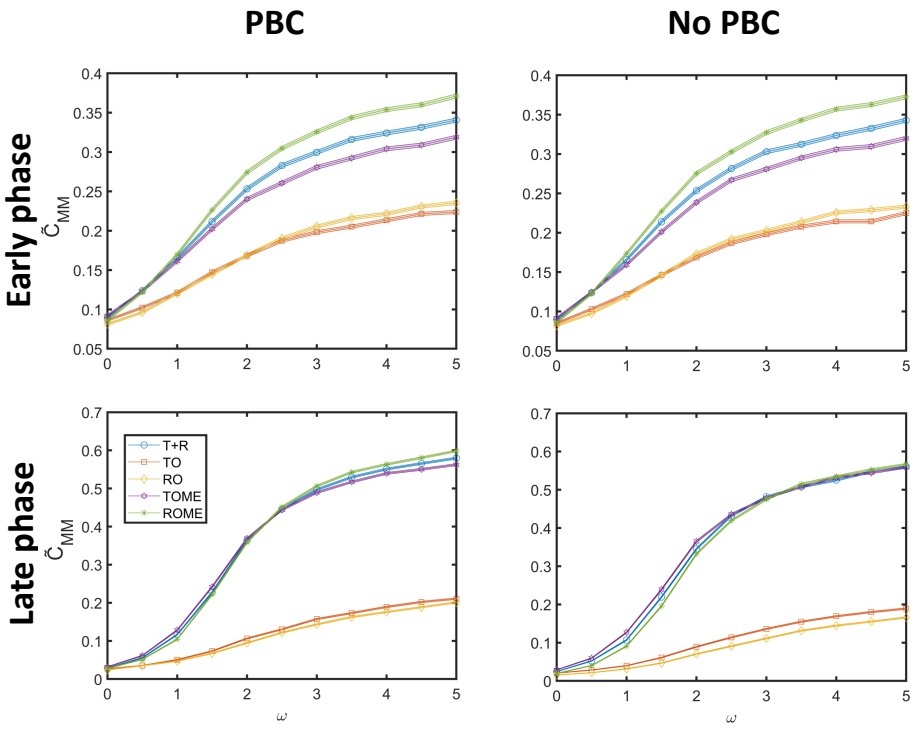

Figure 57: Results of the ω parameter sweep for the early and late phase of the non-dimensional simulation. The shaded region indicates the standard error in $\tilde{C}_{\mathrm{MM}}$ between 25,000 agents.

reverse, most likely due to cells pausing as they diffuse away from the nutrient source. The effect of chemotaxis is introduced as $\tilde{\chi}$ approaches zero, where we see similar performance between TO and RO agents, but an increased performance for cells that reverse for the T+R, TOME and ROME cases in the early phase. The benefit of reversing diminishes in the late phase, with a negligible separation in performance in twiddling agents when periodic boundary conditions are applied, however when removed, there is a small benefit to twiddling. Taken together, as one might expect cells capable of sensing smaller gradient strengths and are more likely to respond correctly and perform better. Perhaps more importantly though, these sweeps on the chemotactic properties of our simulated agents suggest once again, that reversing cells perform best in early time periods, and the benefit of twiddling is found at later times.

We now consider how the region over which cells are initialised, $\tilde{I}$, and domain size, $\tilde{L}$ has an impact on the chemotactic performance of our agents. Considering the former first, we observe an equal performance between T+R, TOME and ROME cells during the early phase for $\tilde{I} \leq 3$ (**Figure 59**). As $\tilde{I}$ increases, we see ROME cells out competing all other behaviour types. TO cells have a small advantage over RO agents when $\tilde{I} \leq 2$ but this advantage vanishes quickly as the initialisation size increases. During the late phase, cells that twiddle outperform all others when $\tilde{I}$ decreases ($\tilde{I} \leq 3$) however, once $\tilde{I} > 4.5$ we see ROME cells perform highest and the fitness of TOME cells falls

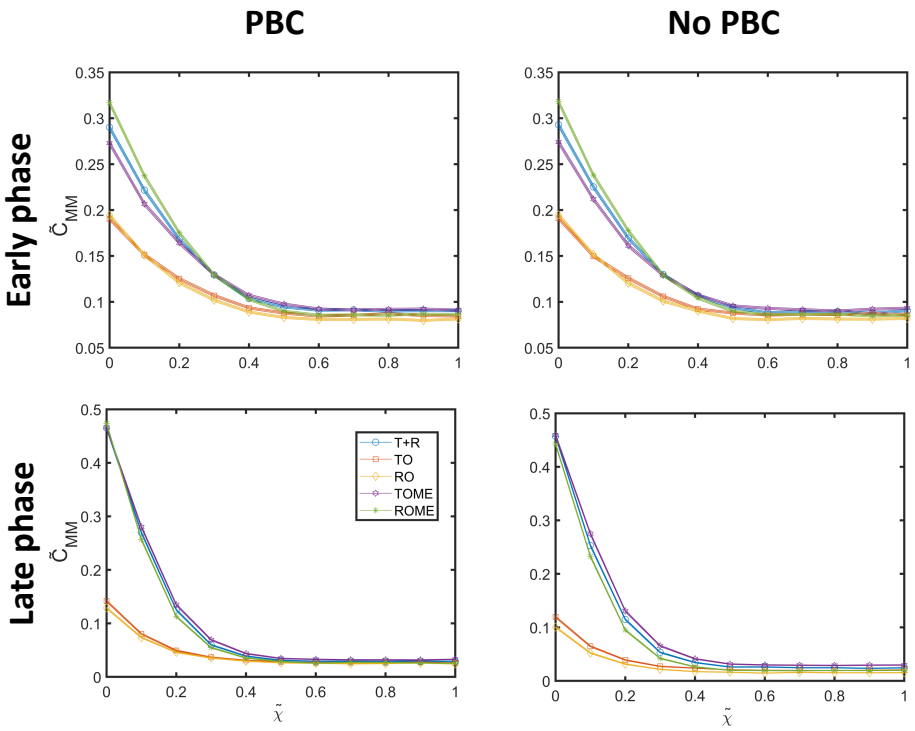

Figure 58: Results of the $\tilde{\chi}$ parameter sweep for the early and late phase of the non-dimensional simulation. The shaded region indicates the standard error in $\tilde{C}_{\mathrm{MM}}$ between 25,000 agents.

rapidly for the periodic boundary case. We observe the same crossover when periodic boundaries are removed but to a smaller extent. We attribute the improved relative performance of agents that can twiddle at reduced $\tilde{I}$ to the reduced diffusivity of TOME cells. As cells are already close to the nutrient source, they have a large probability of staying there through biased twiddle exits and experience a greater concentration of nutrients as they pause before undergoing reorientations. However, when $\tilde{I}$ increases ($\tilde{I} \geq 5$), the random placement of agents occurs over a greater area, the increased diffusivity that reversals offer aid the agents in finding the nutrient patch. Of course, this increase in diffusivity is helped by the periodic boundary conditions, as the agents are always within a set distance of the nutrient patch and are capable of finding it in a shorter time period.

We now consider how $\tilde{L}$ influences chemotaxis. As the no boundary case has no domain size it has not been included here. We reach the anticipated result that smaller domain sizes improve the chemotactic performance of all behaviour types, as the nutrient patch of the same size is confined to a smaller area, increasing each agent's probability of encountering it (**Figure 61**). Given the agents are initialised in a region of fixed size $4\tilde{I}^2$ in an area of size $4\tilde{L}^2$ it is likely that for large $\tilde{L}$ the simulation is essentially running without boundaries, as agents have not reached the edge in the simulation time. We see a plateau in the stable phase as $\tilde{L}$ increases, and the simulation behaves as if there are no boundary conditions. With $\tilde{L}$ discussed, this completes our parameter sweeps based

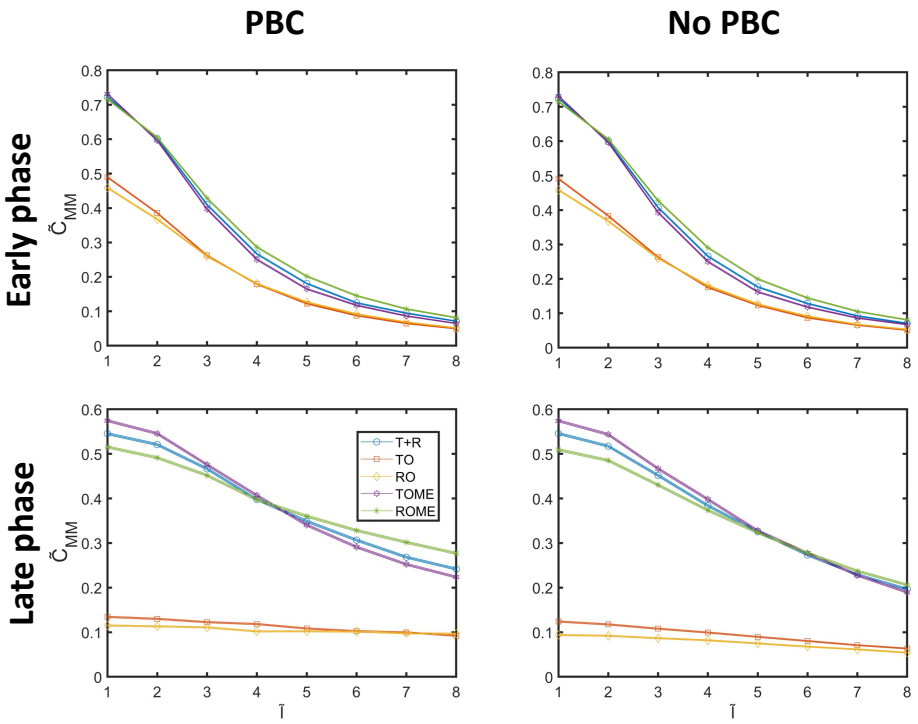

Figure 59: Results of the $\tilde{I}$ parameter sweep for the early and late phase of the non-dimensional simulation. The shaded region indicates the standard error in $\tilde{C}_{\mathrm{MM}}$ between 25,000 agents.

on experimentally derived parameters.

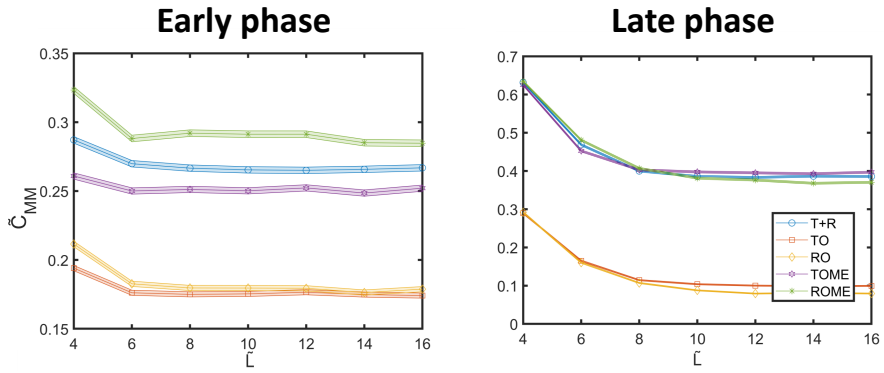

Figure 60: Results of the $\tilde{L}$ parameter sweep for the early and late phase of the non-dimensional simulation. The shaded region indicates the standard error in $\tilde{C}_{\mathrm{MM}}$ between 25,000 agents.

When discussing our sweeps of α and $\tilde{P}_{TX}$, it was noted that twiddles appear to benefit cells in environments where rotation is restricted by allowing agents to turn, and that they appear to allow cells to experience greater nutrient concentrations on average when velocity is large due to the pause in movement they facilitate. To investigate these conditions further, we ran sweeps of β when $\alpha = 0.01\alpha_0$, and for $\tilde{P}_{\mathrm{TX}}$ when $\beta/\beta_0 = 2$. In the reduced α, β sweep we observe T+R agents out competing all other behaviour types during the early phase when when β/β_0 is small ($\beta/\beta_0 \leq 1.167$)

(**Figure 61**). We noted previously that over short time periods, reversals offer a faster method of climbing chemical gradients than twiddles when velocity is reduced. Here we see the combined effect of reversals boosting chemotaxis at relatively small velocities, and twiddles enabling reorientation at reduced rotational diffusion. The combined effect of the two behaviours makes the T+R strategy the most effective at small values of β. When $\beta/\beta_0 \geq 1.5$, agents will begin to overshoot the nutrient patch and the TOME strategy becomes more beneficial, due to the frequent pauses that occur during twiddles. During the late phase, we observe reversing agents being out performed by those that can twiddle for the majority of β/β_0 values. These benefits vanish during the advanced phase when

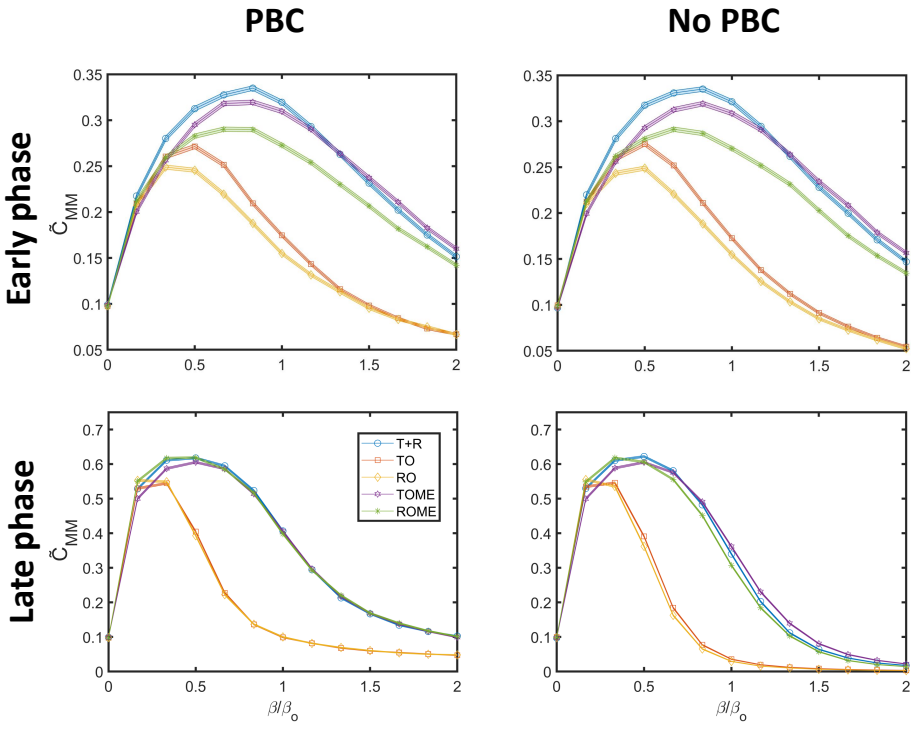

Figure 61: Results of the $\alpha = 0.01\alpha_0$ parameter sweep for the early and late phase of the non-dimensional simulation. The shaded region indicates the standard error in $\tilde{C}_{\mathrm{MM}}$ between $25,000$ agents.

periodic boundaries are applied, but are present when removed.

Finally, we consider the sweeps of $\tilde{P}_{\mathrm{TX}}$ when $\beta/\beta_{\mathrm{o}} = 2$ (**Figure 62**). Compared to the equivalent sweep when $\beta/\beta_{\mathrm{o}} = 1$ (**Figure 55**), there is an overall reduction in the fitness of each behaviour type. However, the performance of cells that twiddle compared to those unable to has improved relatively. In the early phase, we see that as $\log_{10}\left(\tilde{P}_{\mathrm{TX}}\right)$ decreases, twiddling strategies outcompete the RO case, where as previously they performed worse. At $\log_{10}\left(\tilde{P}_{\mathrm{TX}}\right) = 0$ we even see an increase in performance in T+R and TOME cells compared to ROME cells in the early phase where we previously did not. In all cases we still observe the convergence to reversing behaviour with increasing

$\log_{10}\left(\tilde{P}_{\mathrm{TX}}\right)$. Considering the advanced phase, we see large improvements in all types of twiddling behaviour. In fact, when $\log_{10}\left(\tilde{P}_{\mathrm{TX}}\right) \leq -2$ when cells enter a twiddle and do not leave, all behaviour types match the performance of ROME cells with periodic boundaries, and when $\log_{10}\left(\tilde{P}_{\mathrm{TX}}\right) \leq -1$ and no boundaries are applied they out compete ROME cells. With boundaries removed, fast cells will become lost to the concentration gradient at a faster rate than slower ones, hence the more notable difference between the boundary cases. Our original value of $\tilde{P}_{\mathrm{TX}}$ is one, and we see that in all cases when $\log_{10}\left(\tilde{P}_{\mathrm{TX}}\right)$ is below zero, twiddling cells experience a boost in performance when agents are allowed to become lost. By remaining stationary for long periods of time, cells are able

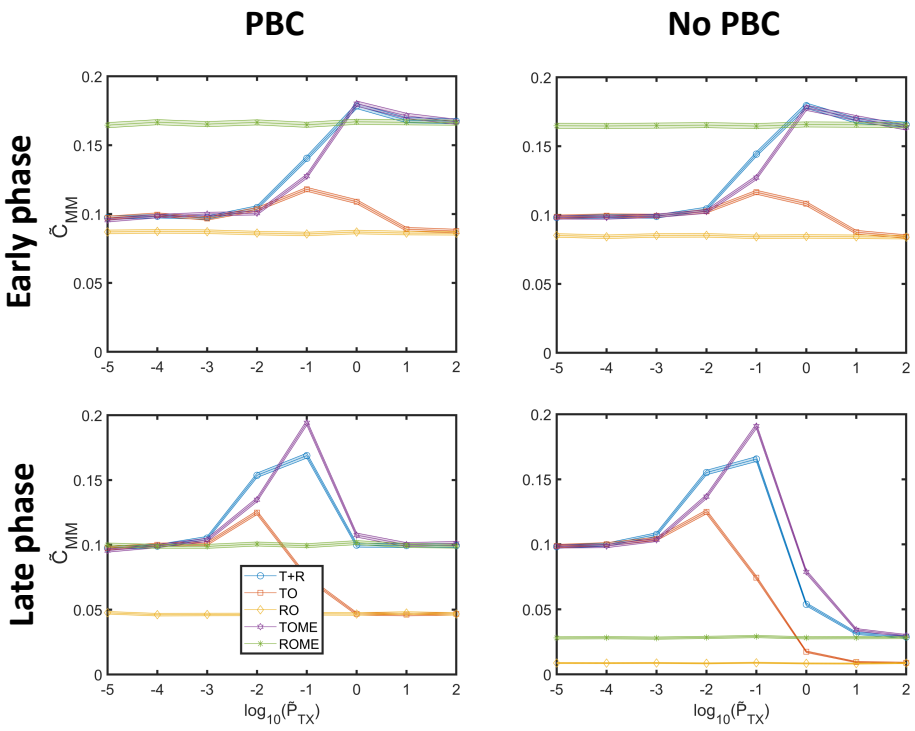

Figure 62: Results of the $\tilde{P}_{\mathrm{TX}}$ parameter sweep with $\beta/\beta_{\mathrm{o}} = 2$. The shaded region indicates the standard error in $\tilde{C}_{\mathrm{MM}}$ between $25,000$ agents.

to outcompete those that do not pause and diffuse rapidly away from the nutrient source.

Through our parameter sweeps we have identified that a balance of physical and biological parameters dictate how twiddles and reversals contribute to chemotaxis and influence the overall fitness of twitching bacteria. We found that reversals increase the ability of a cell to move across a surface at faster rates, increasing the probability of finding a nutrient patch and subsequently climbing up gradients towards one. As velocity decreases, reversals become much more beneficial than twiddles, as their instantaneous action enables the rapid climbing of chemical gradients. The instantaneous nature of reversals also aids agents capable of making correct chemotactic decisions quickly, as instantaneous reorientations are made if moving away from a chemical source, where as twiddles take

time.

When at the same coordinates and orientation, twiddles and reversals have equal capacity to drive agents towards increased nutrient concentrations, and therefore the time it takes to perform a twiddle is a key distinction between the two behaviour types. We even observe twiddles acting like reversals once $\tilde{P}_{\mathrm{TX}}$ is suitably large. The most obvious benefit as shown by our sweeps, is that twiddles enable the turning of a bacterium when rotational diffusion from twitching motility is restricted, as identified by the better performance of twiddling cells when α is reduced compared to those that only reverse. We then see twiddling cells displaying improved fitness in conditions where otherwise diffusion would cause our agents to become lost from the nutrient patch rapidly, including at large velocity, and when it is challenging for a bacterium to sense the chemical gradient, as there is no chemotactic bias. Additionally, when cells are initialised close to the chemical source, twiddling cells perform most highly, implying that they help prevent a cell becoming lost once cells have reached a sufficiently large nutrient concentration region.

Therefore, we conclude that twiddles and reversals contribute to chemotaxis and therefore cell fitness in different ways. Reversals appear to aid *P. aeruginosa* in finding a nutrient patch due to the rapid exploration of a surface they facilitate, and allowing them to climb chemical gradients quickly. Reversals can be detrimental if employed in certain regimes, such as when cell velocity is large, and are more likely to cause a cell to become lost to the nutrient patch over time. Twiddles therefore aid in preventing an individual from becoming lost by limiting translational diffusion through their pauses. After a pause and rotation, twiddles are able to redirect a cell back towards a nutrient source through a biased exit, and are crucial in reorienting a cell when rotation in normal twitching motility is restricted.

5.3 Discussion

Through performing time-lapse microscopy on surface-associated *P. aeruginosa* at the interface between glass and liquid, a novel form of twitching behaviour called twiddling has been identified. A twiddle involves the persistent rotation of the cell body via pili retraction at both cell poles, differing from normal twitching motility that is normally driven by pili retraction at a single pole [179]. In the presence of a chemical gradient, we found that twiddle exits display a bias of direction towards increasing chemoattractant concentrations. Therefore, we sought to investigate if and how twiddles give *P. aeruginosa* a fitness advantage through chemotaxis.

We experimentally quantified the behaviour of *P. aeruginosa* cells in the presence and absence of a succinate gradient, showing that cells display a bi-bias chemotaxis strategy, elevating the rate

of correct reversals and correct twiddle exits and suppressing the respective incorrect behaviours that reorient cells towards reduced concentrations of nutrients. A non-dimensional model of bacteria performing chemotaxis through biased reversals and twiddle exits was developed using these experimentally derived parameters, allowing for parameter sweeps to simulate different conditions under which twiddles are more or less beneficial to chemotaxis and overall cell fitness. We found that twiddles and reversals bring different benefits to bacterial chemotaxis and overall fitness. Twiddles allow for the reorientation of cells towards the nutrient source when rotational diffusion is reduced, and they also act to reduce translational diffusion, which helps to prevent *P. aeruginosa* becoming lost from nutrient patches. Additionally, when already in regions of large nutrient concentration, twiddles show an increased ability over other behaviours to keep a cell at that location. Reversals on the other hand allow cells to quickly climb chemical gradients and elevate the level of translational diffusion, meaning they could be used as a strategy to search larger areas of a surface for a nutrient source.

Both reversals and twiddles have a chemotactic element to their behaviour that propels *P. aeruginosa* towards increased nutrient concentrations, but our results hint that the two behaviour types could have evolved for different purposes. Reversals act to increase translational diffusion to find a nutrient source and climb it quickly, where as twiddles act to keep a cell in a region of large concentration. *P. aeruginosa* has already been shown to employ differing twitching behaviours depending on nutrient concentration, showing a greater tendency to explore a surface in nutrient devoid conditions, and cease movement when conditions are favourable [74]. However, this work did not identify twiddles, and does not consider how chemotaxis influences bacterial movement.

Previous studies have highlighted the ability of *P. aeruginosa* to use twitching motility in diverse ways, for example, walking upright on one pole or using slingshots to explore surfaces at a faster rate than conventional twitching motility [32, 34, 39]. The work described in this chapter is part of a wider body of research that seeks to understand the forms of twitching motility not yet reported. Here, our non-dimensional model seeks to understand how twiddles and reversals could provide *P. aeruginosa* with an increase in fitness through improved chemotaxis. In other lines of study, we are also seeking through modelling and experiment to understand how the rotation of twiddles arises through TFP retraction.

Despite the information discovered on how twiddles and reversals contribute to chemotaxis and cell fitness, there are still areas of this research that need further exploration. Our results hint that twiddles keep *P. aeruginosa* in nutrient dense regions and it would be instructive to investigate this phenomenon further, both experimentally and through simulation. For instance, it would be

instructive to compare the rates and durations of twiddles in different nutrient regimes.

We propose a model of twitching motility in which twiddles and reversals both have chemotactic potential and the capability of influencing the amount of translational diffusion displayed by a cell. We possess some preliminary experimental validation for this claim in that cells enter twiddles more often in TB + succinate (an additional carbon source) compared to TB (**Figure 44**). We therefore hypothesise that *P. aeruginosa* activates twiddles when it senses a nutrient concentration that is sufficiently large, and given twiddles are capable of facilitating chemotaxis, the opportunistic pathogen never ceases to try and improve its fitness further through biasing its rate of twiddle exits towards larger nutrient gradients.

Then there are modifications to the simulation that can be made to make it more compar to nature. We used a steady Gaussian shaped nutrient distribution in our model, which bears resemblance to those that occur in nature [183]. However, food sources often arise and are then consumed i.e. they can be highly transient [79]. Alternatively, we could have considered a nutrient distribution that could be depleted over time due to the agents actively consuming nutrients. Then we could compare different chemotactic strategies head to head, by allowing them to compete for the same nutrient source. Our simulations are also run with a finite number of individuals, however, bacteria increase their rate of division when nutrient conditions are more favourable. Therefore, the simulation could be modified so that the agents are able to divide at different rates, depending on their past exposure to nutrients. Then we could potentially change our measure of fitness to instead consider the overall number of agents at the end of the simulation [92]. In addition, we could explore a more ephemeral nutrient landscape where patches spontaneously appear in random locations and then diffuse away [186], such that agents must rapidly accumulate in nutrient patches before they vanish.

We set out to understand how a novel form of twitching behaviour, twiddling, could potentially benefit cell fitness through chemotaxis. Using experimentally derived parameters, we constructed a non-dimensional simulation of *P. aeruginosa* performing pili-based chemotaxis mediated by reversals and twiddles, that exhibit a bi-bias response strategy. Although we see that reversals quickly drive cells towards greater nutrient concentrations, cells unable to twiddle can find themselves lost and unable to return to the nutrient patch if moving too quickly. We therefore conclude that both behaviours enable chemotaxis, however each serve different purposes. Reversals act to increase the amount of surface exploration and the rapid climbing of chemical gradients through their instantaneous action, whereas twiddles enable rotation when cells experience limited rotational diffusion and keep *P. aeruginosa* in regions of increased concentration for as long as possible.

6 Conclusion

In this thesis we have investigated how the opportunistic pathogen *P. aeruginosa* navigates surfaces using twitching motility during biofilm formation.

We first showed that *P. aeruginosa* cells tend to align their twitching motility in the same direction as their neighbours both in the bacterial monolayer and at the edge of the colony, where it likely helps to facilitate colony expansion. We then showed that reversals help drive this collective polar behaviour, by demonstrating that cells tend to reverse at greater frequencies when moving against the collective than when they move with it. Our findings indicate that *P. aeruginosa* uses mechanosensing to sense its movement relative to that of its neighbours to actively polarise its collective movement. While bacterial colonies have previously been modelled as a nematic system, the collective behaviour we observed may help to both distribute the transport of nutrients into the interior of bacterial colonies through the maintenance of active turbulence, and to facilitate the collective expansion of colonies by allowing them to spread more rapidly and thus better exploit nutrients further afield [147]. Our work provides excellent motivation for future modelling studies to investigate how the behaviour of individual cells affects collective movement by helping to facilitate polarisation.

We then investigated the processes that drive pili-based chemotaxis of solitary cells on surfaces. We developed an individual-based model of *P. aeruginosa* responding to a two-dimensional chemical gradient, which was motivated and parameterised using experimental observations. We found that twiddles and reversals each can drive chemotaxis, but show differences in the parameter regimes where they are found to be most effective. Twiddles enable a cell to access larger nutrient concentrations when rotational diffusion is relatively weak, when cells move more rapidly, or when the cell's have a relatively weak chemosensory response. Reversals on the other hand were found to allow cells to more rapidly accumulate in nutrient patches compared to twiddles. We therefore propose that *P. aeruginosa* has evolved both orientation behaviours to maximise their ability to position themselves within nutrient sources across a wide diversity of different environmental conditions.

To perform the research in this thesis, we have developed a number of new techniques. In particular, we have developed an automated image analysis pipeline that can quantify the distribution of fluorescent proteins within bacterial cells and how they depend on both individual and collective movement. This pipeline is sufficiently general that one could apply it to a number of other rod shaped organisms and across a wide variety of different experimental assays. Thus, these tools could potentially be used to interpret the how cells distribute proteins within their bodies in response to a range of different environmental stimuli to understand how bacteria regulate emergent collective

phenomena that occur when they are tightly packed together [64]. For example, one might expect groups of cells to localise proteins in a particular pattern as they collectively respond to gradients of nutrients, surfactants, antibiotics, or light.

The non-dimensional model developed to investigate pili-based chemotaxis also could be extended to look at how bacteria have evolved to respond to more realistic chemical environments that both vary in time and contain multiple localised hotspots of nutrients with different strengths. In addition, this model could also be extended to understand the behaviours that cells exhibit when they are confronted with contain gradients of more than one chemical – a scenario frequently encountered in biofilms where cells often experience opposing gradient of nutrients and waste products [109]. Our simulation could also be extended to include cell division to investigate how each behaviour type could affect average cell fitness. Within a nutrient rich medium *P. aeruginosa* can undergo division in 30 minutes [187], meaning over the course of our five week-long simulations each agent has the potential to divide 1680 times. However, division rates in the natural environment are expected to be much smaller than that typically observed in optimised laboratory conditions. Recent work from our group has shown that *P. aeruginosa* uses pili-based motility to actively chemotax towards the clinical antibiotics that are used to treat infections. When confronted with steady, opposing gradients of nutrients and antibiotics, cells first move towards the nutrients before ultimately changing course to move towards the antibiotics [81]. Our model could thus be extended to interpret how cells process and combine information from multiple stimuli. In particular, it could be used to methodically interpret how the response to multiple stimuli can be related to the responses observed to each stimuli individually.

This thesis has focused on identifying the movement behaviour that bacteria use to respond to their local environment and how it affects their ability to navigate both individually and collectively as a group. This work constitutes an important step towards understanding the strategies that bacteria use to move across surfaces. A deeper understanding of pili-based motility might ultimately allow us to engineer bacterial communities to our advantage, with many potential applications across medicine by preventing or eradicating infections [109], in agriculture to facilitate the symbiosis of plants that cannot fix nitrogen with bacteria on their roots that do [188], and in biotechnology, to pattern bacteria on surfaces in specific spatial orientations [189].

The work performed in this thesis has revealed that bacteria moving on a surface through twitching motility are able to modify their movement behaviour to influence the physical properties of themselves and the collective. With these discoveries also come new questions, which we hope are investigated further, perhaps through collaboration, and just like cells at the colony edge will push

our understanding of the stunning dynamics observed into currently unknown territory.

References

[1] Anne E Mattingly, Abigail A Weaver, Aleksandar Dimkovikj, and Joshua D Shrout. Assessing travel conditions: environmental and host influences on bacterial surface motility, 2018.

[2] Howard C Berg. How to track bacteria. *Review of Scientific Instruments*, 42(6):868–871, 1971.

[3] Scott A Rice, Chuan Hao Tan, Per Jensen Mikkelsen, Vanderlene Kung, Jerry Woo, Martin Tay, Alan Hauser, Diane McDougald, Jeremy S Webb, and Staffan Kjelleberg. The biofilm life cycle and virulence of pseudomonas aeruginosa are dependent on a filamentous prophage. *The ISME journal*, 3(3):271–282, 2009.

[4] Alexey J Merz, Magdalene So, and Michael P Sheetz. Pilus retraction powers bacterial twitching motility. *Nature*, 407(6800):98–102, 2000.

[5] Mustafa Fazli, Thomas Bjarnsholt, Klaus Kirketerp-Møller, Bo Jørgensen, Anders Schou Andersen, Karen A Krogfelt, Michael Givskov, and Tim Tolker-Nielsen. Nonrandom distribution of pseudomonas aeruginosa and staphylococcus aureus in chronic wounds. *Journal of clinical microbiology*, 47(12):4084–4089, 2009.

[6] Vincent Nieto, Abby R Kroken, Melinda R Grosser, Benjamin E Smith, Matteo ME Metruccio, Patrick Hagan, Mary E Hallsten, David J Evans, and Suzanne MJ Fleiszig. Type iv pili can mediate bacterial motility within epithelial cells. *MBio*, 10(4):e02880–18, 2019.

[7] Courtney K Ellison, Triana N Dalia, Alfredo Vidal Ceballos, Joseph Che-Yen Wang, Nicolas Biais, Yves V Brun, and Ankur B Dalia. Retraction of dna-bound type iv competence pili initiates dna uptake during natural transformation in vibrio cholerae. *Nature microbiology*, 3(7):773–780, 2018.

[8] Kun Zhao, Boo Shan Tseng, Bernard Beckerman, Fan Jin, Maxsim L Gibiansky, Joe J Harrison, Erik Luijten, Matthew R Parsek, and Gerard CL Wong. Psl trails guide exploration and microcolony formation in pseudomonas aeruginosa biofilms. *Nature*, 497(7449):388–391, 2013.

[9] Chunhui Zhai, Wenchao Zhang, Jingchao Zhang, Luyan Z Ma, and Kun Zhao. Overshadow effect of psl on bacterial response to physiochemically distinct surfaces through motility-based characterization. *Frontiers in cellular and infection microbiology*, page 383, 2018.

[10] Hans-Curt Flemming, Thomas R Neu, and Daniel J Wozniak. The eps matrix: the "house of biofilm cells". *Journal of bacteriology*, 189(22):7945–7947, 2007.

[11] Catherine R Armbruster, Tom Coenye, Lhousseine Touqui, and Jennifer M Bomberger. Interplay between host-microbe and microbe-microbe interactions in cystic fibrosis. *Journal of Cystic Fibrosis*, 19:S47–S53, 2020.

[12] He-Peng Zhang, Avraham Be'er, E-L Florin, and Harry L Swinney. Collective motion and density fluctuations in bacterial colonies. *Proceedings of the National Academy of Sciences*, 107(31):13626–13630, 2010.

[13] Samuel R McCandlish, Aparna Baskaran, and Michael F Hagan. Spontaneous segregation of self-propelled particles with different motilities. *Soft Matter*, 8(8):2527–2534, 2012.

[14] George A O'Toole and Roberto Kolter. Flagellar and twitching motility are necessary for pseudomonas aeruginosa biofilm development. *Molecular microbiology*, 30(2):295–304, 1998.

[15] Amin Doostmohammadi, Jordi Ignés-Mullol, Julia M Yeomans, and Francesc Sagués. Active nematics. *Nature communications*, 9(1):1–13, 2018.

[16] Inmaculada Sampedro, Rebecca E Parales, Tino Krell, and Jane E Hill. Pseudomonas chemotaxis. *FEMS microbiology reviews*, 39(1):17–46, 2015.

[17] Lorenzo Tala, Marco Kuhn, Yuki Inclan, Ramiro Patino, Xavier Pierrat, Iscia Vos, Zainebe Al-Mayyah, Henriette MacMillan, Jose Negrete, Joanne N Engel, et al. Mechanotaxis directs pseudomonas aeruginosa twitching motility. *bioRxiv*, 2021.

[18] M Mehdi Salek, Francesco Carrara, Vicente Fernandez, and Roman Stocker. Bacterial maze runners reveal hidden diversity in chemotactic performance. *Microbial Cell*, 6(8):370, 2019.

[19] Oliver J Meacock and William M Durham. Tracking bacteria at high density with fast, the feature-assisted segmenter/tracker. *bioRxiv*, 2021.

[20] Ken F Jarrell and Mark J McBride. The surprisingly diverse ways that prokaryotes move. *Nature reviews microbiology*, 6(6):466–476, 2008.

[21] Alexandre Persat, Carey D Nadell, Minyoung Kevin Kim, Francois Ingremeau, Albert Siryaporn, Knut Drescher, Ned S Wingreen, Bonnie L Bassler, Zemer Gitai, and Howard A Stone. The mechanical world of bacteria. *Cell*, 161(5):988–997, 2015.

[22] Jacob J Bertrand, Joyce T West, and Joanne N Engel. Genetic analysis of the regulation of type iv pilus function by the chp chemosensory system of pseudomonas aeruginosa. *Journal of bacteriology*, 192(4):994–1010, 2010.

[23] Daniel B Kearns. A field guide to bacterial swarming motility. *Nature Reviews Microbiology*, 8(9):634–644, 2010.

[24] Caroline Giraud, Christophe Bernard, Ségolène Ruer, and Sophie De Bentzmann. Biological 'glue'and 'velcro': molecular tools for adhesion and biofilm formation in the hairy and gluey bug pseudomonas aeruginosa. *Environmental Microbiology Reports*, 2(3):343–358, 2010.

[25] Ferenc Vonderviszt and Keiichi Namba. Structure, function and assembly of flagellar axial proteins. *Fibrous Proteins*, 2008:58–76, 2008.

[26] Shuichi Nakamura and Tohru Minamino. Flagella-driven motility of bacteria. *Biomolecules*, 9(7):279, 2019.

[27] Howard C Berg and Douglas A Brown. Chemotaxis in escherichia coli analysed by three-dimensional tracking. *nature*, 239(5374):500–504, 1972.

[28] Maojin Tian, Zhengyu Wu, Rongjing Zhang, and Junhua Yuan. A new mode of swimming in singly flagellated pseudomonas aeruginosa. *Proceedings of the National Academy of Sciences*, 119(14):e2120508119, 2022.

[29] Eric Lauga, Willow R DiLuzio, George M Whitesides, and Howard A Stone. Swimming in circles: motion of bacteria near solid boundaries. *Biophysical journal*, 90(2):400–412, 2006.

[30] Lori L Burrows. Pseudomonas aeruginosa twitching motility: type iv pili in action. *Annual review of microbiology*, 66:493–520, 2012.

[31] Chien-Yi Chang. Surface sensing for biofilm formation in pseudomonas aeruginosa. *Frontiers in microbiology*, 8:2671, 2018.

[32] Lorenzo Talà, Adam Fineberg, Philipp Kukura, and Alexandre Persat. Pseudomonas aeruginosa orchestrates twitching motility by sequential control of type iv pili movements. *Nature microbiology*, 4(5):774–780, 2019.

[33] Stephen P Diggle and Marvin Whiteley. Microbe profile: Pseudomonas aeruginosa: opportunistic pathogen and lab rat. *Microbiology*, 166(1):30, 2020.

[34] Oliver J Meacock, Amin Doostmohammadi, Kevin R Foster, Julia M Yeomans, and William M Durham. Bacteria solve the problem of crowding by moving slowly. *Nature Physics*, 17(2):205–210, 2021.

[35] Jeffrey M Skerker and Howard C Berg. Direct observation of extension and retraction of type iv pili. *Proceedings of the National Academy of Sciences*, 98(12):6901–6904, 2001.

[36] Fan Jin, Jacinta C Conrad, Maxsim L Gibiansky, and Gerard CL Wong. Bacteria use type-iv pili to slingshot on surfaces. *Proceedings of the National Academy of Sciences*, 108(31):12617–12622, 2011.

[37] Marco J Kühn, Lorenzo Talà, Yuki F Inclan, Ramiro Patino, Xavier Pierrat, Iscia Vos, Zainebe Al-Mayyah, Henriette Macmillan, Jose Negrete Jr, Joanne N Engel, et al. Mechanotaxis directs pseudomonas aeruginosa twitching motility. *Proceedings of the National Academy of Sciences*, 118(30):e2101759118, 2021.

[38] Maxsim L Gibiansky, Jacinta C Conrad, Fan Jin, Vernita D Gordon, Dominick A Motto, Margie A Mathewson, Wiktor G Stopka, Daria C Zelasko, Joshua D Shrout, and Gerard CL Wong. Bacteria use type iv pili to walk upright and detach from surfaces. *Science*, 330(6001):197–197, 2010.

[39] Rongrong Zhang, Lei Ni, Zhenyu Jin, Jiahong Li, and Fan Jin. Bacteria slingshot more on soft surfaces. *Nature communications*, 5(1):1–6, 2014.

[40] Avraham Be'er, Bella Ilkanaiv, Renan Gross, Daniel B Kearns, Sebastian Heidenreich, Markus Bär, and Gil Ariel. A phase diagram for bacterial swarming. *Communications Physics*, 3(1):1–8, 2020.

[41] Mark J McBride. Bacterial gliding motility: multiple mechanisms for cell movement over surfaces. *Annual Reviews in Microbiology*, 55(1):49–75, 2001.

[42] Mark J McBride and Daisuke Nakane. Flavobacterium gliding motility and the type ix secretion system. *Current opinion in microbiology*, 28:72–77, 2015.

[43] Abhishek Shrivastava, Pushkar P Lele, and Howard C Berg. A rotary motor drives flavobacterium gliding. *Current Biology*, 25(3):338–341, 2015.

[44] Emilia MF Mauriello and David R Zusman. Polarity of motility systems in myxococcus xanthus. *Current opinion in microbiology*, 10(6):624–629, 2007.

[45] Shashi Thutupalli, Mingzhai Sun, Filiz Bunyak, Kannappan Palaniappan, and Joshua W Shaevitz. Directional reversals enable myxococcus xanthus cells to produce collective one-dimensional streams during fruiting-body formation. *Journal of The Royal Society Interface*, 12(109):20150049, 2015.

[46] Dale Kaiser. Social gliding is correlated with the presence of pili in myxococcus xanthus. *Proceedings of the National Academy of Sciences*, 76(11):5952–5956, 1979.

[47] Tyson Carter, Ryan NC Buensuceso, Stephanie Tammam, Ryan P Lamers, Hanjeong Harvey, P Lynne Howell, and Lori L Burrows. The type iva pilus machinery is recruited to sites of future cell division. *MBio*, 8(1):e02103–16, 2017.

[48] Yi-Wei Chang, Lee A Rettberg, Anke Treuner-Lange, Janet Iwasa, Lotte Søgaard-Andersen, and Grant J Jensen. Architecture of the type iva pilus machine. *Science*, 351(6278):aad2001, 2016.

[49] Tamilarasi Shanmugasundarasamy, Deenadayalan Karaiyagowder Govindarajan, and Kumaravel Kandaswamy. A review on pilus assembly mechanisms in gram-positive and gram-negative bacteria. *The Cell Surface*, 8:100077, 2022.

[50] Lisa Craig, Ronald K Taylor, Michael E Pique, Brian D Adair, Andrew S Arvai, Mona Singh, Sarah J Lloyd, David S Shin, Elizabeth D Getzoff, Mark Yeager, et al. Type iv pilin structure and assembly: X-ray and em analyses of vibrio cholerae toxin-coregulated pilus and pseudomonas aeruginosa pak pilin. *Molecular cell*, 11(5):1139–1150, 2003.

[51] Shanice S Webster, Gerard CL Wong, and George A O'Toole. The power of touch: Type 4 pili, the von willebrand a domain, and surface sensing by pseudomonas aeruginosa. *Journal of Bacteriology*, pages e00084–22, 2022.

[52] Carmen L Giltner, Ylan Nguyen, and Lori L Burrows. Type iv pilin proteins: versatile molecular modules. *Microbiology and Molecular Biology Reviews*, 76(4):740–772, 2012.

[53] Vladimir Jakovljevic, Simone Leonardy, Michael Hoppert, and Lotte Søgaard-Andersen. Pilb and pilt are atpases acting antagonistically in type iv pilus function in myxococcus xanthus. *Journal of bacteriology*, 190(7):2411–2421, 2008.

[54] Matthias D Koch, Chenyi Fei, Ned S Wingreen, Joshua W Shaevitz, and Zemer Gitai. Competitive binding of independent extension and retraction motors explains the quantitative dynamics of type iv pili. *Proceedings of the National Academy of Sciences*, 118(8), 2021.

[55] Laura M Nolan, Laura C McCaughey, Jessica Merjane, Lynne Turnbull, and Cynthia B Whitchurch. Chpc controls twitching motility-mediated expansion of pseudomonas aeruginosa biofilms in response to serum albumin, mucin and oligopeptides. *Microbiology*, 166(7):669, 2020.

[56] Irandokht Zolfaghar, David J Evans, and Suzanne MJ Fleiszig. Twitching motility contributes to the role of pili in corneal infection caused by pseudomonas aeruginosa. *Infection and immunity*, 71(9):5389–5393, 2003.

[57] Courtney K Ellison, Chenyi Fei, Triana N Dalia, Ned S Wingreen, Ankur B Dalia, Joshua W Shaevitz, and Zemer Gitai. Subcellular localization of type iv pili regulates bacterial multicellular development. *Nature communications*, 13(1):6334, 2022.

[58] Jonathan D Partridge, Nguyen TQ Nhu, Yann S Dufour, and Rasika M Harshey. Escherichia coli remodels the chemotaxis pathway for swarming. *MBio*, 10(2):10–1128, 2019.

[59] Paul A DeLange, Tracy L Collins, George E Pierce, and Jayne B Robinson. Pilj localizes to cell poles and is required for type iv pilus extension in pseudomonas aeruginosa. *Current microbiology*, 55(5):389–395, 2007.

[60] Cynthia B Whitchurch, Andrew J Leech, Michael D Young, Derek Kennedy, Jennifer L Sargent, Jacob J Bertrand, Annalese BT Semmler, Albert S Mellick, Paul R Martin, Richard A Alm, et al. Characterization of a complex chemosensory signal transduction system which controls twitching motility in pseudomonas aeruginosa. *Molecular microbiology*, 52(3):873–893, 2004.

[61] Kaitlin D Yarrington, Tyler N Shendruk, and Dominique H Limoli. Twitching cells use a chemoreceptor to detect bacterial competitors. *bioRxiv*, pages 2022–11, 2022.

[62] Yuki F Inclan, Alexandre Persat, Alexander Greninger, John Von Dollen, Jeffery Johnson, Nevan Krogan, Zemer Gitai, and Joanne N Engel. A scaffold protein connects type iv pili with the chp chemosensory system to mediate activation of virulence signaling in pseudomonas aeruginosa. *Molecular microbiology*, 101(4):590–605, 2016.

[63] Iryna Bulyha, Carmen Schmidt, Peter Lenz, Vladimir Jakovljevic, Andrea Höne, Berenike Maier, Michael Hoppert, and Lotte Søgaard-Andersen. Regulation of the type iv pili molecular machine by dynamic localization of two motor proteins. *Molecular microbiology*, 74(3):691–706, 2009.

[64] Poney Chiang, Marc Habash, and Lori L Burrows. Disparate subcellular localization patterns of pseudomonas aeruginosa type iv pilus atpases involved in twitching motility. *Journal of bacteriology*, 187(3):829–839, 2005.

[65] Ruchi Jain, Oleksii Sliusarenko, and Barbara I Kazmierczak. Interaction of the cyclic-di-gmp binding protein fimx and the type 4 pilus assembly atpase promotes pilus assembly. *PLoS pathogens*, 13(8):e1006594, 2017.

[66] Barbara I Kazmierczak, Maria B Lebron, and Thomas S Murray. Analysis of fimx, a phosphodiesterase that governs twitching motility in pseudomonas aeruginosa. *Molecular microbiology*, 60(4):1026–1043, 2006.

[67] Nuno M Oliveira, Kevin R Foster, and William M Durham. Single-cell twitching chemotaxis in developing biofilms. *Proceedings of the National Academy of Sciences*, 113(23):6532–6537, 2016.

[68] Yves F Dufrêne and Alexandre Persat. Mechanomicrobiology: how bacteria sense and respond to forces. *Nature Reviews Microbiology*, 18(4):227–240, 2020.

[69] Vernita D Gordon and Liyun Wang. Bacterial mechanosensing: the force will be with you, always. *Journal of Cell Science*, 132(7):jcs227694, 2019.

[70] Albert Siryaporn, Sherry L Kuchma, George A O'Toole, and Zemer Gitai. Surface attachment induces pseudomonas aeruginosa virulence. *Proceedings of the National Academy of Sciences*, 111(47):16860–16865, 2014.

[71] Alexandre Persat, Yuki F Inclan, Joanne N Engel, Howard A Stone, and Zemer Gitai. Type iv pili mechanochemically regulate virulence factors in pseudomonas aeruginosa. *Proceedings of the National Academy of Sciences*, 112(24):7563–7568, 2015.

[72] Katie L Thornton, Jaimi K Butler, Seth J Davis, Bonnie K Baxter, and Laurence G Wilson. Haloarchaea swim slowly for optimal chemotactic efficiency in low nutrient environments. *Nature communications*, 11(1):1–9, 2020.

[73] Farzan Beroz, Jing Yan, Yigal Meir, Benedikt Sabass, Howard A Stone, Bonnie L Bassler, and Ned S Wingreen. Verticalization of bacterial biofilms. *Nature physics*, 14(9):954–960, 2018.

[74] Lei Ni, Shuai Yang, Rongrong Zhang, Zhenyu Jin, Hao Chen, Jacinta C Conrad, and Fan Jin. Bacteria differently deploy type-iv pili on surfaces to adapt to nutrient availability. *NPJ biofilms and microbiomes*, 2(1):1–10, 2016.

[75] Annalese BT Semmler, Cynthia B Whitchurch, and John S Mattick. A re-examination of twitching motility in pseudomonas aeruginosa. *Microbiology*, 145(10):2863–2873, 1999.

[76] Jφrgen Henrichsen. Bacterial surface translocation: a survey and a classification. *Bacteriological reviews*, 36(4):478–503, 1972.

[77] Tâm Mignot, John P Merlie Jr, and David R Zusman. Regulated pole-to-pole oscillations of a bacterial gliding motility protein. *Science*, 310(5749):855–857, 2005.

[78] Kimberly N Cowles and Zemer Gitai. Surface association and the mreb cytoskeleton regulate pilus production, localization and function in pseudomonas aeruginosa. *Molecular microbiology*, 76(6):1411–1426, 2010.

[79] Roman Stocker, Justin R Seymour, Azadeh Samadani, Dana E Hunt, and Martin F Polz. Rapid chemotactic response enables marine bacteria to exploit ephemeral microscale nutrient patches. *Proceedings of the National Academy of Sciences*, 105(11):4209–4214, 2008.

[80] JR Seymour, T Ahmed, and R Stocker. A microfluidic chemotaxis assay to study microbial behavior in diffusing nutrient patches. *Limnology and Oceanography: Methods*, 6(9):477–488, 2008.

[81] Nuno M Oliveira, James HR Wheeler, Cyril Deroy, Sean C Booth, Edmond J Walsh, William M Durham, and Kevin R Foster. Suicidal chemotaxis in bacteria. *bioRxiv*, 2021.

[82] Nikita Vladimirov, Linda Løvdok, Dirk Lebiedz, and Victor Sourjik. Dependence of bacterial chemotaxis on gradient shape and adaptation rate. *PLoS computational biology*, 4(12):e1000242, 2008.

[83] Victor Sourjik and Ned S Wingreen. Responding to chemical gradients: bacterial chemotaxis. *Current opinion in cell biology*, 24(2):262–268, 2012.

[84] Mark J Schnitzer. Theory of continuum random walks and application to chemotaxis. *Physical Review E*, 48(4):2553, 1993.

[85] David F Blair. How bacteria sense and swim. *Annual review of microbiology*, 49:489–523, 1995.

[86] Tanvir Ahmed, Thomas S Shimizu, and Roman Stocker. Bacterial chemotaxis in linear and nonlinear steady microfluidic gradients. *Nano letters*, 10(9):3379–3385, 2010.

[87] Pietro de Anna, Amir A Pahlavan, Yutaka Yawata, Roman Stocker, and Ruben Juanes. Chemotaxis under flow disorder shapes microbial dispersion in porous media. *Nature Physics*, 17(1):68–73, 2021.

[88] Tanvir Ahmed and Roman Stocker. Experimental verification of the behavioral foundation of bacterial transport parameters using microfluidics. *Biophysical journal*, 95(9):4481–4493, 2008.

[89] Peter A Spiro, John S Parkinson, and Hans G Othmer. A model of excitation and adaptation in bacterial chemotaxis. *Proceedings of the National Academy of Sciences*, 94(14):7263–7268, 1997.

[90] Marcus J Tindall, SL Porter, PK Maini, G Gaglia, and Judith P Armitage. Overview of mathematical approaches used to model bacterial chemotaxis i: the single cell. *Bulletin of mathematical biology*, 70(6):1525–1569, 2008.

[91] G Caviglia and A Morro. Continuum model of cell motility and chemotaxis. *European Journal of Mechanics-B/Fluids*, 49:235–242, 2015.

[92] Congjian Ni and Ting Lu. Individual-based modeling of spatial dynamics of chemotactic microbial populations. *ACS Synthetic Biology*, 11(11):3714–3723, 2022.

[93] Ferdi L Hellweger and Vanni Bucci. A bunch of tiny individuals—individual-based modeling for microbes. *Ecological Modelling*, 220(1):8–22, 2009.

[94] Joe J Harrison, Raymond J Turner, Lyriam LR Marques, and Howard Ceri. Biofilms: a new understanding of these microbial communities is driving a revolution that may transform the science of microbiology. *American Scientist*, 93(6):508–515, 2005.

[95] Philip S Stewart. Antimicrobial tolerance in biofilms. *Microbiology spectrum*, 3(3):3–3, 2015.

[96] Philip Pearce, Boya Song, Dominic J Skinner, Rachel Mok, Raimo Hartmann, Praveen K Singh, Hannah Jeckel, Jeffrey S Oishi, Knut Drescher, and Jörn Dunkel. Flow-induced symmetry breaking in growing bacterial biofilms. *Physical Review Letters*, 123(25):258101, 2019.

[97] Karin Sauer, Paul Stoodley, Darla M Goeres, Luanne Hall-Stoodley, Mette Burmølle, Philip S Stewart, and Thomas Bjarnsholt. The biofilm life cycle: expanding the conceptual model of biofilm formation. *Nature Reviews Microbiology*, 20(10):608–620, 2022.

[98] Kendra P Rumbaugh and Karin Sauer. Biofilm dispersion. *Nature Reviews Microbiology*, 18(10):571–586, 2020.

[99] Gerard CL Wong, Jyot D Antani, Pushkar P Lele, Jing Chen, Beiyan Nan, Marco J Kühn, Alexandre Persat, Jean-Louis Bru, Nina Molin Høyland-Kroghsbo, Albert Siryaporn, et al.

Roadmap on emerging concepts in the physical biology of bacterial biofilms: from surface sensing to community formation. *Physical biology*, 18(5):051501, 2021.

[100] Catherine R Armbruster and Matthew R Parsek. New insight into the early stages of biofilm formation. *Proceedings of the National Academy of Sciences*, 115(17):4317–4319, 2018.

[101] Calvin K Lee, Jaime De Anda, Amy E Baker, Rachel R Bennett, Yun Luo, Ernest Y Lee, Joshua A Keefe, Joshua S Helali, Jie Ma, Kun Zhao, et al. Multigenerational memory and adaptive adhesion in early bacterial biofilm communities. *Proceedings of the National Academy of Sciences*, 115(17):4471–4476, 2018.

[102] Ruchi Jain and Barbara I Kazmierczak. Should i stay or should i go? pseudomonas just can't decide. *Cell Host & Microbe*, 25(1):5–7, 2019.

[103] Catherine R Armbruster, Calvin K Lee, Jessica Parker-Gilham, Jaime de Anda, Aiguo Xia, Kun Zhao, Keiji Murakami, Boo Shan Tseng, Lucas R Hoffman, Fan Jin, et al. Heterogeneity in surface sensing suggests a division of labor in pseudomonas aeruginosa populations. *Elife*, 8:e45084, 2019.

[104] Jacinta C Conrad, Maxsim L Gibiansky, Fan Jin, Vernita D Gordon, Dominick A Motto, Margie A Mathewson, Wiktor G Stopka, Daria C Zelasko, Joshua D Shrout, and Gerard CL Wong. Flagella and pili-mediated near-surface single-cell motility mechanisms in p. aeruginosa. *Biophysical journal*, 100(7):1608–1616, 2011.

[105] Patrick Di Martino. Extracellular polymeric substances, a key element in understanding biofilm phenotype. *AIMS microbiology*, 4(2):274, 2018.

[106] Kelly M Colvin, Yasuhiko Irie, Catherine S Tart, Rodolfo Urbano, John C Whitney, Cynthia Ryder, P Lynne Howell, Daniel J Wozniak, and Matthew R Parsek. The pel and psl polysaccharides provide pseudomonas aeruginosa structural redundancy within the biofilm matrix. *Environmental microbiology*, 14(8):1913–1928, 2012.

[107] Cynthia B Whitchurch, Tim Tolker-Nielsen, Paula C Ragas, and John S Mattick. Extracellular dna required for bacterial biofilm formation. *Science*, 295(5559):1487–1487, 2002.

[108] Amelia L Hynen, James J Lazenby, George M Savva, Laura C McCaughey, Lynne Turnbull, Laura M Nolan, and Cynthia B Whitchurch. Multiple holins contribute to extracellular dna release in pseudomonas aeruginosa biofilms. *Microbiology*, 167(2), 2021.

[109] Zohra Khatoon, Christopher D McTiernan, Erik J Suuronen, Thien-Fah Mah, and Emilio I Alarcon. Bacterial biofilm formation on implantable devices and approaches to its treatment and prevention. *Heliyon*, 4(12):e01067, 2018.

[110] A Simon Lynch and Gregory T Robertson. Bacterial and fungal biofilm infections. *Annual review of medicine*, 59(1):415–428, 2008.

[111] Miguel Cámara, William Green, Cait E MacPhee, Paulina D Rakowska, Rasmita Raval, Mark C Richardson, Joanne Slater-Jefferies, Katerina Steventon, and Jeremy S Webb. Economic significance of biofilms: a multidisciplinary and cross-sectoral challenge. *npj Biofilms and Microbiomes*, 8(1):1–8, 2022.

[112] Berenike Maier. How physical interactions shape bacterial biofilms. *Annual review of biophysics*, 50:401–417, 2021.

[113] Raimo Hartmann, Praveen K Singh, Philip Pearce, Rachel Mok, Boya Song, Francisco Díaz-Pascual, Jörn Dunkel, and Knut Drescher. Emergence of three-dimensional order and structure in growing biofilms. *Nature physics*, 15(3):251–256, 2019.

[114] Philip S Stewart. Diffusion in biofilms. *Journal of bacteriology*, 185(5):1485–1491, 2003.

[115] Jonas Stenløkke Madsen, Mette Burmølle, Lars Hestbjerg Hansen, and Søren Johannes Sørensen. The interconnection between biofilm formation and horizontal gene transfer. *FEMS Immunology & Medical Microbiology*, 65(2):183–195, 2012.

[116] Divakar Sharma, Lama Misba, and Asad U Khan. Antibiotics versus biofilm: an emerging battleground in microbial communities. *Antimicrobial Resistance & Infection Control*, 8(1):1–10, 2019.

[117] Kim B Barken, Sünje J Pamp, Liang Yang, Morten Gjermansen, Jacob J Bertrand, Mikkel Klausen, Michael Givskov, Cynthia B Whitchurch, Joanne N Engel, and Tim Tolker-Nielsen. Roles of type iv pili, flagellum-mediated motility and extracellular dna in the formation of mature multicellular structures in pseudomonas aeruginosa biofilms. *Environmental microbiology*, 10(9):2331–2343, 2008.

[118] Alice Cont, Joseph Vermeil, and Alexandre Persat. Mechanoregulation of biofilm architecture promotes pseudomonas aeruginosa antibiotic tolerance. *bioRxiv*, 2022.

[119] Japinder Nijjer, Changhao Li, Qiuting Zhang, Haoran Lu, Sulin Zhang, and Jing Yan. Self-patterning in bacterial biofilms: A mechanical blueprint. *arXiv e-prints*, pages arXiv–2104, 2021.

[120] William PJ Smith, Yohan Davit, James M Osborne, Wook Kim, Kevin R Foster, and Joe M Pitt-Francis. Cell morphology drives spatial patterning in microbial communities. *Proceedings of the National Academy of Sciences*, 114(3):E280–E286, 2017.

[121] Alice Cont, Tamara Rossy, Zainebe Al-Mayyah, and Alexandre Persat. Biofilms deform soft surfaces and disrupt epithelia. *Elife*, 9:e56533, 2020.

[122] Katharine Z Coyte, Hervé Tabuteau, Eamonn A Gaffney, Kevin R Foster, and William M Durham. Microbial competition in porous environments can select against rapid biofilm growth. *Proceedings of the National Academy of Sciences*, 114(2):E161–E170, 2017.

[123] Cyril Guilhen, Christiane Forestier, and Damien Balestrino. Biofilm dispersal: multiple elaborate strategies for dissemination of bacteria with unique properties. *Molecular microbiology*, 105(2):188–210, 2017.

[124] J áB Kaplan. Biofilm dispersal: mechanisms, clinical implications, and potential therapeutic uses. *Journal of dental research*, 89(3):205–218, 2010.

[125] Derek Fleming and Kendra P Rumbaugh. Approaches to dispersing medical biofilms. *Microorganisms*, 5(2):15, 2017.

[126] Jing Lu, Nural N Cokcetin, Catherine M Burke, Lynne Turnbull, Michael Liu, Dee A Carter, Cynthia B Whitchurch, and Elizabeth J Harry. Honey can inhibit and eliminate biofilms produced by pseudomonas aeruginosa. *Scientific reports*, 9(1):1–13, 2019.

[127] Hangjian Ling, Guillam E Mclvor, Kasper van der Vaart, Richard T Vaughan, Alex Thornton, and Nicholas T Ouellette. Local interactions and their group-level consequences in flocking jackdaws. *Proceedings of the Royal Society B*, 286(1906):20190865, 2019.

[128] Irene Giardina. Collective behavior in animal groups: theoretical models and empirical studies. *HFSP journal*, 2(4):205–219, 2008.

[129] William H Warren. Collective motion in human crowds. *Current directions in psychological science*, 27(4):232–240, 2018.

[130] Andrew Berdahl, Anieke van Leeuwen, Simon A Levin, and Colin J Torney. Collective behavior as a driver of critical transitions in migratory populations. *Movement ecology*, 4(1):1–12, 2016.

[131] M Cristina Marchetti, Jean-François Joanny, Sriram Ramaswamy, Tanniemola B Liverpool, Jacques Prost, Madan Rao, and R Aditi Simha. Hydrodynamics of soft active matter. *Reviews of modern physics*, 85(3):1143, 2013.

[132] Sriram Ramaswamy. The mechanics and statistics of active matter. *Annu. Rev. Condens. Matter Phys.*, 1(1):323–345, 2010.

[133] Denis Andrienko. Introduction to liquid crystals. *Journal of Molecular Liquids*, 267:520–541, 2018.

[134] Oliver J. Meacock. Collective twitching motility in *Pseudomonas aeruginosa* and its evolutionary consequences, 2018.

[135] Amin Doostmohammadi, Sumesh P Thampi, and Julia M Yeomans. Defect-mediated morphologies in growing cell colonies. *Physical review letters*, 117(4):048102, 2016.

[136] Kristian Thijssen and Amin Doostmohammadi. Binding self-propelled topological defects in active turbulence. *Physical Review Research*, 2(4):042008, 2020.

[137] Dario Cortese, Jens Eggers, and Tanniemola B Liverpool. Pair creation, motion, and annihilation of topological defects in two-dimensional nematic liquid crystals. *Physical Review E*, 97(2):022704, 2018.

[138] Aboutaleb Amiri, Romain Mueller, and Amin Doostmohammadi. Unifying polar and nematic active matter: emergence and co-existence of half-integer and full-integer topological defects. *Journal of Physics A: Mathematical and Theoretical*, 55(9):094002, 2022.

[139] Amin Doostmohammadi, Tyler N Shendruk, Kristian Thijssen, and Julia M Yeomans. Onset of meso-scale turbulence in active nematics. *Nature communications*, 8(1):1–7, 2017.

[140] Amin Doostmohammadi, Michael F Adamer, Sumesh P Thampi, and Julia M Yeomans. Stabilization of active matter by flow-vortex lattices and defect ordering. *Nature communications*, 7(1):1–9, 2016.

[141] Kristian Thijssen, Luuk Metselaar, Julia M Yeomans, and Amin Doostmohammadi. Active nematics with anisotropic friction: the decisive role of the flow aligning parameter. *Soft Matter*, 16(8):2065–2074, 2020.

[142] D Dell'Arciprete, ML Blow, AT Brown, FDC Farrell, Juho S Lintuvuori, AF McVey, D Marenduzzo, and Wilson CK Poon. A growing bacterial colony in two dimensions as an active nematic. *Nature communications*, 9(1):1–9, 2018.

[143] Thuan Beng Saw, Amin Doostmohammadi, Vincent Nier, Leyla Kocgozlu, Sumesh Thampi, Yusuke Toyama, Philippe Marcq, Chwee Teck Lim, Julia M Yeomans, and Benoit Ladoux. Topological defects in epithelia govern cell death and extrusion. *Nature*, 544(7649):212–216, 2017.

[144] Yonit Maroudas-Sacks, Liora Garion, Lital Shani-Zerbib, Anton Livshits, Erez Braun, and Kinneret Keren. Topological defects in the nematic order of actin fibres as organization centres of hydra morphogenesis. *Nature Physics*, 17(2):251–259, 2021.

[145] Katherine Copenhagen, Ricard Alert, Ned S Wingreen, and Joshua W Shaevitz. Topological defects promote layer formation in myxococcus xanthus colonies. *Nature Physics*, 17(2):211–215, 2021.

[146] Yilin Wu, A Dale Kaiser, Yi Jiang, and Mark S Alber. Periodic reversal of direction allows myxobacteria to swarm. *Proceedings of the National Academy of Sciences*, 106(4):1222–1227, 2009.

[147] Varun Venkatesh, Chandana Mondal, and Amin Doostmohammadi. Distinct impacts of polar and nematic self-propulsion on active unjamming. *The Journal of Chemical Physics*, 157(16):164901, 2022.

[148] Elisa T Granato and Kevin R Foster. The evolution of mass cell suicide in bacterial warfare. *Current Biology*, 30(14):2836–2843, 2020.

[149] Erin S Gloag, Lynne Turnbull, Alan Huang, Pascal Vallotton, Huabin Wang, Laura M Nolan, Lisa Mililli, Cameron Hunt, Jing Lu, Sarah R Osvath, et al. Self-organization of bacterial biofilms is facilitated by extracellular dna. *Proceedings of the National Academy of Sciences*, 110(28):11541–11546, 2013.

[150] Binjie Xu and Daniel J Wozniak. Development of a novel method for analyzing pseudomonas aeruginosa twitching motility and its application to define the amrz regulon. *PLoS One*, 10(8):e0136426, 2015.

[151] Sebastian Zobel, Ilaria Benedetti, Lara Eisenbach, Victor de Lorenzo, Nick Wierckx, and Lars M Blank. Tn7-based device for calibrated heterologous gene expression in pseudomonas putida. *ACS synthetic biology*, 4(12):1341–1351, 2015.

[152] Howard M Salis, Ethan A Mirsky, and Christopher A Voigt. Automated design of synthetic ribosome binding sites to control protein expression. *Nature biotechnology*, 27(10):946–950, 2009.

[153] Xiaoying Chen, Jennica L Zaro, and Wei-Chiang Shen. Fusion protein linkers: property, design and functionality. *Advanced drug delivery reviews*, 65(10):1357–1369, 2013.

[154] Kyoung-Hee Choi and Herbert P Schweizer. mini-tn7 insertion in bacteria with single atttn7 sites: example pseudomonas aeruginosa. *Nature protocols*, 1(1):153–161, 2006.

[155] Robert D Deegan, Olgica Bakajin, Todd F Dupont, Greb Huber, Sidney R Nagel, and Thomas A Witten. Capillary flow as the cause of ring stains from dried liquid drops. *Nature*, 389(6653):827–829, 1997.

[156] Johannes Schindelin, Ignacio Arganda-Carreras, Erwin Frise, Verena Kaynig, Mark Longair, Tobias Pietzsch, Stephan Preibisch, Curtis Rueden, Stephan Saalfeld, Benjamin Schmid, et al. Fiji: an open-source platform for biological-image analysis. *Nature methods*, 9(7):676–682, 2012.

[157] Tugba Andac, Pascal Weigmann, Sabareesh KP Velu, Erçağ Pinçe, Giorgio Volpe, Giovanni Volpe, and Agnese Callegari. Active matter alters the growth dynamics of coffee rings. *Soft Matter*, 15(7):1488–1496, 2019.

[158] William Thielicke. The flapping flight of birds. *Diss. University of Groningen*, 2014.

[159] William Thielicke and René Sonntag. Particle image velocimetry for matlab: Accuracy and enhanced algorithms in pivlab. *Journal of Open Research Software*, 9(1), 2021.

[160] William Thielicke and Eize Stamhuis. Pivlab–towards user-friendly, affordable and accurate digital particle image velocimetry in matlab. *Journal of open research software*, 2(1), 2014.

[161] Yaroslav Ispolatov. Collective behaviour: Computing in fish schools. *ELife*, 5:e12852, 2016.

[162] Tamás Vicsek and Anna Zafeiris. Collective motion. *Physics reports*, 517(3-4):71–140, 2012.

[163] Gerhard Gompper, Roland G Winkler, Thomas Speck, Alexandre Solon, Cesare Nardini, Fernando Peruani, Hartmut Löwen, Ramin Golestanian, U Benjamin Kaupp, Luis Alvarez, et al.

The 2020 motile active matter roadmap. *Journal of Physics: Condensed Matter*, 32(19):193001, 2020.

[164] Daniel B Kearns, Jayne Robinson, and Lawrence J Shimkets. Pseudomonas aeruginosa exhibits directed twitching motility up phosphatidylethanolamine gradients. *Journal of bacteriology*, 183(2):763–767, 2001.

[165] Wenlong Zuo and Yilin Wu. Dynamic motility selection drives population segregation in a bacterial swarm. *Proceedings of the National Academy of Sciences*, 117(9):4693–4700, 2020.

[166] Rahul Marathe, Claudia Meel, Nora C Schmidt, Lena Dewenter, Rainer Kurre, Lilo Greune, M Alexander Schmidt, Melanie JI Müller, Reinhard Lipowsky, Berenike Maier, et al. Bacterial twitching motility is coordinated by a two-dimensional tug-of-war with directional memory. *Nature communications*, 5(1):1–10, 2014.

[167] Kazumasa Takeuchi and Takuro Shimaya. 3d-induced polar order and topological defects in growing bacterial populations. *Bulletin of the American Physical Society*, 2022.

[168] L Huber, R Suzuki, T Krüger, E Frey, and AR Bausch. Emergence of coexisting ordered states in active matter systems. *Science*, 361(6399):255–258, 2018.

[169] Takuro Shimaya and Kazumasa A Takeuchi. 3d-induced polar order and topological defects in growing bacterial populations. *arXiv preprint arXiv:2106.10954*, 2021.

[170] Daniel B Kearns and Lawrence J Shimkets. Chemotaxis in a gliding bacterium. *Proceedings of the National Academy of Sciences*, 95(20):11957–11962, 1998.

[171] Kyogo Kawaguchi, Ryoichiro Kageyama, and Masaki Sano. Topological defects control collective dynamics in neural progenitor cell cultures. *Nature*, 545(7654):327–331, 2017.

[172] Henricus H Wensink, Jörn Dunkel, Sebastian Heidenreich, Knut Drescher, Raymond E Goldstein, Hartmut Löwen, and Julia M Yeomans. Meso-scale turbulence in living fluids. *Proceedings of the national academy of sciences*, 109(36):14308–14313, 2012.

[173] Qiang Du, Vance Faber, and Max Gunzburger. Centroidal voronoi tessellations: Applications and algorithms. *SIAM review*, 41(4):637–676, 1999.

[174] Philip S Stewart and Michael J Franklin. Physiological heterogeneity in biofilms. *Nature Reviews Microbiology*, 6(3):199–210, 2008.

[175] Berenike Maier and Gerard CL Wong. How bacteria use type iv pili machinery on surfaces. *Trends in microbiology*, 23(12):775–788, 2015.

[176] Siavash Monfared, Guruswami Ravichandran, José E Andrade, and Amin Doostmohammadi. Mechanics of live cell elimination. *arXiv preprint arXiv:2108.07657*, 2021.

[177] Hugo Wioland, Enkeleida Lushi, and Raymond E Goldstein. Directed collective motion of bacteria under channel confinement. *New Journal of Physics*, 18(7):075002, 2016.

[178] Laurent Potvin-Trottier, Scott Luro, and Johan Paulsson. Microfluidics and single-cell microscopy to study stochastic processes in bacteria. *Current opinion in microbiology*, 43:186–192, 2018.

[179] James H. R. Wheeler. Navigation of surface-motile bacteria in developing bacterial biofilms, 2019.

[180] Jean-Yves Tinevez, Nick Perry, Johannes Schindelin, Genevieve M Hoopes, Gregory D Reynolds, Emmanuel Laplantine, Sebastian Y Bednarek, Spencer L Shorte, and Kevin W Eliceiri. Trackmate: An open and extensible platform for single-particle tracking. *Methods*, 115:80–90, 2017.

[181] Yifat Brill-Karniely, Fan Jin, Gerard CL Wong, Daan Frenkel, and Jure Dobnikar. Emergence of complex behavior in pili-based motility in early stages of p. aeruginosa surface adaptation. *Scientific reports*, 7(1):1–10, 2017.

[182] RN Bearon and WM Durham. A model of strongly biased chemotaxis reveals the trade-offs of different bacterial migration strategies. *Mathematical Medicine and Biology: A Journal of the IMA*, 37(1):83–116, 2020.

[183] Douglas R Brumley, Francesco Carrara, Andrew M Hein, Yutaka Yawata, Simon A Levin, and Roman Stocker. Bacteria push the limits of chemotactic precision to navigate dynamic chemical gradients. *Proceedings of the National Academy of Sciences*, 116(22):10792–10797, 2019.

[184] Momir Futo, Tin Široki, Sara Koska, Nina Čorak, Anja Tušar, Mirjana Domazet-Lošo, and Tomislav Domazet-Lošo. A novel time-lapse imaging method for studying developing bacterial biofilms. *Scientific Reports*, 12(1):21120, 2022.

[185] Andres Plata Stapper, Giri Narasimhan, Dennis E Ohman, Johnny Barakat, Morten Hentzer, Søren Molin, Arsalan Kharazmi, Niels Høiby, and Kalai Mathee. Alginate production affects

pseudomonas aeruginosa biofilm development and architecture, but is not essential for biofilm formation. *Journal of medical microbiology*, 53(7):679–690, 2004.

[186] Daniel Grünbaum. The logic of ecological patchiness. *Interface Focus*, 2(2):150–155, 2012.

[187] Annette E LaBauve and Matthew J Wargo. Growth and laboratory maintenance of pseudomonas aeruginosa. *Current protocols in microbiology*, 25(1):6E–1, 2012.

[188] Di Wang, Anming Xu, Claudine Elmerich, and Luyan Z Ma. Biofilm formation enables free-living nitrogen-fixing rhizobacteria to fix nitrogen under aerobic conditions. *The ISME journal*, 11(7):1602–1613, 2017.

[189] Fei Chen, Julia Ricken, Dongdong Xu, and Seraphine V Wegner. Bacterial photolithography: patterning escherichia coli biofilms with high spatial control using photocleavable adhesion molecules. *Advanced Biosystems*, 3(3):1800269, 2019.